Title

Multiphase Chemical Kinetics in Aqueous Microdroplets

Permalink

https://escholarship.org/uc/item/9s99998n

Author

Prophet, Alexander

Publication Date

2024

Multiphase Chemical Kinetics in Aqueous Microdroplets

by

Alexander M. Prophet

A dissertation submitted in partial satisfaction of the
requirements for the degree of
Doctor of Philosophy
in
Chemistry
in the
Graduate Division
of the
University of California, Berkeley

Committee in charge:
Dr. Kevin R. Wilson, co-chair
Professor Richard J. Saykally, co-chair
Professor David T. Limmer
Professor Allen H. Goldstein
Summer 2024

Multiphase Chemical Kinetics in Aqueous Microdroplets

Abstract

Multiphase Chemical Kinetics in Aqueous Microdroplets

by

Alexander M. Prophet

Doctor of Philosophy in Chemistry

University of California, Berkeley

Dr. Kevin R. Wilson, Co-chair

Professor Richard J. Saykally, Co-chair

Multiphase chemistry occurs when reactivity involves two or more distinct phases. Chemical transformations of this kind are ubiquitous in all domains of science, with particular relevance to environmental and biological chemistry. Aerosols, including cloud droplets, sea-spray, smoke, and dust are prime examples of gas-liquid and gas-solid systems that undergo heterogeneous chemical changes while persisting in the atmosphere. A fundamental understanding of how multiphase reactions proceed is critical, then, to the study of our environment and the causal networks between anthropogenic activity, global ecosystems, and atmospheric composition. Moreover, a mechanistic perspective of reactivity in gas-liquid or gas-solid systems provides a useful framework for the study of multiphase interactions more generally, even informing on similar mechanics encountered in liquid-liquid and solid-liquid systems.

In this work, experiment and theory are brought together to develop a kinetic framework of multiphase reactivity in aqueous microdroplets with particular focus on the role of the air-water interface. The experiments presented investigate the ozone-oxidation of aqueous sodium iodide contained in levitated microdroplets. This system is not only relevant to oxidation reactions in the environment, but also a compelling platform for studying mass-transfer across the air-water interface due to its unique reactive properties. As explored in Chapters 2 and 3, both I^- and O_3 possess a unique affinity for the air-water interface relative to their bulk phases, which directly affects the chemical kinetics at the microdroplet surface. This effect is studied by measuring microdroplet-oxidation kinetics while varying the solution pH and the concentration of both reactants. Experiments in Chapter 4 perturb this surface chemistry by the addition of surfactant to the microdroplet solution—effectively suppressing the surface reaction and producing a kinetic signature consistent with a diffusion limited reaction rate in the bulk phase. Insights from the specific systems in Chapters 2-4 provide the basis for a general framework of mass-transport and chemical reactivity in microdroplets which is developed in Chapter 5. This work aims to provide a route to analyzing an array of multiphase experiments from a critical lens by disentangling the underlying physical and chemical phenomena.

Acknowledgements

I owe many thanks to those who have supported me during this work. I'm incredibly fortunate to have had the guidance of my advisor Kevin—whose advice and encouragement has provided me with ongoing inspiration and resilience. Likewise, Rich's boundless enthusiasm for science and music has motivated me to see much of this work through. Both advisors have greatly influenced my perspective on the philosophy and application of science, for which I'll always be grateful. I also owe great thanks to all past and present members of the Wilson and Saykally research groups, whose contributions have provided practical and intellectual support to this work along with many of the foundations on which it was built. Similarly, I'd like to thank all of my collaborators who have expanded the horizon of this work and inspired me to pursue a number of different research avenues.

Lastly, I am greatly indebted to the endless support from all my friends and family—without your encouragement, none of this would have been possible.

It’s the same story the crow told me; it’s the only one he knows.
Like the morning sun you come and like the wind you go.
—Robert Hunter

Table of Contents

Chapter Number & Title *Page Number*

Chapter 1: Introduction

Chapter 2: Iodide Oxidation by Ozone at the Surface of Aqueous Microdroplets

Chapter 3: Distinguishing Surface and Bulk Reactivity—Concentration Dependent Kinetics of Iodide Oxidation in Microdroplets

Chapter 4: Surfactant Adsorption Inhibits Surface Reactions in Aqueous Microdroplets

Chapter 5: A General Kinetic Description of Multiphase Chemistry in Microdroplets

Chapter 1: Introduction

1.1: Multiphase and Microdroplet Chemistry

1.1.A: *Overview*

The subject of chemistry universally invokes images of beakers and flasks filled with liquids—the chemist mixing, stirring, and heating them in various proportions. Most of us first encounter remedial chemistry in a similar context while performing titrations or simple one-pot syntheses. Wet chemistry of this type, involving a single phase, becomes vanishingly rare when considering the complex systems encountered in reality, from the environment around us to the mechanics of our own biology. Some familiar examples of multiphase processes include ocean acidification by uptake of CO_2 on the sea-surface,[1–3] the formation of smog over densely populated regions,[4–6] conversion of carbon dioxide and water to O_2 by photosynthesis, and the absorption of particulate matter, pollutants, and bioaerosol into the mammalian respiratory tract.[7–9] The latter has major implications in light of the COVID-19 pandemic that emerged in early 2020, as the primary route to infection is understood to occur through viral transmission via exhaled aerosol.[10–12] Major efforts have since explored how exhaled droplets and finer aerosol originating from the respiratory system undergo multiphase transformations driven by ambient conditions such as humidity, temperature, and the trace gas composition of the suspending air.[13–16] Such chemical transformations in turn directly affect the viability of included viruses (and other microorganisms), ultimately influencing infectivity and the efficiency of transmission between individuals.

On a global scale, multiphase interactions between the Earth's surface and the atmosphere span an incredibly broad range—from familiar phenomena like the hydrologic cycle and weather patterns to more subtle effects like the influence of ground emissions on cloud formation and the oxidizing capacity of the atmosphere. Microscopic aerosol particles in the atmosphere are known to have a direct effect on climate through the scattering or absorption of radiation in the atmosphere.[17–20] Additionally, particulates have an indirect effect on climate through their influence on cloud formation and precipitation—ultimately altering the intensity of radiation reaching the Earth's surface.[21–24] Macro-scale regions of the Earth's surface like oceans, deserts, and forests also have unique contributions to the global environment intimately tied with multiphase transport and chemistry. Covering over 70% of the Earth, the sea-surface plays a critical role in exchanging volatile chemicals with the marine atmosphere[25] where complex (photo)chemistry occurs.[26,27] Deposition of oxidants such as O_3 onto the ocean surface[28] regulates the chemical makeup of the atmosphere—as the oxidizing capacity ultimately regulates the lifetime of both gas- and condensed- phase species.[29–31] Arid regions of the Earth, on the other hand, emit massive amounts of inorganic and organic matter into the atmosphere through dust storm activity,[32,33] having local impacts on agriculture and respiratory health[34,35] and global impacts on the transport of inorganic materials. Minerals and nutrients such as iron, phosphorous, and magnesium originating from the Sahara, for instance, are found in Amazonian rainforests, providing an important source of nutrients for both the flora of the canopy and microorganisms in the forest soil.[36,37]

Likewise, the study of ecology is rich with examples of dynamic multiphase interactions. Chemical signaling is known to occur between both the leaves of nearby trees[38,39] and between neighboring plant roots and microorganisms in the soil.[40,41] In such environments, the distribution of acidity, nutrients, and hormones (ultimately governed by gas and aqueous diffusion in damp soils)[42] provides a route for organisms to exchange information pertaining to environmental perturbations.[43] Lastly, multiphase applications abound in biology—many of them fundamental to our own existence. On the cellular level, not only does the distinct boundary of the cell wall permit the electrochemical gradient necessary for cellular function, but recent work has demonstrated the central role of liquid-liquid phase separation (LLPS) within the cell.[44–46] LLPS underlies the formation of numerous membrane-less organelles involved in cellular signaling, DNA repair, disease prevention, and immune responses.[47] While still an emerging field, work to date suggests that understanding the mechanisms of phase-separation in cells and the underlying chemistry that emerges in relation to cellular function will provide insight into an array of applications to human health.[48,49]

Multiphase systems envelop virtually every aspect of our lived experience and are practically unavoidable in chemistry and biology. As these systems by definition contain distinct domains and often complex mixtures, multiphase research in the field of physical chemistry has sought to identify general trends and descriptions for the mechanisms that dictate their physicochemical evolution. Of course, the identification of generality and achieving a broad understanding invariably begins with establishing the mechanics for specific systems. The chemistry of aerosol—liquids or solids suspended in a gas—will be the focus of the current work. This particular realm of multiphase chemistry can also be classified under the study of "microcompartments" in general, concerning chemistry or physics occurring in micron-sized volumes.

1.1.B: Reactivity in Microcompartments, Uniqueness and Complications

Chemical reactivity in microcompartments, while present in many of the examples above, has a number of features that motivate scientific inquiry on its own. One that appeals to a physical chemist is the fact that microdroplets provide a relatively simple platform to probe aspects of gas-liquid interactions and the chemical reactivity of liquid surfaces. A key property of microdroplets compared to macroscopic liquids is their high surface area-to-volume ratio, resulting in a larger fraction of the total molecular makeup residing at the phase boundary for decreasing droplet radii. A simple calculation illustrated in Fig. 1.1 demonstrates how dramatic this effect is. Consider 1 liter of water contained in a standard glass beaker; the surface area of water exposed to the air would be ~ 100 cm^2 or so. Imagine this 1 liter of water is then "aerosolized" such that the initial volume is broken up into a uniform cloud of droplets, each possessing a radius of 10 μm. The amount of surface area exposed to air is now ~ 3000 m^2. Given that the surface-to-volume ratio for the cloud droplets is ~ 10^5 times greater than that of the beaker, we would expect any effects of the interface to be markedly more pronounced in the former than the latter. Indeed, this principle is perhaps the defining feature in the study of microcompartments. Throughout Chapters 2-5 we encounter a number of consequences derived from this principle, which can be broadly considered as impacting two important domains: (1) physical timescales involved in the gas-liquid equilibration process and (2) chemical properties of the interface such as altered reaction kinetics due to unique thermodynamics and concentration profiles.

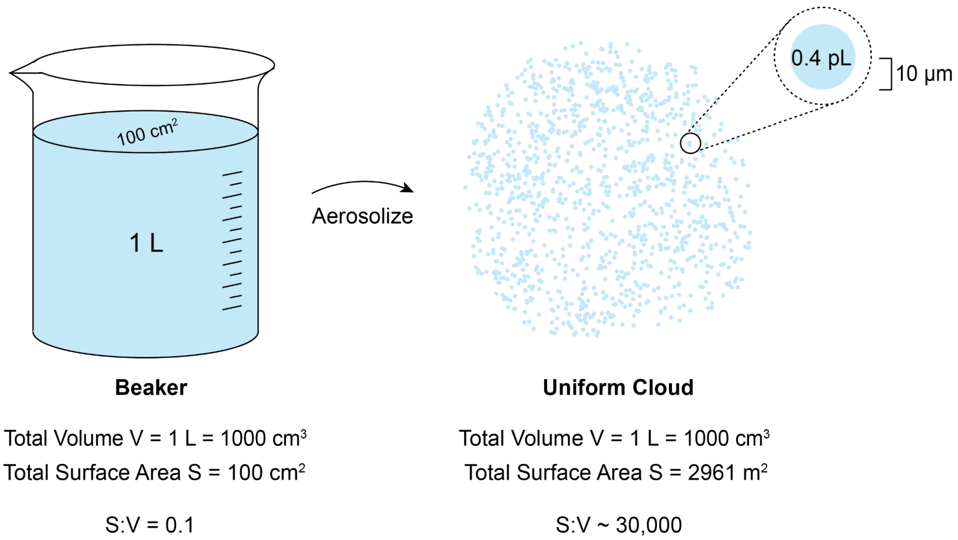

Fig. 1.1: Comparison of the surface-to-volume ratio (S:V) for a macroscopic system and a micron-scale system. The total amount of surface area for the cloud composed of droplets with radius r = 10 μm is over 10^5 times greater than the surface area of the same volume of water in a standard-sized beaker.

The first domain has long been recognized as a central aspect for studying the transformation of atmospheric aerosol.[50–53] Over the past decade, however, a staggering number of reports have invoked elements of the second domain of interfacial chemistry to explain an array of chemical phenomena. A large fraction of this body of literature has observed "enhanced" or "accelerated" reactivity in microdroplets due to the chemical uniqueness of the air-water interface.[54–56] A related branch of literature submits that this uniqueness can even promote "spontaneous" chemistry that would not generally be expected to occur in the bulk solution.[57–59] The vast majority of these reports employ an experimental approach that consists of aerosolizing a bulk solution of some reactants X and Y with an electrospray ionization (ESI) assembly or a more generic nebulization assembly directly in front of the inlet to a mass spectrometer (MS). In such experiments, researchers typically observe some product Z at a particular m/z in the mass spectrum and vary the nebulizing distance from the MS inlet to introduce a "time" dimension by estimating the velocity of the spray plume. Changes in the mass spectrum for different "times" are then analyzed to identify a rate coefficient for the reaction X + Y in microdroplets which is often remarkably "enhanced" from the known rate coefficient in a bulk aqueous solution.[60]

This type of quantitative interpretation has several ambiguities that should give pause to a physical chemist. One that immediately arises is the difficulty in quantifying the velocity of a spray plume and the size distribution of droplets. A plume of droplets generated by ESI or a nebulizer contains a broad size distribution of droplets which, along with their velocity, will be highly dependent on the particular conditions in which the spray is generated, including flow rates, capillary sizes used in the nebulizer, and ambient conditions such as temperature and humidity in the surrounding gas.[61–64] As such, accurately quantifying a time-scale and determining the surface area present in a spray plume (and even more relevant, within the actual population of droplets that are sampled by the mass spectrometer) is a difficult task that is generally not rigorously quantified in most of the microdroplet-acceleration literature. A related and perhaps more troubling aspect of this approach originates from the evaporation of microdroplets in a spray plume. After all, the original intent for placing an electrospray or a nebulizer in front of a mass spectrometer inlet was to provide a source of rapidly evaporating solution that facilitates the production of gas-phase ions amenable to analysis by a mass spectrometer.[65,66] This ionization process relies on the evaporating droplets becoming extremely small and concentrated, promoting ion ejection from the condensed phase and coulomb fission of the charged droplets producing smaller, highly charged droplets.[67–69] Work by Jacobs et al.,[70] for example, demonstrated that chemistry that was previously reported to be greatly accelerated in microdroplets[56] was more likely to originate from gas-phase chemistry occurring in parallel within the spray plume. An extensive investigation of microdroplet evaporation and gas-phase effects in the context of reaction acceleration has been undertaken by Rovelli et al.[71] in which experimental and numerical methods are used to study the timescales of microdroplet evaporation how this couples to the process of ionization, including the fission and fusion of microdroplets in a spray plume. In addition, Chen and Williams[72] show that concentration enhancement driven by microdroplet evaporation can account for factors up to 10^7 observed in apparent reaction acceleration with mass spectrometric detection.

Concurrently, a leading hypothesis to explain numerous observations of "spontaneous" microdroplet chemistry is the production of H_2O_2 at the air-water interface driven by a large, static electric field residing at the air water interface.[73–76] A related hypothesis posits that water contains low concentrations of short-lived radical water species such as the water cation which leads to what appears to be spontaneous oxidation of solutes in microdroplets.[59,77] Experimental validation of these claims have unfortunately been obscured by many of the ambiguities outlined in the previous paragraph, where key parameters such as droplet size, concentrations, droplet lifetimes, and gas-phase contributions are generally unconstrained, leading to potential artifacts.[78] In addition, a significant obstacle in this particular application is identifying the particular locale of reaction—as most spray-type microdroplet setups operate by forcing liquids through small capillaries to facilitate spray-generation. Work from Eatoo et al.[79] recently demonstrated that H_2O_2 observed in microdroplet spray-type experiments appears directly related to solid-water interfaces and the availability of dissolved O_2. Additionally, microjets of pure water have been observed to manifest charge separation, leading to a significant potential at the water-solid interface within the jetting capillary.[80,81] This "electrokinetic" effect was observed to facilitate the apparent "spontaneous" product of molecular hydrogen, suggesting that redox reactions may be particularly influenced by the presence of solid-liquid interfaces.[81] Similarly, H_2O_2 has been observed to be generated in the sonication process or simply the flow of water through a glass capillary, the chemistry of which has been dubbed "contact-electro-catalysis."[82–84] These examples illustrate that redox chemistry occurring at the solid-liquid interface cannot be ignored in experiments where microdroplet sprays are generated by a jetting process where solid-liquid interfaces are apparent.

1.1.C: A Kinetic Description of Coupled Surface and Bulk Chemistry

In an effort to disentangle the specific role of the air-water interface in purported accelerated chemistry, we have developed a chemical kinetic model framework that separates surface and bulk reactivity.[85] This framework, graphically summarized in Fig. 1.2, was deployed using the stochastic simulator Kinetiscope©, providing detailed concentration profiles for reactants over time. Further details on the use of Kinetiscope© are provided in Section 1.3 and throughout Chapters 2 and 3. Simulations run using the microdroplet reaction framework were first employed to analyze reaction acceleration in a water-oil emulsion as reported by Fallah-Araghi et al.[86] In this work, a condensation reaction between an amine and aldehyde resulting in imine formation appeared increasingly favored with decreasing droplet radius.[86] Using our kinetic framework assisted with simulations, it was found that the surface rate of reaction appeared to be a factor of ~100 greater than the bulk rate of reaction in order to agree with kinetic measurements.[85] This work further explored the kinetic consequences of an asymmetry between bulk and surface reaction rates, with focus on the radial and concentration dependence of the observed chemical kinetics. With decreasing droplet radius, simulations show that the fraction of molecules in the droplet that encounter the surface increases. Consequently, the reactivity at the surface becomes increasingly relevant for smaller droplets, with the overall observed reactivity being governed by the bulk rate of reaction in the large droplet limit, and the surface rate for the small droplet limit.

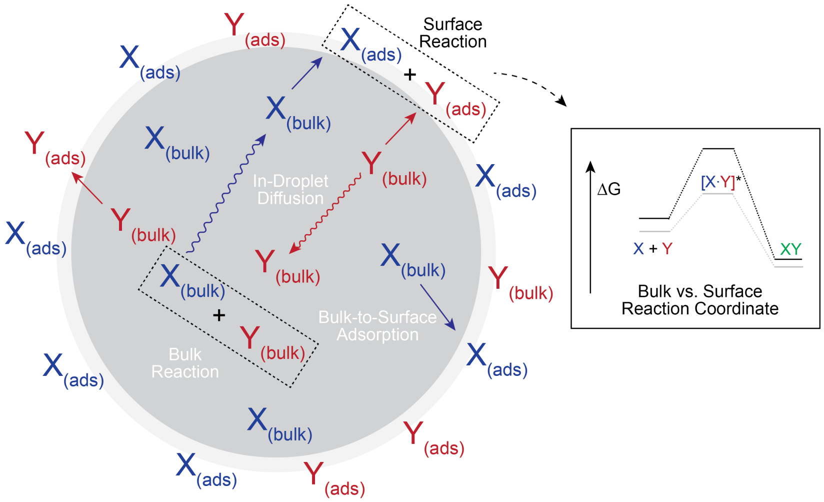

Fig. 1.2: Graphical summary of a kinetic description of chemical reactivity in microdroplets for a generic reaction X + Y. Relevant kinetic steps are labeled such as liquid diffusion inside the droplet, adsorption (or desolvation) of reactants to the surface, and reactions at the surface and in the bulk. This framework allows for the exploration of specific surface effects that are related to the thermodynamic stability of reagents at the interface and the reaction coordinate.

Since this work, a number of similar frameworks have been used to further study the impact of surface rates on bulk observed reactivity. Work by Ruiz-López and Martins-Costa has specifically investigated the origin of asymmetries in bulk vs. surface rate coefficients, with consideration of the reaction coordinate in the partial-solvation environment of the interface.[87] Within their framework, acceleration factors are defined by considering the difference in free energy for reactants, products, and transition states at the droplet surface. The behavior of observed acceleration factors can then be investigated by modifying the preference of reactant species for the interface, and the order of reaction. Similar considerations are made by Ben-Amotz,[88] with focus given to how reactant and product bulk-to-surface partitioning influences bulk properties like concentration, leading to a broad range of potential effects. Using kinetic models to investigate the origins of accelerated microdroplet chemistry in this manner provides some basis for evaluating proposed mechanisms in the "electrospray-type" acceleration or spontaneous reports discussed above. With emerging experimental techniques combined with the modeling approaches outlined here, there is increasing potential for isolating and identifying unique aspects of interfacial chemistry that have unexpected and dramatic effects on microdroplet experiments. Founded in the the kinetic basis outlined here, a consistent theme throughout the remainder of this work is the disentanglement of mass-transport phenomena like diffusion, adsorption, and evaporation from chemical effects such as distinct surface reaction kinetics.

1.2: Experimental Approaches in Microdroplet Chemistry

The field of aerosol chemistry contains a wide variety of approaches to study multiphase transformation in aqueous microdroplets, submicron organic aerosol, molecular clusters, and the precursors that generate aerosol in the atmosphere. Here we briefly outline the experimental components used in the current work, encompassing only a small fraction of techniques that are routinely employed in this field. In the following, we focus on electrodynamic trapping methods for interrogation of individual microdroplets—followed by an introduction to droplet analysis via mass spectrometry. Since these methods are also discussed alongside their application in Chapters 2-4, we focus here on the fundamentals of the techniques.

1.2.A: Quadrupole Electrodynamic Trapping and Particle Analysis

The use of electrodynamics for single-particle trapping was developed following the invention of the quadrupole mass filter used for mass spectrometry.[89] The fundamentals underlying this technique are almost identical to the operation of the quadrupole filter. The Quadrupole Electrodynamic Trap (QET) assembly[90,91] used in the current work comprises four rod-electrodes running in parallel (see Fig. 1.3A), with an AC voltage V_{ac} applied at some operating frequency ω. Adjacent electrodes are held $\varphi = 180°$ out of phase as indicated in Fig. 1.3B. The equation of motion for a charged particle with charge-to-mass ratio e/m in the direction r within this electrodynamic configuration is described by the Matthieu equation:

$$\frac{d^2 r}{d\zeta^2} - 2\, r\, q \cos 2\zeta = 0, \qquad \text{Eq. 1.1}$$

where $\zeta = \omega t/2$ and $q = {}^{4eV_{ac}}\!\big/_{m(r_0\omega)^2}$. According to Eq. 1.1, a stability point within the trap will be realized for a certain range of values q. For typical masses and charges on microdroplets encountered in this work, the stability condition applies using AC voltages ranging from ~ 100 V to ~ 5 kV and frequencies from ~ 200 Hz to ~ 5 kHz. Although not pictured in Fig. 1.3 for clarity, balancing electrodes are placed between the quadrupole rods and held at a fixed V_{DC} to counter-act gravity and the gas flow to keep the charged microdroplet levitated.

Particle trapping using this general configuration and parameter set has been used routinely by a number of different research groups for characterizing aerosol particles.[92–94] Several reports using this trapping technique deploy optical means to investigate molecular or reactive properties of the levitated particles, with fluorescence, scattering, Raman, and absorbance spectroscopy being commonly applied techniques. Analysis of scattered light from the trapped particle is of particular importance since this is routinely used to quantify the size of the levitated particle. When light of wavelength λ is scattered by a particle with a radius on the same order, the observed scattered light is termed Mie scattered light. The observed Mie scattering pattern depends highly on the radius of the scatterer, a fact that can be exploited to obtain the radius of the particle to a high degree of accuracy after collecting the Mie scattered light.[95] Fig. 1.3C provides an example of simulated perpendicular scattering intensity vs. collection angle for a series of water droplets using a wavelength of λ = 532 nm.

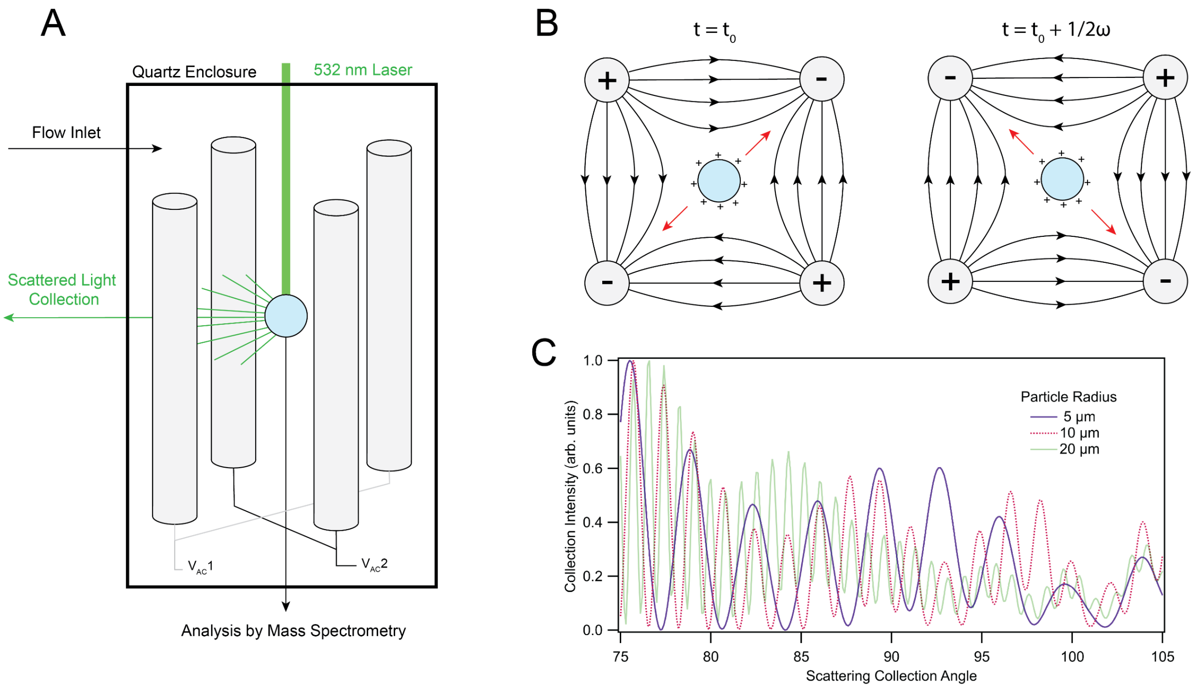

Fig. 1.3: Overview of the QET assembly and operation. Panel (A) provides a summary of the components necessary to trap and size a single charged microdroplet. In (B), electric field lines within the quadrupole are illustrated at some initial time t_0 and a half-cycle later $t_0 + 1/\,2\omega$. The red arrows show the directions of instantaneous force exerted on a positively charged microdroplet at the specified times. Given the correct ω, this system is stable in time. Panel (C) presents simulated Mie scattering patterns for microdroplets of various radius.

1.2.B: Microdroplet Analysis by Mass Spectrometry

In addition to the use of optical techniques for chemical analysis, the coupling of electrodynamic traps to particle analysis with mass spectrometry (MS) has recently been developed—opening a broader range of chemical analysis than is available with optical techniques.[96] A variety of ionization techniques can be used to ionize the contents of individual microdroplets, with recent work by Willis et al.[91] comparing the performance of soft-ionization techniques such as paper-spray ionization and thermal-desorption glow-discharge ionization. These techniques were shown to have a high degree of reproducibility for analysis of droplets of similar radius. However, a number of experimental challenges persist in operating such ionization techniques that can lead to high signal variability. One of these challenges (particularly in the study of heterogeneous chemistry) is the separation of the reactive-gas environment of the QET from the ambient environment of the ionization region. A recently developed assembly termed the open-port sampling interface (OPSI)[97] coupled to electrospray ionization (ESI) largely circumvents this issue by providing greater spatial separation between the droplet collection region and the analysis region.

Coupling the open-port sampling interface with commercially available ESI sources has been shown in numerous recent publications[98–101] to provide high-accuracy and quantitative detection of single-microdroplet events and chemical composition with mass spectrometry. Using the QET reactor combined with OPSI-MS for analysis enables the high-resolution study of heterogenous chemical kinetics—providing rich information on the decay of reactants and appearance of products due to chemical reaction within the trapped particles. To date, this approach has been applied to a number of reactions involving ozone in the gas phase, with organics such as maleic and oleic acid being analyzed in the particle phase, and inorganics like iodide, sulfite, and thiosulfate in aqueous droplets. This experimental approach is used throughout Chapters 2-4, with further information on operation and performance included therein.

1.3: Modeling Methods

1.3.A: Intro to Multiphase Chemical Kinetics

Multiphase chemical kinetics have been described using a variety of methods—each striving towards a more detailed understanding of phase interactions, surface effects, and trends in heterogeneous chemistry. In general, multiphase kinetic descriptions aim to identify a series of physical and chemical steps that govern the overall interaction. For example, the first step would typically describe the collision of gas molecules onto a liquid surface. The next is transport across the interface in parallel with surface reaction, followed by diffusion throughout the liquid in parallel with the bulk reaction. As we explore throughout this work, the coupling between mass transport and chemistry can manifest in a number of ways depending on rates of reaction and the density of reactants in the bulk phases and at the interface.

Early works studying multiphase kinetics addressed the underlying differential equations of reaction-diffusion systems to obtain concentration profiles of reactants originating from a gas phase absorbing into a solution. Work by Danckwerts and coworkers[102–104] presents analytical solutions and approximations to the governing equations under a variety of geometries and assumptions. The mathematics of much of this early work is analogous to solutions of the heat-equation, an exemplar in the study of partial differential equations. This model approach, which we've termed "continuous methods" is outlined graphically in Fig. 1.4, representing the absorption of a gas X into a liquid containing a solute Y. The solvated form of X manifests a spatial gradient as a consequence of simultaneous diffusion and reaction with Y. This approach assumes that the surface concentration of X is static and equal to the concentration that X would manifest in the liquid in the absence of Y, i.e., the concentration determined by Henry's law. While this approach can describe a number of reaction systems that approximate these underlying assumptions, increasingly advanced models have since been developed to address the molecular makeup of the surface and near-surface regions, along with how a dynamic surface can affect bulk reactivity.

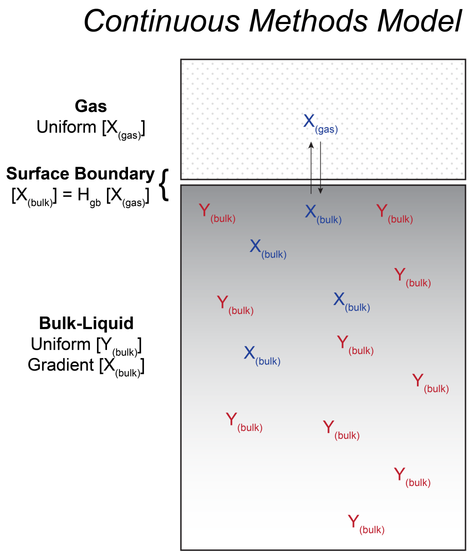

Fig. 1.4: Conceptual scheme of the simplest treatment of multiphase chemistry. Here, the concentration of X is assumed static at the liquid surface, allowing for a solution to the reaction-diffusion equation describing transport of X through the bulk-liquid.

A development in early treatments of multiphase chemistry came with the reckoning of these continuous descriptions with the inherent molecularity of processes at interface. Work from Schwartz[50] and Schwartz & Freiberg[51] pioneered the modern treatment of multiphase chemistry by positing the elementary molecular processes for transport at the interface. This approach introduced the concept of wedding molecular or more discrete treatments of interfacial models with continuous-type descriptions encountered in the standard treatment of reaction-diffusion systems. As outlined by Schwartz[50] and further formulated by Davidovits and coworkers,[105–107] and Hanson and coworkers,[108,109] the consideration of multiphase interactions can be conceptualized with a series of elementary steps. Gas molecules impinging onto a liquid surface can either adsorb to the surface and become thermally accommodated, or scatter off the liquid surface back into the gas phase. The coefficient σ generally referred to as the "sticking coefficient" describes the probability that the gas molecule adsorbs to the surface rather than scatters away. For water surfaces under ambient conditions, σ is typically close to 1. After adsorbing to the liquid surface (which we consider to be synonymous with thermalizing with the surface) the molecule will reside at the interface before either dissolving into the bulk of the liquid phase or desorbing back off the surface into the gas phase. The coefficient α referred to as the "accommodation coefficient" denotes the probability that this surface-bound molecule will solvate into the liquid before desorbing off the surface. After solvating, transport through the liquid phase can be treated using standard diffusional descriptions.

In the field of multiphase chemistry, the uptake coefficient γ is a ubiquitous quantity that is used to describe the overall efficiency of this absorption process in the face of chemical reactions. The uptake coefficient denotes the probability that an impinging gas molecule will be "taken-up" by the liquid either by solvation or by reaction with some solute molecule. From a kinetic point of view, γ can be thought of as the ratio of the number of gas molecules that solvate or react to the number of gas molecules that collide with the surface. Various contributions to the uptake coefficient originating from distinct processes are often accounted for using the widely used "resistor" model, outlined conceptually in Fig. 1.5. In this model, individual contributions to the overall uptake γ are modeled in analogy to resistors in an electrical circuit. For example, using the formalism of Shi et al.,[110] the "resistance" due to the accommodation of the impinging gas ($1/\alpha'$) results from the sum of the resistance of the sticking process ($1/\sigma$) and the resistance of the solvation process

$$\frac{1}{\alpha'} = \frac{1}{\sigma} + \frac{k_{des}}{\sigma\, k_{solv}}. \qquad \text{Eq. 1.2}$$

We note that convention for this particular process varies in the literature, with α in more recent works being defined strictly as the probability of solvation $\alpha = \frac{k_{solv}}{k_{des}+k_{solv}}$, as opposed to earlier works defining the mass accommodation coefficient as the combined process α' expressed in Eq. 1.2. Using the updated α terminology, we can think of uptake due to the accommodation process γ_{accom}, or the probability that an impinging gas will solvate into the bulk-liquid, as the product

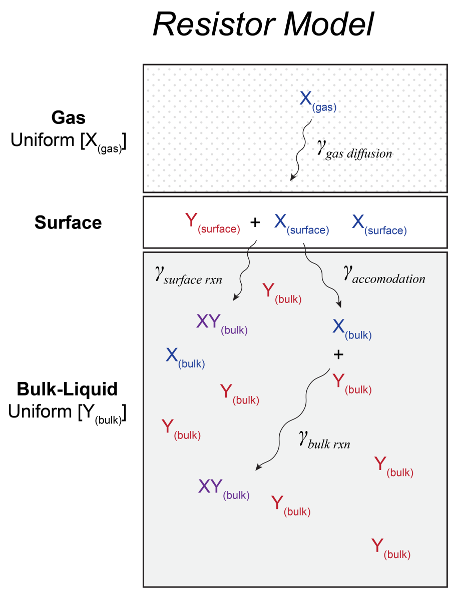

Fig. 1.5: Conceptual scheme of the resistor model of multiphase chemistry. Elementary contributions to the overall uptake γ are denoted in each spatial region.

$$\gamma_{accom} = \sigma \cdot \alpha. \qquad \text{Eq. 1.3}$$

Note that γ_{accom} in Eq. 1.3 is mathematically equivalent to α' defined in the resistor formulation Eq. 1.2. Using the resistor model approach, the "resistance" resulting from α' or γ_{accom} is just one of many potential contributions to the overall observed uptake γ_{obs}, as illustrated in Fig. 1.5. For example, the resistance of the observed uptake may include contributions from gas-phase diffusion and reaction in the bulk-liquid:

$$\frac{1}{\gamma_{obs}} = \frac{1}{\gamma_{diff}^{gas}} + \frac{1}{\gamma_{accom}} + \frac{1}{\gamma_{rxn}^{liq}}. \qquad \text{Eq. 1.4}$$

For an overview of the different processes contributing to γ_{obs}, see Worsnop et al.[107] While this formalism has proven to be incredibly useful in the development and application of chemical kinetic models in multiphase chemistry, we note that identifying the correct expression for an elementary processes to hold in Eq. 1.4 is not always trivial and can lead to potential confusion in model application.

1.3.B: Framework for Multiphase Kinetic Model

The framework used to address multiphase chemical kinetics in this work builds off the earlier approaches outlined above. In all of these approaches, the rate of reaction between two reagents X and Y is described by the bimolecular rate law

$$\frac{d[\mathrm{Y}]}{dt} = \frac{d[\mathrm{X}]}{dt} = -k_{rxn} \cdot [\mathrm{Y}][\mathrm{X}] \qquad \text{Eq. 1.5}$$

which relates the rate of loss of concentration of [Y] and [X] with the concentrations themselves. In the current work, this rate law is defined in separable spatial regions which we identify as having unique concentrations of [X] and [Y] which are defined in reference to the species' mass-transport behavior. To obtain the relevant concentrations in each region, a steady-state analysis approach is used in which kinetic coefficients describing mass-transport steps in and out of a particular spatial region are combined in an expression with the reaction rate coefficient to obtain steady-state [X] or [Y]. Here, we briefly outline these mass-transport descriptions for a gas X and a solute Y in a model microdroplet system. This model, which we term "coupled-equilibria" as shown Fig. 1.6 will be explored extensively in Chapter 5 where we obtain expressions for uptake coefficients under a range of conditions.

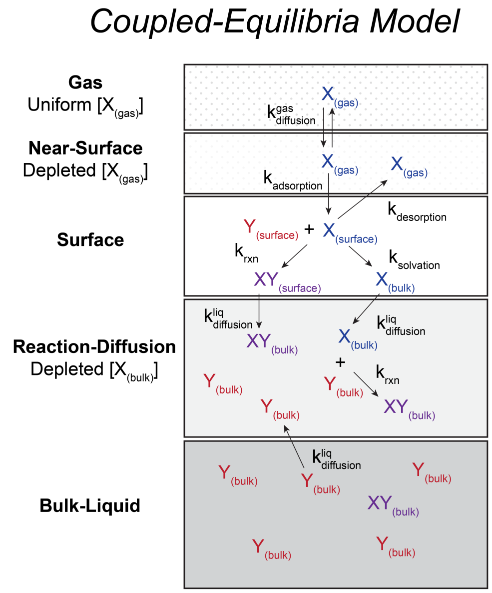

Fig. 1.6: Graphical scheme of the coupled-equilibria or spatially discrete model that we employ throughout this work.

(i) Mass Transport of Gas X

To introduce the transport kinetics of X and Y for this generic system, we use a spatial description involving three separable regions: the gas phase, the interface, and the liquid phase. Fig. 1.6 shows how the near-surface regions of the gas and liquid can also be considered as discrete regions. This complexity is explored in more detail throughout Chapter 3-5, but for now, we consider a simplified description to outline the fundamental transport steps. The diffusional description of X or Y moving between adjacent regions follows a general diffusion description replicating the diffusion mechanics of Kinetiscope© and treated explicitly in Appendix 5A. For example, the loss rate of $[X_g]$ in the gas compartment (length L_g) due to diffusion of X into the surface compartment (length L_s) is expressed with a discretized formulation of Fick's law of diffusion

$$\frac{d[\mathrm{X}_g]}{dt} = -\frac{2\, D_{gas}^{X}\left([\mathrm{X}_g] - [\mathrm{X}_s]\right)}{L_g + L_s}, \qquad \text{Eq. 1.6}$$

where D_{gas}^{X} is the diffusion coefficient of X in the gas phase. As we will encounter in Chapters 3-5, the treatment of gas-phase diffusion is complicated by the fact of spatial geometry and flow considerations over length scales on the order of the microdroplet radius. This fact is investigated in full detail in Appendix 5C, where a more detailed description is provided.

Nonetheless, once reactant X has diffused to the liquid surface, adsorption to the surface is described using a Langmuir Adsorption model, where the species can adsorb to a surface site:

$$\mathrm{X}_{(gas)} + \mathrm{site}_{\mathrm{X}} \underset{k_{des}}{\overset{k_{ads}}{\rightleftarrows}} \mathrm{X}_{(ads)}. \qquad \text{S1.1}$$

The maximum concentration of sites in this framework is generally defined using the molecular area A_{X} for species X, modified to a volumetric concentration using the thickness of the interface:

$$[\mathrm{site}_{\mathrm{X}}]_{max} = \frac{1}{A_{\mathrm{X}}\, \delta}. \qquad \text{Eq. 1.7}$$

Here we assume that the thickness of the interface is $\delta \sim 1$ nm, an approximation determined by the length of density attenuation across the air-water interface as discussed more in Chapters 2 & 3. The coefficient k_{ads} is chosen such that the pseudo-first order adsorption rate is consistent with the collision frequency obtained by a simple Maxwellian picture of molecular translation:

$$[\mathrm{site}_{\mathrm{X}}]_{max} \cdot k_{ads} = \sigma \cdot \frac{\bar{c}}{4}, \qquad \text{Eq. 1.8}$$

where $\bar{c}$ is the average velocity of X in the gas phase and σ the sticking coefficient introduced in the previous section. See Chapter 5 and related Appendices 5B & 5C for more detailed information on the choice of k_{ads} and how gas-phase diffusion is treated in the current model. The desorption rate, k_{des} can be related to the average molecular lifetime at the interface, $\tau = \frac{1}{k_{des}}$, which is on the order of ~10-100 ps for many gases on water surfaces under ambient atmospheric conditions. Knowledge of these lifetimes can be obtained through a variety of theoretical and experimental techniques.[111] Solvation of X into the liquid phase is then described by the parallel step

$$\mathrm{X}_{(bulk)} + \mathrm{site}_{\mathrm{X}} \underset{k_{solv}}{\overset{k_{desolv}}{\rightleftarrows}} \mathrm{X}_{(ads)}. \qquad \text{S1.2}$$

The solvation parameters in S1.2 indicate the transport terms for X into the liquid from the surface (k_{solv}) and from liquid phase to the surface (k_{desolv}). An important constraint for these terms comes from the consideration of the overall Henry's law for X in the liquid solution. According to steps S1.1 and S1.2, the Henry's law coefficient for a gas with liquid solubility described at equilibrium by $[\mathrm{X}_{bulk}] = H_{gb}[\mathrm{X}_{gas}]$ can be recast as[112]

$$H_{gb} = \frac{k_{ads}}{k_{des}} \cdot \frac{k_{solv}}{k_{desolv}}. \qquad \text{Eq. 1.9}$$

We use the subscript gas-bulk (*gb*) for H_{gb} to refer to the bulk-liquid concentration since we can also distinguish a gas-surface (H_{gs}) coefficient and surface-bulk (H_{sb}) coefficient that can be obtained by decomposing Eq. 1.9 to

$$H_{gs} = \frac{k_{ads}\,[\mathrm{site_X}]}{k_{des}}, \qquad \text{Eq. 1.10}$$

$$H_{sb} = \frac{k_{solv}}{k_{desolv}\,[\mathrm{site_X}]}, \qquad \text{Eq. 1.11}$$

$$H_{gb} = H_{gs} \cdot H_{sb}. \qquad \text{Eq. 1.12}$$

These "partial" Henry's law coefficients are conceptually useful since the concentration of a X at the interface may be significantly different than both the gaseous and liquid-phase concentrations at equilibrium. Although this constraint identifies a unique value for the ratio $\frac{k_{solv}}{k_{desolv}\,[\mathrm{site_X}]}$, further information is necessary to be confident in absolute values for k_{solv} and k_{desolv}. Mirroring the argument for determining k_{des}, k_{solv} can be determined from molecular simulations where the lifetime of the molecule X at the interface before solvation is observed. An example of this determination is provided in Chapter 2 for the transport of O_3 across the air-water interface. Obtaining a timescale for the solvation process therefore determines the reverse "desolvation" coefficient k_{desolv} by the constraint in Eq. 1.11.

(ii) Mass Transport of Solute Y

Diffusion of Y from the liquid phase to the surface operates with the same mechanics as in Eq. 1.6, over some relevant liquid length-scale. The treatment of Y at the surface similarly follows a Langmuir Adsorption model, where Y adsorbs (or, as termed here, desolvates) to a surface site in analogy to step S1.2:

$$\mathrm{Y}_{(bulk)} + \mathrm{site_Y} \underset{k_{solv}}{\overset{k_{desolv}}{\rightleftarrows}} \mathrm{Y}_{(ads)}. \qquad \text{S1.3}$$

In the case of a liquid solute, the determination of the maximum surface concentration is less clear than in the case of a gas. Some solutes like surfactant molecules have a relatively well-defined molecular area that can be used in a similar manner to Eq. 1.7, while others such as inorganic ions may have more complex interactions at interfaces and therefore a less certain site constraint. This case is investigated more closely in Chapter 3—where molecular simulations are employed to determine an approximate maximum surface density for the iodide anion. This chapter also investigates how surface densities of the iodide ion are influenced by the presence of the chloride ion. These simulations can be used to obtain a Langmuir coefficient $K_{eq} = \frac{k_{desolv}}{k_{solv}}$ for a given solute Y by fitting the Langmuir adsorption isotherm:

$$[\mathrm{Y}_{(ads)}] = [\mathrm{site_Y}]_{max} \frac{K_{eq}\,[\mathrm{Y}_{(bulk)}]}{1 + K_{eq}[\mathrm{Y}_{(bulk)}]}. \qquad \text{Eq. 1.13}$$

We provide some further discussion around the fitting this equation, the value of K_{eq}, and related values k_{desolv} and k_{solv} in Chapters 2 & 3.

1.3.C: Implementation of Stochastic Simulations

After defining terms in the mass-transport framework, chemistry throughout the system can be included by defining reactivity in any of the defined regions with a simple rate law such as Eq. 1.5. For much of this work, implementation of the model was accomplished by using the stochastic kinetics simulator Kinetiscope©,[113] a software package designed to simulate the kinetics of complex systems using a stochastic algorithm as opposed to integrating systems of differential equations. Kinetiscope© has been used in a number of different chemical and physical applications, including previously reported microdroplet chemistry.[85,114–116] The spatial regions outlined above and the mass-transport step between them can be defined directly in Kinetiscope© alongside chemical reactions. Simulation output then provides the time-dependent profiles for reactant concentrations along with simulation details such as the number of reactive or transport events selected. The following Chapters 2 & 3 provide detailed information on the implementation of these simulations using Kinetiscope©, with the complete list of kinetic steps included for the chemistry under investigation.

1.3.D: Analytical and Numerical Approach

In addition to stochastic simulations, a number of analytical forms for uptake coefficients and time-dependent kinetics can be obtained using this same multiphase reaction framework. In the analytical approach, the steady-state assumption is applied to each individual spatial region which provides simple algebraic expressions defining local concentrations. The logic behind this approach is that during reaction, local concentrations in each region will quickly achieve a quasi-steady-state condition where concentrations of [X] and [Y] are governed by the reaction term and the transport terms in and out of the region. As demonstrated in Chapters 4 & 5, this approach predicts a broad range of dynamics for a variety of different reactant conditions. Although a number of examples are provided throughout the following chapters, it is appropriate to include a succinct example of the steady-state approach here for the surface-adsorbed gas [$\mathrm{X}_{(ads)}$]. After reaction begins between gas X and solute Y, [$\mathrm{X}_{(ads)}$] rapidly achieves a steady state condition described by the rate law:

$$\frac{d[\mathrm{X}_{(ads)}]}{dt} = 0 = k_{ads}\,[\mathrm{site_X}][\mathrm{X}_{(gas)}] + k_{desolv}\,[\mathrm{site_X}][\mathrm{X}_{(bulk)}] - k_{des}[\mathrm{X}_{(ads)}] - k_{solv}[\mathrm{X}_{(ads)}]$$
$$-k_{rxn}[\mathrm{X}_{(ads)}][\mathrm{Y}_{(ads)}]. \qquad \text{Eq. 1.14}$$

Eq. 1.14 is rearranged to define the steady-state concentration

$$\left[\mathrm{X}_{(ads)}\right] = \frac{k_{ads}\,[\mathrm{site_X}]\left[\mathrm{X}_{(gas)}\right] + k_{desolv}\,[\mathrm{site_X}]\left[\mathrm{X}_{(bulk)}\right]}{k_{des} + k_{solv} + k_{rxn}\left[\mathrm{Y}_{(ads)}\right]}. \qquad \text{Eq. 1.15}$$

The approach outlined here to determine local concentrations is used extensively in Chapter 5, where we explore analytical forms of uptake coefficients and compare time-dependent concentration profiles obtained analytically with numerical evaluations of the governing equations.

1.4: References

(1) Doney, S. C.; Fabry, V. J.; Feely, R. A.; Kleypas, J. A. Ocean Acidification: The Other CO2 Problem. *Annu. Rev. Mar. Sci.* **2009**, *1* (Volume 1, 2009), 169–192. https://doi.org/10.1146/annurev.marine.010908.163834.

(2) Fabry, V. J.; Seibel, B. A.; Feely, R. A.; Orr, J. C. Impacts of Ocean Acidification on Marine Fauna and Ecosystem Processes. *ICES J. Mar. Sci.* **2008**, *65* (3), 414–432. https://doi.org/10.1093/icesjms/fsn048.

(3) Hönisch, B.; Ridgwell, A.; Schmidt, D. N.; Thomas, E.; Gibbs, S. J.; Sluijs, A.; Zeebe, R.; Kump, L.; Martindale, R. C.; Greene, S. E.; Kiessling, W.; Ries, J.; Zachos, J. C.; Royer, D. L.; Barker, S.; Marchitto, T. M.; Moyer, R.; Pelejero, C.; Ziveri, P.; Foster, G. L.; Williams, B. The Geological Record of Ocean Acidification. *Science* **2012**, *335* (6072), 1058–1063. https://doi.org/10.1126/science.1208277.

(4) Husar, R. B.; Whitby, K. T.; Liu, B. Y. H. Physical Mechanisms Governing the Dynamics of Los Angeles Smog Aerosol. *J. Colloid Interface Sci.* **1972**, *39* (1), 211–224. https://doi.org/10.1016/0021-9797(72)90155-5.

(5) Hecht, T. A.; Seinfeld, J. H.; Dodge, M. C. Generalized Kinetic Mechanism for Photochemical Smog. *Environ. Sci. Technol.* **1974**, *8* (4), 327–339. https://doi.org/10.1021/es60089a004.

(6) Whitten, G. Z. The Chemistry of Smog Formation: A Review of Current Knowledge. *Environ. Int.* **1983**, *9* (6), 447–463. https://doi.org/10.1016/0160-4120(83)90003-X.

(7) Chang, J.-H.; Lee, Y.-L.; Chang, L.-T.; Chang, T.-Y.; Hsiao, T.-C.; Chung, K. F.; Ho, K. F.; Kuo, H.-P.; Lee, K.-Y.; Chuang, K.-J.; Chuang, H.-C. Climate Change, Air Quality, and Respiratory Health: A Focus on Particle Deposition in the Lungs. *Ann. Med.* **2023**, *55* (2), 2264881. https://doi.org/10.1080/07853890.2023.2264881.

(8) Sznitman, J. Revisiting Airflow and Aerosol Transport Phenomena in the Deep Lungs with Microfluidics. *Chem. Rev.* **2022**, *122* (7), 7182–7204. https://doi.org/10.1021/acs.chemrev.1c00621.

(9) Edwards, D. A. The Macrotransport of Aerosol Particles in the Lung: Aerosol Deposition Phenomena. *J. Aerosol Sci.* **1995**, *26* (2), 293–317. https://doi.org/10.1016/0021-8502(94)00101-4.

(10) Jayaweera, M.; Perera, H.; Gunawardana, B.; Manatunge, J. Transmission of COVID-19 Virus by Droplets and Aerosols: A Critical Review on the Unresolved Dichotomy. *Environ. Res.* **2020**, *188*, 109819. https://doi.org/10.1016/j.envres.2020.109819.

(11) Asadi, S.; Bouvier, N.; Wexler, A. S.; Ristenpart, W. D. The Coronavirus Pandemic and Aerosols: Does COVID-19 Transmit via Expiratory Particles? *Aerosol Sci. Technol.* **2020**, *54* (6), 635–638. https://doi.org/10.1080/02786826.2020.1749229.

(12) Anderson, E. L.; Turnham, P.; Griffin, J. R.; Clarke, C. C. Consideration of the Aerosol Transmission for COVID-19 and Public Health. *Risk Anal.* **2020**, *40* (5), 902–907. https://doi.org/10.1111/risa.13500.

(13) Oswin, H. P.; Haddrell, A. E.; Otero-Fernandez, M.; Mann, J. F. S.; Cogan, T. A.; Hilditch, T. G.; Tian, J.; Hardy, D. A.; Hill, D. J.; Finn, A.; Davidson, A. D.; Reid, J. P. The Dynamics of SARS-CoV-2 Infectivity with Changes in Aerosol Microenvironment. *Proc. Natl. Acad. Sci.* **2022**, *119* (27), e2200109119. https://doi.org/10.1073/pnas.2200109119.

(14) Haddrell, A.; Oswin, H.; Otero-Fernandez, M.; Robinson, J. F.; Cogan, T.; Alexander, R.; Mann, J. F. S.; Hill, D.; Finn, A.; Davidson, A. D.; Reid, J. P. Ambient Carbon Dioxide Concentration Correlates with SARS-CoV-2 Aerostability and Infection Risk. *Nat. Commun.* **2024**, *15* (1), 3487. https://doi.org/10.1038/s41467-024-47777-5.

(15) Alsved, M.; Nyström, K.; Thuresson, S.; Nygren, D.; Patzi-Churqui, M.; Hussein, T.; Fraenkel, C.-J.; Medstrand, P.; Löndahl, J. Infectivity of Exhaled SARS-CoV-2 Aerosols Is Sufficient to Transmit Covid-19 within Minutes. *Sci. Rep.* **2023**, *13* (1), 21245. https://doi.org/10.1038/s41598-023-47829-8.

(16) Jaumdally, S.; Tomasicchio, M.; Pooran, A.; Esmail, A.; Kotze, A.; Meier, S.; Wilson, L.; Oelofse, S.; van der Merwe, C.; Roomaney, A.; Davids, M.; Suliman, T.; Joseph, R.; Perumal, T.; Scott, A.; Shaw, M.; Preiser, W.; Williamson, C.; Goga, A.; Mayne, E.; Gray, G.; Moore, P.; Sigal, A.; Limberis, J.; Metcalfe, J.; Dheda, K. Frequency, Kinetics and Determinants of Viable SARS-CoV-2 in Bioaerosols from Ambulatory COVID-19 Patients Infected with the Beta, Delta or Omicron Variants. *Nat. Commun.* **2024**, *15* (1), 2003. https://doi.org/10.1038/s41467-024-45400-1.

(17) Hansen, J.; Sato, M.; Ruedy, R. Radiative Forcing and Climate Response. *J. Geophys. Res. Atmospheres* **1997**, *102* (D6), 6831–6864. https://doi.org/10.1029/96JD03436.

(18) Myhre, G. Consistency Between Satellite-Derived and Modeled Estimates of the Direct Aerosol Effect. *Science* **2009**, *325* (5937), 187–190. https://doi.org/10.1126/science.1174461.

(19) Andreae, M. O.; Jones, C. D.; Cox, P. M. Strong Present-Day Aerosol Cooling Implies a Hot Future. *Nature* **2005**, *435* (7046), 1187–1190. https://doi.org/10.1038/nature03671.

(20) Li, J.; Carlson, B. E.; Yung, Y. L.; Lv, D.; Hansen, J.; Penner, J. E.; Liao, H.; Ramaswamy, V.; Kahn, R. A.; Zhang, P.; Dubovik, O.; Ding, A.; Lacis, A. A.; Zhang, L.; Dong, Y. Scattering and Absorbing Aerosols in the Climate System. *Nat. Rev. Earth Environ.* **2022**, *3* (6), 363–379. https://doi.org/10.1038/s43017-022-00296-7.

(21) Jones, A.; Roberts, D. L.; Slingo, A. A Climate Model Study of Indirect Radiative Forcing by Anthropogenic Sulphate Aerosols. *Nature* **1994**, *370* (6489), 450–453. https://doi.org/10.1038/370450a0.

(22) Lohmann, U.; Feichter, J. Global Indirect Aerosol Effects: A Review. *Atmospheric Chem. Phys.* **2005**, *5* (3), 715–737. https://doi.org/10.5194/acp-5-715-2005.

(23) Huang, Y.; Dickinson, R. E.; Chameides, W. L. Impact of Aerosol Indirect Effect on Surface Temperature over East Asia. *Proc. Natl. Acad. Sci.* **2006**, *103* (12), 4371–4376. https://doi.org/10.1073/pnas.0504428103.

(24) Scott, C. E.; Farmer, D. K.; Evans, M. J.; Swietlicki, E.; D'Andrea, S. D.; Spracklen, D. V.; Pierce, J. R. Weak Global Sensitivity of Cloud Condensation Nuclei and the Aerosol Indirect Effect to Criegee + SO_2 Chemistry. *Atmospheric Chem. Phys.* **2013**, *13* (6), 3163–3176. https://doi.org/10.5194/acp-13-3163-2013.

(25) J. Carpenter, L.; D. Archer, S.; Beale, R. Ocean-Atmosphere Trace Gas Exchange. *Chem. Soc. Rev.* **2012**, *41* (19), 6473–6506. https://doi.org/10.1039/C2CS35121H.

(26) George, C.; Ammann, M.; D'Anna, B.; Donaldson, D. J.; Nizkorodov, S. A. Heterogeneous Photochemistry in the Atmosphere. *Chem. Rev.* **2015**, *115* (10), 4218–4258. https://doi.org/10.1021/cr500648z.

(27) Katoshevski, D.; Nenes, A.; Seinfeld, J. H. A Study of Processes That Govern the Maintenance of Aerosols in the Marine Boundary Layer. *J. Aerosol Sci.* **1999**, *30* (4), 503–532. https://doi.org/10.1016/S0021-8502(98)00740-X.

(28) Pound, R. J.; Sherwen, T.; Helmig, D.; Carpenter, L. J.; Evans, M. J. Influences of Oceanic Ozone Deposition on Tropospheric Photochemistry. *Atmospheric Chem. Phys.* **2020**, *20* (7), 4227–4239. https://doi.org/10.5194/acp-20-4227-2020.

(29) Thompson, A. M. The Oxidizing Capacity of the Earth's Atmosphere: Probable Past and Future Changes. *Science* **1992**, *256* (5060), 1157–1165. https://doi.org/10.1126/science.256.5060.1157.

(30) Chu, W.; Li, L.; Li, H.; Zhang, Y.; Chen, Y.; Zhi, G.; Yang, X.; Ji, Y.; Chai, F. Atmospheric Oxidation Capacity and Its Impact on the Secondary Inorganic Components of PM2.5 in Recent Years in Beijing: Enlightenment for PM2.5 Pollution Control in the Future. *Atmosphere* **2023**, *14* (8), 1252. https://doi.org/10.3390/atmos14081252.

(31) Liu, T.; Hong, Y.; Li, M.; Xu, L.; Chen, J.; Bian, Y.; Yang, C.; Dan, Y.; Zhang, Y.; Xue, L.; Zhao, M.; Huang, Z.; Wang, H. Atmospheric Oxidation Capacity and Ozone Pollution Mechanism in a Coastal City of Southeastern China: Analysis of a Typical Photochemical Episode by an Observation-Based Model. *Atmospheric Chem. Phys.* **2022**, *22* (3), 2173–2190. https://doi.org/10.5194/acp-22-2173-2022.

(32) Mahowald, N. M.; Kloster, S.; Engelstaedter, S.; Moore, J. K.; Mukhopadhyay, S.; McConnell, J. R.; Albani, S.; Doney, S. C.; Bhattacharya, A.; Curran, M. a. J.; Flanner, M. G.; Hoffman, F. M.; Lawrence, D. M.; Lindsay, K.; Mayewski, P. A.; Neff, J.; Rothenberg, D.; Thomas, E.; Thornton, P. E.; Zender, C. S. Observed 20th Century Desert Dust Variability: Impact on Climate and Biogeochemistry. *Atmospheric Chem. Phys.* **2010**, *10* (22), 10875–10893. https://doi.org/10.5194/acp-10-10875-2010.

(33) Mahowald, N.; Albani, S.; Kok, J. F.; Engelstaeder, S.; Scanza, R.; Ward, D. S.; Flanner, M. G. The Size Distribution of Desert Dust Aerosols and Its Impact on the Earth System. *Aeolian Res.* **2014**, *15*, 53–71. https://doi.org/10.1016/j.aeolia.2013.09.002.

(34) Bauer, S. E.; Im, U.; Mezuman, K.; Gao, C. Y. Desert Dust, Industrialization, and Agricultural Fires: Health Impacts of Outdoor Air Pollution in Africa. *J. Geophys. Res. Atmospheres* **2019**, *124* (7), 4104–4120. https://doi.org/10.1029/2018JD029336.

(35) Boroughani, M.; Mohammadi, M.; Mirchooli, F.; Fiedler, S. Assessment of the Impact of Dust Aerosols on Crop and Water Loss in the Great Salt Desert in Iran. *Comput. Electron. Agric.* **2022**, *192*, 106605. https://doi.org/10.1016/j.compag.2021.106605.

(36) Rizzolo, J. A.; Barbosa, C. G. G.; Borillo, G. C.; Godoi, A. F. L.; Souza, R. A. F.; Andreoli, R. V.; Manzi, A. O.; Sá, M. O.; Alves, E. G.; Pöhlker, C.; Angelis, I. H.; Ditas, F.; Saturno, J.; Moran-Zuloaga, D.; Rizzo, L. V.; Rosário, N. E.; Pauliquevis, T.; Santos, R. M. N.; Yamamoto, C. I.; Andreae, M. O.; Artaxo, P.; Taylor, P. E.; Godoi, R. H. M. Soluble Iron Nutrients in Saharan Dust over the Central Amazon Rainforest. *Atmospheric Chem. Phys.* **2017**, *17* (4), 2673–2687. https://doi.org/10.5194/acp-17-2673-2017.

(37) Koren, I.; Kaufman, Y. J.; Washington, R.; Todd, M. C.; Rudich, Y.; Martins, J. V.; Rosenfeld, D. The Bodélé Depression: A Single Spot in the Sahara That Provides Most of the Mineral Dust to the Amazon Forest. *Environ. Res. Lett.* **2006**, *1* (1), 014005. https://doi.org/10.1088/1748-9326/1/1/014005.

(38) Baldwin, I. T.; Schultz, J. C. Rapid Changes in Tree Leaf Chemistry Induced by Damage: Evidence for Communication Between Plants. *Science* **1983**, *221* (4607), 277–279. https://doi.org/10.1126/science.221.4607.277.

(39) Rasheed, M. U.; Brosset, A.; Blande, J. D. Tree Communication: The Effects of "Wired" and "Wireless" Channels on Interactions with Herbivores. *Curr. For. Rep.* **2023**, *9* (1), 33–47. https://doi.org/10.1007/s40725-022-00177-8.

(40) Guerrieri, A.; Dong, L.; Bouwmeester, H. J. Role and Exploitation of Underground Chemical Signaling in Plants. *Pest Manag. Sci.* **2019**, *75* (9), 2455–2463. https://doi.org/10.1002/ps.5507.

(41) Oliveira Chagas, F.; Cassia Pessotti, R. de; Mauricio Caraballo-Rodríguez, A.; Tallarico Pupo, M. Chemical Signaling Involved in Plant–Microbe Interactions. *Chem. Soc. Rev.* **2018**, *47* (5), 1652–1704. https://doi.org/10.1039/C7CS00343A.

(42) Sparks, D. L. Kinetics and Mechanisms of Chemical Reactions at the Soil Mineral/Water Interface. In *Soil Physical Chemistry*; CRC Press, 1998.

(43) Tuteja, N.; Sopory, S. K. Chemical Signaling under Abiotic Stress Environment in Plants. *Plant Signal. Behav.* **2008**, *3* (8), 525–536. https://doi.org/10.4161/psb.3.8.6186.

(44) Alberti, S.; Gladfelter, A.; Mittag, T. Considerations and Challenges in Studying Liquid-Liquid Phase Separation and Biomolecular Condensates. *Cell* **2019**, *176* (3), 419–434. https://doi.org/10.1016/j.cell.2018.12.035.

(45) Shin, Y.; Brangwynne, C. P. Liquid Phase Condensation in Cell Physiology and Disease. *Science* **2017**, *357* (6357), eaaf4382. https://doi.org/10.1126/science.aaf4382.

(46) Choi, J.-M.; Holehouse, A. S.; Pappu, R. V. Physical Principles Underlying the Complex Biology of Intracellular Phase Transitions. *Annu. Rev. Biophys.* **2020**, *49* (Volume 49, 2020), 107–133. https://doi.org/10.1146/annurev-biophys-121219-081629.

(47) Banani, S. F.; Lee, H. O.; Hyman, A. A.; Rosen, M. K. Biomolecular Condensates: Organizers of Cellular Biochemistry. *Nat. Rev. Mol. Cell Biol.* **2017**, *18* (5), 285–298. https://doi.org/10.1038/nrm.2017.7.

(48) Silva, J. L.; Foguel, D.; Ferreira, V. F.; Vieira, T. C. R. G.; Marques, M. A.; Ferretti, G. D. S.; Outeiro, T. F.; Cordeiro, Y.; de Oliveira, G. A. P. Targeting Biomolecular Condensation and Protein Aggregation against Cancer. *Chem. Rev.* **2023**, *123* (14), 9094–9138. https://doi.org/10.1021/acs.chemrev.3c00131.

(49) Millar, S. R.; Huang, J. Q.; Schreiber, K. J.; Tsai, Y.-C.; Won, J.; Zhang, J.; Moses, A. M.; Youn, J.-Y. A New Phase of Networking: The Molecular Composition and Regulatory Dynamics of Mammalian Stress Granules. *Chem. Rev.* **2023**, *123* (14), 9036–9064. https://doi.org/10.1021/acs.chemrev.2c00608.

(50) Schwartz, S. E. Mass-Transport Considerations Pertinent to Aqueous Phase Reactions of Gases in Liquid-Water Clouds; Springer Berlin Heidelberg: Berlin, Heidelberg, 1986; pp 415–471.

(51) Schwartz, S. E.; Freiberg, J. E. Mass-Transport Limitation to the Rate of Reaction of Gases in Liquid Droplets: Application to Oxidation of SO2 in Aqueous Solutions. *Atmospheric Environ. 1967* **1981**, *15* (7), 1129–1144. https://doi.org/10.1016/0004-6981(81)90303-6.

(52) Meng, Z.; Seinfeld, J. H. Time Scales to Achieve Atmospheric Gas-Aerosol Equilibrium for Volatile Species. *Atmos. Environ.* **1996**, *30* (16), 2889–2900. https://doi.org/10.1016/1352-2310(95)00493-9.

(53) Shiraiwa, M.; Seinfeld, J. H. Equilibration Timescale of Atmospheric Secondary Organic Aerosol Partitioning. *Geophys. Res. Lett.* **2012**, *39* (24). https://doi.org/10.1029/2012GL054008.

(54) Lee, J. K.; Banerjee, S.; Nam, H. G.; Zare, R. N. Acceleration of Reaction in Charged Microdroplets. *Q. Rev. Biophys.* **2015**, *48* (4), 437–444. https://doi.org/10.1017/S0033583515000086.

(55) Wei, Z.; Li, Y.; Cooks, R. G.; Yan, X. Accelerated Reaction Kinetics in Microdroplets: Overview and Recent Developments. *Annu. Rev. Phys. Chem.* **2020**, *71* (Volume 71, 2020), 31–51. https://doi.org/10.1146/annurev-physchem-121319-110654.

(56) Lee, J. K.; Kim, S.; Nam, H. G.; Zare, R. N. Microdroplet Fusion Mass Spectrometry for Fast Reaction Kinetics. *Proc. Natl. Acad. Sci.* **2015**, *112* (13), 3898–3903. https://doi.org/10.1073/pnas.1503689112.

(57) Lee, J. K.; Samanta, D.; Nam, H. G.; Zare, R. N. Micrometer-Sized Water Droplets Induce Spontaneous Reduction. *J. Am. Chem. Soc.* **2019**. https://doi.org/10.1021/jacs.9b03227.

(58) Lee, J. K.; Walker, K. L.; Han, H. S.; Kang, J.; Prinz, F. B.; Waymouth, R. M.; Nam, H. G.; Zare, R. N. Spontaneous Generation of Hydrogen Peroxide from Aqueous

Microdroplets. *Proc. Natl. Acad. Sci.* **2019**, *116* (39), 19294–19298. https://doi.org/10.1073/pnas.1911883116.

(59) Qiu, L.; Cooks, R. G. Spontaneous Oxidation in Aqueous Microdroplets: Water Radical Cation as Primary Oxidizing Agent. *Angew. Chem.* **2024**, *136* (17), e202400118. https://doi.org/10.1002/ange.202400118.

(60) Banerjee, S.; Gnanamani, E.; Yan, X.; Zare, R. N. Can All Bulk-Phase Reactions Be Accelerated in Microdroplets? *Analyst* **2017**, *142* (9), 1399–1402. https://doi.org/10.1039/c6an02225a.

(61) Olumee, Z.; Callahan, J. H.; Vertes, A. Droplet Dynamics Changes in Electrostatic Sprays of Methanol−Water Mixtures. *J. Phys. Chem. A* **1998**, *102* (46), 9154–9160. https://doi.org/10.1021/jp982027z.

(62) Smith, J. N.; Flagan, R. C.; Beauchamp, J. L. Droplet Evaporation and Discharge Dynamics in Electrospray Ionization. *J. Phys. Chem. A* **2002**, *106* (42), 9957–9967. https://doi.org/10.1021/jp025723e.

(63) Nemes, P.; Marginean, I.; Vertes, A. Spraying Mode Effect on Droplet Formation and Ion Chemistry in Electrosprays. *Anal. Chem.* **2007**, *79* (8), 3105–3116. https://doi.org/10.1021/ac062382i.

(64) Rubio, M.; Sadek, S. H.; Gañán-Calvo, A. M.; Montanero, J. M. Diameter and Charge of the First Droplet Emitted in Electrospray. *Phys. Fluids* **2021**, *33* (3), 032002. https://doi.org/10.1063/5.0041428.

(65) Fenn, J. B.; Mann, M.; Meng, C. K.; Wong, S. F.; Whitehouse, C. M. Electrospray Ionization for Mass Spectrometry of Large Biomolecules. *Science* **1989**, *246* (4926), 64–71. https://doi.org/10.1126/science.2675315.

(66) Yamashita, M.; Fenn, J. B. Electrospray Ion Source. Another Variation on the Free-Jet Theme. *J. Phys. Chem.* **1984**, *88* (20), 4451–4459. https://doi.org/10.1021/j150664a002.

(67) Wilm, M. Principles of Electrospray Ionization. *Mol. Cell. Proteomics* **2011**, *10* (7). https://doi.org/10.1074/mcp.M111.009407.

(68) Kebarle, P. A Brief Overview of the Present Status of the Mechanisms Involved in Electrospray Mass Spectrometry. *J. Mass Spectrom.* **2000**, *35* (7), 804–817. https://doi.org/10.1002/1096-9888(200007)35:7<804::AID-JMS22>3.0.CO;2-Q.

(69) Fenn, J. B. Ion Formation from Charged Droplets: Roles of Geometry, Energy, and Time. *J. Am. Soc. Mass Spectrom.* **1993**, *4* (7), 524–535. https://doi.org/10.1016/1044-0305(93)85014-O.

(70) Jacobs, M. I.; Davis, R. D.; Rapf, R. J.; Wilson, K. R. Studying Chemistry in Micro-Compartments by Separating Droplet Generation from Ionization. *J. Am. Soc. Mass Spectrom.* **2019**, *30* (2), 339–343. https://doi.org/10.1007/s13361-018-2091-y.

(71) Rovelli, G.; Jacobs, M. I.; Willis, M. D.; Rapf, R. J.; Prophet, A. M.; Wilson, K. R. A Critical Analysis of Electrospray Techniques for the Determination of Accelerated Rates

and Mechanisms of Chemical Reactions in Droplets. *Chem. Sci.* **2020**, *11* (48), 13026–13043. https://doi.org/10.1039/D0SC04611F.

(72) J. Chen, C.; R. Williams, E. The Role of Analyte Concentration in Accelerated Reaction Rates in Evaporating Droplets. *Chem. Sci.* **2023**, *14* (18), 4704–4713. https://doi.org/10.1039/D3SC00259D.

(73) Xiong, H.; Lee, J. K.; Zare, R. N.; Min, W. Strong Electric Field Observed at the Interface of Aqueous Microdroplets. *J. Phys. Chem. Lett.* **2020**, *11* (17), 7423–7428. https://doi.org/10.1021/acs.jpclett.0c02061.

(74) Hao, H.; Leven, I.; Head-Gordon, T. Can Electric Fields Drive Chemistry for an Aqueous Microdroplet? *Nat. Commun.* **2022**, *13* (1), 280. https://doi.org/10.1038/s41467-021-27941-x.

(75) Heindel, J. P.; LaCour, R. A.; Head-Gordon, T. The Role of Charge in Microdroplet Redox Chemistry. *Nat. Commun.* **2024**, *15* (1), 3670. https://doi.org/10.1038/s41467-024-47879-0.

(76) Martins-Costa, M. T. C.; Ruiz-López, M. F. Electrostatics and Chemical Reactivity at the Air–Water Interface. *J. Am. Chem. Soc.* **2023**, *145* (2), 1400–1406. https://doi.org/10.1021/jacs.2c12089.

(77) Ben-Amotz, D. Electric Buzz in a Glass of Pure Water. *Science* **2022**, *376* (6595), 800–801. https://doi.org/10.1126/science.abo3398.

(78) Gallo, A.; Farinha, A. S. F.; Dinis, M.; Emwas, A.-H.; Santana, A.; Nielsen, R. J.; Goddard, W. A.; Mishra, H. The Chemical Reactions in Electrosprays of Water Do Not Always Correspond to Those at the Pristine Air–Water Interface. *Chem. Sci.* **2019**, *10* (9), 2566–2577. https://doi.org/10.1039/C8SC05538F.

(79) Ahmad Eatoo, M.; Mishra, H. Busting the Myth of Spontaneous Formation of H 2 O 2 at the Air–Water Interface: Contributions of the Liquid–Solid Interface and Dissolved Oxygen Exposed. *Chem. Sci.* **2024**, *15* (9), 3093–3103. https://doi.org/10.1039/D3SC06534K.

(80) Duffin, A. M.; J. Saykally, R. Electrokinetic Power Generation from Liquid Water Microjets. *J. Phys. Chem. C* **2008**, *112* (43), 17018–17022. https://doi.org/10.1021/jp8015276.

(81) Duffin, A. M.; Saykally, R. J. Electrokinetic Hydrogen Generation from Liquid Water Microjets. *J. Phys. Chem. C* **2007**, *111* (32), 12031–12037. https://doi.org/10.1021/jp072994m.

(82) Berbille, A.; Li, X.-F.; Su, Y.; Li, S.; Zhao, X.; Zhu, L.; Wang, Z. L. Mechanism for Generating H2O2 at Water-Solid Interface by Contact-Electrification. *Adv. Mater.* **2023**, *35* (46), 2304387. https://doi.org/10.1002/adma.202304387.

(83) Zhao, J.; Zhang, X.; Xu, J.; Tang, W.; Lin Wang, Z.; Ru Fan, F. Contact-Electro-Catalysis for Direct Synthesis of H2O2 under Ambient Conditions. *Angew. Chem. Int. Ed.* **2023**, *62* (21), e202300604. https://doi.org/10.1002/anie.202300604.

(84) Chen, B.; Xia, Y.; He, R.; Sang, H.; Zhang, W.; Li, J.; Chen, L.; Wang, P.; Guo, S.; Yin, Y.; Hu, L.; Song, M.; Liang, Y.; Wang, Y.; Jiang, G.; Zare, R. N. Water–Solid Contact Electrification Causes Hydrogen Peroxide Production from Hydroxyl Radical Recombination in Sprayed Microdroplets. *Proc. Natl. Acad. Sci.* **2022**, *119* (32), e2209056119. https://doi.org/10.1073/pnas.2209056119.

(85) Wilson, K. R.; Prophet, A. M.; Rovelli, G.; Willis, M. D.; Rapf, R. J.; Jacobs, M. I. A Kinetic Description of How Interfaces Accelerate Reactions in Micro-Compartments. *Chem. Sci.* **2020**, *11* (32), 8533–8545. https://doi.org/10.1039/D0SC03189E.

(86) Fallah-Araghi, A.; Meguellati, K.; Baret, J.-C.; Harrak, A. E.; Mangeat, T.; Karplus, M.; Ladame, S.; Marques, C. M.; Griffiths, A. D. Enhanced Chemical Synthesis at Soft Interfaces: A Universal Reaction-Adsorption Mechanism in Microcompartments. *Phys. Rev. Lett.* **2014**, *112* (2), 028301–028301. https://doi.org/10.1103/PhysRevLett.112.028301.

(87) Ruiz-López, M. F.; Martins-Costa, M. T. C. Disentangling Reaction Rate Acceleration in Microdroplets. *Phys. Chem. Chem. Phys.* **2022**, *24* (48), 29700–29704. https://doi.org/10.1039/D2CP04998H.

(88) Ben-Amotz, D. Interfacial Chemical Reactivity Enhancement. *J. Chem. Phys.* **2024**, *160* (8), 084704. https://doi.org/10.1063/5.0186945.

(89) Davis, E. J. A History of Single Aerosol Particle Levitation. *Aerosol Sci. Technol.* **1997**, *26* (3), 212–254. https://doi.org/10.1080/02786829708965426.

(90) Jacobs, M. I.; Davies, J. F.; Lee, L.; Davis, R. D.; Houle, F.; Wilson, K. R. Exploring Chemistry in Microcompartments Using Guided Droplet Collisions in a Branched Quadrupole Trap Coupled to a Single Droplet, Paper Spray Mass Spectrometer. *Anal. Chem.* **2017**, *89* (22), 12511–12519. https://doi.org/10.1021/acs.analchem.7b03704.

(91) Willis, M. D.; Rovelli, G.; Wilson, K. R. Combining Mass Spectrometry of Picoliter Samples with a Multicompartment Electrodynamic Trap for Probing the Chemistry of Droplet Arrays. *Anal. Chem.* **2020**, *92* (17), 11943–11952. https://doi.org/10.1021/acs.analchem.0c02343.

(92) Hart, M. B.; Sivaprakasam, V.; Eversole, J. D.; Johnson, L. J.; Czege, J. Optical Measurements from Single Levitated Particles Using a Linear Electrodynamic Quadrupole Trap. *Appl. Opt.* **2015**, *54* (31), F174–F174. https://doi.org/10.1364/ao.54.00f174.

(93) Singh, M.; Mayya, Y. S.; Gaware, J.; Thaokar, R. M. Levitation Dynamics of a Collection of Charged Droplets in an Electrodynamic Balance. *J. Appl. Phys.* **2017**, *121* (5), 054503. https://doi.org/10.1063/1.4974470.

(94) Kaur Kohli, R.; Davis, R. D.; Davies, J. F. Tutorial: Electrodynamic Balance Methods for Single Particle Levitation and the Physicochemical Analysis of Aerosol. *J. Aerosol Sci.* **2023**, *174*, 106255. https://doi.org/10.1016/j.jaerosci.2023.106255.

(95) Davies, J. F. Mass, Charge, and Radius of Droplets in a Linear Quadrupole Electrodynamic Balance. *Aerosol Sci. Technol.* **2019**, *53* (3), 309–320. https://doi.org/10.1080/02786826.2018.1559921.

(96) Birdsall, A. W.; Krieger, U. K.; Keutsch, F. N. Electrodynamic Balance–Mass Spectrometry of Single Particles as a New Platform for Atmospheric Chemistry Research. *Atmospheric Meas. Tech.* **2018**, *11* (1), 33–47. https://doi.org/10.5194/amt-11-33-2018.

(97) Berkel, G. J. V. Open Port Sampling Interface. US11885778B2, January 30, 2024. https://patents.google.com/patent/US11885778B2/en.

(98) Kaur Kohli, R.; Van Berkel, G. J.; Davies, J. F. An Open Port Sampling Interface for the Chemical Characterization of Levitated Microparticles. *Anal. Chem.* **2022**, *94* (8), 3441–3445. https://doi.org/10.1021/acs.analchem.1c05550.

(99) Van Berkel, G. J.; Kertesz, V.; Boeltz, H. Immediate Drop on Demand Technology (I-DOT) Coupled with Mass Spectrometry via an Open Port Sampling Interface. *Bioanalysis* **2017**, *9* (21), 1667–1679. https://doi.org/10.4155/bio-2017-0104.

(100) Van Berkel, G. J.; Kertesz, V. An Open Port Sampling Interface for Liquid Introduction Atmospheric Pressure Ionization Mass Spectrometry. *Rapid Commun. Mass Spectrom.* **2015**, *29* (19), 1749–1756. https://doi.org/10.1002/rcm.7274.

(101) Liu, C.; Van Berkel, G. J.; Kovarik, P.; Perot, J. B.; Inguva, V.; Covey, T. R. Fluid Dynamics of the Open Port Interface for High-Speed Nanoliter Volume Sampling Mass Spectrometry. *Anal. Chem.* **2021**, *93* (24), 8559–8567. https://doi.org/10.1021/acs.analchem.1c01312.

(102) Danckwerts, P. V. Absorption by Simultaneous Diffusion and Chemical Reaction. *Trans. Faraday Soc.* **1950**, *46* (0), 300–304. https://doi.org/10.1039/TF9504600300.

(103) Danckwerts, P. V. Absorption by Simultaneous Diffusion and Chemical Reaction into Particles of Various Shapes and into Falling Drops. *Trans. Faraday Soc.* **1951**, *47* (0), 1014–1023. https://doi.org/10.1039/TF9514701014.

(104) Danckwerts, P. V.; Kennedy, A. M. The Kinetics of Absorption of Carbon Dioxide into Neutral and Alkaline Solutions. *Chem. Eng. Sci.* **1958**, *8* (3), 201–215. https://doi.org/10.1016/0009-2509(58)85027-7.

(105) Davidovits, P.; Jayne, J. T.; Duan, S. X.; Worsnop, D. R.; Zahniser, M. S.; Kolb, C. E. Uptake of Gas Molecules by Liquids: A Model. *J. Phys. Chem.* **1991**. https://doi.org/10.1021/j100169a048.

(106) Kolb, C. E.; Davidovits, P.; Jayne, J. T.; Shi, Q.; Worsnop, D. R. Kinetics of Trace Gas Uptake by Liquid Surfaces. *Prog. React. Kinet. Mech.* **2002**, *27* (1), 1–46. https://doi.org/10.3184/007967402103165324.

(107) Worsnop, D. R.; Morris, J. W.; Shi, Q.; Davidovits, P.; Kolb, C. E. A Chemical Kinetic Model for Reactive Transformations of Aerosol Particles. *Geophys. Res. Lett.* **2002**, *29* (20), 57-1-57–4. https://doi.org/10.1029/2002GL015542.

(108) Hanson, D. R.; Ravishankara, A. R.; Solomon, S. Heterogeneous Reactions in Sulfuric Acid Aerosols: A Framework for Model Calculations. *J. Geophys. Res. Atmospheres* **1994**, *99* (D2), 3615–3629. https://doi.org/10.1029/93JD02932.

(109) Hanson, D. R.; Ravishankara, A. R.; Lovejoy, E. R. Reaction of BrONO2 with H2O on Submicron Sulfuric Acid Aerosol and the Implications for the Lower Stratosphere. *J. Geophys. Res. Atmospheres* **1996**, *101* (D4), 9063–9069. https://doi.org/10.1029/96JD00347.

(110) Shi, Q.; Davidovits, P.; Jayne, J. T.; Worsnop, D. R.; Kolb, C. E. Uptake of Gas-Phase Ammonia. 1. Uptake by Aqueous Surfaces as a Function of pH. *J. Phys. Chem. A* **1999**, *103* (44), 8812–8823. https://doi.org/10.1021/jp991696p.

(111) Knopf, D. A.; Ammann, M.; Berkemeier, T.; Pöschl, U.; Shiraiwa, M. Desorption Lifetimes and Activation Energies Influencing Gas–Surface Interactions and Multiphase Chemical Kinetics. *Atmospheric Chem. Phys.* **2024**, *24* (6), 3445–3528. https://doi.org/10.5194/acp-24-3445-2024.

(112) Willis, M. D.; Wilson, K. R. Coupled Interfacial and Bulk Kinetics Govern the Timescales of Multiphase Ozonolysis Reactions. *J. Phys. Chem. A* **2022**, *126* (30), 4991–5010. https://doi.org/10.1021/acs.jpca.2c03059.

(113) Hinsberg, W. D.; Houle, F. A. *Kinetiscope*. https://hinsberg.net/kinetiscope/.

(114) Wiegel, A. A.; Liu, M. J.; Hinsberg, W. D.; Wilson, K. R.; Houle, F. A. Diffusive Confinement of Free Radical Intermediates in the OH Radical Oxidation of Semisolid Aerosols. *Phys. Chem. Chem. Phys.* **2017**, *19* (9), 6814–6830. https://doi.org/10.1039/C7CP00696A.

(115) Houle, F. A.; Wiegel, A. A.; Wilson, K. R. Predicting Aerosol Reactivity Across Scales: From the Laboratory to the Atmosphere. *Environ. Sci. Technol.* **2018**, *52* (23), 13774–13781. https://doi.org/10.1021/acs.est.8b04688.

(116) Brown, E. K.; Rovelli, G.; Wilson, K. R. pH Jump Kinetics in Colliding Microdroplets: Accelerated Synthesis of Azamonardine from Dopamine and Resorcinol. *Chem. Sci.* **2023**, *14* (23), 6430–6442. https://doi.org/10.1039/D3SC01576A.

Chapter 2: Iodide Oxidation by Ozone at the Surface of Aqueous Microdroplets

This chapter is adapted from "Prophet, A.M.; Polley, K.; Van Berkel, G.J.; Limmer, D.T.; Wilson, K.R. Iodide Oxidation by Ozone at the Surface of Aqueous Microdroplets. Chem. Sci.* ***2024**, 15 (2), 736–756."*

2.1: Introduction

Oxidation reactions of iodine in the environment constitute a set of important pathways for mediating global atmospheric oxidant concentrations and reactive emissions.[1,2] Iodine oxides, the primary products from such reactions, play a particularly significant role in catalytic destruction cycles of ozone in the troposphere, affect the overall atmospheric budget of HO_x and NO_x species, and serve as higher molecular-weight precursors for new particle formation.[3–7] The iodide anion, I^-, resides in seawater where oxidation at the sea-surface initiates the release of reactive iodine into the atmosphere. Furthermore, the $I^- + O_3$ reaction on the sea-surface makes up a major fraction of overall ozone deposition from the marine boundary layer.[8] Since discovery of the environmental impact of iodine chemistry through field-based measurements, a host of laboratory-based experiments have aimed to understand the fundamentals underlying this multiphase reaction. Here we employ laboratory measurements on individual microdroplets together with molecular and continuum modeling to clarify the mechanism of iodide oxidation by ozone.

The earliest laboratory measurements of the heterogenous $I^- + O_3$ reaction found evidence for a bimolecular rate coefficient that approaches the diffusion limit with $k_{rxn} \sim 1\times10^9$ M^{-1} s^{-1}.[9–11] This rate coefficient is similar in magnitude to what has been observed in both gas phase experiments[12,13] and in the bulk aqueous phase using fast-mixing techniques.[14] This chemistry has been investigated by a number of researchers studying the oxidation of bulk aqueous solutions,[15–18] micron-scale aerosol,[19–21] and single iodide-water clusters.[22,23] Recent theoretical work has aimed to understand the kinetics and energetics of this reaction using a variety of modeling approaches ranging from numerical simulations to *ab initio* calculations of aqueous iodide oxidation by ozone.[24–27] Although this system has been under investigation for decades, questions remain regarding the detailed reaction mechanism at the air-water interface, under what conditions surface reactions dominate over bulk, and how such processes are coupled to mass transport of reactants, emissions of volatile products, and the overall uptake of ozone from the gas phase. As such, novel experimental and modeling approaches are warranted. Willis & Wilson[28] and Wilson et al.[29] introduced a model framework for analyzing multiphase ozone oxidation reactions in aqueous microdroplets by describing ozone partitioning at the air-water interface and subsequent solvation of O_3 into the droplet interior. This approach, implemented through stochastic reaction-diffusion simulations, allows for dynamic concentrations of reactants to be computed at the surface and bulk regions of the droplet using a set of detailed elementary steps describing adsorption, desorption, and solvation of O_3. As we aim to show in this work by combining experiments, kinetic models, and molecular simulations—the dynamics of ozone at the air-water interface are critical for understanding the multiphase chemical mechanism driving surface reactions of I^- and O_3.

In the current study, we examine oxidation kinetics of iodide by ozone in individual microdroplets by trapping and reacting charged microdroplets in a quadrupole electrodynamic trap (QET). Reaction kinetics are obtained by measuring droplet composition using an open-port sampling interface for mass spectrometry (OPSI-MS) as recently demonstrated by Kohli et al.[30]

Iodide decay kinetics are monitored as a function of [O_3] and pH. Using the framework of Willis & Wilson,[28] a kinetic model is constructed to explain the observed kinetics. Key model constraints that include the desorption and solvation rates of O_3 at the air-water interface are obtained directly from analysis of molecular simulations. Kinetic modeling results suggest the I^- + O_3 reaction occurs almost exclusively at the droplet surface under our experimental conditions where surficial O_3 may become substantially depleted by the reaction due to diffusion limitations in the gas phase. Experimental kinetics also show a strong pH dependence, related in part to the different chemical mechanisms relevant for destruction of I^- as a function of acidity. However, to fully explain the observed pH dependence, we postulate the existence of a relatively short-lived reaction intermediate $IOOO^-$. This ozonide intermediate has been previously proposed to exist through both experiment and theory, and is analogous to the intermediate observed in Br^- oxidation at the air-water interface.[31] A steady-state analysis of the surface concentrations is also provided which, in conjunction with recently developed expressions for uptake, are used to compute uptake coefficients of O_3 over a range of reactant concentrations.

2.2: Materials & Methods

To investigate droplet reaction kinetics, a quadrupole electrodynamic trap (QET) is used to react arrays of individual microdroplets, which are then analyzed with mass spectrometry to monitor droplet composition as recently described by Willis & Wilson[28] and elsewhere.[32,33] As this technique has been previously described, we provide an overview with a particular focus on the features relevant to the current experiments, including the recently implemented open-port sampling interface (OPSI) for single droplet mass spectrometry.

2.2.A: Quadrupole Electrodynamic Trap (QET)

The QET is used to charge and trap individual microdroplets under a controlled flow of humidified zero air (600 cm^3 min^{-1} for all experiments) at room temperature (295 K). Microdroplets are generated by a piezo-electric dispenser (Microfab, MJ-ABP-01, 30 µm orifice) oriented co-axially with the QET trapping rods (Fig. 2.1A). Droplets are charged by applying ± 200-500 V DC bias to an induction plate located directly below the dispensing region. An array of 10-100 droplets is trapped in an upper balancing region of the trap during a typical experiment. Single droplets can be individually transferred from the upper region to a lower trapping region. Microdroplets in the lower trapping region are sized by illuminating the droplet with a 532 nm laser focused axially across the QET interior. Mie scattered light from the microdroplet is then collected and analyzed as previously described by Davies[34] to obtain a droplet radius. Once sized, single microdroplets are ejected from the QET and into the analysis region. Ozone is generated using a corona discharge ozone generator supplied with a low flow of oxygen (20-100 cm^3 min^{-1}), which is then diluted into 1.5 – 3 L min^{-1} of nitrogen. 50 cm^3 min^{-1} of the resulting dilution flow is combined with the humidified airflow and directed through the QET. Ozone concentrations in the QET are monitored at the reactor outlet using a UV ozone analyzer (2B Technologies, model 106-M).

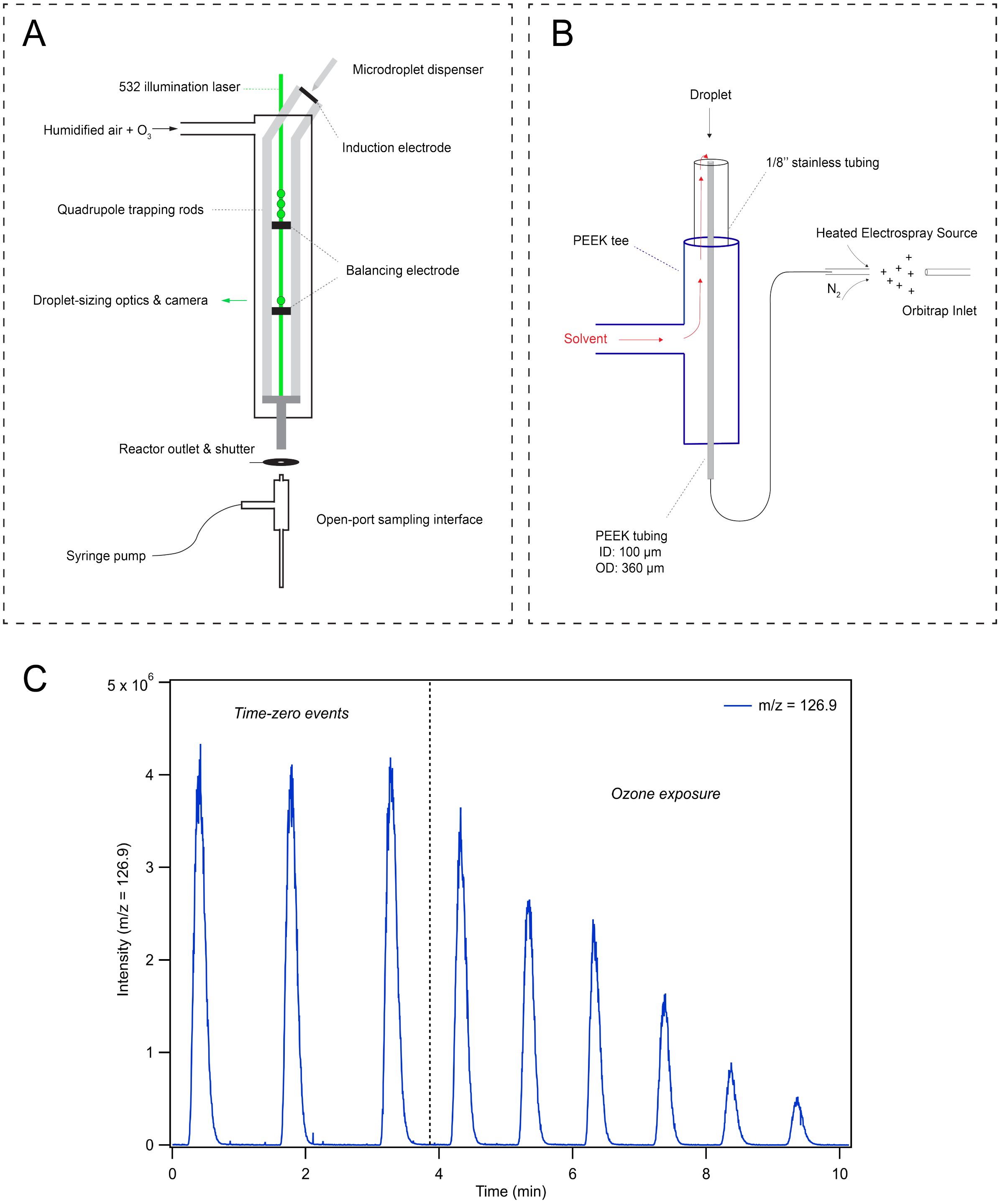

Fig. 2.1: Experimental schematic of the QET is shown in (A) and an overview of the OPSI-MS assembly is shown in (B). Panel (C) provides example iodide decay kinetics as observed in the MS using an initial 250 mM solution of NaI at pH 3 with droplet radius r = 24 μm. Time-zero events demonstrate the stability between successive droplet events before exposure to ozone, while the dashed vertical line denotes the time when the droplets are exposed to ~1 ppm [O$_3$] flow.

2.2.B: Open-Port Sampling Interface (OPSI) Mass Spectrometry

Droplets ejected into the analysis region are carried by the gas-flow and collide with the inlet of an open-port sampling interface (OPSI) for analysis by mass spectrometry (MS). A schematic of the OPSI is shown in Fig. 2.1B, outlining the major components of the assembly. A number of studies utilizing a similar design have been recently published for liquid droplet and particle capture,[30,35–40] and thus, we briefly review the general construction of the OPSI and provide details on the specific components used. The OPSI design consists of a PEEK 3-way tee connected to a stainless 1/8'' tube on the top port. A smaller (360 μm OD, 100 μm ID) PEEK tube runs axially inside the outer tube and tee, connecting the top of the assembly to a commercial heated-electrospray source (Thermo-Fischer HESI-II probe) separated by a length of ~20 cm. An additional length of PEEK tubing delivers solvent (methanol in the current experiments) into the perpendicular tee port, allowing solvent to flow through the outer stainless 1/8'' tubing and around the inner PEEK tubing. This solvent then flows to the top of the OPSI where it enters the inner tube given sufficient sheath gas flow is used in the HESI to generate a pressure differential between the top of the inner tube and the electrospray needle.

By balancing the solvent delivery flow and sheath gas pressure, a stable flow of solvent through the inlet tube and into the ionization region is achieved. For the current experiments, the OPSI is operated in a slightly overfilled mode wherein the solvent delivery rate is marginally larger than the flowrate through the inner tube. A typical flow rate is ~2.5 mL/hr. Contents of the microdroplets landing in the solvent pool on top of the OPSI are first diluted before traveling through the inner tube and analyzed using electrospray ionization mass spectrometry (MS, Q Exactive Orbitrap, Thermo Fischer Scientific, Inc.) Measuring the iodide signal as a function of analysis time provides a time-series showing single droplet detection events (Fig. 2.1C), with typical peak widths of ~30 s. Peak areas from these single droplet events are then used to quantitatively determine concentrations of analytes in microdroplets. A calibration curve for droplet concentration response is provided in Appendix 2B, demonstrating the linear response of the signal with droplet [NaI]. Fig. 2.1C shows that the observed [I^-] decays when droplets are exposed to a gas phase flow of 1 ppm [O_3] through the QET. After time-zero (marked with a dashed vertical line in Fig. 2.1C), the peak area of subsequent droplet events is observed to decay as I^- is consumed by O_3. Typical mass spectra observed in the experiment are provided in Fig. 2B.2 in Appendix 2B, where an initial pre-reaction spectrum is provided along with a spectrum obtained from a droplet after undergoing ozone exposure.

During reaction, a shutter is placed between the QET outlet and the OPSI inlet to avoid the solvation and buildup of O_3 in the ionization region of the mass spectrometer. During a typical measurement the shutter is opened for ~0.5 s for each droplet detection event. Without this shutter, gas-phase chemistry (likely ion-molecule reactions) in the ESI source occurs even in the presence of trace O_3. Using the shutter configuration outlined in Fig. 2.1A, gas-phase interference can be ruled out by shutting off the ozone flow midway through the experiment and analyzing droplet composition to ensure the iodide ion signal does not recover. No noticeable recovery of iodide signal is observed with the current approach, indicating all the chemistry observed originates from reactions occurring in the microdroplets and not gas-phase chemistry in the ionization region of the mass spectrometer.

2.2.C: Droplet Composition

All reactions are performed using an initial [NaI] of 250 mM and [NaCl] between 500 mM and 700 mM. NaCl is used to decrease the water activity of solution to $a_w = 0.95$, matching the gas phase relative humidity of 95 ± 1% in the QET. Maintaining the same water activity in both the dispenser solution and the gas phase prevents droplets from significantly changing size when equilibrating inside the QET. Using this approach, the 30 μm orifice dispenser reliably provides droplets of radius 24 ± 1 μm. The use of NaCl also ensures that the droplet size remains relatively stable during the reaction, with droplet radius changing only ~1 μm during reaction as I^- is consumed. pH 3 droplets are dispensed from a bulk aqueous solution containing 300 mM citric acid/sodium citrate, buffered at pH 3, and [NaCl] = 500 mM. Likewise, pH 8 droplets are dispensed from a bulk solution containing 300 mM Tris base (tris(hydroxymethyl)aminomethane), buffered at pH 8, and [NaCl] = 700 mM. The particular organic buffers used were chosen due to the presence of multiple hydroxyl groups in both buffer systems, which decreases the interfacial preference of the organics and therefore minimizes any interference with iodide surface chemistry. However, we anticipate that most buffers in this pH range would not have a strong surface propensity and therefore, our results would not be sensitive to the particular buffer used.

Slightly different NaCl concentrations are used to compensate for the differences in the hygroscopicity of the citrate/citric acid and Tris base salt buffers. The [NaCl] is selected for each solution to give the same final droplet size of 24 μm, yielding a [NaI] concentration that is constant across pH given the same QET relative humidity. Unlike the pH 8 and pH 3 droplets, the pH 13 droplets are unbuffered due to the lack of viable buffers for this region and the constraint on the overall salt concentration to maintain stable droplet sizes. However, the consequence of an unbuffered solution in this case is minor as the reaction mechanism under basic conditions does not incorporate production or consumption of H^+ or OH^-. Fresh solutions were prepared daily using HPLC-grade water (Sigma-Aldrich), NaI (Sigma-Aldrich, ≥ 99.5%), NaCl (Sigma-Aldrich, ≥ 99.5%), citric acid (Sigma-Aldrich, ≥ 99.5%), sodium citrate monobasic (≥ 99.5%), Tris(hydroxymethyl)aminomethane (Sigma-Aldrich, ≥ 99.8%) and NaOH (Sigma-Aldrich, ≥ 98%).

2.3: Experimental Results & Discussion

2.3.A: Iodide Decay Kinetics

Droplet reaction kinetics for a series of pH and [O_3] are shown in Fig. 2.2. Experimental results (shown as points) are compared with kinetic simulations (lines), described below in Sections 2.4 and 2.5. Error bars for individual data points are estimated using the standard deviation of droplet peak areas from a set of unreacted droplet events prior to each experiment (e.g., droplet events in the "time-zero" section in Fig. 2.1C). Figs. 2.2A and 2.2B show iodide decay in microdroplets dispensed from solutions buffered at pH 3 and pH 8, respectively. A number of qualitative features are observed as a function of pH and [O_3]. For each droplet pH, the iodide consumption rate is first order in [O_3]. This is summarized in Fig. 2.3, where initial rates of decay are shown to increase linearly with increasing ozone concentration. A strong dependence on dispensed-solution pH is also observed. The overall rate of the reaction increases significantly with decreasing pH. From the most basic to acidic conditions, the observed initial decay rate increases by almost an order of magnitude. As considered further in the model discussion Section 2.6.B and as noted previously from product emission studies,[15–17] a major contribution to the apparent reaction acceleration with decreasing pH originates from the reaction of I^- with its primary oxidation product HOI to produce I_2. However, an additional pH dependence of the reaction is proposed below to account for the complete set of pH dependent observations shown in Figs. 2.2 and 2.3.

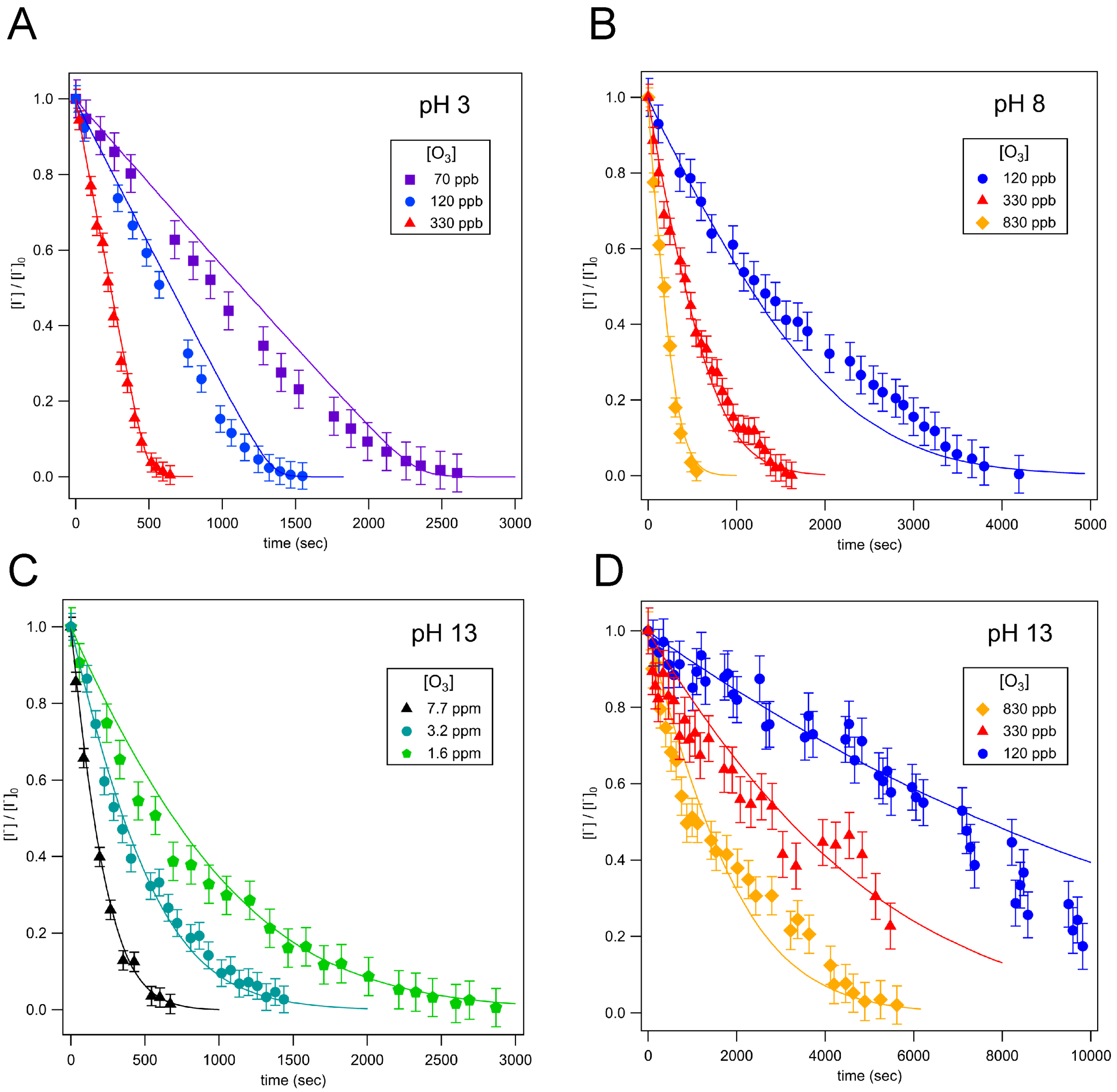

Fig. 2.2: Iodide decay kinetics showing ozone oxidation of 24 μm droplets containing 250 mM initial [NaI] for varying $[O_3]$ and dispensed solution pH. Experimental data is shown as points in A-D and simulation results as solid lines. Panel (A) shows results using droplets dispensed from pH 3 solution buffered with citrate/citric acid. Panel (B) shows results using pH 8 solution buffered with Tris base. Panels (C) and (D) shows results for unbuffered solution with an initial pH of 13, with $[O_3]$ above 1 ppm given in (C) and below 1 ppm given in (D).

Beyond a difference in the overall rate, changes in the shape of the decay kinetics in Fig. 2.2 are also observed as a function of pH and even $[O_3]$ under strongly basic conditions. The decay of iodide in acidic solution appears mostly linear in time, with a small but significant tail as the iodide concentration approaches zero. Conversely, the decay of iodide under strongly basic conditions appears exponential for $[O_3] > 1$ ppm but becomes increasingly bi-exponential or linear in time as [O_3] decreases below 1 ppm. The origin of these functional forms for the decay kinetics appears to be driven by the complex interplay of reaction and surface adsorption of iodide, reaction intermediates, and products and will be examined in more detail below in Section 2.6.

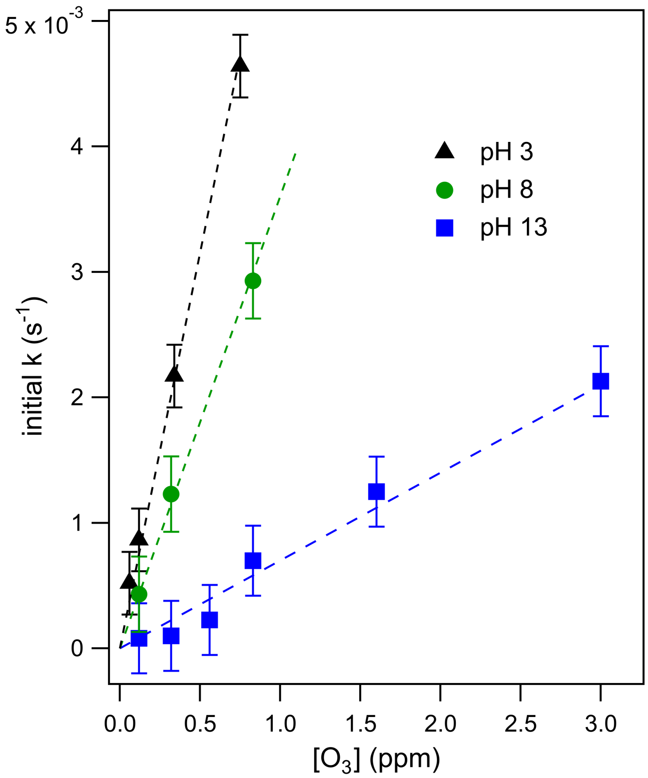

Fig. 2.3: Kinetic plot showing initial iodide decay rate vs. [O_3]. Initial rates from experiments using solutions with pH 3, 8, 13 are shown as points and simulation results are shown as dashed lines. Linear scaling with [O_3] is observed for all cases, with dramatic acceleration between pH 13 and pH 3. Error bars for data points reflect a combined uncertainty in reactor [O_3] concentration and deviation between individual droplet measurements.

2.3.B: Reaction Product Yields and Kinetics

Utilizing droplet composition analysis with the OPSI-MS, products formed and remaining in the condensed phase of the droplet are detected in positive- or negative-mode electrospray ionization. For experiments done using pH 3 and 8, however, no condensed-phase products are observed as all I^- in solution is quickly oxidized to I_2, which evaporates into the continuous gas flow through the QET. However, under strongly basic conditions (notably, above the pKa of HOI of 10.8) IO_3^- is observed in the mass spectrometer at m/z = 174 as shown in Appendix 2B, Fig. 2B.2. Peak areas from time-traces of the ion signal at m/z 174 are monitored throughout the reaction under basic conditions and provided in Fig. 2B.3 for three example ozone concentrations. As discussed further in Appendix 2B, the iodate yield appears to decrease with decreasing [O_3]. While the origin of this shift in product yield is unknown, this may suggest a change in surface mechanism with decreasing availability of O_3.

2.4: Model Description

2.4.A: Framework & Methods

To understand the reactivity observed in the droplet experiments, a kinetic model is constructed. This model describes the partitioning and reaction of gas- and liquid-phase species at the droplet surface and within the bulk interior. The model framework is based on work from Willis & Wilson[28] where a kinetic description of O_3 adsorption and desorption at the microdroplet surface and subsequent solvation into the bulk liquid is presented and benchmarked using a set of ozone oxidation reactions. Further analysis of this approach in Wilson et al.[29] provides closed-form expressions for predicting uptake and reaction of trace gases into microdroplets. In the current work, molecular dynamics (MD) simulations are used to study the solvation of ozone at the air-water interface and the kinetics of both the solvation and desorption processes. A water slab with 768 water molecules and sodium halide salts, modeled with a classical polarizable force field,[41] was used to represent an aqueous droplet at 300 K. A snapshot from the simulation of O_3 adsorption is shown in Fig. 2.4A. The free energy profile for transferring an ozone molecule through the air-water interface, with sodium halide salts (0.28 M NaI + 0.84 M NaCl) in the solution, is shown in Fig. 2.4B where the shaded blue region is the (scaled and shifted) water density profile. Results and details of the MD simulations and the procedures for obtaining the solvation and desorption rates are included in Appendix 2C. In the following modeling sections, we briefly outline the kinetic model and detail the specific novel components relevant for the application of this framework to the analysis of the $I^- + O_3$ reaction.

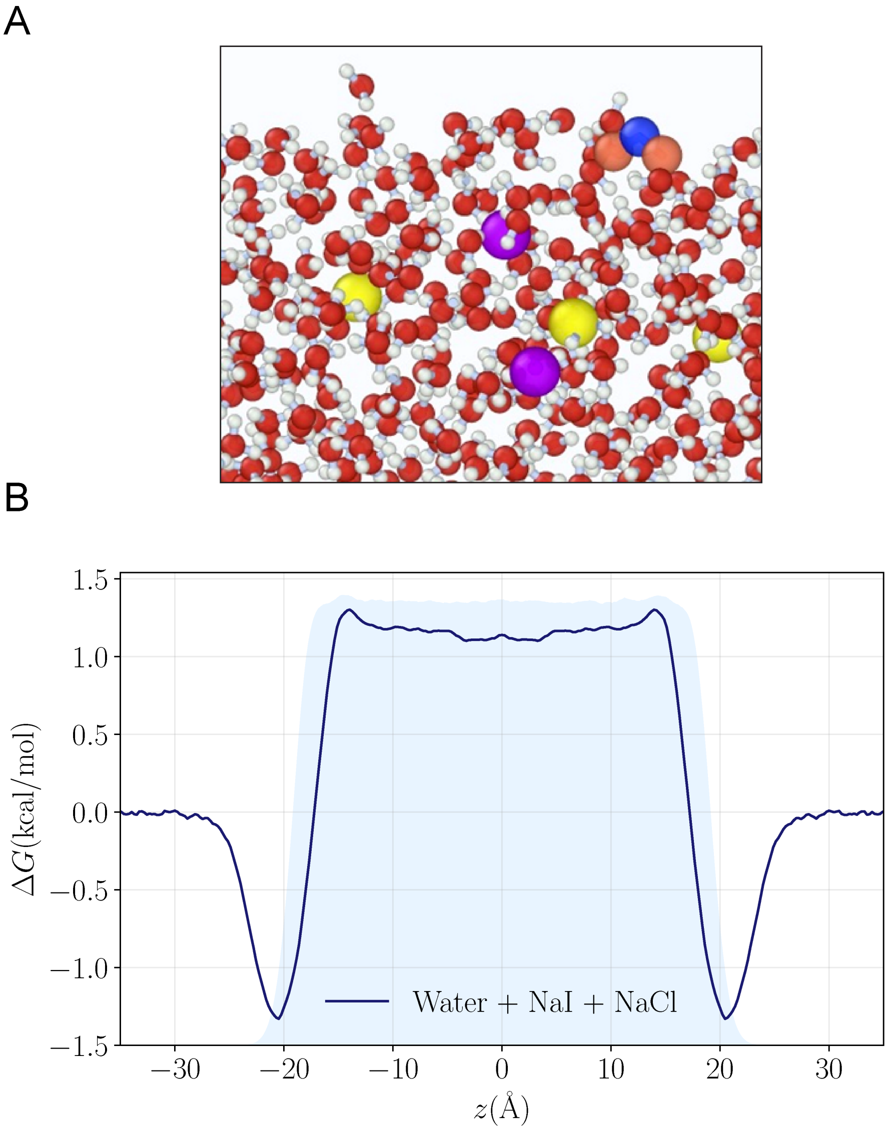

Fig. 2.4: (A) Snapshot of the MD simulation where an ozone molecule is adsorbed near the air-water interface. (B) The free energy profile for transferring an ozone molecule through a water slab with 0.28 M NaI and 0.84 M NaCl is displayed. The shaded blue region shows the (scaled and shifted) water density profile.

The model developed in this section is implemented in Kinetiscope©,[42] a software package previously used to simulate kinetics in a variety of systems such as organic aerosol, aqueous microdroplets, and emulsions.[43–45] Droplet kinetics are simulated by conceptualizing the droplet bulk interior and surface as two separate compartments that have a rectangular prism geometry. Both compartments have the same 1×1 nm^2 cross-sectional area but have different compartment lengths. The length of the bulk compartment is chosen to be $r/3$, in order to preserve the correct surface-to-volume ratio of a sphere with radius, r. The surface compartment length (δ) is 1 nm and represents the thickness of the air-water interface. This surface depth corresponds to the approximate length scale over which the water density changes across the air-water interface as observed by the MD results in Fig. 2.4B and previous simulations.[46] Molecules move between the surface and bulk compartments in Kinetiscope by Fickian diffusion, which is governed by the relative concentrations in each compartment and the compartment lengths. Solutes that diffuse into the surface compartment from the bulk can then adsorb to the air-water interface through a kinetic description of solvation/desolvation to establish surface concentrations. Similarly, gas-phase species partition to the surface through a set of adsorption-desorption steps described in the following sections and summarized in the multiphase framework in Fig. 2.5A.

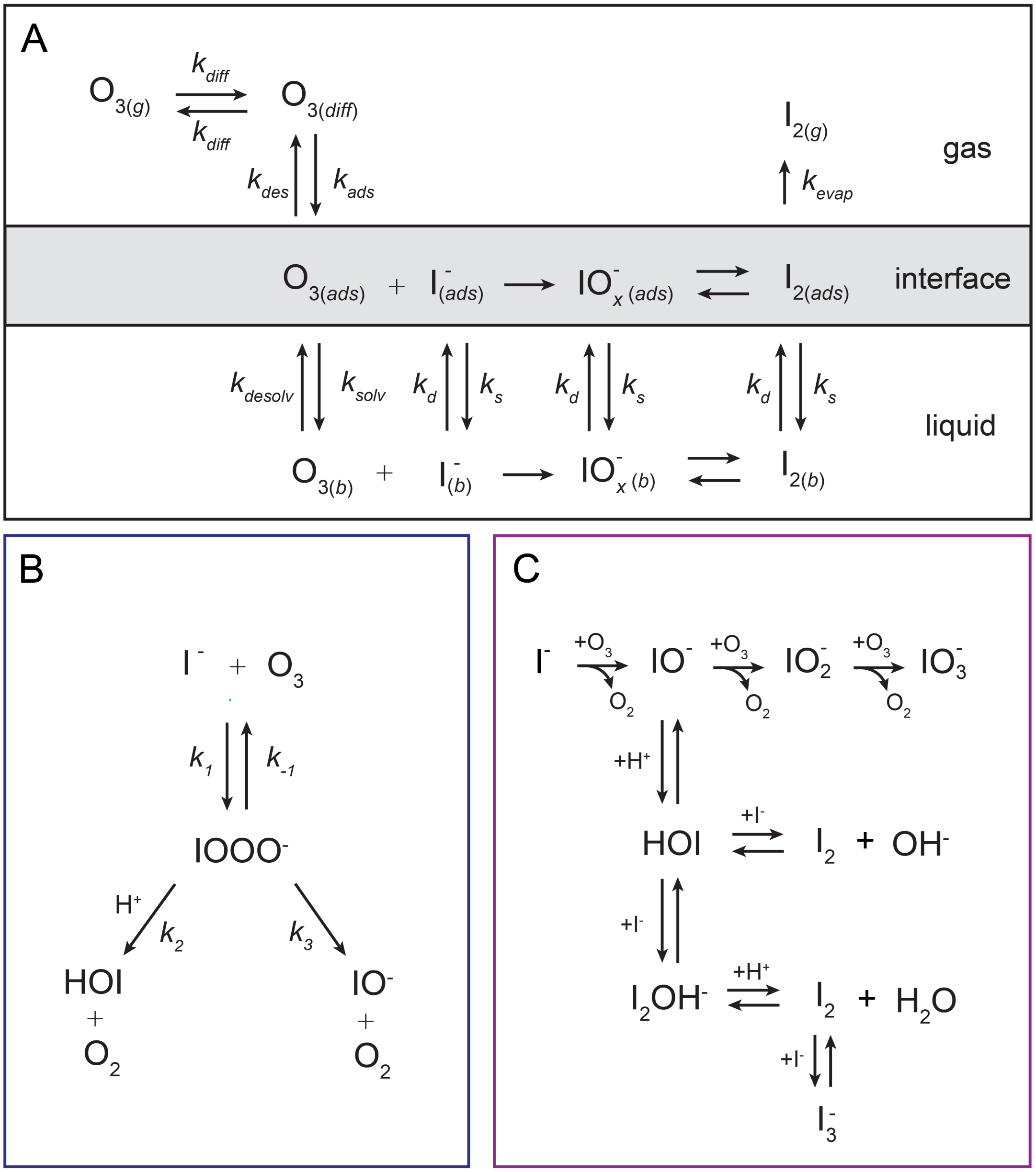

Fig. 2.5: The multiphase framework and chemical mechanisms implemented in the simulations. Panel (A) outlines the heterogenous ozone oxidation model framework showing adsorption of liquid- and gas-phase species to the interface. Panel (B) shows the primary $I^- + O_3$ reaction mechanism involving the reactive intermediate $IOOO^-$. Panel (C) shows subsequent chemistry with HOI and IO^- including both further oxidation by O_3 and secondary chemistry with I^-. Chemistry shown in (B) and (C) is included in both the bulk liquid and the droplet interface as denoted in (A) through an abbreviated reaction scheme.

2.4.B: Ozone Partitioning Scheme

The ozone partitioning scheme is conceptualized as two parallel processes: one describing the kinetic adsorption process at the gas-liquid interface, and one describing diffusion of ozone through the gas phase to the droplet surface. As the kinetic partitioning description draws from the work of Willis & Wilson,[28] we revisit the mechanics of this description before introducing the description of ozone diffusion.

(i) Ozone Gas-Liquid Kinetic Equilibrium

The kinetic description of O_3 equilibration between phases begins with decomposing the overall dimensionless Henry's law coefficient (H_{cc}) for ozone solvation into gas-to-surface (gs) and surface-to-bulk (sb) components, the product of which preserves the overall gas-to-bulk (gb) coefficient $H_{cc}^{gb} = H_{cc}^{gs} \cdot H_{cc}^{sb}$. The individual components H_{cc}^{gs} and H_{cc}^{sb}, which link the gas, interface and bulk O_3 concentrations, are computed[28] from solvation free energies obtained from MD simulation results shown in Fig. 2.4 and discussed in Appendix 2C, yielding $H_{cc}^{gs} = 9.3$ and $H_{cc}^{sb} = 0.0156$ with $H_{cc}^{gb} = 0.145$. The value of H_{cc}^{gb} is consistent with literature values for solvation of O_3 in 1M sodium chloride solutions.[47,48] Surface components H_{cc}^{gs} and H_{cc}^{sb} can in turn be expressed kinetically (Eqs. 2.1 and 2.2), relating the ozone partitioning steps shown in Fig. 2.5A, i.e., adsorption/desorption from the gas-phase and solvation/desolvation from the liquid phase:

$$H_{cc}^{gs} = \frac{[O_{3(ads)}]}{[O_{3(g)}]} = \frac{k_{ads} \cdot \Gamma_{O_3}^{\infty} \cdot \sigma}{k_{des} \cdot \delta}, \qquad \text{Eq. 2.1}$$

$$H_{cc}^{sb} = \frac{[O_{3(b)}]}{[O_{3(ads)}]} = \frac{k_{solv} \cdot \delta}{k_{desolv} \cdot \Gamma_{O_3}^{\infty}}. \qquad \text{Eq. 2.2}$$

In Equations 2.1 and 2.2, the O_3 subscript (*ads*) denotes surface-adsorbed ozone, (*g*) denotes gas-phase O_3 and (*b*) refers to bulk solvated O_3. In the case of fast surface reactions, the effective $[O_{3(g)}]$ near the interface may become depleted due to gas-phase diffusion limitations. To address this in the model, we introduce the species $[O_{3(diff)}]$ that denotes the gas-phase O_3 concentration that has diffused across a characteristic diffusion length in the gas phase. This characteristic length and the kinetic steps governing $[O_{3(diff)}]$ are addressed below in Section 2.4.A and Appendix 2D. The diffusional O_3 description is implemented in the model through modification of Eq. 2.1

$$H_{cc}^{gs} = \frac{[O_{3(ads)}]}{[O_{3(diff)}]} = \frac{k_{ads} \cdot \Gamma_{O_3}^{\infty} \cdot \sigma}{k_{des} \cdot \delta}, \qquad \text{Eq. 2.1a}$$

where the diffusion-limited $[O_{3(diff)}]$ description replaces the overall gas phase concentration $[O_{3(g)}]$. Values for the individual coefficients k_{des} and k_{solv} are computed directly from the MD simulations detailed in Appendix 2C with results shown in Fig. 2C.3. k_{ads} and k_{desolv} can then be calculated using the equilibrium expressions in Eqs. 2.1 and 2.2. The complete set of coefficients is included in Table 2A.1.

Simulating the adsorption and solvation steps for O_3 within the kinetic model is done using a modified Langmuir adsorption framework[49] where O_3 adsorbs (from either the gas or liquid phase) to a surface site (steps A1 and A2, respectively):

$$\mathrm{O}_{3(diff)} + \mathrm{site}_{\mathrm{O}_3} \underset{k_{des}}{\overset{k_{ads}}{\rightleftarrows}} \mathrm{O}_{3(ads)}, \qquad (A1)$$

$$\mathrm{O}_{3(bulk)} + \mathrm{site}_{\mathrm{O}_3} \underset{k_{solv}}{\overset{k_{desolv}}{\rightleftarrows}} \mathrm{O}_{3(ads)}. \qquad (A2)$$

Surface sites for ozone (not pictured in Fig. 2.5 for brevity), are conceptualized as available regions of the interface where ozone can adsorb. In this case, we assume the area of one surface site is equal to the molecular area of O_3 (18.5 Å^2) as computed by Vieceli et al.[50] The maximum number of surface sites is $\Gamma_{\mathrm{O}_3}^{\infty}$ and can be expressed in volumetric units using surface thickness $\Gamma_{\mathrm{O}_3}^{\infty}/\delta$. Throughout the simulation, the total number of surface sites is conserved and expressed as,

$$[\mathrm{site}_{\mathrm{O}_3}] = \frac{\Gamma_{\mathrm{O}_3}^{\infty}}{\delta} - [\mathrm{O}_{3(ads)}]. \qquad \text{Eq. 2.3}$$

Eq. 2.1 includes a dependence on σ, the sticking coefficient (or the thermal accommodation coefficient) for a single O_3 molecule onto a site. The sticking coefficient σ is distinct in the present model from the accommodation coefficient α, defined[51] as the probability of solvation relative to desorption: $\alpha = k_{solv}/(k_{des} + k_{solv})$. From the simulations presented in Appendix 2C, α = 0.0097. While Willis & Wilson could identify a lower bound for σ as $>10^{-4}$, the conditions they analyzed were insensitive to values of σ above this value and the treatment of O_3 gas-phase diffusion was not addressed. In the current work, a greater sensitivity is observed in the kinetic model, and a value $\sigma = 0.93$ is obtained from molecular simulations, in general agreement with measurements from direct scattering experiments.[52–54] A value of $\sigma \sim 1$ means that every O_3 molecule that collides with the interface thermalizes before undergoing desorption, solvation, or reaction.

(ii) Ozone Gas Diffusion Description

Diffusion limitations for surface reactions become relevant for a select range of droplet sizes and reaction rates, where the reactive loss on the surface exceeds the maximum rate O_3 can diffuse to replenish the droplet interface. In this case, the diffusion limit generates an ozone concentration gradient extending from the droplet surface across some characteristic diffusive length L_{diff} into the gas phase (see Appendix 2D, Fig. 2D.1 for illustration of relevant length scales). Previous work studying gas diffusion limitations to droplet surfaces assumed L_{diff} to be equal to the droplet radius r for droplet sizes large enough that the gas phase can be described by the continuum regime (Kn < 0.01).[55,56] The diffusion rate for O_3 in air with diffusion coefficient D_g across a length of $L_{diff} = r$ in one dimension is

$$k_{L_{diff}} = \frac{2 \cdot D_g}{r^2}. \qquad \text{Eq. 2.4}$$

We note that the simulation geometry effectively simulates mass transport using a one-dimensional description, meaning that higher order geometric diffusional corrections are unnecessary.

As the present model avoids explicitly simulating concentration gradients in preference for discretized spatial compartments, an additional characteristic length (the adsorption length L_{ads}) is necessary for describing the local O_3 concentrations near the interface. Originally introduced in the context of surfactant adsorption,[57] L_{ads} denotes the length over which O_3 is depleted in the gas-phase directly from the adsorption and desorption kinetics introduced above as step A1. Conceptually, as shown in Fig. 2D.1, a shell of width L_{ads} surrounding the droplet contains the same number of O_3 molecules as the droplet interface when the system comes to equilibrium. When the droplet surface reaches equilibrium, the number of O_3 molecules on the interface can be calculated as $n_{O_3} = [O_{3(g)}] \cdot H_{cc}^{gs} \cdot V_{surf}$ where V_{surf} is the simulated surface volume (1x1x δ nm^3 in current simulations). The rapid kinetic process at the surface draws n_{O_3} molecules contained in a gas-adsorption volume V_{ads} extending radially from the droplet surface. Maintaining the rectangular prism simulation geometry introduced above then necessitates V_{ads} have length $H_{cc}^{gs} \cdot \delta$ nm. This defines the simulation adsorption length $L_{ads} = H_{cc}^{gs} \cdot \delta$ nm (see Appendix 2D Fig. 2D.1 for summary illustration of characteristic diffusion and adsorption lengths). Since the volume defined by L_{ads} is the relevant gas volume for O_3 adsorption to the interface, the relevant rate for diffusion into the adsorption volume is found by multiplying Eq. 2.4 by L_{diff} / L_{ads}

$$k_{diff} = \frac{2 \cdot D_g}{r^2} \cdot \frac{L_{diff}}{L_{ads}} = \frac{2 \cdot D_g}{r \cdot L_{ads}}. \qquad \text{Eq. 2.5}$$

This definition of k_{diff} is used in the simulation to supply $O_{3(diff)}$ directly to the interface, providing an upper bound on diffusional transport of $O_{3(g)}$ to the surface. Diffusion is simulated in the kinetic model by including the following step directly in the surface compartment:

$$O_{3(g)} \underset{k_{diff}}{\overset{k_{diff}}{\rightleftarrows}} O_{3(diff)}. \qquad (A3)$$

In this implementation, the concentration of species $[O_{3(g)}]$ is defined to remain constant, while $[O_{3(diff)}]$ may deviate from $[O_{3(g)}]$ due to competition between steps A1-A3, as well as any chemistry downstream of these steps.

2.4.C: Aqueous Solute Surface Partitioning Scheme

Surface-adsorption of solutes to the air-water interface is treated using a similar Langmuir description where species in solution, after diffusing into the surface compartment, may adsorb to the surface with a rate proportional to the bulk ion concentration and number of available surface sites. Equilibrium surface-adsorbed $[I^-]$ is expressed by a Langmuir isotherm:

$$[I^-_{(ads)}] = \frac{\Gamma_{I^-}^{\infty}}{\delta} \cdot \frac{K_{eq}^{I^-} \cdot [I^-_{(b)}]}{1 + K_{eq}^{I^-} \cdot [I^-_{(b)}]}, \qquad \text{Eq. 2.6}$$

where the Langmuir equilibrium coefficient is defined kinetically as

$$K_{eq}^{I^-} = \frac{k_{desolv}^{I^-}}{k_{solv}^{I^-}}. \qquad \text{Eq. 2.7}$$

The isotherm in Eq. 2.6 expresses the surface concentration of iodide in terms of the bulk concentration when the system is at equilibrium (i.e., without reaction). While the adsorption description of iodide follows an analogous scheme to the ozone adsorption expression in step A1, iodide and ozone are assumed to occupy a distinct set of surface sites. This is not the case for other solutes, where we assume that reaction products and intermediates in the aqueous phase compete for the same set of surface sites as iodide. A maximum surface site concentration $\Gamma_{\mathrm{I}^-}^{\infty}/\delta$ is defined for these solutes. We estimate a maximum concentration $\Gamma_{\mathrm{I}^-}^{\infty}/\delta$ from previous measurements and simulations of iodide at the air-water interface that indicate surface concentrations ranging from ~ 3M to 10.5 M.[58–60] In the model we use $\Gamma_{\mathrm{I}^-}^{\infty}/\delta$ = 10.5 M as a representative maximum concentration for solutes at the air-water interface, in accordance with measurements of surficial iodide concentrations using nonlinear spectroscopy.[60]

Previous investigations of I^- at the air-water interface have repeatedly found a strong surface preference for iodide relative to other aqueous ions. Such determinations have been made through a variety of techniques including kinetic measurements,[61,62] photoemission spectroscopy,[19,63,64] and second-harmonic generation spectroscopy.[65,66] Measurements of surface-affinity are quantified for iodide through a Gibbs free energy of adsorption to the air-water interface, $\Delta\mathrm{G}_{ads}^{\mathrm{I}^-}$ which can be directly related to a Langmuir equilibrium coefficient using a commonly employed Langmuir adsorption framework:[65] $K_{eq}^{\mathrm{I}^-} = e^{-\Delta\mathrm{G}_{ads}^{\mathrm{I}^-}/RT}/C_w$ where C_w is the solvent concentration (assuming water with C_w ~ 55 M) . Values for $\Delta\mathrm{G}_{ads}^{\mathrm{I}^-}$ have also been computed from ion density profiles obtained by MD simulations of sodium iodide at the air-water interface.[58,67] Reports of $\Delta\mathrm{G}_{ads}^{\mathrm{I}^-}$ from experiment and simulations range from -0.8 kcal/mol to -6.2 kcal/mol, demonstrating a strong dependence on solution composition and model framework employed for analysis.[61–63,65,66,68] This range of $\Delta\mathrm{G}_{ads}^{\mathrm{I}^-}$ corresponds to a large uncertainty in $K_{eq}^{\mathrm{I}^-}$, ranging from 0.1 M^{-1} to 650 M^{-1}. To determine the appropriate $K_{eq}^{\mathrm{I}^-}$ for the present model, we first performed MD simulations of the initial experimental solution composition and observe the initial surface concentration under these conditions to be $[\mathrm{I}_{(ads)}^-]$ = 780 mM (see Fig. 2C.2 in Appendix 2C). Assuming a maximum surface concentration of $\Gamma_{\mathrm{I}^-}^{\infty}/\delta$ = 10.5 M, the simulated $[\mathrm{I}_{(ads)}^-]$ constrains $K_{eq}^{\mathrm{I}^-}$= 0.32 M^{-1}, a value on the lower side of the reported range in the literature.

Although the surface concentrations in the kinetic model are constrained by the MD simulation results, a number of uncertainties persist due to the complex nature of the air-water interface. The surface selectivity of the halide ions depends strongly on the choice of water model and force field parameters in molecular dynamics simulations.[64,69–71] The prediction of our current model and force field is in agreement with recent observation from experiments and MD simulations.[60,69,72] One clear deficiency of the current approach is the coarse-grain perspective of the surface, where a single kinetic volume is used to define the entire interface. In reality, small angstrom-scale features in the density profiles of the solutes and solvent at the interface are important for understanding the structure of the interface. Such features can be observed in the free energy and density profiles for aqueous iodide and ozone included in Fig. 2C.1 and Fig. 2C.2 in Appendix 2C. Fine structural details of this aqueous system have also been observed using liquid microjet techniques combined with X-ray photoemission spectroscopy.[71] From the perspective of reactivity, however, the interface may in fact be sufficiently represented without such fine details in some instances since the chemical loss of I^- at the interface will be determined most strongly by the overlap region of the density profiles of I^- and O_3 at the interface, where concentrations will remain approximately constant (in the absence of diffusive limitations).

The surface affinities of the reaction products are known with less accuracy than iodide. However, some of the oxidation products in solution have been observed to be depleted from the interface and are suspected to be ~10-100x less surface active than I^-.[73,74] Nevertheless, for the sake of simplicity we use the same $K_{eq}^{\mathrm{I}^-}$ for all solutes in the simulation. Furthermore, we also assign the volatile, neutral products generated in solution (I_2 and HOI) to possess the same partitioning behavior with $K_{eq}^{I^-}$. Forward and reverse rates, k_{desolv} and k_{solv}, describing the kinetic components of $K_{eq}^{I^-}$ are included for each simulated species in Table 2A.1 in Appendix 2A and the sensitivity of these rates analyzed in Appendix 2E.

2.4.D: Product Evaporation Description

Volatile products generated by oxidation of iodide (e.g., I_2 and HOI) evaporate from the simulated droplet surface through an irreversible step. As with ions in solution, the first step for a volatile species to partition out of the condensed phase is an adsorption step to the air-water interface. Once adsorbed, the species may evaporate from the surface described by a first-order rate. First-order evaporative rate coefficients for each volatile species are derived using the Hertz-Knudsen equation, where the flux of gas from the surface is calculated[75]

$$J = \frac{\alpha_e \cdot p_{vap}}{\sqrt{2\pi \cdot m k_B T}},$$

where α_e is the evaporation coefficient (assumed to be 1 for simplicity), m is the molecular weight of the volatile species, k_B is the Boltzmann constant and T is the absolute temperature. The saturation vapor pressure of the species, p_{vap}, is related to its Henry law coefficient and adsorbed surface concentration $p_{vap} = [I_{2(ads)}]/H_{cc}^{gb}$. The surface flux is converted to a rate coefficient by scaling J with the surface area-to volume ratio (SA/V) to account for the overall surface accessibility from the bulk. Individual rate coefficients for volatile species are therefore calculated to be[76]

$$k_{evap} = \frac{\mathrm{SA}}{V} \cdot \frac{\alpha_e \cdot \left(\frac{1}{H_{cc}^{gb}}\right)}{\sqrt{2\pi \cdot m k_B T}}.$$

k_{evap} for HOI and I_2, computed from their associated Henry's law constants,[77,78] are used to define evaporative rates for the following steps E1 & E2 (and simulation steps S21 and S22 in Table 2A.1).

$$\mathrm{HOI}_{(ads)} \rightarrow \mathrm{HOI}_{(gas)} + \text{site}, \qquad (E1)$$

$$\mathrm{I}_{2(ads)} \rightarrow \mathrm{I}_{2(gas)} + \text{site}. \qquad (E2)$$

2.4.E: Reaction Steps

The chemical mechanism used in the present model relies on previous literature describing the $I^- + O_3$ reaction in both the gas and liquid phase. The complete set of reactive steps and associated rate coefficients are shown in Table 2A.1. A scheme showing each reaction step is shown in Fig. 2.5B and 2.5C. Below we first review the primary oxidation step of iodide outlined in Fig. 2.5B, followed by the subsequent reactions involving the primary oxidation products found in Fig. 2.5C.

(i) Primary Oxidation Reaction

The initial oxidation step illustrated in Fig. 2.5B is proposed to proceed through a reaction intermediate $IOOO^-$ in analogy to the $BrOOO^-$ intermediate produced during bromide ozonation.[14,31] Although the intermediate $IOOO^-$ has not been directly observed, previous experimental and theoretical work proposed its existence at the air-water interface.[17,22,23,26] The mechanism implemented in the model framework here is adapted from the mechanism for aqueous Br^- oxidation by ozone as introduced by Liu et al.[14] wherein a stable ozonide adduct is first generated, followed by dissociation to HOI or IO^-.

$$\mathrm{I^- + O_3} \underset{k_{-1}}{\overset{k_1}{\rightleftarrows}} \mathrm{IOOO^-}, \tag{$R1$}$$

$$\mathrm{IOOO^- + H^+} \overset{k_2}{\rightarrow} \mathrm{HOI + O_2}, \tag{$R2$}$$

$$\mathrm{IOOO^-} \overset{k_3}{\rightarrow} \mathrm{IO^- + O_2}. \tag{$R3$}$$

The initiation reaction step (R1) involves a fast equilibrium for adduct formation between I^- and O_3. Once formed, the $IOOO^-$ adduct subsequently reacts with a proton or water to form HOI. The proton-assisted pathway is provided as step (R2) and the water-assisted pathway is defined as a unimolecular decay step (R3), assuming the droplet water content remains constant. While rate coefficients for these individual steps are unknown, we propose that previous measurements of the consumption rate of ozone in bulk solutions[14,18] provide the rate of adduct formation, *i.e.,* $k_1 = 1.2\times10^9$ M^{-1} s^{-1}. For the sake of simplicity, and in the absence of evidence to the contrary, we assume steps R1-R3 have the same rate at the surface and within the bulk. Given the measured gas- and liquid-phase rate coefficients for this reaction are nearly identical,[12,14] we believe this is a reasonable assumption. We anticipate the validity of this assumption will be tested by measuring the iodide concentration dependence of the oxidation kinetics, and ideally through future experiments targeting the chemical lifetime of the ozonide intermediate in the bulk and at the surface. We also assume that the proton-assisted decay rate (R2) is diffusion limited, with a rate coefficient of $k_2 = 10^{11}$ M^{-1} s^{-1}, an estimated upper bound for the ion recombination rate in solution as measured previously in the proton-hydroxide recombination reaction.[79,80] While this assumption likely overestimates the rate of (R2), we similarly suggest that such details could be gathered from future experiments studying the ozonide intermediate directly, particularly in light of HOI and IO^- formation kinetics in solution.

Using the aforementioned values of k_1 and k_2, coefficients k_{-1} and k_3 are treated as adjustable parameters in the model. A single set of values for k_{-1} (3.6×10^4 s^{-1}) and k_3 (220 s^{-1}) produce simulation results that agree with the observed droplet kinetics shown in Fig. 2.2. As presented by Liu et al. and shown below in Eq. 2.8, the four rate coefficients k_1, k_{-1}, k_2, and k_3 combined with a steady-state approximation for reaction intermediate $IOOO^-$ yields an effective bimolecular rate coefficient (k_{obs}) for the overall $I^- + O_3$ reaction:

$$k_{obs} = \frac{k_1\left(\frac{k_2}{k_{-1}}\cdot[\mathrm{H^+}] + \frac{k_3}{k_{-1}}\right)}{1 + \frac{k_2}{k_{-1}}\cdot[\mathrm{H^+}] + \frac{k_3}{k_{-1}}}. \tag{Eq. 2.8}$$

k_{obs} quickly approaches measured rate of $k_{exp} = 1.2\times10^9$ L mol^{-1} s^{-1} for neutral to acidic solutions but slows significantly to ~ 7×10^6 L mol^{-1} s^{-1} under strongly basic conditions. Fig. 2.6 shows the behavior of k_{obs} from Eq. 2.8 from pH 0 to 13. As discussed further in Section 2.6, this effective decrease in rate is compounded by the changing overall reactivity of I^- in basic solutions, where secondary chemistry involving I^- is negligible. We note the experimental rate measured by Liu et al.[14] in aqueous solution at pH 6.7 is ~50 times larger than k_{obs} predicted from the parametrization shown in Fig. 2.6. However, this deviation would be expected for bulk measurements of O_3 decay due to $IOOO^-$ formation, as the fast initial adduct formation would not be influenced by differences in bulk pH affecting the overall rate of steps R1-R3.

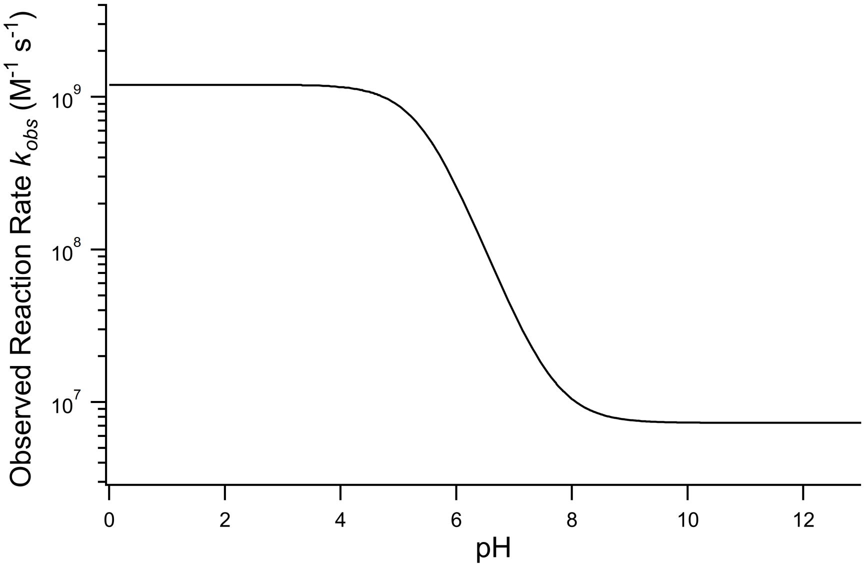

Fig. 2.6: Calculated pH dependence of the primary oxidation rate from combined reaction steps R1-R3. Observed rate k_{obs} is calculated form Eq. 2.8, following the framework of Liu et al.[13] used in the bulk aqueous Br^- + O_3 reaction system.

(ii) Secondary Oxidation Reactions

Once formed, the conjugate pair HOI and IO^- react further with O_3 and I^- yielding different final products depending on pH. For pH values above the pKa of HOI (pKa = 10.8), the unimolecular decay pathway of $IOOO^-$ shown in R3 dominates the overall reactivity and the conjugate base IO^- is stable in solution. Aqueous IO^- can then undergo further oxidation to produce IO_2^- and ultimately the iodate anion IO_3^-. This oxidation process has been studied extensively in wastewater treatment where hypoiodous acid and similar species are used as disenfectants.[81,82] Mechanistic studies of I^- + O_3 in the gas-phase also show IO^- as the first oxidation product in the sequential oxidation of I^- to IO_3^-. The sequential addition mechanism of O_3 to the primary oxidation product IO^- is implemented as observed by Bhujel et al.[12]

$$IO^- + O_3 \rightarrow IO_2^- + O_2, \qquad (R4)$$

$$IO_2^- + O_3 \rightarrow IO_3^- + O_2. \qquad (R5)$$

Reactions R4 and R5 are included directly in the model at both the surface region and the bulk. Here we assume that R4-R5 are irreversible given the relatively slow reverse rate of reaction.[12] As suggested in previous literature, rate coefficients for R4-R5 depend on the phase, where the rate in the gas-phase appears collision limited but the analogous liquid phase rate is ~1000x slower. In the current model, we assume reactions R4-R5 at the droplet surface resemble the gas-phase reactivity more than the liquid phase, and therefore use an approximate diffusion-limited reaction rate coefficient $k \sim 10^{10}$ M^{-1} s^{-1} for steps R4-R5 at the surface. The slower liquid-phase reaction rates $k \sim 10^6$ M^{-1} s^{-1} are used in the bulk phase and are based on past measurements in aqueous solution.[81]

For solutions below pH = 10.8, the primary oxidation product is HOI. Here, the proton-assisted decay of $IOOO^-$ to HOI contributes to the overall loss of the intermediate and quickly becomes the dominate pathway below pH 10. To fully capture the reaction mechanism under neutral to acidic conditions, it is important to account for HOI/IO^- speciation and associated reactions with I^-, OH^-, and I_2. The fate of the HOI/IO^- conjugate pair and their reactivities with iodine in solution have long been studied using spectroscopic techniques in an attempt to unravel this complex mechanism relevant to oxidation processes in disinfection, nuclear chemistry, and halogen chemistry in biological systems.[83–88] Here, we include the steps in the model that are most relevant for the fate of I^- and the pH dependent reactivity in solution. This is summarized in the mechanistic overview in Fig. 2.5C. The most elementary of these reactions is simply the conjugate acid-base conversion

$$\mathrm{H^+ + IO^- \rightleftarrows HOI}. \qquad (R6)$$

As introduced above for reaction R2, we assume that recombination reactions occur at the proton neutralization rate[79,80] in solution $k_{\mathrm{neutral}} = 10^{11}$ M^{-1} s^{-1}. This forward rate of R6 then constrains the reverse dissociation rate of HOI using the pKa = 10.8. Solution pH is then simulated in the model using the fixed dissociation rate coefficient for HOI along with the pseudo-first order reaction rate (i.e., $k_{\mathrm{IO}}' = [H^+]\times k_{\mathrm{neutral}}$).

Having defined solution pH through the speciation of HOI, subsequent chemistry with I^- is addressed. We note that while the O_3 + HOI reaction has been previously observed,[81] this reaction is not included in the model since this reaction rate is 10^5 times slower than the $O_3 + I^-$ reaction and is significantly slower than other sinks for HOI. In the presence of I^-, HOI is quickly converted to I_2 under acidic and neutral pH.[86] Production of I_2 has been reported to occur through two distinct mechanisms that dominate at different pH values, both included in the model as R7-R9. The first pathway involves the formation of reactive intermediate I_2OH^- (R7) which dissociates to I_2 through the proton-assisted reaction in R8. The second formation pathways shown in R9 involves the direct elimination of OH^- from HOI by I^-.[89,90]

$$\mathrm{HOI + I^- \rightleftarrows I_2OH^-}, \qquad (R7)$$

$$\mathrm{I_2OH^- + H^+ \rightleftarrows I_2 + H_2O}, \qquad (R8)$$

$$\mathrm{HOI + I^- \rightleftarrows I_2 + OH^-}. \qquad (R9)$$

The forward and reverse rate coefficients for R7-R9 with literature references[82,89,90] are included in Table 2A.1. While step R7 is independent of solution pH, reactions R8 and R9 both depend directly on pH explicitly through $[H^+]$ and $[OH^-]$. As in the association between IO^- and H^+, pseudo-first order rate coefficients are calculated using $[H^+]$ and $[OH^-]$, as to avoid the computational cost of simulating these species directly. Lastly, once I_2 is produced in solution, the triiodide anion[91] is formed by,

$$\mathrm{I_2 + I^- \rightleftarrows I_3^-}. \qquad (R10)$$

Simulation results, however, predict I_3^- concentrations under all pH conditions are negligible due to the rapid evaporative loss of I_2, which is a dominant sink for iodine in small volumes (*i.e.*, droplets).

The complete set of reactions (R1-R10) as shown in Fig. 2.5B and 2.5C, is included in both the surface and bulk compartments of the kinetic model. As mentioned above, since surface partitioning behaviors of most species involved are unknown, we generally assume the surface partitioning of all solutes match the iodide anion, likely an overestimation of surface activity for most species due to the high surface propensity of I^-. Model sensitivity to absolute k_{desolv} and k_{solv} values is revisited in Appendix 2E for the iodide ion only. We note that the sensitivity of these rates for other solutes is negligible due to the large proportion of bulk chemistry that drives the observed pH sensitivity. All rate coefficients for R1-R10 are also assumed to be equal between the surface and bulk compartments, except for the difference in IO^- and IO_2^- reactivity mentioned above and noted in Table 2A.1.

2.5: Model Results

The simulation results are compared to experiments in Figs. 2.2-2.4 (Section 2.2). Overall, the simulations capture the observed trends in the iodide-decay kinetics and how they depend upon $[O_3]$ and pH. As discussed further below, the initial rate scaling with $[O_3]$ can be understood from transport limitations and surface concentrations, while the pH dependence arises from a surface-rate pH dependence (i.e., R1-R3) and the bulk reaction mechanism (i.e., R6-R9). Although the simulations generally recreate the shape of iodide decay kinetics, the observed experimental decay shapes are not fully replicated. Under basic conditions where $[O_3] < 1$ ppm, simulations predict kinetics that appear more exponential in time, with experiments trending closer to a bi-exponential or linear time-dependence, albeit with larger experimental uncertainty. Although we cannot fully rationalize the origin of these deviations, the differences are relatively small, and the simulated trends generally agree with experiment. Some factors contributing to the shape of time-dependent kinetics will be examined in Section 2.6, with some potential reasons identified for the disagreement between model and experiment.

2.6: Analysis & Discussion

Here we analyze the major features observed in the experimental and simulated kinetics to provide greater insight into the underlying chemical and physical processes governing this heterogenous reaction. First, in Section 2.6.A, the pH dependence of the reaction is examined in more detail, with attention given to identifying which chemical steps appear to determine the overall reaction rate and products observed. Section 2.6.B examines how adsorbed ozone concentrations evolve during the reaction, where an approximate kinetic derivation is used to predict steady-state surface concentrations of ozone during reaction. Results from this derivation are then used in Section 2.6.C to understand the behavior of the overall uptake coefficient for O_3 across a range of reactant concentrations. Results from experiment, simulation, and closed form expressions are compared with past measurements of this system to provide broader context to the current findings.

2.6.A: pH Dependent Reaction Kinetics and Product Distributions

As shown in Fig. 2.4, the experimental and simulated kinetics exhibit a strong pH dependence. In the model, this pH dependence has two distinct origins; the first is the pH rate dependence in the primary oxidation step (R1-R3) and the second is the network of secondary iodide loss channels involving H^+ and OH^- (R6-R9). Model results shown in Appendix 2F demonstrate that the secondary chemistry of iodide alone cannot achieve the model/experiment agreement shown in Figs. 2.2-2.4. As summarized in Fig. 2F.1, this suggests an additional mechanism is responsible for the kinetics observed when varying pH. We propose this additional pH dependence results from the proton-assisted decay of an ozonide intermediate $IOOO^-$ as was first proposed (and later observed) for the analogous Br^- system.[14,31] To the best of our knowledge, no direct evidence of the $IOOO^-$ intermediate has been reported, likely due to a short chemical lifetime. However, according to the parameterization of steps R1-R3 introduced above, such an intermediate may be relatively long lived under strongly basic solutions (with lifetimes on the order of 10-100 μs). On the other hand, as the surface lifetime of $IOOO^-$ and any degree of surface-stabilization is unknown, the overall lifetime may be significantly smaller if bulk solvation occurs on a timescale much faster than chemical decomposition. We also acknowledge that the bulk mechanism for the primary oxidation step may deviate significantly from the surface mechanism, and the kinetics of any intermediates involved may result in a different overall pH dependence. Recent theoretical work investigating the energetics of possible ozonide intermediates for aqueous iodide oxidation suggests a series of possible conformations of the intermediate.[26] The evolution of such conformations and the kinetics involved may again depend greatly on the presence of the interface and local pH.

Across the range of pH studied, a clear difference is observed in the overall product distribution predicted through the kinetic model. While the soluble, terminal product IO_3^- can be observed directly (Fig. 2B.3), volatile products such as I_2 and HOI go undetected in the experiments. Appendix 2G provides the modeled product distribution across the pH range analyzed for an example ozone concentration of $[O_{3(g)}] = 820$ ppb. As expected, for simulations below the pKa of HOI, the dominant product is I_2, with a small fraction of HOI emitted. For strongly basic solution, IO_3^- dominates the product distribution. As observed in the iodate formation kinetics shown in Appendix 2B, the overall fraction of IO_3^- appears to decrease with decreasing $[O_3]$ below 1 ppm. This trend is not observed in the simulations (Fig. 2B.3), and the origin of the changing mechanism is currently unknown.

2.6.B: Surface-Adsorbed Ozone Concentrations

The kinetic simulations indicate that surface-adsorbed ozone concentrations fall below the concentration predicted by Henry's law for a range of solution pH. Fig. 2.7 shows surface-adsorbed $[O_{3(ads)}]$ for three solution pH values at early times in the simulation. For the simulation at pH 13, $[O_{3(ads)}]$ rapidly approaches its Henry's law concentration at the surface, achieving a steady-state concentration that is ~50% of the expected Henry's law concentration. In the pH 8 simulation, however, $[O_{3(ads)}]$ finds its steady-state value that is ~8x smaller. In the acidic extreme at pH 3, $[O_{3(ads)}]$ is ~100x depleted from the Henry's law concentration, indicating that the primary oxidation step for $I^- + O_3$ is substantially limited by O_3 transport to the air-water interface. This transport limitation results from the diffusive rate to the surface being slower than the reactive loss of $O_{3(ads)}$, ultimately depleting both $O_{3(ads)}$ and $O_{3(diff)}$ in the model results. We expect more generally that surface reactions will be limited by ozone diffusion for cases when $k'_{rxn} > k_{diff}$ where the pseudo-first order reaction rate is $k'_{rxn} = k_{obs} \cdot \left[I^-_{(ads)}\right]$. This concept can be concisely expressed using the second Damköhler number, defined in this system as the ratio of the surface reaction rate to the characteristic gas-phase diffusion rate: $Da_{II} = k'_{rxn}/k_{diff}$. Using this notation, the oxidation reaction under conditions with $Da_{II} < 1$ will be limited by the surface reaction itself, whereas $Da_{II} > 1$ denotes the rate will be limited by gas-phase diffusion and will display surface depletion of O_3. As expressed in Eq. 2.5, k_{diff} depends on both the droplet radius and the equilibrium partitioning of O_3 which is captured in the model by use of L_{ads}. While we reserve a more thorough investigation of the droplet-size and molecular specificity of k_{diff} to future work, the MD results in Appendix 2C Section B show that the characteristic rate of surface equilibration ($\sim k_{des}$) is faster than k_{diff} for the particular droplet radius studied—indicating that transport limits of O_3 do not result from kinetic limitations. However, this is not generally the case for smaller droplet sizes, where kinetic limitations at the interface may become dominant.

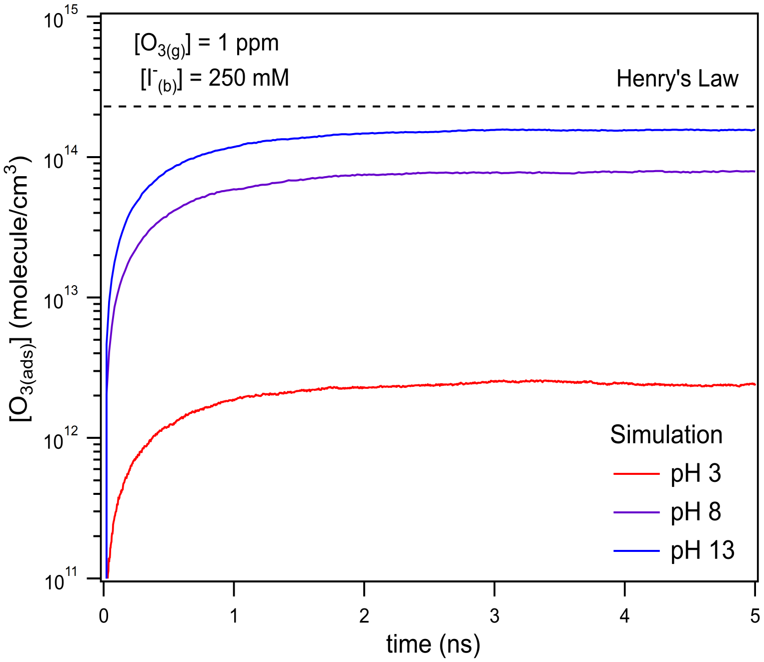

Fig. 2.7: Simulated $[O_{3(ads)}]$ for the first 5 ns of reaction with $[O_{3(g)}]$ = 1 ppm and bulk iodide $[I^-_{(b)}]$ = 250 mM. Adsorbed O_3 is seen reaching a steady state concentration after ~1 ns. Simulation results demonstrate $[O_{3(ads)}]$ is ~100x smaller than the predicted Henry's Law concentration for a pH 3 solution due to the fast chemical loss rate on the surface.

Fig. 2.8 shows that the degree of ozone depletion at the interface is also dependent on the bulk $[I^-_{(b)}]$. Simulations in this case are initialized for each given $[I^-_{(b)}]$ by first computing the corresponding equilibrium $[I^-_{(ads)}]$ as dictated by the Langmuir isotherm (Eq. 2.6). The simulation is then run until a steady state $[O_{3(ads)}]$ is observed. The inflection point noted as a vertical line in Fig. 2.8 indicates the point at which $k'_{rxn} = k_{diff}$, when the reactive loss rate of O_3 on the surface equals the rate of O_3 diffusion into the adsorption length. For ease of example, the pH dependent mechanism and adduct formation is not considered in Fig. 2.8 and a simple second order rate coefficient of $k_{rxn} = 1.2\times10^9$ M^{-1} s^{-1} is used for the $I^- + O_3$ reaction. As all experiments performed in the present work utilize $[I^-]$ = 250 mM, Fig. 2.8 suggests for $k_{obs} \sim 10^9$ M^{-1} s^{-1}, $[O_{3(ads)}]$ is greatly depleted from its Henry's Law concentration. Since the reaction under this condition is limited by O_3 transport, the kinetics scale as first-order in $[O_3]$ as demonstrated through the high linearity of initial rates vs. $[O_3]$ reported in Fig. 2.3.

The surface depletion of O_3 can also be computed analytically using a simple steady-state analysis of $[O_{3(ads)}]$ and $[O_{(diff)}]$ at early reaction times. As shown in Fig. 2.7, $[O_{3(ads)}]$ approaches steady state after approximately 1 ns. Assuming that $[I^-_{(ads)}]$ is equal to the Langmuir equilibrium concentration, the steady-state expressions for $[O_{3(ads)}]$ and $[O_{(diff)}]$ are

$$\frac{d\left[\mathrm{O}_{3(ads)}\right]}{dt} = 0 = \sigma \cdot k_{ads} \cdot \left[\mathrm{O}_{3(diff)}\right] \cdot \left[\mathrm{Site}_{\mathrm{O}_3}\right] - k_{rxn} \cdot \left[\mathrm{O}_{3(ads)}\right] \cdot \frac{\Gamma_{\mathrm{I}^-}^{\infty}}{\delta} \cdot \frac{K_{eq}^{\mathrm{I}^-} \cdot \left[\mathrm{I}_{(b)}^-\right]}{1 + K_{eq}^{\mathrm{I}^-} \cdot \left[\mathrm{I}_{(b)}^-\right]}$$

$$-k_{des} \cdot \left[\mathrm{O}_{3(ads)}\right], \qquad \text{Eq. 2.9a}$$

$$\frac{d\left[\mathrm{O}_{3(diff)}\right]}{dt} = 0 = k_{diff} \cdot \left[\mathrm{O}_{3(gas)}\right] + k_{des} \cdot \left[\mathrm{O}_{3(ads)}\right] - k_{diff} \cdot \left[\mathrm{O}_{3(diff)}\right]$$

$$-\sigma \cdot k_{ads} \cdot \left[\mathrm{O}_{3(diff)}\right] \cdot \left[\mathrm{Site}_{\mathrm{O}_3}\right]. \qquad \text{Eq. 2.9b}$$

Rearranging Eq. 2.9a and 2.9b while substituting for $[\mathrm{O}_{3(diff)}]$ produces an expression for $[\mathrm{O}_{3(ads)}]$ as a function of $[\mathrm{I}^-_{(b)}]$:

$$\left[\mathrm{O}_{3(ads)}\right] = \frac{\sigma \cdot k_{ads} \cdot k_{diff} \cdot \left[\mathrm{O}_{3(gas)}\right] \cdot \left[\mathrm{Site}_{\mathrm{O}_3}\right]}{k_{des} \cdot k_{diff} + k_{rxn} \cdot \frac{\Gamma_{\mathrm{I}^-}^{\infty}}{\delta} \cdot \frac{K_{eq}^{\mathrm{I}^-} \cdot \left[\mathrm{I}_{(b)}^-\right]}{1 + K_{eq}^{\mathrm{I}^-} \cdot \left[\mathrm{I}_{(b)}^-\right]} \cdot \left(k_{diff} + \sigma \cdot k_{ads} \cdot \left[\mathrm{Site}_{\mathrm{O}_3}\right]\right)}.$$

$$\text{Eq. 2.10}$$

Equation 2.10 accounts for the surface depletion of O_3 by the surface reaction only and does not include solvation dynamics of O_3, which quickly become insignificant when surface O_3 becomes depleted by reaction. Furthermore, we highlight that Eq. 2.10 assumes adsorbed I^- equilibrates on a timescale much faster than the O_3 depletion dynamics such that $[\mathrm{I}^-_{(ads)}]$ is equal to the Langmuir equilibrium value calculated from Eq. 2.6. Relaxing this assumption leads to a case where both surface reactants may be depleted. Results from Eq. 2.10 as a function of bulk iodide concentration $[\mathrm{I}^-_{(b)}]$ are compared with simulation results in Fig. 2.8 for $[\mathrm{O}_{3(g)}]$ = 1 ppm. For simplicity, the results from Eq. 2.10 in Fig. 2.8 utilize a simple bimolecular $\mathrm{I}^- + \mathrm{O}_3$ reaction rate of $k_{rxn} = 1.2\times10^9$ M^{-1} s^{-1}. Output from Eq. 2.10 and the simulation predict the same surface behavior for adsorbed O_3, where reaction depletion becomes significant for bulk $[\mathrm{I}^-_{(b)}] > 1$ mM. Only for $[\mathrm{I}^-_{(b)}] <$ 1mM does adsorbed ozone remain at its Henry's Law value. At these lower iodide concentrations, the multiphase kinetics are driven by bulk-reaction dynamics and should be accurately predicted using the closed formed analytical expressions derived in Wilson et al.[29]

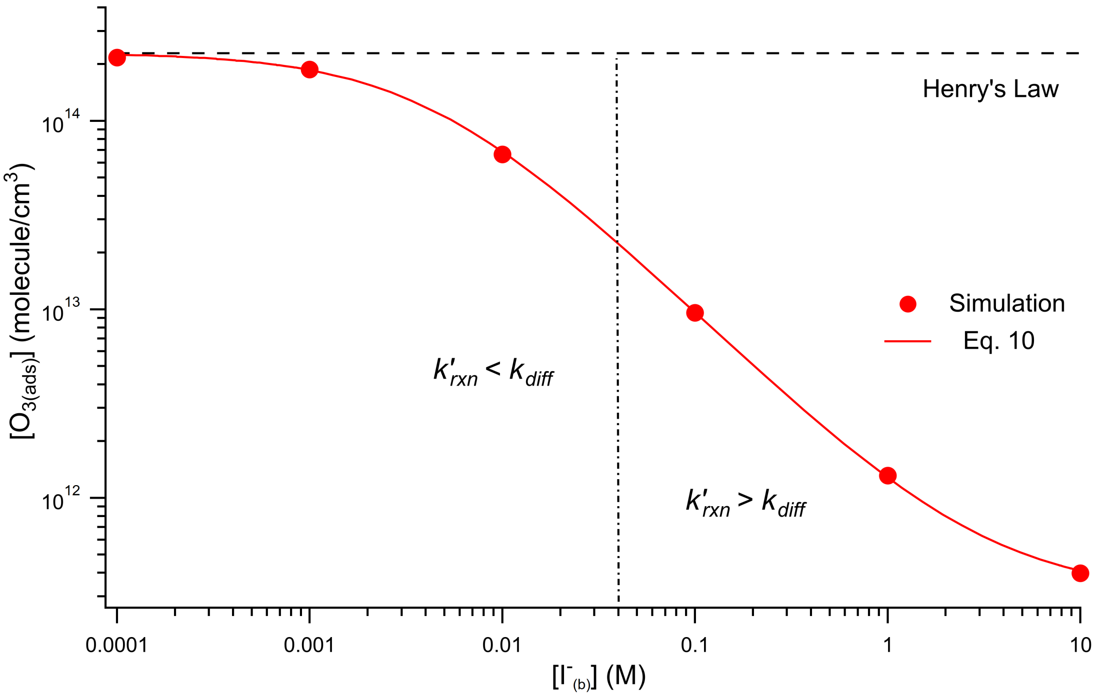

Fig. 2.8: Steady state $[O_{3(ads)}]$ dependence on $[I^-_{(b)}]$ from µM to M concentrations for $[O_{3(g)}]$ = 1 ppm. Points denote simulation results from early steady-state analysis of ozone. The red curve shows steady-state expression from Eq. 2.10. Results are compared to the Henry's Law concentration of $[O_{3(ads)}]$. The dashed vertical line indicates the $[I^-_{(b)}]$ where the chemical loss rate of O_3 at the surface ($k'_{rxn} = [I^-_{(ads)}] \times k_{rxn}$) is equal to the simulated diffusion rate of O_3 (i.e., k_{diff}).

2.6.C: Uptake Coefficients

In this section we compute uptake coefficients from the experimental kinetics shown in Fig. 2.3 and introduce an expression for computing uptake while accounting for surface depletion of O_3. This approach builds on the recent work by Wilson et al.[28,29] where uptake expressions were derived to describe reaction conditions when O_3 is depleted from the bulk solution, but not depleted from the microdroplet surface.

(i) Experimental Uptake Calculation

Reactive uptake coefficients for O_3 are computed from the experimental kinetics shown in Fig. 2.3 using the initial observed reaction rate, k_{init}, to compute γ_{exp},[92]

$$\gamma_{exp} = \frac{4 \cdot r \cdot S_{rxn} \cdot k_{init} \cdot \left[I^-_{(b)}\right]_0}{3 \cdot [O_{3(g)}] \cdot c}, \qquad \text{Eq. 2.11}$$

where r is the droplet radius, c is the mean molecular speed of O_3 in the gas phase, and S_{rxn} is an additional reaction-stoichiometry factor. The S_{rxn} factor is included in Eq. 2.11 since the experiments yield k_{init} for the decay of iodide, whereas the expression for γ_{exp} refers explicitly to the reactive loss of O_3. Secondary chemistry of I^- is coupled to solution pH, and therefore, measurements of k_{init} reflect chemical loss of I^- in addition to the primary $I^- + O_3$ reaction. Following the stoichiometry of reaction, however, allows uptake to be compared across pH using

S_{rxn} to properly compute γ_{exp}. Simulation results predict molecular iodine I_2 as the major product for pH 3 and 8 (demonstrated in Appendix 2G), indicating that for every $I^- + O_3$ reaction an additional I^- is consumed. This 1:2 ozone-to-iodide reaction equivalence is accounted for when calculating γ_{exp} by simply using $S_{rxn} = 0.5$. At pH 13, however, the only relevant loss channel for I^- is O_3 and as such, $S_{rxn} = 1$. We note that only conditions where $[O_{3(g)}] > 1$ppm were used in calculating uptake for pH 13 conditions given the apparent mechanistic complexity for sub-ppm concentrations of O_3. Fig. 2.9 shows average γ_{exp} as a function of pH resulting from Eq. 2.11, where a modest increase in γ_{exp} from ~ 4×10^{-4} at pH 13 to 2×10^{-3} at pH 3 is observed. Experimental results in Fig. 2.9 are compared to the values obtained from the analytical expression introduced in the following section.

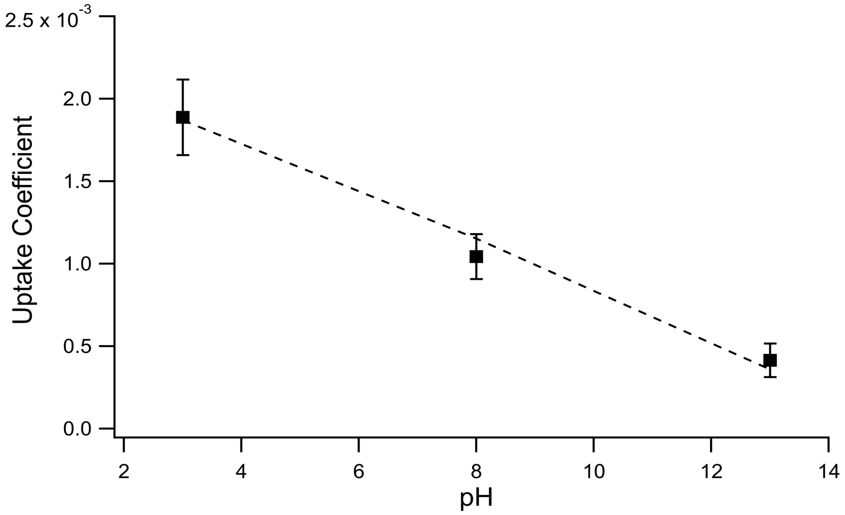

Fig. 2.9: Experimental reactive uptake coefficients for O_3 calculated from Eq. 2.11 (points) compared with the analytical expression for surface uptake coefficients using Eq. 2.12 (dashed line). Error for uptake coefficients reflects the standard deviation of uptake across different $[O_3]$ for each pH.

(ii) Analytic Expression for O_3 Uptake

To compute reactive uptake in this system directly, we begin with the expressions for surface and bulk reactive uptake of O_3 in microdroplets as recently introduced by Wilson *et al.* [29]:

$$\gamma_s = \frac{4 \cdot r \cdot k_{rxn} \cdot [O_{3(ads)}][I^-_{(ads)}]}{3 \cdot c \cdot [O_{3(g)}]} \cdot \frac{(r^3 - (r-\delta)^3)}{r^3}, \qquad \text{Eq. 2.12}$$

$$\gamma_b = \frac{4 \cdot r \cdot k_{rxn} \cdot [I^-_{(b)}]}{3 \cdot c} \cdot \left[\frac{k_{transport} \cdot H^{gb}_{cc}}{k_{rxn} \cdot [I^-_{(b)}] + k_{transport}}\right]. \qquad \text{Eq. 2.13}$$

The radial term in Eq. 2.12 accounts for the relative scaling of surface to bulk volume with changing radius *r* and surface thickness δ. In Eq. 2.13, $k_{transport}$ is a term introduced by Wilson *et al.*[29] that describes an overall ozone equilibration rate into the bulk solution that includes liquid diffusion and kinetic contributions. While previous work utilized the equilibrium assumption $[O_{3(ads)}] = H^{gb}_{cc} \times [O_{3(g)}]$, the current investigation with iodide has shown $[O_{3(ads)}]$ resides far below this equilibrium value. Therefore, Eq. 2.10 which accounts for reactive depletion of $[O_{3(ads)}]$ is used in Eq. 2.12 rather than assuming the Henry's Law concentration.

The surface uptake coefficient calculated from Eq. 2.12 is compared to experimental uptake coefficients in Fig. 2.9. The pH dependence of γ_s is captured by using the pH-scaling of k_{obs} discussed in Section 2.4.E above and provided in Eq. 2.8. As shown in Fig. 2.9, agreement is observed between experiment and the uptake expression in Eq. 2.12, reinforcing the conclusion that the surface reaction dominates iodide loss under our experimental conditions. The agreement between experiment and uptake expressions further motives the use of Eqs. 2.12 and 2.13 to predict uptake across a much larger concentration range. Fig. 2.10 shows uptake predictions from Eqs. 2.12 and 2.13 as well as the sum total $\gamma_{total} = \gamma_s + \gamma_b$ for a constant $[O_{3(g)}]$ = 1 ppm and droplet radius r = 24 µm. Average uptake from the experiments at $[I^-_{(b)}]$ = 250 mM and pH 3 are included for comparison in Fig. 2.10, as well as two limiting cases from resistor-based models discussed in more detail below.

For very low iodide concentrations shown in Fig. 2.10, below 100 nM, the uptake coefficient is dominated by the bulk reaction and is limited by the oxidation reaction rate in the bulk. At approximately $[I^-_{(b)}]$ = 100 nM, uptake of O_3 by a bulk reaction starts becoming limited due to depletion of O_3 in the droplet interior and the surface reaction starts to dominate the reactive uptake. For increasing iodide concentrations, the surface reaction totally governs the uptake of O_3. When iodide concentrations increase above 1 mM, results from Fig. 2.8 suggest $[O_{3(ads)}]$ becomes greatly depleted due to gas-phase diffusion limitations. This depletion effect is similarly observed in Fig. 2.10 in the limiting of surface uptake to values ~ 10^{-3}.

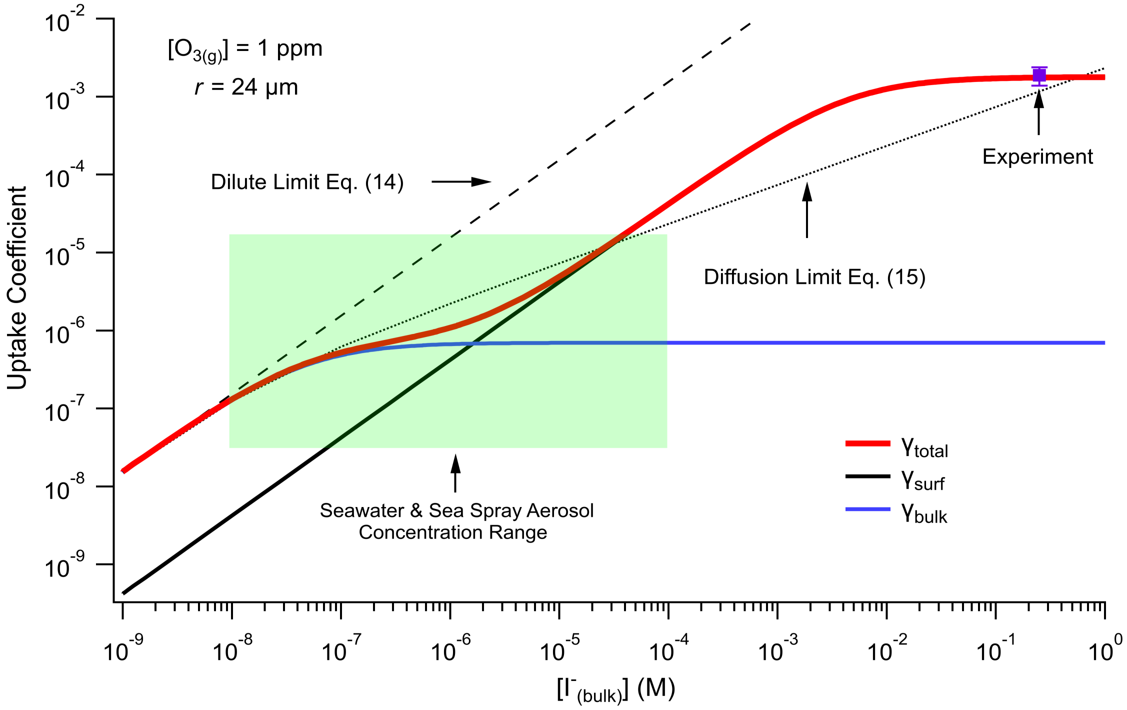

Fig. 2.10: Uptake coefficients computed from Eqs. 2.12 and 2.13 using $[O_{3(g)}]$ = 1 ppm and droplet radius r = 24 µm. Total uptake is the sum of surface and bulk components. Results from the analytical approach are compared with two limiting cases from resistor-based uptake modeling shown as dashed and dotted lines. Experimental uptake at pH 8 is compared with the models.

Fig. 2.10 also compares the uptake coefficient expressions with commonly used resistor model limits shown with dashed lines. For very low $[I^-_{(b)}]$, computed γ_{total} values agree with the dilute limit or "phase-mixed" case introduced by Schwartz *et al.*[93]

$$\gamma_{dilute} = \frac{4 \cdot r \cdot H_{cc}^{gb}}{3 \cdot c} \cdot k_{rxn} \cdot \left[\mathrm{I}^-_{(b)}\right]. \qquad \text{Eq. 2.14}$$

As bulk iodide concentrations increase and γ_s dominates γ_{total}, results approach the "uptake controlled by fast reaction" case from Worsnop *et al.*[51] or the "diffusion limit" case by Schwartz *et al.*

$$\gamma_{diff} = \frac{4 \cdot H_{cc}^{gb}}{c} \cdot \sqrt{D_{\mathrm{O}_{3(b)}} \cdot k_{rxn} \cdot \left[\mathrm{I}^-_{(b)}\right]} \cdot \left[\coth\left(\frac{r}{L_{rxn}}\right) - \frac{L_{rxn}}{r}\right], \qquad \text{Eq. 2.15}$$

where the reaction-diffusion length L_{rxn} is defined as $\sqrt{D_{\mathrm{O}_{3(b)}} / k_{rxn} \cdot \left[\mathrm{I}^-_{(b)}\right]}$. Deviation from the diffusion limit becomes pronounced for intermediate $[I^-_{(b)}]$ as the surface first becomes enriched with $[I^-_{(ads)}]$ relative to the bulk concentration, followed by the depletion of $[O_{3(ads)}]$ for $[I^-_{(b)}] > 1$ mM.

2.6.D: Atmospheric Implications & Literature Comparison

Here, we comment on the relevance of our findings to uptake of O_3 by seawater concentrations of I^- in droplets, and subsequently discuss our findings in context of previous literature results. The expressions for uptake in Eqs. 2.12 and 2.13 allow for the prediction of uptake in systems such as seawater and sea spray aerosol (SSA) interacting with the marine boundary layer, where near-surface seawater iodide concentrations range from ~10-200 nM[94] and typical ozone concentrations in the marine boundary layer are ~20 ppb.[95–98] For these concentrations, uptake of O_3 by a droplet with radius $r = 24$ μm is on the order of 5×10^{-7} with bulk chemistry dominating the overall uptake. As previously reported, salt concentrations in SSA can increase dramatically upon emission from the sea surface, with I^- becoming potentially enhanced by factors up to ~1000[99–101] and, in some measurements, making up a third of the total soluble iodine content of aerosol with particle radius r < 500 nm.[102] Additionally, rapid acidification of SSA[103] may contribute to an apparent acceleration of iodide oxidation by ozone relative to the pH of seawater (~ pH 8). Under these concentrated and acidic conditions where iodide concentrations could approach ~100 μM, the expression obtained for γ_{total} predicts the uptake of ozone is driven almost exclusively by the surface reaction. However, we acknowledge that the current model construction employs a coarse-grain depiction of the droplet surface and bulk regions and therefore potentially overlooks important "sub-surface" dynamics which would affect the predicted transition in bulk vs. surface uptake. For reference we include the range of iodide concentrations encountered in seawater and SSA in the highlighted box in Fig. 2.10, where the transition from bulk to surface chemistry is observed.

While the model predictions presented in Fig. 2.10 suggest both surface and bulk contributions to the uptake of O_3 under relevant salt concentrations, we emphasize that results in Fig. 2.10 have resulted from evaluating Eqs. 2.12 and 2.13 for the droplet radius r = 24 μm investigated in the experiments. For SSA and marine aerosol a broad range of sizes are encountered, where typical aerosols have radii r < 10 μm and submicron particles make up the vast majority of aerosol by total number. For such small sizes, we expect the surface contribution to the overall uptake of O_3 by I^- to become even more significant due to the inverse radial scaling of the surface to volume ratio. On the other hand, Eqs. 2.12 and 2.13 predict the uptake of ozone by a macro-scale system such as the sea surface would be dominated by bulk chemistry using the same radial scaling argument. However, correctly calculating uptake for macro-scale systems utilizing the current model would require detailed knowledge of the system dimensions and the governing gas-phase mass transport steps for O_3 across large systems such as the marine boundary layer. As such, we reserve a more complete discussion of the size-dependence of γ_{total} under relevant concentrations to future work.

Uptake coefficients calculated from the analysis above and observed in experiments can also be compared to previous laboratory measurements of uptake of O_3 on aqueous iodide solutions and aerosol. One of the most comparable previous reports by Magi et al.[10] measures uptake of O_3 using a droplet-train apparatus, with droplet sizes ~100 μm and NaI concentrations ranging from 0.5 to 3 M. The reported uptake coefficient from this work under conditions 293 K and $[I^-] = 0.5$ M is $\gamma = 5\times10^{-3}$, only about 2-3 times greater than the maximum uptake measured in this work. However, as the droplet-train apparatus operates at reduced pressure (10-30 torr), deviations from uptake measured at ambient pressure may be expected. Additional relevant experiments performed by Ammann and coworkers[20,21] use submicron sodium iodide aerosol to measure the uptake of ozone. The main difference between the conditions of these experiments and ours is particle size, as the present experiments all utilize much larger microdroplets. Nevertheless, measurements on submicron aerosol composed of iodide/chloride mixtures by Rouvière et al.[20] yield uptake coefficients of $\gamma \sim 4.4\times10^{-3}$, which differ by a factor of ~2 from the largest uptake coefficients observed in our experiments. This reference also reports a relatively weak concentration dependence, where increasing $[I^-]$ from 0.9 M to 7.3 M increases the ozone reactive uptake coefficient by ~2.5. This may point to a similar surface ozone depletion effect observed for sub-micron aerosol, although a more in-depth analysis of the experimental conditions used is needed to draw any specific conclusions from this past work.

Lastly, we note that while the conditions studied and modeled in the current work generally do not accurately represent conditions found in real-world systems, our current approach aims to identify and analyze the molecular-scale processes governing reactivity in simple multiphase systems. A deep understanding of these simple systems, in turn, builds the foundation for investigating the complex systems encountered in the environment.

2.7: Conclusion

Kinetics of iodide oxidation by ozone in single microdroplets are reported and analyzed with a recently developed multiphase model that describes individual surface and bulk processes occurring during the course of reaction. A kinetic model is constructed using literature references, basic assumptions about rate coefficients, and is further constrained using molecular simulations of O_3 and iodide at the air-water interface. Use of the model provides insight into important surface mechanisms that govern the overall reactivity in microdroplets and provide a benchmark for developing more general expressions for O_3 uptake in aerosol. Experimental results in conjunction with modeling work suggest the $I^- + O_3$ reaction under the conditions studied occurs exclusively at the air-water interface. Nevertheless, we note that since the model employed discretizes the entire droplet into two compartments, a detailed account of sub-surface diffusion and reaction processes may be lacking which could be important for a clear accounting of surface vs. bulk reactivity. We anticipate future work will clarify these subsurface processes to fully understand the transition between surface and bulk reactivity.

A strong dependence on the consumption rate of I^- with bulk solution pH is observed, as previously reported for bulk solution. However, the modeled pH-dependent chemistry involving I^- in solution cannot fully explain the observed kinetics. To explain the observed pH dependence of the $I^- + O_3$ reaction we invoke an $IOOO^-$ intermediate, which is analogous to reaction intermediates found in the mechanism governing bromide oxidation by ozone at the air-water interface. A kinetic analysis also demonstrates a first-order dependence on $[O_{3(gas)}]$ for all pH conditions. Simulation and analytical results suggest this reaction order originates from the depletion of ozone at the droplet surface during reaction for neutral to acidic conditions, and the linear scaling of surface adsorbed O_3 for mild to extremely basic conditions. Surface depletion of reagents appears to be a general feature of fast surface-reactions and may be relevant across scales for many systems involving uptake of trace gases. A kinetic expression for steady-state ozone concentrations on the droplet surface, Eq. 2.10, is derived and subsequently used in a recently developed set of expressions, Eq. 2.12 and Eq. 2.13, for predicting uptake coefficients in droplets due to both surface and bulk reactions. Surface uptake coefficients calculated using Eq. 2.10 for surface-adsorbed O_3 indicate a large sensitivity to reactive depletion of species at the air-water interface, warranting the further study of the conditions under which reactants become depleted at interfaces.

Total uptake coefficients predicted by the analytical expressions obtained are analyzed across a range of concentrations and compared to the experimental uptake values of $\gamma \sim 10^{-3}$ and previous aerosol uptake experiments from the literature. The applicability of the present findings to reaction in seawater and sea spray aerosol is considered, with a brief discussion of the major findings and limitations of the modeling approach. Future work aims to expand the current approach to understand mass transport limitations in heterogeneous chemistry more broadly while investigating which key parameters control uptake coefficients and how these processes are related to reaction mechanisms at the droplet surface, where a number of factors such as partial solvation, pH, and reaction depletion may significantly alter expected uptake.

2.8: Chapter 2 Appendix – Supplemental Information

Appendix 2A: Model reaction steps

The complete set of elementary steps used in the model and implemented in Kinetiscope© are shown in Table 2A.1. As outlined in the main text, kinetic steps can occur within the surface or bulk compartment (steps labeled S or B, respectively in Table 2A.1). Diffusion steps are labeled D. Each labeled step is shown along with rate or diffusion coefficients used for the physical adsorption, chemical reactions, diffusion, and evaporative steps. References for literature equilibrium coefficients, rate constants, diffusion coefficients, and Henry's law constants are provided in the right-most column.

Table 2A.1: Elementary reaction steps, rate and diffusion coefficients used in the Kinetiscope© simulations. Reaction steps that occur in the surface compartment, diffusion coefficients for the transfer of species between surface and bulk compartments, and bulk compartment steps are labeled by S, D, and B respectively. Literature references for the rate coefficients, diffusion constants, and Henry's Law constants are also provided.

#	Step	Rate coefficient	Reference
S1	$O_{3(g)} \underset{k_{diff}}{\overset{k_{diff}}{\rightleftarrows}} O_{3(diff)}$	$k_{diff} = 1.6 \times 10^{8}\ s^{-1}$	see sections 2.4.A & Appx. 2D
S2	$O_{3(diff)} + \text{site}_{O_3} \underset{k_{des}}{\overset{k_{ads}}{\rightleftarrows}} O_{3(ads)}$	$k_{ads} = 3.31 \times 10^{-11}\ cm^{3} \cdot molec.^{-1} \cdot s^{-1}$ $k_{des} = 1.93 \times 10^{10}\ s^{-1}$	see sections 2.4.A & Appx 2C
S3	$O_{3(ads)} \underset{k_{desolv}}{\overset{k_{solv}}{\rightleftarrows}} O_{3(b)} + \text{site}_{O_3}$	$k_{solv} = 1.90 \times 10^{8}\ s^{-1}$ $k_{desolv} = 2.25 \times 10^{-12}\ cm^{3} \cdot molec.^{-1} \cdot s^{-1}$	see sections 2.4.A & Appx 2C
S4	$I^{-}_{(ads)} \underset{k_{desolv}}{\overset{k_{solv}}{\rightleftarrows}} I^{-}_{(b)} + \text{site}_{I}$	$k_{solv} = 1 \times 10^{3}\ s^{-1}$ $k_{desolv} = 5.35 \times 10^{-19}\ cm^{3} \cdot molec.^{-1} \cdot s^{-1}$	19,58
S5	$IO^{-}_{(ads)} \underset{k_{desolv}}{\overset{k_{solv}}{\rightleftarrows}} IO^{-}_{(b)} + \text{site}_{I}$	$k_{solv} = 1 \times 10^{3}\ s^{-1}$ $k_{desolv} = 5.35 \times 10^{-19}\ cm^{3} \cdot molec.^{-1} \cdot s^{-1}$	19,58
S6	$IO^{-}_{2(ads)} \underset{k_{desolv}}{\overset{k_{solv}}{\rightleftarrows}} IO^{-}_{2(b)} + \text{site}_{I}$	$k_{solv} = 1 \times 10^{3}\ s^{-1}$ $k_{desolv} = 5.35 \times 10^{-19}\ cm^{3} \cdot molec.^{-1} \cdot s^{-1}$	19,58
S7	$IO^{-}_{3(ads)} \underset{k_{desolv}}{\overset{k_{solv}}{\rightleftarrows}} IO^{-}_{3(b)} + \text{site}_{I}$	$k_{solv} = 1 \times 10^{3}\ s^{-1}$ $k_{desolv} = 5.35 \times 10^{-19}\ cm^{3} \cdot molec.^{-1} \cdot s^{-1}$	19,58
S8	$I_{2(ads)} \underset{k_{desolv}}{\overset{k_{solv}}{\rightleftarrows}} I_{2(b)} + \text{site}_{I}$	$k_{solv} = 1 \times 10^{3}\ s^{-1}$ $k_{desolv} = 5.35 \times 10^{-19}\ cm^{3} \cdot molec.^{-1} \cdot s^{-1}$	19,58
S9	$HOI_{(ads)} \underset{k_{desolv}}{\overset{k_{solv}}{\rightleftarrows}} HOI_{(b)} + \text{site}_{I}$	$k_{solv} = 1 \times 10^{3}\ s^{-1}$ $k_{desolv} = 5.35 \times 10^{-19}\ cm^{3} \cdot molec.^{-1} \cdot s^{-1}$	19,58
S10	$I^{-}_{3(ads)} \underset{k_{desolv}}{\overset{k_{solv}}{\rightleftarrows}} I^{-}_{3(b)} + \text{site}_{I}$	$k_{solv} = 1 \times 10^{3}\ s^{-1}$ $k_{desolv} = 5.35 \times 10^{-19}\ cm^{3} \cdot molec.^{-1} \cdot s^{-1}$	19,58
S11	$I^{-}_{(ads)} + O_{3(ads)} \underset{k_{r}}{\overset{k_{f}}{\rightleftarrows}} IOOO^{-}_{(ads)} + \text{site}_{O_3}$	$k_{f} = 2 \times 10^{-12}\ cm^{3} \cdot molec.^{-1} \cdot s^{-1}$ $k_{r} = 3.6 \times 10^{4}\ s^{-1}$	14 see note§
S12	$IOOO^{-}_{(ads)} + H^{+} \xrightarrow{k_{f}} HOI_{(ads)}$	$^{\dagger}k_{f} = 1.66 \times 10^{-10}\ cm^{3} \cdot molec.^{-1} \cdot s^{-1}$	§
S13	$IOOO^{-}_{(ads)} \xrightarrow{k_{f}} IO^{-}_{(ads)}$	$k_{f} = 2.2 \times 10^{2}\ s^{-1}$	§
S14	$IO^{-}_{(ads)} + O_{3(ads)} \xrightarrow{k_{f}} IO^{-}_{2(ads)} + \text{site}_{O_3}$	$k_{f} = 1.66 \times 10^{-11}\ cm^{3} \cdot molec.^{-1} \cdot s^{-1}$	12 see note ∫
S15	$IO^{-}_{2(ads)} + O_{3(ads)} \xrightarrow{k_{f}} IO^{-}_{3(ads)} + \text{site}_{O_3}$	$k_{f} = 1.66 \times 10^{-11}\ cm^{3} \cdot molec.^{-1} \cdot s^{-1}$	12 see note ∫
S16	$IO^{-}_{(ads)} + H^{+} \underset{k_{r}}{\overset{k_{f}}{\rightleftarrows}} HOI_{(ads)}$	$^{\dagger}k_{f} = 1.66 \times 10^{-10}\ cm^{3} \cdot molec.^{-1} \cdot s^{-1}$ $k_{r} = 1.58\ s^{-1}$	81,88 see note†
S17	$HOI_{(ads)} + I^{-}_{(ads)} \underset{k_{r}}{\overset{k_{f}}{\rightleftarrows}} I_{2}OH^{-}_{(ads)} + \text{site}_{I}$	$k_{f} = 6.64 \times 10^{-17}\ cm^{3} \cdot molec.^{-1} \cdot s^{-1}$ $k_{r} = 1.34 \times 10^{2}\ s^{-1}$	90

S18	$I_2OH^-_{(ads)} + H^+ \underset{k_r}{\overset{k_f}{\rightleftarrows}} I_{2(ads)}$	${}^{\dagger}k_f = 3.32 \times 10^{-11}\ cm^3 \cdot molec.^{-1} \cdot s^{-1}$ $k_r = 3.2\ s^{-1}$	90
S19	$HOI_{(ads)} + I^-_{(ads)} \underset{k_r}{\overset{k_f}{\rightleftarrows}} I_{2(ads)} + OH^- + site_I$	$k_f = 3.5 \times 10^{-18}\ cm^3 \cdot molec.^{-1} \cdot s^{-1}$ ${}^{\dagger}k_r = 1.16 \times 10^{-16}\ s^{-1}$	89
S20	$I_{2(ads)} + I^-_{(ads)} \leftrightarrow I^-_{3(ads)} + site_I$	${}^{+}k_f = 1 \times 10^{-15}\ cm^3 \cdot molec.^{-1} \cdot s^{-1}$ $k_r = 8.64 \times 10^2\ s^{-1}$	91
S21	$I_{2(ads)} \xrightarrow{k_{evap}} I_{2(g)} + site_I$	$k_{evap} = 10^5\ s^{-1}$	77
S22	$HOI_{(ads)} \xrightarrow{k_{evap}} HOI_{(g)} + site_I$	$k_{evap} = 1.76 \times 10^3\ s^{-1}$	78
D1	$I^-_{(b)}$	$D = 1.53 \times 10^{-5}\ cm^2 \cdot s^{-1}$	104
D2	$IO^-_{(b)}$	$D = 1.53 \times 10^{-5}\ cm^2 \cdot s^{-1}$	104
D3	$IO^-_{2(b)}$	$D = 1.53 \times 10^{-5} cm^2 \cdot s^{-1}$	104
D4	$IO^-_{3(b)}$	$D = 1.53 \times 10^{-5}\ cm^2 \cdot s^{-1}$	104
D5	$I_2OH^-_{(b)}$	$D = 1.53 \times 10^{-5}\ cm^2 \cdot s^{-1}$	104
D6	$I^-_{3(b)}$	$D = 1.07 \times 10^{-5}\ cm^2 \cdot s^{-1}$	105
D7	$I_{2(b)}$	$D = 1.15 \times 10^{-5}\ cm^2 \cdot s^{-1}$	106
D8	$HOI_{(b)}$	$D = 1.53 \times 10^{-5}\ cm^2 \cdot s^{-1}$	104
D9	$O_{3(b)}$	$D = 1.76 \times 10^{-5}\ cm^2 \cdot s^{-1}$	107
B1	$I^-_{(b)} + O_{3(b)} \underset{k_r}{\overset{k_f}{\rightleftarrows}} IOOO^-_{(b)}$	$k_f = 2 \times 10^{-12}\ cm^3 \cdot molec.^{-1} \cdot s^{-1}$ $k_r = 3.6 \times 10^4\ s^{-1}$	14 see note[§]
B2	$IOOO^-_{(b)} + H^+ \xrightarrow{k_f} HOI_{(b)}$	${}^{\dagger}k_f = 1.66 \times 10^{-10}\ cm^3 \cdot molec.^{-1} \cdot s^{-1}$	§
B3	$IOOO^-_{(b)} \xrightarrow{k_f} IO^-_{(b)}$	$k_f = 2.2 \times 10^2\ s^{-1}$	§
B4	$IO^-_{(b)} + O_{3(b)} \xrightarrow{k_f} IO^-_{2(b)}$	$k_f = 2.65 \times 10^{-15}\ cm^3 \cdot molec.^{-1} \cdot s^{-1}$	81
B5	$IO^-_{2(b)} + O_{3(b)} \xrightarrow{k_f} IO^-_{3(b)}$	$k_f = 2.65 \times 10^{-15}\ cm^3 \cdot molec.^{-1} \cdot s^{-1}$	81
B6	$IO^-_{(b)} + H^+ \underset{k_r}{\overset{k_f}{\rightleftarrows}} HOI_{(b)}$	${}^{\dagger}k_f = 1.66 \times 10^{-10}\ cm^3 \cdot molec.^{-1} \cdot s^{-1}$ $k_r = 1.58\ s^{-1}$	81,88 see note[†]
B7	$HOI_{(b)} + I^-_{(b)} \underset{k_r}{\overset{k_f}{\rightleftarrows}} I_2OH^-_{(b)}$	$k_f = 6.64 \times 10^{-17}\ cm^3 \cdot molec.^{-1} \cdot s^{-1}$ $k_r = 1.34 \times 10^2\ s^{-1}$	90
B8	$I_2OH^-_{(b)} + H^+ \underset{k_r}{\overset{k_f}{\rightleftarrows}} I_{2(b)}$	${}^{\dagger}k_f = 3.32 \times 10^{-11}\ cm^3 \cdot molec.^{-1} \cdot s^{-1}$ $k_r = 3.2\ s^{-1}$	90
B9	$HOI_{(b)} + I^-_{(b)} \underset{k_r}{\overset{k_f}{\rightleftarrows}} I_{2(b)} + OH^-$	$k_f = 3.5 \times 10^{-18}\ cm^3 \cdot molec.^{-1} \cdot s^{-1}$ ${}^{\dagger}k_r = 1.16 \times 10^{-16}\ s^{-1}$	89
B10	$I_{2(b)} + I^-_{(b)} \underset{k_r}{\overset{k_f}{\rightleftarrows}} I^-_{3(b)} + site_I$	${}^{+}k_f = 1 \times 10^{-15}\ cm^3 \cdot molec.^{-1} \cdot s^{-1}$ $k_r = 8.64 \times 10^2\ s^{-1}$	91

[§] As discussed in main text, forward rates for steps S11, S16, B2, and B6 utilize a diffusion limitation assumption. Rate coefficient k_r for step S11 and k_f for step S13 (and corresponding bulk steps B1 & B3) are treated as adjustable parameters in the model, yielding a single pair that agrees with experimental data.

[ʃ] Rate coefficients from gas-phase measurements are faster than liquid-phase diffusion limit. Therefore, we estimate the rate to be equal to an approximate liquid-diffusion limited rate of 10^{10} $M^{-1}\ s^{-1}$.

†$[H^+]$ and $[OH^-]$ are not defined explicitly in the simulations, where instead a pseudo-first order rate constant (e.g. $k \cdot [H^+]$) is used to simulate reactions in solution assuming constant $[H^+]$ and $[OH^-]$.

+Literature rate coefficients for the forward and reverse directions of this equilibrium are both 10^4 larger than coefficients used here. Because such a rapid equilibrium creates lengthy simulations times, the absolute rates have been diminished. However, model sensitivities tests have shown simulation results are insensitive to these rate coefficients above their presented values.

Appendix 2B: OPSI-MS droplet concentration response, example mass spectra, iodate formation kinetics

In Fig. 2B.1, the iodide peak area detected by the OPSI is compared against droplet solution concentration to analyze the linearity of droplet response. Measurements of peak area vs. concentration are compared to measurements using an internal standard ($NaClO_3$). In both cases, a high degree of linearity between droplet signal and concentration is observed. Slight deviations for total peak area are observed, likely due to variation in droplet radius between measurements on the order of ±1 μm, a result of slightly different water activities between conditions studied (NaCl concentrations adjusted accordingly to initial solution as to maintain constant water activity).

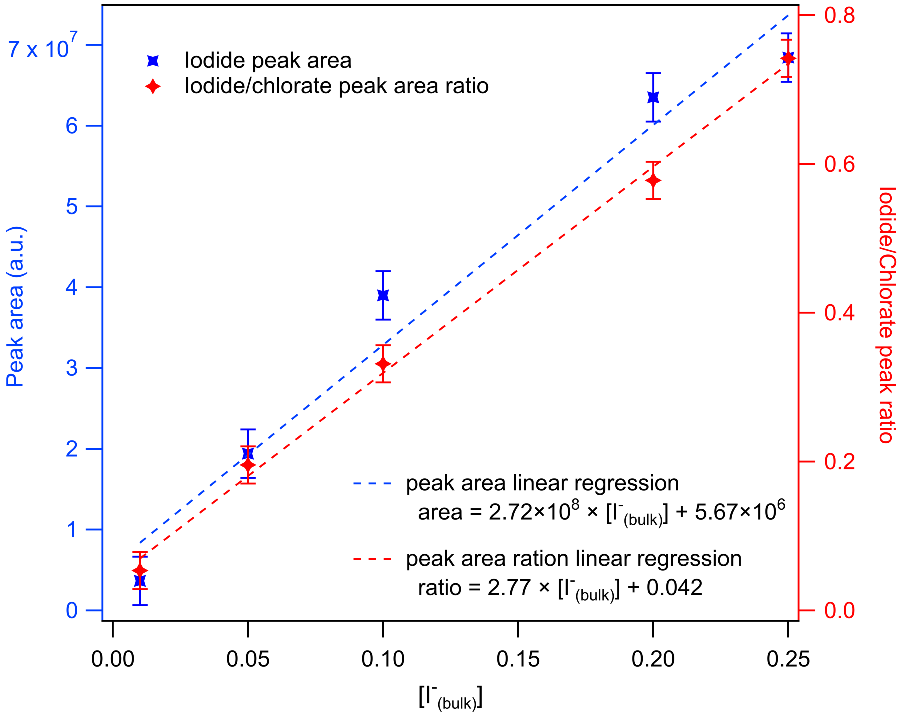

Fig. 2B.1: Iodide peak area vs concentration to observe droplet response using the open-port sampling interface. Peak area ratios of iodide to an internal standard (ClO_3^-) are also provided to demonstrate linearity of both approaches.

Mass spectra for typical droplet detection events are included in Fig. 2B.2 demonstrating the overall intensity of the iodide anion signal before reaction, and the decreased signal after oxidation by ozone. This particular example shows production of IO_3^- at m/z = 174 under strong basic conditions after ~35 minutes of exposure to a 1.6 ppm [O_3] flow. Typical background ions observed by the mass spectrometer are labeled in the "reacted" spectrum where the overall iodide signal is diminished. These background ions ($C_3H_5O_3^-$ m/z = 89.0, $C_2H_5O_3^-$ m/z = 77.0, $C_2H_3O_3^-$ m/z = 75.0) are small organics that originate either from dilute impurities in the methanol used as the OPSI solvent, or simply from the interaction between the laboratory air and the electrospray plume. These background peaks are also present in the unreacted spectrum in Fig. 2B.2 but are dwarfed by the intensity of the iodide peak at m/z = 126.9. While small impurities are commonly observed in all of our experiments, these species have not been observed to impact the kinetic measurements. Formation kinetics of IO_3^- are also provided in Fig. 2B.3 for three ozone concentrations < 1 ppm. Notably, we observe the production of IO_3^- to diminish with decreasing O_3, an effect not observed in the kinetic simulations. The origin of this effect is unknown, but we speculate this is possibly due to I_2 production and evaporation when the oxidation rate of IO^- becomes sufficiently slow under low [O_3].

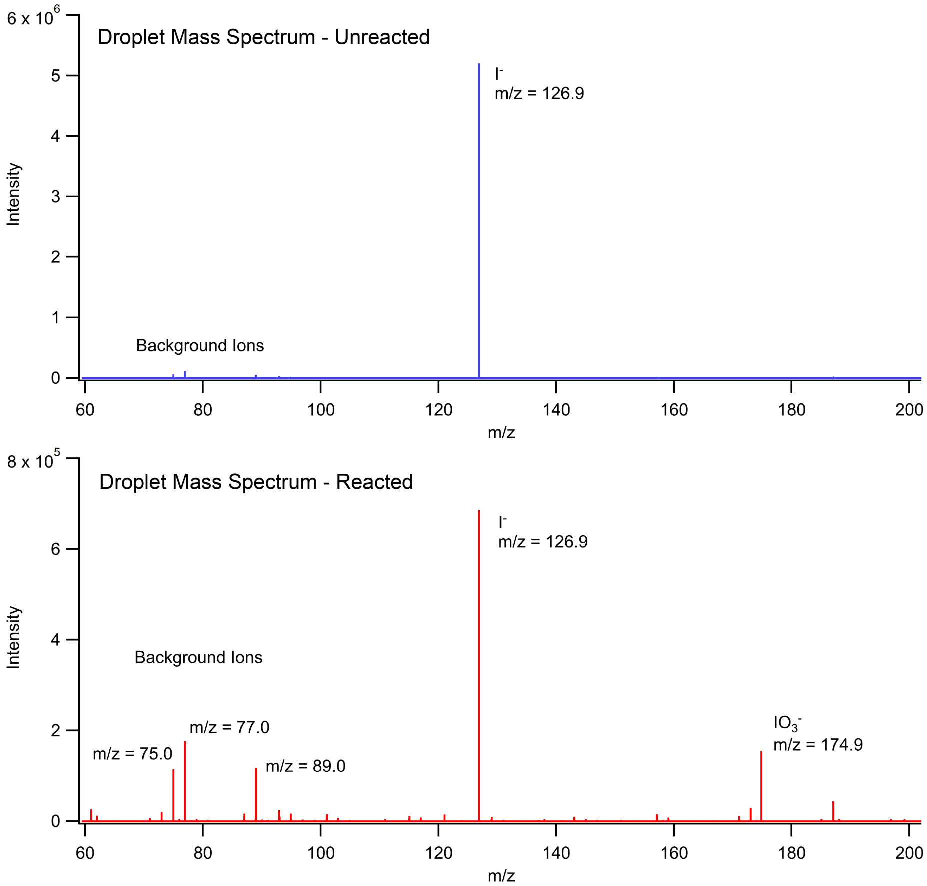

Fig. 2B.2: Mass spectra for unreacted and reacted microdroplets containing NaI at pH 13. Reacted droplet spectrum results from 35 minutes of oxidation using [O_3] = 1.6 ppm. In this case, IO_3^- is observed as a soluble product in the spectrum.

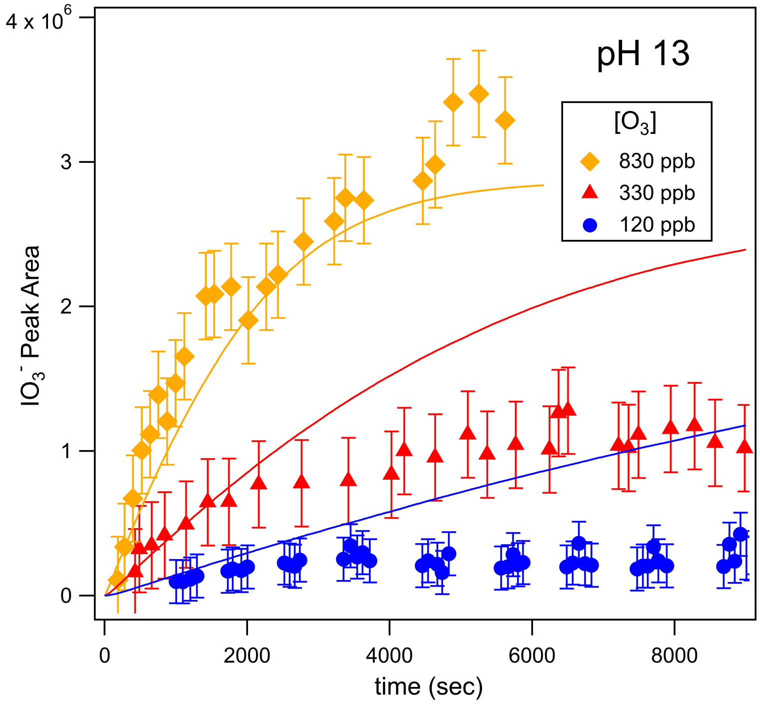

Fig. 2B.3: Experiment and simulation results showing production of IO_3^- for a series of sub-ppm $[O_3]$ with initial droplet pH =13 and a droplet radius of 24 μm. Total ion signal at m/z 174 is observed to decrease as $[O_3]$ decreases, indicating a change in the surface mechanism of I^- oxidation not predicted by the model results.

Appendix 2C: Molecular Dynamics simulations: methodology, results, and discussion

(i) Free Energy Profiles

We used a classical polarizable force field to model the air water interface. A water slab with 768 water molecules at 300 K in a box of size a box of size $24.8 \times 24.8 \times 111.76$ Å^3 was used to represent an aqueous droplet where the larger dimension, denoted the z-axis, is perpendicular to the interface. A periodic boundary condition was applied in all directions. Water, ions and ozone were simulated with a polarizable force field in conjunction with SWM4-NDP[41] as the water model. To use a large time step of 1 fs, we employed a rigid body dynamics for the water and ozone.[108] The non-bonded pair interactions were described with a '12-6' Lennard-Jones model

$$U_{LJ} = \sum_{i,j} 4\epsilon_{ij} \left[\left(\frac{\sigma_{ij}}{r_{ij}} \right)^{12} - \left(\frac{\sigma_{ij}}{r_{ij}} \right)^{6} \right], \qquad \text{Eq. 2C. 1}$$

where r_{ij} is the distance between sites i and j and σ_{ij} and ϵ_{ij} are Lennard-Jones parameters. These parameters are summarized in Table 2C.1. A Lorentz-Berthelot mixing rule was used where $\sigma_{ij} = (\sigma_{ii} + \sigma_{jj})/2$ and $\epsilon_{ij} = \sqrt{\epsilon_{ii}\epsilon_{jj}}$. A Drude[109] oscillator model was used to replicate polarization in the simulation. A spring constant, k_D, of 1000 kcal mol^{-1} Å^{-2} was set for all the Drude oscillators in system,[110] which determines the charge q_D that the Drude particle must carry to produce the correct polarizability through the relation $\zeta = q_D^2/k_D$.

Table 2C.1: The force field parameters used in MD simulation. The water force field parameters are taken from Lamoureux et al.,[41] the ozone force field from Vieceli et al.,[50] and the alkali halide force field from Dang et al.[67] For an ozone molecule, $r_{eq}(\mathrm{O_{center}} - \mathrm{O_{side}}) = 1.28$ Å , and $\theta_{eq} = 116.7°$.

Species	Atom	$\epsilon(\mathrm{kcal\ mol^{-1}})$	σ(Å)	ζ, Polarizability (Å^3)
H_2O	H	0.0000	0.0000	0.0000
	O	0.2109	3.1839	0.9783
O_3	O_{center}	0.1560	3.2037	0.9500
	O_{side}	0.1560	3.2037	0.9500
Na^+	Na	0.1000	2.2718	0.2400
Cl^-	Cl	0.1000	4.3387	3.6900
I^-	I	0.1000	5.1245	6.9200

An extended Lagrangian dynamics, with velocity-Verlet[111] time integration scheme, was used in which a small mass and kinetic energy are attributed to the Drude particles. The amplitude of the Drude oscillator was controlled with a low temperature thermostat (1 K) acting in the local center-of-mass frame of each atom-Drude pair.[110] Thole damping[112] was used to modulate the electrostatic interaction between particles and induced dipoles. A particle-particle-particle-mesh method[113] was used as the long range Coulomb interaction solver. The force field was symmetrized with the procedure outlined by Dodin & Geissler.[114] The Lennard-Jones interactions were truncated and shifted at a distance of 12 Å.

Free energy for transferring an ozone molecule through the air-water interface, $\Delta G(z)$ was computed using umbrella sampling method.[115] In all simulations, ozone was restrained at a fixed distance from the center of mass of the water slab with a harmonic bias of the form $k_z(z - z_0)^2$ with $k_z = 4\ \mathrm{kcal\ mol^{-1}\ Å^{-2}}$ as the spring constant of the bias and z_0 its center. A total of 71 windows, with z_0 spaced 1 Å were used between -35 Å and 35 Å along z. Each window was run for 15 ns after 1 ns equilibration. The different umbrellas were used together with the Weighted Histogram Analysis Method.[116] The free energy profile was referenced relative to the vacuum, such that far from the interface, $\Delta G(z) = 0$.

Fig. 2C.1 presents the free energy profile for ozone with sodium halide salts in the solution, also found in the main text Fig. 2.4B, and the free energy profile for iodide in the same simulated solution. The density profiles for aqueous ions and ozone are presented below in Fig. 2C.2 where both the iodide ion and ozone exhibit a preference for the interfacial region. The Henry's law constants that determine mass partitioning between the gas and surface, H_{cc}^{gs}, the surface and bulk, H_{cc}^{sb}, and gas and bulk, H_{cc}^{gb} are computable form the free energy profile. We define the free energy difference between the gas and surface as ΔG_{gs} where the surface is taken to be the minimum of the free energy, near $z \sim 20$ Å, and the vapor at taken at large z. The resultant Henry's law constant is then $H_{cc}^{gs} = \exp\left(-\Delta G_{gs}/k_B T\right) = 9.3$ where k_B is Boltzmann's constant and T is the absolute temperature. Analogously, we define the free energy difference between the surface and bulk as ΔG_{sb} where the bulk free energy is taken as the plateau value of $\Delta G(z)$ in the interior of the slab, $z = 0$. The resultant Henry's law constant is then $H_{cc}^{sb} = \exp(-\Delta G_{sb}/k_B T) = 0.0156$. This renders the Henry's law constant from the gas to the bulk, $H_{cc}^{gb} = H_{cc}^{gs} H_{cc}^{sb} = 0.145$.

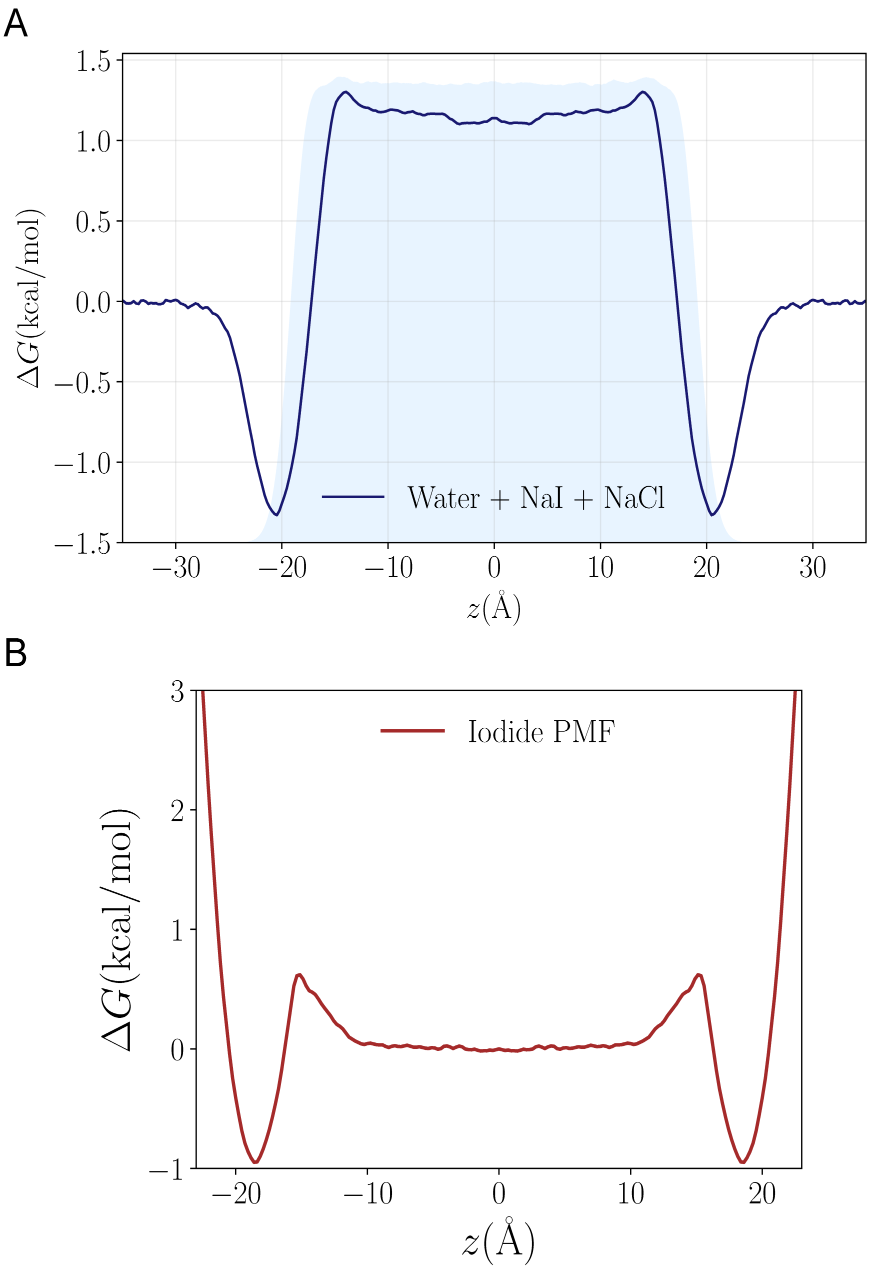

Fig. 2C.1: (A) The free energy profile for transferring an ozone molecule through a water slab with 0.28 M NaI and 0.84 M NaCl is displayed. The shaded blue region shows the (scaled and shifted) water density profile. (B) The free energy profile for transferring an iodide anion through a similar water slab. A cutoff for the free energy approaching the gas-phase is 3 kcal mol^{-1}.

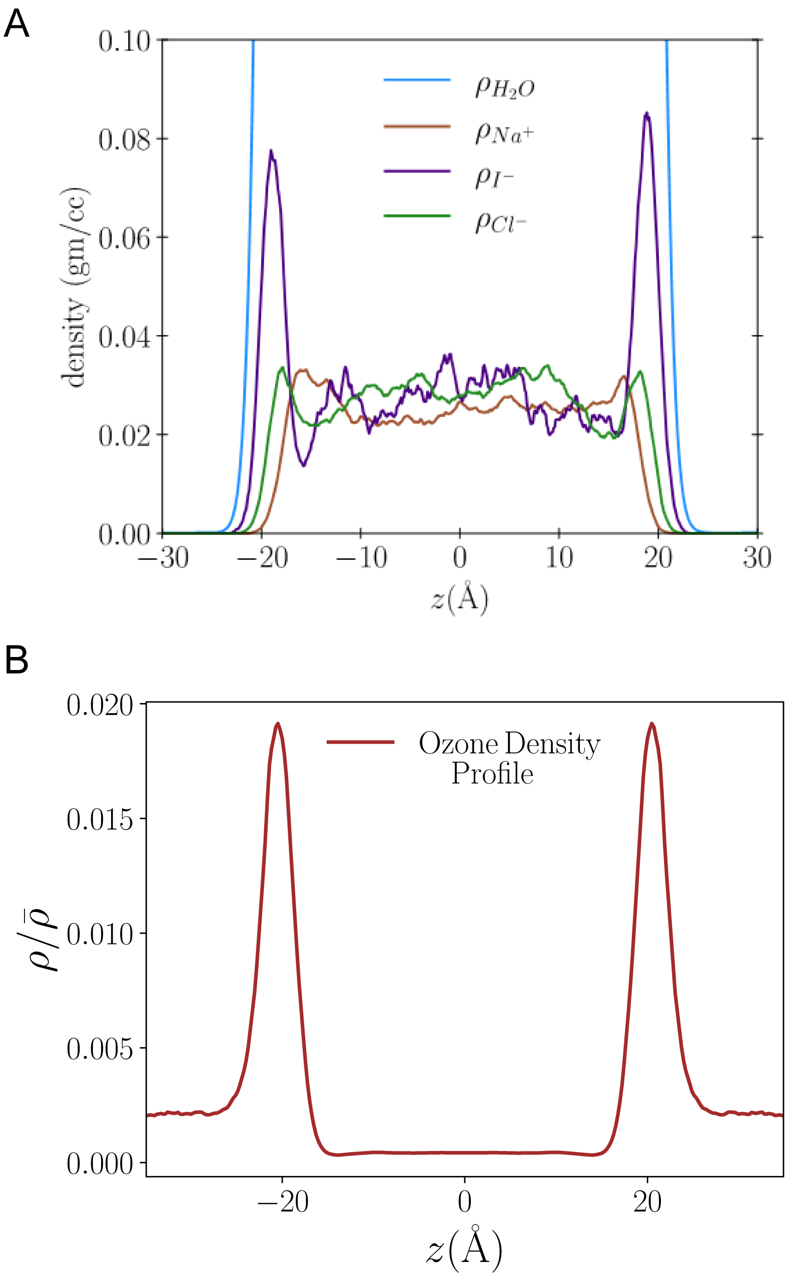

Fig. 2C.2: (A) The density profiles of the ions are presented. The blue line shows the water density profile. The brown, purple, and green curves represent Na^+, I^-, and Cl^- ion densities, respectively. (B) Normalized density profile of ozone through a water slab with 0.28 M NaI and 0.84 M.

(ii) Solvation and Desorption Rates

We define the mass accommodation coefficient (α) as the fraction of collisions of the gas phase species with the interface that results in the transport of the gas phase particle into the condensed phase. The accommodation coefficient can be written as

$$\alpha = \frac{k_{solv}}{k_{solv} + k_{des}}, \qquad \text{Eq. 2C. 2}$$

where k_{des} and k_{solv} are the rate of desorption and rate of solvation, respectively, from interface. This expression is valid in the limit of unit sticking coefficient (σ) and rapid thermalization relative to the absorption and desorption process. We have computed these rates from by propagating an effective Langevin equation parameterized from our explicit molecular dynamics simulations,

$$m\dot{v} = -m\gamma(z)v + f(z) + \sqrt{2m\gamma(t)k_BT}\eta(t), \qquad \text{Eq. 2C. 3}$$

where m is the mass of the particle, v and $\gamma(z)$ (γ has a unit of inverse time) are the velocity and friction coefficient, respectively. In general, the friction is a function of the coordinate, z. We have evaluated using a procedure to be described elsewhere, yielding a functional form $\gamma(z) \sim \left(\tanh(w(-sign(z)z + s))\right)^n$ with $w = 0.2, s = 19.76,$ and $n = 2.34$. $f(z)$ is the force acting on the particle that is obtained from the free energy profiles in Fig. 2.4B as $-\partial\Delta G/\partial z$. k_B is the Boltzmann constant and T is the absolute temperature. $\eta(t)$ is the δ-correlated Gaussian noise with properties $\langle\eta(t)\rangle = 0$ and $\langle\eta(t)\eta(t')\rangle = \delta(t - t')$ where $\langle \cdots \rangle$ is a statistical average. The dot in Eq. (S3) indicates a time derivative. The free energy profile is obtained from molecular dynamics simulation. We adopt the methods detailed in Farago & Grønbech-Jensen[117] for propagating Langevin equation with a coordinate dependent friction function.

To determine the desorption or solvation rates, we compute the fraction of trajectories entering the gas phase or bulk phase as a function of time starting from the interfacial region where trajectories are generated with Eq. 2C.3. The boundaries of the interface, with the bulk solution and with the gas phase, are set where the free energy profile in Fig. 2.4B becomes flat in that given side. Indicator functions (h_r) are used to determine location of a trajectory in different regions, namely bulk liquid phase (b), interface (s), and gas phase (g). From the form of $\Delta G(z)$, for one side of the slab, we take the bulk as $z < 14.5$, the interface as $14.5 < z < 27$ and the vapor as $z > 27$. The rates are then determined by fitting.

$$\chi_r = \frac{\langle h_r(t)h_s(0)\rangle}{\langle h_s(0)\rangle}, \qquad \text{Eq. 2C. 4}$$

$$\chi_r(z) = \begin{cases} 1, & \text{if } z(t) \in r = \{b, s, g\} \\ 0, & \text{otherwise} \end{cases},$$

where $\chi_r(t)$ is a normalized side-side correlation function that determines what fraction of trajectories has entered or left a given region at a given time with an exponential. The side-side correlation functions for desorption and solvation processes are shown in Fig. 2C.3. The desorption rate is obtained by fitting the initial rise of the desorption correlation function with an exponential. This value agrees nicely with the desorption rate obtained from a steady state flux calculation. The ratio of desorption to solvation by examining fraction of density entering the bulk phase compared to the fraction entering the vapor phase starting from the interface region. Also, the solvation rate can be obtained in a similar way like desorption by fitting the initial rise of the correlation function with an exponential. These two results are in close agreement. The mass accommodation coefficient of ozone for this system can be computed from Eq. 2C.2 which gives a value of $\alpha = 0.0097$. The solvation and desorption rates extracted from Fig. 2C.3 are $1.90 \times 10^{8}\ \mathrm{s}^{-1}$ and $1.93 \times 10^{10}\ \mathrm{s}^{-1}$, respectively.

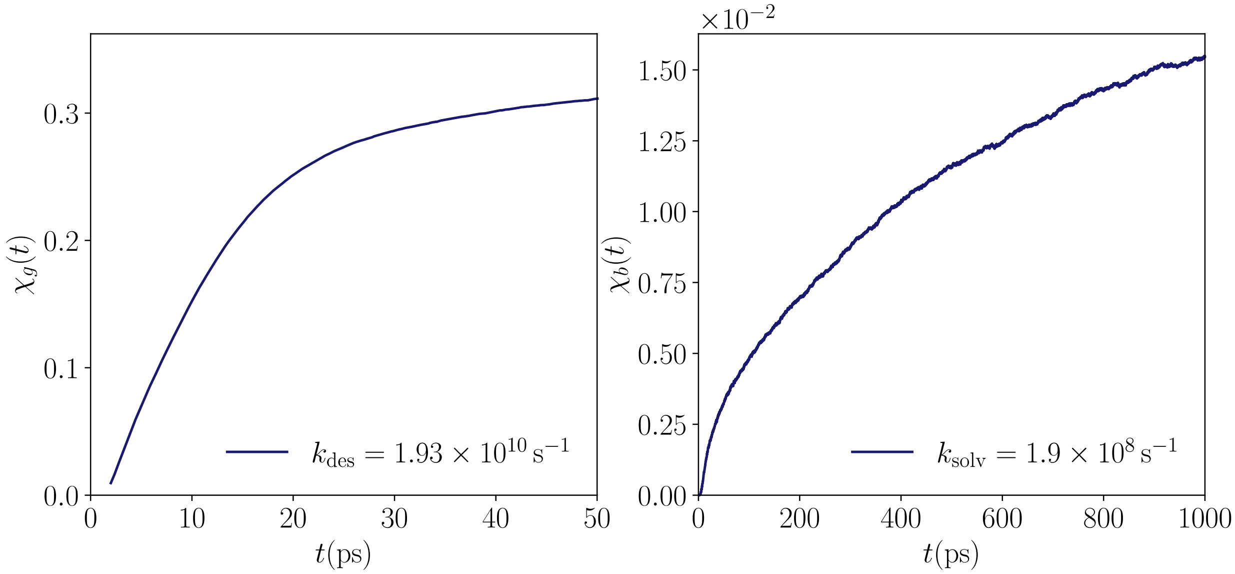

Fig. 2C.3: The side-side correlation functions are plotted above. The rate of desorption and solvation are extracted by fitting the early rise in the correlation function with an exponential function of the form $c_1 - c_2e^{-kt}$ $(c_1, c_2 > 0)$ where k is the rate for the process. The initial position was set at the minima of the free energy profile. The left and right column represent the autocorrelation function for desorption and solvation processes, respectively. Rates are reported in s^{-1}.

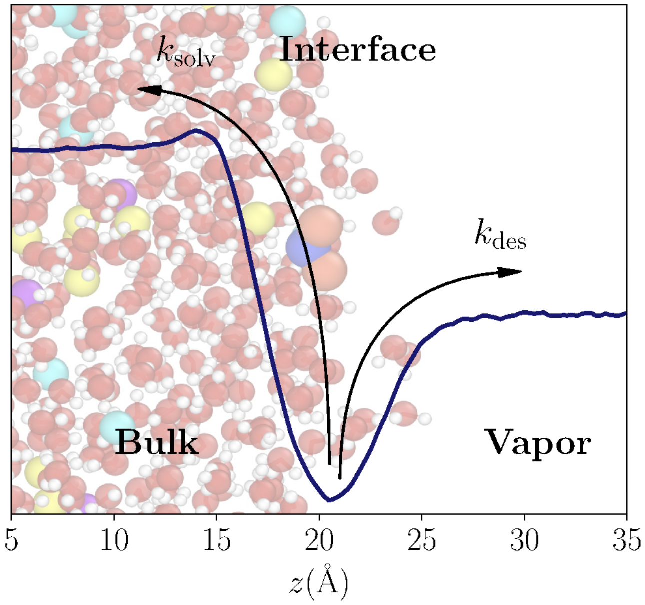

Fig. 2C.4: A diagrammatic representation of the three regions, namely bulk, interface, and vapor, as used in the calculation of solvation and desorption rates.

Appendix 2D: Diffusional length scales

Characteristic lengths for ozone diffusion and adsorption in the gas-phase are introduced in the modeling description section 2.4.A. Here we provide a sketch summarizing these lengths relative to an example droplet radius. While the diffusion length L_{diff} denotes the characteristic size of the chemical gradient by loss of O_3 on the droplet surface, the adsorption length L_{ads} denotes the size of the gas volume directly depleted by the kinetic adsorption equilibrium (step A1 in Table 2A.1). Equivalently, one may conceptualize the volume defined by L_{ads} as the gas-volume that contains the same number of O_3 as the droplet surface at equilibrium. The upper limit for diffusion in the present model can then be constructed as diffusion over the length L_{diff} into the volume defined by L_{ads}.

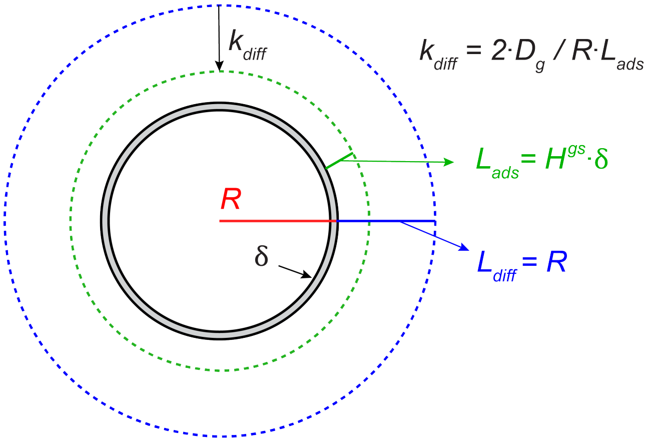

Fig. 2D.1: Illustration of relevant length scales for gas-phase diffusion and a kinetic description of adsorption and diffusion.

Appendix 2E: Model parameter sensitivity

Due to the large number of rate coefficients in the model framework used, we do not include a comprehensive sensitivity test for all coefficients but highlight what results from our work suggest are the main sensitivities in the model. Perhaps the largest uncertainties in the model are the solvation and desolvation rates of solutes in solution. The ratio of these rates, equal to the Langmuir equilibrium coefficient, is less uncertain given the simulated interfacial ion-densities provided in Appendix 2C and previous measurements of iodide surface concentrations. To the best of our knowledge, however, no measurements exist for absolute rates of surface-solvation or desolvation for the anions considered. Therefore, in the present modeling approach, we aim to choose absolute rates of k_{solv} and k_{desolv} of a large enough magnitude such that any sensitivity to the absolute values is lost. A brief illustration in Fig. 2E.1 demonstrates that an example set of k_{solv}/k_{desolv} for I^- that becomes too small will alter the model kinetics. This results from overlapping timescales of ion-desolvation and reaction under the particular reaction conditions. We generally assume that a reaction depletion of ions at the interface is non-physical under these conditions. This in turn derives from an assumption that rates of ion-replenishment at the interface occur on a timescale faster than reaction.

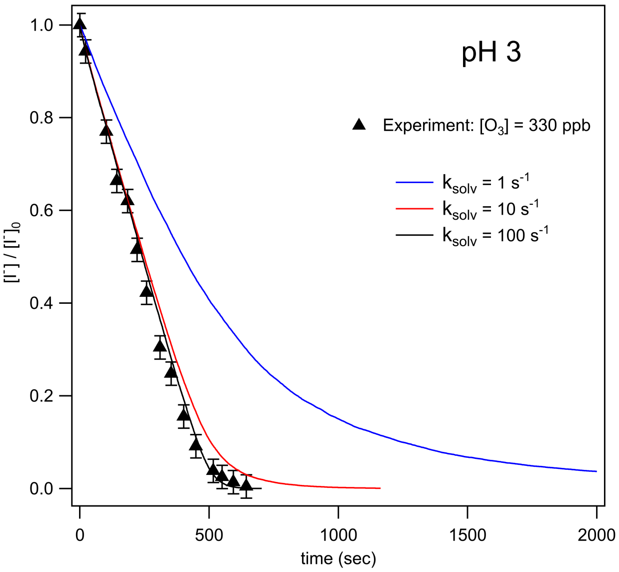

Fig. 2E.1: Simulation results compared to experiment for a pH 3 droplet exposed to 330 ppb [O_3]. Results from scaling the k_{solv} and k_{desolv} rates are shown to display sensitivity to the absolute rates. Simulation results appear greatly sensitive to the absolute rates below k_{solv} = 10 s^{-1}. Above k_{solv} = 10 s^{-1}, the sensitivity quickly drops off and the kinetics remain approximately constant. Note that in each comparison case, k_{desolv} is scaled by the same factor as k_{solv}.

Similar sensitivity tests were also performed for the absolute rate coefficients embedded in the I_3^- equilibrium and I_2OH^- equilibrium, with an analogous finding that the simulation results are unchanged by increasing absolute rate coefficients. Since each of these equilibrium systems was tested individually while keeping the others constant, we note there may be additive effects that will go unobserved unless all equilibria were simulated using the literature forward and reverse rates. However, we expect any differences in a fully simulated case to be relatively small from the present simulations since no obvious deviations were observed while testing the sensitivity of individual equilibria.

Appendix 2F: Model pH test

Model results suggest the pH dependence observed from experiment is a compound effect of pH dependent reaction pathways that consume iodide and the surface reaction rate. In this section we show the effect of the bulk and surface components. Removing the direct pH dependence of the surface reaction can be observed by simply replacing the 3-step surface mechanism (see Fig. 2.5B and reaction steps R1-R3) with a 1-step bimolecular rate expression, as has been observed in the gas phase:

$$I^- + O_3 \rightarrow IO^- + O_2, \qquad (SR1)$$

To demonstrate the effect of surficial pH reaction dependence, reaction steps R1-R3 in the model are replaced with SR1. Fig. 2F.1 below reproduces experimental results as shown in Fig. 2.3 of the main text while comparing model output using step SR1 instead of R1-R3 (simulation results given in dashed lines). Here, a pH dependence is still observed between basic and neutral/acidic conditions due to sensitivity of reaction steps R6-R9 in the main text. However, this dependence in the secondary chemical pathways of I^- fails to reproduce the kinetics observed in the experiment.

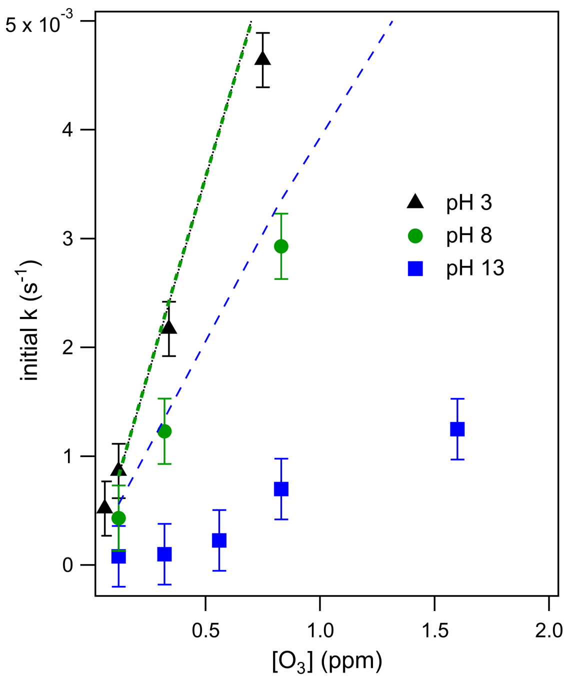

Fig. 2F.1: Results of pH-dependence sensitivity test. Kinetics from Fig. 2.3 in the main text are reproduced along with simulation results (dashed lines) obtained by replacing steps R1-R3 in the model with a single bimolecular reaction step $I^- + O_3$ with rate coefficient $k = 1.2 \times 10^9$ M^{-1} s^{-1}. Model output under these conditions overpredicts all observed kinetics and lacks sensitivity to pH between pH 3 and pH 8.

Appendix 2G: Simulated Product Distributions

Example simulation kinetics are provided in Fig. 2G.1 to demonstrate the difference in modeled oxidation product distributions across droplet pH for an example ozone concentration of $[O_3]$ = 820 ppb. For droplet solutions with pH 3 and pH 8, I_2 is the major emission product with a fraction of HOI also emitted. Iodide conversion to HOI is seen to increase slightly as $[I^-]$ decreases. This is due to the reactive timescale of HOI conversion to I_2 becoming longer with decreasing $[I^-]$, allowing the evaporative channel of HOI to become more significant. In strongly basic solution, IO_3^- is the main product, with close to 100% conversion. As mentioned in Appendix 2B and Fig. 2B.3, the simulated product kinetics under pH 13 differ from what is observed in experiment, where the yield of IO_3^- appears to decrease with decreasing $[O_3]$. While the origin of the observation is not clear, potential coupling between the surface-solvation lifetimes of HOI/IO^- and I_2, their respective chemical lifetimes, and evaporation rates may lead to unexpected changes in mechanism for lower $[O_3]$.

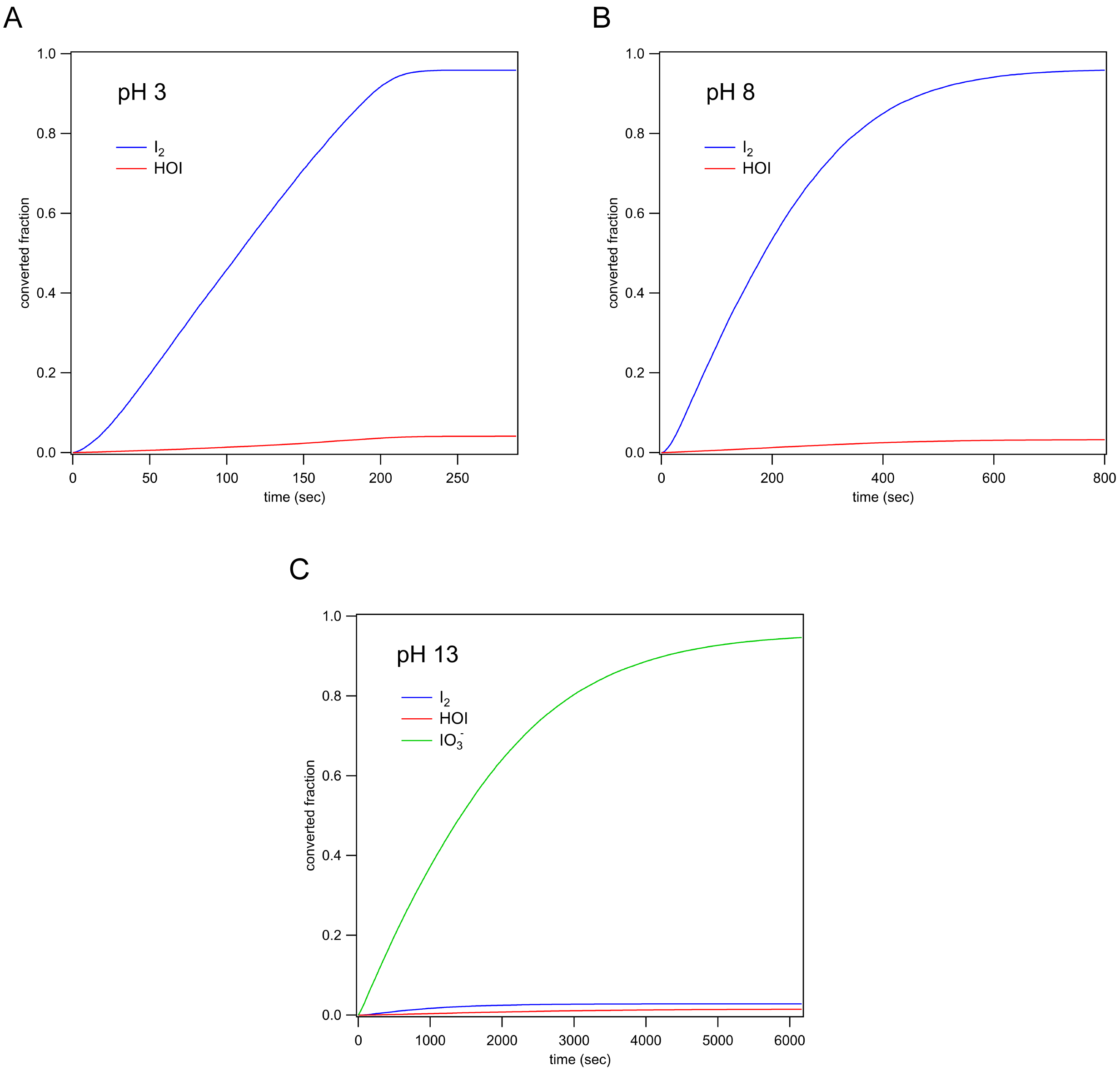

Fig. 2G.1: Product distribution from three example simulations for pH 3, 8, and 13 labeled in panels A, B, and C, respectively. Example simulations are run using $[O_3]$ = 820 ppb. For pH conditions below the pKa of HOI (10.8), no IO_3^- is observed in solution and only volatile products remain. For both pH 3 and pH 8, I_2 is dominate with a small fraction of HOI emitted. For pH 13, IO_3^- dominates the overall products. As mentioned in the main text and Appendix 2E, volatile products for pH 13 are observed to increase in overall fraction with decreasing $[O_3]$.

2.9: References:

(1) Saiz-Lopez, A.; Plane, J. M. C.; Baker, A. R.; Carpenter, L. J.; von Glasow, R.; Gómez Martín, J. C.; McFiggans, G.; Saunders, R. W. Atmospheric Chemistry of Iodine. *Chem. Rev.* **2012**, *112* (3), 1773–1804. https://doi.org/10.1021/cr200029u.

(2) Carpenter, L. J. Iodine in the Marine Boundary Layer. *Chem. Rev.* **2003**, *103* (12), 4953–4962. https://doi.org/10.1021/cr0206465.

(3) Carpenter, L. J.; MacDonald, S. M.; Shaw, M. D.; Kumar, R.; Saunders, R. W.; Parthipan, R.; Wilson, J.; Plane, J. M. C. Atmospheric Iodine Levels Influenced by Sea Surface Emissions of Inorganic Iodine. *Nat. Geosci. 2013 62* **2013**, *6* (2), 108–111. https://doi.org/10.1038/ngeo1687.

(4) Carpenter, L. J.; Chance, R. J.; Sherwen, T.; Adams, T. J.; Ball, S. M.; Evans, M. J.; Hepach, H.; Hollis, L. D. J.; Hughes, C.; Jickells, T. D.; Mahajan, A.; Stevens, D. P.; Tinel, L.; Wadley, M. R. Marine Iodine Emissions in a Changing World. *Proc. R. Soc. A* **2021**, *477* (2247). https://doi.org/10.1098/RSPA.2020.0824.

(5) Gómez Martín, J. C.; Lewis, T. R.; Blitz, M. A.; Plane, J. M. C.; Kumar, M.; Francisco, J. S.; Saiz-Lopez, A. A Gas-to-Particle Conversion Mechanism Helps to Explain Atmospheric Particle Formation through Clustering of Iodine Oxides. *Nat. Commun.* **2020**, *11* (1), 4521. https://doi.org/10.1038/s41467-020-18252-8.

(6) Tham, Y. J.; He, X.-C.; Li, Q.; Cuevas, C. A.; Shen, J.; Kalliokoski, J.; Yan, C.; Iyer, S.; Lehmusjärvi, T.; Jang, S.; Thakur, R. C.; Beck, L.; Kemppainen, D.; Olin, M.; Sarnela, N.; Mikkilä, J.; Hakala, J.; Marbouti, M.; Yao, L.; Li, H.; Huang, W.; Wang, Y.; Wimmer, D.; Zha, Q.; Virkanen, J.; Spain, T. G.; O'Doherty, S.; Jokinen, T.; Bianchi, F.; Petäjä, T.; Worsnop, D. R.; Mauldin, R. L.; Ovadnevaite, J.; Ceburnis, D.; Maier, N. M.; Kulmala, M.; O'Dowd, C.; Maso, M. D.; Saiz-Lopez, A.; Sipilä, M. Direct Field Evidence of Autocatalytic Iodine Release from Atmospheric Aerosol. *Proc. Natl. Acad. Sci.* **2021**, *118* (4), 2021–2021. https://doi.org/10.1073/PNAS.2009951118.

(7) Gómez Martín, J. C.; Lewis, T. R.; James, A. D.; Saiz-Lopez, A.; Plane, J. M. C. Insights into the Chemistry of Iodine New Particle Formation: The Role of Iodine Oxides and the Source of Iodic Acid. *J. Am. Chem. Soc.* **2022**, *144* (21), 9240–9253. https://doi.org/10.1021/jacs.1c12957.

(8) Ganzeveld, L.; Helmig, D.; Fairall, C. W.; Hare, J.; Pozzer, A. Atmosphere-Ocean Ozone Exchange: A Global Modeling Study of Biogeochemical, Atmospheric, and Waterside Turbulence Dependencies. *Glob. Biogeochem. Cycles* **2009**, *23* (4). https://doi.org/10.1029/2008GB003301.

(9) Garland, J. A.; Elzerman, A. W.; Penkett, S. A. The Mechanism for Dry Deposition of Ozone to Seawater Surfaces. *J. Geophys. Res. Oceans* **1980**, *85* (C12), 7488–7492. https://doi.org/10.1029/JC085IC12P07488.

(10) Magi, L.; Schweitzer, F.; Pallares, C.; Cherif, S.; Mirabel, P.; George, C. Investigation of the Uptake Rate of Ozone and Methyl Hydroperoxide by Water Surfaces. *J. Phys. Chem. A* **1997**, *101* (27), 4943–4949. https://doi.org/10.1021/jp970646m.

(11) Hu, J. H.; Shi, Q.; Davidovits, P.; Worsnop, D. R.; Zahniser, M. S.; Kolb, C. E. Reactive Uptake of Cl2(g) and Br2(g) by Aqueous Surfaces as a Function of Br- and I- Ion Concentration: The Effect of Chemical Reaction at the Interface. *J. Phys. Chem.* **1995**, *99* (21), 8768–8776. https://doi.org/10.1021/j100021a050.

(12) Bhujel, M.; L. Marshall, D.; T. Maccarone, A.; I. McKinnon, B.; J. Trevitt, A.; Silva, G. da; J. Blanksby, S.; J. Poad, B. L. Gas Phase Reactions of Iodide and Bromide Anions

with Ozone: Evidence for Stepwise and Reversible Reactions. *Phys. Chem. Chem. Phys.* **2020**, *22* (18), 9982–9989. https://doi.org/10.1039/D0CP01498B.

(13) Teiwes, R.; Elm, J.; Handrup, K.; Jensen, E. P.; Bilde, M.; Pedersen, H. B. Atmospheric Chemistry of Iodine Anions: Elementary Reactions of I−, IO−, and IO2− with Ozone Studied in the Gas-Phase at 300 K Using an Ion Trap. *Phys. Chem. Chem. Phys.* **2018**, *20* (45), 28606–28615. https://doi.org/10.1039/C8CP05721D.

(14) Liu, Q.; Schurter, L. M.; Muller, C. E.; Aloisio, S.; Francisco, J. S.; Margerum, D. W. Kinetics and Mechanisms of Aqueous Ozone Reactions with Bromide, Sulfite, Hydrogen Sulfite, Iodide, and Nitrite Ions. *Inorg. Chem.* **2001**, *40* (17), 4436–4442. https://doi.org/10.1021/ic000919j.

(15) Schneider, S. R.; Lakey, P. S. J.; Shiraiwa, M.; Abbatt, J. P. D. Reactive Uptake of Ozone to Simulated Seawater: Evidence for Iodide Depletion. *J. Phys. Chem. A* **2020**, *124* (47), 9844–9853. https://doi.org/10.1021/acs.jpca.0c08917.

(16) Schneider, S. R.; Lakey, P. S. J.; Shiraiwa, M.; Abbatt, J. P. D. Iodine Emission from the Reactive Uptake of Ozone to Simulated Seawater. *Environ. Sci. Process. Impacts* **2023**, *25* (2), 254–263. https://doi.org/10.1039/D2EM00111J.

(17) Sakamoto, Y.; Yabushita, A.; Kawasaki, M.; Enami, S. Direct Emission of I2 Molecule and IO Radical from the Heterogeneous Reactions of Gaseous Ozone with Aqueous Potassium Iodide Solution. *J. Phys. Chem. A* **2009**, *113* (27), 7707–7713. https://doi.org/10.1021/jp903486u.

(18) Hoigné, J.; Bader, H.; Haag, W. R.; Staehelin, J. Rate Constants of Reactions of Ozone with Organic and Inorganic Compounds in Water—III. Inorganic Compounds and Radicals. *Water Res.* **1985**, *19* (8), 993–1004. https://doi.org/10.1016/0043-1354(85)90368-9.

(19) Woods, E.; Konys, C. A.; Rossi, S. R. Photoemission of Iodide from Aqueous Aerosol Particle Surfaces. *J. Phys. Chem. A* **2019**, *123* (13), 2901–2907. https://doi.org/10.1021/acs.jpca.8b12323.

(20) Rouvière, A.; Sosedova, Y.; Ammann, M. Uptake of Ozone to Deliquesced KI and Mixed KI/NaCl Aerosol Particles. *J. Phys. Chem. A* **2010**, *114* (26), 7085–7093. https://doi.org/10.1021/JP103257D.

(21) Rouvière, A.; Ammann, M. The Effect of Fatty Acid Surfactants on the Uptake of Ozone to Aqueous Halogenide Particles. *Atmospheric Chem. Phys.* **2010**, *10* (23), 11489–11500. https://doi.org/10.5194/acp-10-11489-2010.

(22) Teiwes, R.; Elm, J.; Bilde, M.; Pedersen, H. B. The Reaction of Hydrated Iodide I(H2O)− with Ozone: A New Route to IO2− Products. *Phys. Chem. Chem. Phys.* **2019**, *21* (32), 17546–17554. https://doi.org/10.1039/C9CP01734H.

(23) Pedersen, H. B.; Elm, J.; Frederiksen, C. H.; Jessen, S. P. S.; Teiwes, R.; Bilde, M. The Reaction of Isotope-Substituted Hydrated Iodide I(H182O)− with Ozone: The Reactive Influence of the Solvent Water Molecule. *Phys. Chem. Chem. Phys.* **2020**, *22* (34), 19080–19088. https://doi.org/10.1039/D0CP03219K.

(24) G. Moreno, C.; Gálvez, O.; Moreno, V. L.-A.; María Espildora-García, E.; Teresa Baeza-Romero, M. A Revisit of the Interaction of Gaseous Ozone with Aqueous Iodide. Estimating the Contributions of the Surface and Bulk Reactions. *Phys. Chem. Chem. Phys.* **2018**, *20* (43), 27571–27584. https://doi.org/10.1039/C8CP04394A.

(25) Moreno, C.; Baeza-Romero, M.-T.; Sanz, M.; Gálvez, Ó.; Arza, V. L.; C. Ianni, J.; Espíldora, E. Iodide Conversion to Iodate in Aqueous and Solid Aerosols Exposed to Ozone. *Phys. Chem. Chem. Phys.* **2020**, *22* (10), 5625–5637. https://doi.org/10.1039/C9CP05601G.

(26) Gálvez, Ó.; Baeza-Romero, M. T.; Sanz, M.; Pacios, L. F. A Theoretical Study on the Reaction of Ozone with Aqueous Iodide. *Phys. Chem. Chem. Phys.* **2016**, *18* (11), 7651–7660. https://doi.org/10.1039/C5CP06440F.

(27) Moreno, C.; Baeza-Romero, M. T. A Kinetic Model for Ozone Uptake by Solutions and Aqueous Particles Containing I− and Br−, Including Seawater and Sea-Salt Aerosol. *Phys. Chem. Chem. Phys.* **2019**, *21* (36), 19835–19856. https://doi.org/10.1039/C9CP03430G.

(28) Willis, M. D.; Wilson, K. R. Coupled Interfacial and Bulk Kinetics Govern the Timescales of Multiphase Ozonolysis Reactions. *J. Phys. Chem. A* **2022**, *126* (30), 4991–5010. https://doi.org/10.1021/acs.jpca.2c03059.

(29) Wilson, K. R.; Prophet, A. M.; Willis, M. D. A Kinetic Model for Predicting Trace Gas Uptake and Reaction. *J. Phys. Chem. A* **2022**, *126* (40), 7291–7308. https://doi.org/10.1021/acs.jpca.2c03559.

(30) Kaur Kohli, R.; Van Berkel, G. J.; Davies, J. F. An Open Port Sampling Interface for the Chemical Characterization of Levitated Microparticles. *Anal. Chem.* **2022**, *94* (8), 3441–3445. https://doi.org/10.1021/acs.analchem.1c05550.

(31) Artiglia, L.; Edebeli, J.; Orlando, F.; Chen, S.; Lee, M.-T.; Corral Arroyo, P.; Gilgen, A.; Bartels-Rausch, T.; Kleibert, A.; Vazdar, M.; Andres Carignano, M.; Francisco, J. S.; Shepson, P. B.; Gladich, I.; Ammann, M. A Surface-Stabilized Ozonide Triggers Bromide Oxidation at the Aqueous Solution-Vapour Interface. *Nat. Commun.* **2017**, *8* (1), 700. https://doi.org/10.1038/s41467-017-00823-x.

(32) Willis, M. D.; Rovelli, G.; Wilson, K. R. Combining Mass Spectrometry of Picoliter Samples with a Multicompartment Electrodynamic Trap for Probing the Chemistry of Droplet Arrays. *Anal. Chem.* **2020**, *92* (17), 11943–11952. https://doi.org/10.1021/ACS.ANALCHEM.0C02343/SUPPL_FILE/AC0C02343_SI_001.PDF.

(33) Jacobs, M. I.; Davies, J. F.; Lee, L.; Davis, R. D.; Houle, F.; Wilson, K. R. Exploring Chemistry in Microcompartments Using Guided Droplet Collisions in a Branched Quadrupole Trap Coupled to a Single Droplet, Paper Spray Mass Spectrometer. *Anal. Chem.* **2017**, *89* (22), 12511–12519. https://doi.org/10.1021/acs.analchem.7b03704.

(34) Davies, J. F. Mass, Charge, and Radius of Droplets in a Linear Quadrupole Electrodynamic Balance. *Aerosol Sci. Technol.* **2019**, *53* (3), 309–320. https://doi.org/10.1080/02786826.2018.1559921.

(35) Van Berkel, G. J.; Kertesz, V. An Open Port Sampling Interface for Liquid Introduction Atmospheric Pressure Ionization Mass Spectrometry. *Rapid Commun. Mass Spectrom.* **2015**, *29* (19), 1749–1756. https://doi.org/10.1002/rcm.7274.

(36) Liu, C.; Van Berkel, G. J.; Kovarik, P.; Perot, J. B.; Inguva, V.; Covey, T. R. Fluid Dynamics of the Open Port Interface for High-Speed Nanoliter Volume Sampling Mass Spectrometry. *Anal. Chem.* **2021**, *93* (24), 8559–8567. https://doi.org/10.1021/acs.analchem.1c01312.

(37) Ovchinnikova, O. S.; Bhandari, D.; Lorenz, M.; Van Berkel, G. J. Transmission Geometry Laser Ablation into a Non-Contact Liquid Vortex Capture Probe for Mass Spectrometry Imaging. *Rapid Commun. Mass Spectrom. RCM* **2014**, *28* (15), 1665–1673. https://doi.org/10.1002/rcm.6946.

(38) Van Berkel, G. J.; Kertesz, V.; Boeltz, H. Immediate Drop on Demand Technology (I-DOT) Coupled with Mass Spectrometry via an Open Port Sampling Interface. *Bioanalysis* **2017**, *9* (21), 1667–1679. https://doi.org/10.4155/bio-2017-0104.

(39) Cahill, J. F.; Riba, J.; Kertesz, V. Rapid, Untargeted Chemical Profiling of Single Cells in Their Native Environment. *Anal. Chem.* **2019**, *91* (9), 6118–6126. https://doi.org/10.1021/acs.analchem.9b00680.

(40) Kaur Kohli, R.; Reynolds, R. S.; Wilson, K. R.; Davies, J. F. Exploring the Influence of Particle Phase in the Ozonolysis of Oleic and Elaidic Acid. *Aerosol Sci. Technol.* **2023**, 1–18. https://doi.org/10.1080/02786826.2023.2226183.

(41) Lamoureux, G.; Harder, E.; Vorobyov, I. V.; Roux, B.; MacKerell Jr, A. D. A Polarizable Model of Water for Molecular Dynamics Simulations of Biomolecules. *Chem Phys Lett* **2006**, *418* (1–3), 245–249.

(42) Hinsberg, W. D.; Houle, F. A. *Kinetiscope*. https://hinsberg.net/kinetiscope/. https://hinsberg.net/kinetiscope/ (accessed 2022-02-15).

(43) Heine, N.; Houle, F. A.; Wilson, K. R. Connecting the Elementary Reaction Pathways of Criegee Intermediates to the Chemical Erosion of Squalene Interfaces during Ozonolysis. *Environ. Sci. Technol.* **2017**, *51* (23), 13740–13748. https://doi.org/10.1021/acs.est.7b04197.

(44) Houle, F. A.; Wiegel, A. A.; Wilson, K. R. Predicting Aerosol Reactivity Across Scales: From the Laboratory to the Atmosphere. *Environ. Sci. Technol.* **2018**, *52* (23), 13774–13781. https://doi.org/10.1021/acs.est.8b04688.

(45) Wilson, K. R.; Prophet, A. M.; Rovelli, G.; Willis, M. D.; Rapf, R. J.; Jacobs, M. I. A Kinetic Description of How Interfaces Accelerate Reactions in Micro-Compartments. *Chem. Sci.* **2020**, *11* (32), 8533–8545. https://doi.org/10.1039/D0SC03189E.

(46) Vácha, R.; Slavíček, P.; Mucha, M.; Finlayson-Pitts, B. J.; Jungwirth, P. Adsorption of Atmospherically Relevant Gases at the Air/Water Interface: Free Energy Profiles of Aqueous Solvation of N2, O2, O3, OH, H2O, HO2, and H2O2. *J. Phys. Chem. A* **2004**, *108* (52), 11573–11579. https://doi.org/10.1021/jp046268k.

(47) Sander, R. Compilation of Henry's Law Constants (Version 4.0) for Water as Solvent. *Atmospheric Chem. Phys.* **2015**, *15* (8), 4399–4981. https://doi.org/10.5194/acp-15-4399-2015.

(48) Panich, N. M.; Ershov, B. G.; Seliverstov, A. F.; Basiev, A. G. Ozone Solubility in Concentrated Aqueous Solutions of Salts. *Russ. J. Appl. Chem.* **2007**, *80* (11), 1812–1815. https://doi.org/10.1134/S1070427207110067.

(49) Langmuir, I. The Adsorption of Gases on Plane Surfaces of Glass, Mica and Platinum. *J. Am. Chem. Soc.* **1918**, *40* (9), 1361–1403. https://doi.org/10.1021/ja02242a004.

(50) Vieceli, J.; Roeselová, M.; Potter, N.; Dang, L. X.; Garrett, B. C.; Tobias, D. J. Molecular Dynamics Simulations of Atmospheric Oxidants at the Air−Water Interface: Solvation and Accommodation of OH and O3. *J. Phys. Chem. B* **2005**, *109* (33), 15876–15892. https://doi.org/10.1021/jp051361+.

(51) Worsnop, D. R.; Morris, J. W.; Shi, Q.; Davidovits, P.; Kolb, C. E. A Chemical Kinetic Model for Reactive Transformations of Aerosol Particles. *Geophys. Res. Lett.* **2002**, *29* (20), 57-1-57–4. https://doi.org/10.1029/2002GL015542.

(52) Nathanson, G. M.; Davidovits, P.; Worsnop, D. R.; Kolb, C. E. Dynamics and Kinetics at the Gas−Liquid Interface. *J. Phys. Chem.* **1996**, *100* (31), 13007–13020. https://doi.org/10.1021/jp953548e.

(53) Saecker, M. E.; Nathanson, G. M. Collisions of Protic and Aprotic Gases with Hydrogen Bonding and Hydrocarbon Liquids. *J. Chem. Phys.* **1993**, *99* (9), 7056–7075. https://doi.org/10.1063/1.465425.

(54) Clement, C. F.; Kulmala, M.; Vesala, T. Theoretical Consideration on Sticking Probabilities. *J. Aerosol Sci.* **1996**, *27* (6), 869–882. https://doi.org/10.1016/0021-8502(96)00032-8.

(55) Schwartz, S. E.; Freiberg, J. E. Mass-Transport Limitation to the Rate of Reaction of Gases in Liquid Droplets: Application to Oxidation of SO2 in Aqueous Solutions. *Atmospheric Environ. 1967* **1981**, *15* (7), 1129–1144. https://doi.org/10.1016/0004-6981(81)90303-6.

(56) Seinfeld, J. H.; Pandis, S. N. Mass Transfer Aspects of Atmospheric Chemistry. In *Atmospheric Chemistry and Physics: From Air Polution to Climate Change*; John Wiley & Sons, Inc., 1998.

(57) Jin, F.; Balasubramaniam, R.; Stebe, K. J. Surfactant Adsorption to Spherical Particles: The Intrinsic Length Scale Governing the Shift from Diffusion to Kinetic-Controlled Mass Transfer. *J. Adhes.* **2004**, *80* (9), 773–796. https://doi.org/10.1080/00218460490480770.

(58) Jungwirth, P.; Tobias, D. J. Ions at the Air/Water Interface. *J. Phys. Chem. B* **2002**, *106* (25), 6361–6373. https://doi.org/10.1021/jp020242g.

(59) Stern, A. C.; Baer, M. D.; Mundy, C. J.; Tobias, D. J. Thermodynamics of Iodide Adsorption at the Instantaneous Air-Water Interface. *J. Chem. Phys.* **2013**, *138* (11), 114709–114709. https://doi.org/10.1063/1.4794688.

(60) Piatkowski, L.; Zhang, Z.; Backus, E. H. G.; Bakker, H. J.; Bonn, M. Extreme Surface Propensity of Halide Ions in Water. *Nat. Commun.* **2014**, *5* (1), 4083. https://doi.org/10.1038/ncomms5083.

(61) Reeser, D. I.; Donaldson, D. J. Influence of Water Surface Properties on the Heterogeneous Reaction between O3(g) and I(Aq)−. *Atmos. Environ.* **2011**, *45* (34), 6116–6120. https://doi.org/10.1016/J.ATMOSENV.2011.08.042.

(62) Wren, S. N.; Donaldson, D. J. Glancing-Angle Raman Spectroscopic Probe for Reaction Kinetics at Water Surfaces. *Phys. Chem. Chem. Phys.* **2010**, *12* (11), 2648–2654. https://doi.org/10.1039/B922254E.

(63) Weber, R.; Winter, B.; Schmidt, P. M.; Widdra, W.; Hertel, I. V.; Dittmar, M.; Faubel, M. Photoemission from Aqueous Alkali-Metal−Iodide Salt Solutions Using EUV Synchrotron Radiation. *J. Phys. Chem. B* **2004**, *108* (15), 4729–4736. https://doi.org/10.1021/jp030776x.

(64) Credidio, B.; Pugini, M.; Malerz, S.; Trinter, F.; Hergenhahn, U.; Wilkinson, I.; Thürmer, S.; Winter, B. Quantitative Electronic Structure and Work-Function Changes of Liquid Water Induced by Solute. *Phys. Chem. Chem. Phys.* **2022**, *24* (3), 1310–1325. https://doi.org/10.1039/D1CP03165A.

(65) Petersen, P. B.; Saykally, R. J. Probing the Interfacial Structure of Aqueous Electrolytes with Femtosecond Second Harmonic Generation Spectroscopy. *J. Phys. Chem. B* **2006**, *110* (29), 14060–14073. https://doi.org/10.1021/jp0601825.

(66) Petersen, P. B.; Johnson, J. C.; Knutsen, K. P.; Saykally, R. J. Direct Experimental Validation of the Jones–Ray Effect. *Chem. Phys. Lett.* **2004**, *397* (1–3), 46–50. https://doi.org/10.1016/j.cplett.2004.08.048.

(67) Dang, L. X. Computational Study of Ion Binding to the Liquid Interface of Water. *J. Phys. Chem. B* **2002**, *106* (40), 10388–10394. https://doi.org/10.1021/jp021871t.

(68) Liu, Y. Is the Free Energy Change of Adsorption Correctly Calculated? *J. Chem. Eng. Data* **2009**, *54* (7), 1981–1985. https://doi.org/10.1021/je800661q.

(69) Olivieri, G.; Parry, K. M.; D'Auria, R.; Tobias, D. J.; Brown, M. A. Specific Anion Effects on Na+ Adsorption at the Aqueous Solution–Air Interface: MD Simulations, SESSA Calculations, and Photoelectron Spectroscopy Experiments. *J. Phys. Chem. B* **2018**, *122* (2), 910–918. https://doi.org/10.1021/acs.jpcb.7b06981.

(70) D'Auria, R.; Tobias, D. J. Relation between Surface Tension and Ion Adsorption at the Air−Water Interface: A Molecular Dynamics Simulation Study. *J. Phys. Chem. A* **2009**, *113* (26), 7286–7293. https://doi.org/10.1021/jp810488p.

(71) Ottosson, N.; Faubel, M.; Bradforth, S. E.; Jungwirth, P.; Winter, B. Photoelectron Spectroscopy of Liquid Water and Aqueous Solution: Electron Effective Attenuation Lengths and Emission-Angle Anisotropy. *J. Electron Spectrosc. Relat. Phenom.* **2010**, *177* (2), 60–70. https://doi.org/10.1016/j.elspec.2009.08.007.

(72) Ou, S.; Hu, Y.; Patel, S.; Wan, H. Spherical Monovalent Ions at Aqueous Liquid–Vapor Interfaces: Interfacial Stability and Induced Interface Fluctuations. *J. Phys. Chem. B* **2013**, *117* (39), 11732–11742. https://doi.org/10.1021/jp406001b.

(73) Saha, S.; Roy, S.; Mathi, P.; Mondal, J. A. Polyatomic Iodine Species at the Air–Water Interface and Its Relevance to Atmospheric Iodine Chemistry: An HD-VSFG and Raman-MCR Study. *J. Phys. Chem. A* **2019**, *123* (13), 2924–2934. https://doi.org/10.1021/acs.jpca.9b00828.

(74) Roy, S.; Mondal, J. A. "Breaking" and "Making" of Water Structure at the Air/Water−Electrolyte (NaXO3; X = Cl, Br, I) Interface. *J. Phys. Chem. Lett.* **2021**, *12* (7), 1955–1960. https://doi.org/10.1021/acs.jpclett.0c03827.

(75) Huthwelker, T.; Peter, T. Analytical Description of Gas Transport across an Interface with Coupled Diffusion in Two Phases. *J. Chem. Phys.* **1996**, *105* (4), 1661–1667. https://doi.org/10.1063/1.472025.

(76) Wiegel, A. A.; Liu, M. J.; Hinsberg, W. D.; Wilson, K. R.; Houle, F. A. Diffusive Confinement of Free Radical Intermediates in the OH Radical Oxidation of Semisolid Aerosols. *Phys. Chem. Chem. Phys.* **2017**, *19* (9), 6814–6830. https://doi.org/10.1039/C7CP00696A.

(77) Sanemasa, I.; Kobayashi, T.; Piao, C. Y.; Deguchi, T. Equilibrium Solubilities of Iodine Vapor in Water. *Bull. Chem. Soc. Jpn.* **1984**, *57* (5), 1352–1357. https://doi.org/10.1246/bcsj.57.1352.

(78) Lin, C.-C. Volatility of Iodine in Dilute Aqueous Solutions. *J. Inorg. Nucl. Chem.* **1981**, *43* (12), 3229–3238. https://doi.org/10.1016/0022-1902(81)80094-2.

(79) Barker, G. C.; Sammon, D. C. Kinetics of Proton-Transfer Reactions. *Nature* **1967**, *213* (5071), 65–66. https://doi.org/10.1038/213065b0.

(80) Eigen, M.; De Maeyer, L. Untersuchungen über die Kinetik der Neutralisation. I. *Z. Für Elektrochem. Berichte Bunsenges. Für Phys. Chem.* **1955**, *59* (10), 986–993. https://doi.org/10.1002/bbpc.19550591020.

(81) Bichsel, Y.; von Gunten, U. Oxidation of Iodide and Hypoiodous Acid in the Disinfection of Natural Waters. *Environ. Sci. Technol.* **1999**, *33* (22), 4040–4045. https://doi.org/10.1021/es990336c.

(82) Bichsel, Y. Behavior of Iodine Species in Oxidative Processes during Drinking Water Treatment. Doctoral Thesis, ETH Zurich, 2000. https://doi.org/10.3929/ethz-a-003861380.

(83) Allen, T. L.; Keefer, R. M. The Formation of Hypoiodous Acid and Hydrated Iodine Cation by the Hydrolysis of Iodine. *J. Am. Chem. Soc.* **1955**, *77* (11), 2957–2960. https://doi.org/10.1021/ja01616a008.

(84) Li, C. H.; White, C. F. Kinetics of Hypoiodite Decomposition. *J. Am. Chem. Soc.* **1943**, *65* (3), 335–339. https://doi.org/10.1021/ja01243a011.

(85) Buxton, G. V.; Mulazzani, Q. G. On the Hydrolysis of Iodine in Alkaline Solution: A Radiation Chemical Study. *Radiat. Phys. Chem.* **2007**, *76* (6), 932–940. https://doi.org/10.1016/j.radphyschem.2006.06.009.

(86) Eigen, Manfred.; Kustin, Kenneth. The Kinetics of Halogen Hydrolysis. *J. Am. Chem. Soc.* **1962**, *84* (8), 1355–1361. https://doi.org/10.1021/ja00867a005.

(87) Wren, J. C.; Paquette, J.; Sunder, S.; Ford, B. L. Iodine Chemistry in the +1 Oxidation State. II. A Raman and Uv–Visible Spectroscopic Study of the Disproportionation of Hypoiodite in Basic Solutions. *Can. J. Chem.* **1986**, *64* (12), 2284–2296. https://doi.org/10.1139/v86-375.

(88) Paquette, J.; Wren, J. C.; Sunder, S.; Ford, B. L. *The Disproportionation of Iodine (I)*; 0-7058-1073–9; United Kingdom, 1986; pp 29–45.

(89) Sebők-Nagy, K.; Körtvélyesi, T. Kinetics and Mechanism of the Hydrolytic Disproportionation of Iodine. *Int. J. Chem. Kinet.* **2004**, *36* (11), 596–602. https://doi.org/10.1002/kin.20033.

(90) Lengyel, I.; Epstein, I. R.; Kustin, K. Kinetics of Iodine Hydrolysis. *Inorg. Chem.* **1993**, *32* (25), 5880–5882. https://doi.org/10.1021/ic00077a036.

(91) Palmer, D. A.; Ramette, R. W.; Mesmer, R. E. Triiodide Ion Formation Equilibrium and Activity Coefficients in Aqueous Solution. *J. Solut. Chem.* **1984**, *13* (9), 673–683. https://doi.org/10.1007/BF00650374.

(92) Smith, J. D.; Kroll, J. H.; Cappa, C. D.; Che, D. L.; Liu, C. L.; Ahmed, M.; Leone, S. R.; Worsnop, D. R.; Wilson, K. R. The Heterogeneous Reaction of Hydroxyl Radicals with Sub-Micron Squalane Particles: A Model System for Understanding the Oxidative Aging of Ambient Aerosols. *Atmospheric Chem. Phys.* **2009**, *9* (9), 3209–3222. https://doi.org/10.5194/acp-9-3209-2009.

(93) Schwartz, S. E. Mass-Transport Considerations Pertinent to Aqueous Phase Reactions of Gases in Liquid-Water Clouds; Springer Berlin Heidelberg: Berlin, Heidelberg, 1986; pp 415–471.

(94) Chance, R.; Baker, A. R.; Carpenter, L.; Jickells, T. D. The Distribution of Iodide at the Sea Surface. *Environ. Sci. Process. Impacts* **2014**, *16* (8), 1841–1859. https://doi.org/10.1039/C4EM00139G.

(95) Johnson, J. E.; Gammon, R. H.; Larsen, J.; Bates, T. S.; Oltmans, S. J.; Farmer, J. C. Ozone in the Marine Boundary Layer over the Pacific and Indian Oceans: Latitudinal Gradients and Diurnal Cycles. *J. Geophys. Res. Atmospheres* **1990**, *95* (D8), 11847–11856. https://doi.org/10.1029/JD095iD08p11847.

(96) Singh, H. B.; Gregory, G. L.; Anderson, B.; Browell, E.; Sachse, G. W.; Davis, D. D.; Crawford, J.; Bradshaw, J. D.; Talbot, R.; Blake, D. R.; Thornton, D.; Newell, R.; Merrill, J. Low Ozone in the Marine Boundary Layer of the Tropical Pacific Ocean: Photochemical Loss, Chlorine Atoms, and Entrainment. *J. Geophys. Res. Atmospheres* **1996**, *101* (D1), 1907–1917. https://doi.org/10.1029/95JD01028.

(97) Dickerson, R. R.; Rhoads, K. P.; Carsey, T. P.; Oltmans, S. J.; Burrows, J. P.; Crutzen, P. J. Ozone in the Remote Marine Boundary Layer: A Possible Role for Halogens. *J. Geophys. Res. Atmospheres* **1999**, *104* (D17), 21385–21395. https://doi.org/10.1029/1999JD900023.

(98) Watanabe, K.; Nojiri, Y.; Kariya, S. Measurements of Ozone Concentrations on a Commercial Vessel in the Marine Boundary Layer over the Northern North Pacific Ocean. *J. Geophys. Res. Atmospheres* **2005**, *110* (D11310). https://doi.org/10.1029/2004JD005514.

(99) Seto, F. Y. B.; Duce, R. A. A Laboratory Study of Iodine Enrichment on Atmospheric Sea-Salt Particles Produced by Bubbles. *J. Geophys. Res. 1896-1977* **1972**, *77* (27), 5339–5349. https://doi.org/10.1029/JC077i027p05339.

(100) Duce, R. A.; Hoffman, E. J. Chemical Fractionation at the Air/Sea Interface. *Annu. Rev. Earth Planet. Sci.* **1976**, *4* (1), 187–228. https://doi.org/10.1146/annurev.ea.04.050176.001155.

(101) Gilfedder, B. S.; Lai, S. C.; Petri, M.; Biester, H.; Hoffmann, T. Iodine Speciation in Rain, Snow and Aerosols. *Atmospheric Chem. Phys.* **2008**, *8* (20), 6069–6084. https://doi.org/10.5194/acp-8-6069-2008.

(102) Gómez Martín, J. C.; Saiz-Lopez, A.; Cuevas, C. A.; Baker, A. R.; Fernández, R. P. On the Speciation of Iodine in Marine Aerosol. *J. Geophys. Res. Atmospheres* **2022**, *127* (4), e2021JD036081. https://doi.org/10.1029/2021JD036081.

(103) Angle, K. J.; Crocker, D. R.; Simpson, R. M. C.; Mayer, K. J.; Garofalo, L. A.; Moore, A. N.; Mora Garcia, S. L.; Or, V. W.; Srinivasan, S.; Farhan, M.; Sauer, J. S.; Lee, C.; Pothier, M. A.; Farmer, D. K.; Martz, T. R.; Bertram, T. H.; Cappa, C. D.; Prather, K. A.; Grassian, V. H. Acidity across the Interface from the Ocean Surface to Sea Spray Aerosol. *Proc. Natl. Acad. Sci.* **2021**, *118* (2), e2018397118. https://doi.org/10.1073/pnas.2018397118.

(104) Dunlop, P. J.; Stokes, R. H. The Diffusion Coefficients of Sodium and Potassium Iodides in Aqueous Solution at 25°1. *J. Am. Chem. Soc.* **1951**, *73* (11), 5456–5457. https://doi.org/10.1021/ja01155a520.

(105) Darrall, K. G.; Oldham, G. The Diffusion Coefficients of the Tri-Iodide Ion in Aqueous Solutions. *J. Chem. Soc. Inorg. Phys. Theor.* **1968**, 2584. https://doi.org/10.1039/j19680002584.

(106) Gregory, D. P.; Riddiford, A. C. 731. Transport to the Surface of a Rotating Disc. *J. Chem. Soc. Resumed* **1956**, 3756. https://doi.org/10.1039/jr9560003756.

(107) Gottschalk, C.; Libra, J. A.; Saupe, A. *Ozonation of Water and Waste Water: A Practical Guide to Understanding Ozone and Its Applications*, 2nd Edition.; Wiley-VCH Verlag GmbH & Co., 2010.

(108) Miller III, T.; Eleftheriou, M.; Pattnaik, P.; Ndirango, A.; Newns, D.; Martyna, G. Symplectic Quaternion Scheme for Biophysical Molecular Dynamics. *J Phys Chem* **2002**, *116* (20), 8649–8659.

(109) Lopes, P. E.; Roux, B.; MacKerell, A. D. Molecular Modeling and Dynamics Studies with Explicit Inclusion of Electronic Polarizability: Theory and Applications. *Theor Chem Acc* **2009**, *124*, 11–28.

(110) Lamoureux, G.; Roux, B. Modeling Induced Polarization with Classical Drude Oscillators: Theory and Molecular Dynamics Simulation Algorithm. *J Chem Phys* **2003**, *119* (6), 3025–3039.

(111) Frenkel, D.; Smit, B. *Understanding Molecular Simulation: From Algorithms to Applications*; Elsevier, 2001.

(112) Noskov, S. Y.; Lamoureux, G.; Roux, B. Molecular Dynamics Study of Hydration in Ethanol- Water Mixtures Using a Polarizable Force Field. *J Phys Chem B* **2005**, *109* (14), 6705–6713.

(113) Pollock, E.; Glosli, J. Comments on P3M, FMM, and the Ewald Method for Large Periodic Coulombic Systems. *Comput. Phys Comm* **1996**, *95* (2–3), 93–110.

(114) Dodin, A.; Geissler, P. L. Symmetrized Drude Oscillator Force Fields Improve Numerical Performance of Polarizable Molecular Dynamics. *J. Chem. Theory Comput.* **2023**, *19* (10), 2906–2917. https://doi.org/10.1021/acs.jctc.3c00278.

(115) Torrie, G. M.; Valleau, J. P. Nonphysical Sampling Distributions in Monte Carlo Free-Energy Estimation: Umbrella Sampling. *J Comput Phys* **1977**, *23* (2), 187–199.

(116) Kumar, S.; Rosenberg, J. M.; Bouzida, D.; Swendsen, R. H.; Kollman, P. A. The Weighted Histogram Analysis Method for Free-Energy Calculations on Biomolecules. I. The Method. *J Comput Chem* **1992**, *13* (8), 1011–1021.

(117) Farago, O.; Grønbech-Jensen, N. Fluctuation–Dissipation Relation for Systems with Spatially Varying Friction. *J. Stat. Phys.* **2014**, *156* (6), 1093–1110. https://doi.org/10.1007/s10955-014-1045-4.

Chapter 3: Distinguishing Surface and Bulk Reactivity—Concentration Dependent Kinetics of Iodide Oxidation in Microdroplets

3.1: Introduction

Global chemical models investigating iodine chemistry in the atmosphere have sought to understand how global concentrations and local emissions influence oxidant concentrations.[1–4] Recent work demonstrated that iodine oxides are a significant source of atmospheric new particle formation,[5,6] with the potential to influence climate through aerosol chemistry and cloud formation.[7,8] In these largely gas-phase environments, volatile iodine species originate from the sea surface—the release of which begins with oxidation of aqueous I^- in the chemically-complex environment of the sea surface microlayer.[9] Iodide is also emitted into the atmosphere in sea spray aerosol, an environment where salt concentrations can increase dramatically compared to seawater.[10] Differences in the chemical reactivity of iodine between sea spray aerosol and seawater, and potential implications for overall marine O_3 deposition rates remains under investigation.[11] From this environmental perspective, the multiphase chemistry of iodine consists of a reaction network that connects ocean processes with atmospheric microphysics and chemistry.

The $I^- + O_3$ reaction is often used to measure the mass accommodation coefficient of O_3 in water, with I^- acting as a reactive scavenger due to its high reactivity in solution.[12,13] An understanding of O_3 accommodation, however, is obscured by the chemical makeup of the air-water interface and by changes in iodide availability in the presence of different salts under various concentrations. While it is generally observed from both experiment and theory that the iodide is surface active[14–19] (the degree to which is still contested),[20] how this bulk-to-surface partitioning affects the observed reaction kinetics and therefore O_3 uptake remains unclear. More generally for multiphase kinetics, the degree to which a surface reaction will contribute to measured kinetics relative to the bulk depends sensitively on underlying physical processes such as trace gas diffusion, adsorption to the interface, solvation into the liquid, and liquid diffusion. In this context, the $I^- + O_3$ reaction is an important model system for assessing mass transport mechanisms governing multiphase chemistry.

Due to the challenges outlined above, a detailed understanding of the multiphase $I^- + O_3$ reaction mechanism has proven elusive, particularly in distinguishing surface vs. bulk reactivity. As we previously observed in aqueous microdroplets, the $I^- + O_3$ reaction under concentrated salt conditions occurs almost exclusively at the air-water interface, but is complicated by the apparent pH dependence of the reaction.[21] This previous work focused on the I^- decay kinetics at a single iodide concentration, which limits our knowledge of how the O_3 uptake mechanism evolves with concentration especially under dilute conditions. Here, we report reaction kinetics of aqueous iodide with O_3 in levitated microdroplets for a range of initial iodide concentration using an open-port sampling interface (OPSI) coupled with mass spectrometry (MS) as described previously.[21–23] Molecular simulations of I^- at the air water interface and a recently developed reaction-diffusion kinetic model are used to interpret the experimental results. Emphasis is placed on the further development of the kinetic model, which is refined to address liquid- and gas- diffusion. The model is constrained by results of molecular dynamics simulations of O_3 and ions at the air-water interface. Together, model and experiment suggest the $I^- + O_3$ surface reaction is considerably slower than the bulk, and at pH 3 more closely resembles the lower reaction efficiency of the gas-phase reaction. Under basic conditions, the surface reaction effectively vanishes, suggesting a fundamental relationship between solution pH and stability of reactants or intermediates at the air-water interface. These results demonstrate the necessity for accurate mass transport descriptions across the gas-liquid interface in order to isolate surface-specific reaction information.

3.2: Experimental

Measurements of the oxidation kinetics of iodide by ozone in single microdroplets were carried out as described in Prophet et al.[21] and previous reports from co-workers.[24–26] Experiments were conducted using a quadrupole electrodynamic trap (QET) where microdroplets, generated by a piezoelectric microdroplet dispenser (Microfab, 30 μm orifice), are charged and trapped by a quadrupole field. Within the QET, DC electrodes are used to balance a collection of ~100 microdroplets over the course of an oxidation experiment. Once droplets are trapped, a steady flow of O_3 mixed with humidified air is directed through the reactor to oxidize the droplets. During oxidation, individual microdroplets are released from an upper balancing region to a lower region where the droplet is illuminated by a 532 nm laser diode directed axially through the reactor. Mie scattering from the individual droplets are collected at 90° relative to the illumination axis and the interference pattern analyzed to obtain droplet radius. Droplet radius is quantified by comparing peak spacing to a reference library containing simulated peak positions using a fixed refractive index.[25,27] A representative interference pattern for droplet size analysis is included in Appendix 3B. For the current experiments, the droplet radius was measured to be $r = 17 \pm 1$ μm, with an average change in droplet size during reaction of ~1 μm. The initial droplet radius generated from this model of dispenser before equilibration in the QET is r ~ 25 μm.[28,29]

Once sized, droplets are ejected from the QET and analyzed using an open-port sampling interface (OPSI) for single droplet electrospray mass spectrometry (MS)[22,30] as described by Prophet et al.[21] Droplet composition is monitored throughout the oxidation reaction using OPSI-MS, where each individual detection event yields single droplet composition as a function of O_3 exposure time. A sketch of the experimental diagram is shown in Fig. 3.1, along with example droplet detection events and respective peak areas for a typical oxidation experiment. Example single droplet mass spectra before and after reaction are included in Appendix 3B, together with a discussion of observed peaks in the mass spectra.

While the general experimental setup mirrors that described by recent work,[21] droplet composition for each experimental condition was altered to study the reactive uptake of O_3 as a function of initial NaI (Sigma-Aldrich, ≥ 99.5%) concentration. For all experiments, the relative humidity (RH) inside of the QET was held at RH = 88 ± 1%. The initial droplet solution for each iodide concentration condition was adjusted using NaCl (Sigma-Aldrich, ≥ 99.5%) to establish a water activity of $a_w = 0.96 \pm 0.01$. Salt concentrations necessary for this condition were calculated using the AIOMFAC thermodynamic model[31,32] and further verified using a water-activity meter (Aqualab 4TE). Once dispensed into the QET, the water activity in the droplet equilibrated to the trap RH, and the salt concentration in the droplet was determined with AIOMFAC. Concentrations used for each condition are provided in Tables 3B.1 and 3B.2 in Appendix 3B. Fresh solutions were prepared daily using HPLC-grade water (Sigma-Aldrich), with pH adjusted using citric acid (Sigma-Aldrich, ≥ 99.5%) and NaOH (Sigma-Aldrich, ≥ 98%).

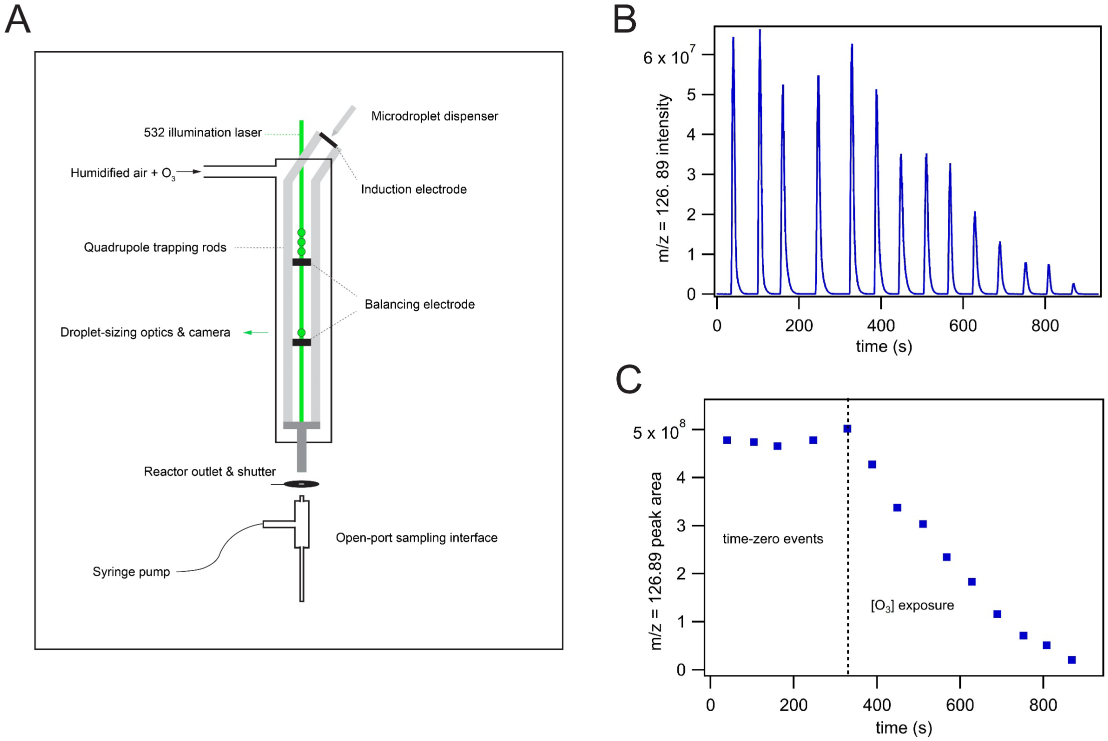

Fig. 3.1: (A) Experimental diagram showing the QET enclosure, dispenser, microdroplet trapping positions, and outlet to open-port sampling. (B) Ion current at m/z = 126.89 (i.e. iodide) vs. time in orbitrap mass spectrometer. Time series shows individual microdroplet detection events for an example ozone oxidation experiment. (C) Integrated peak areas from detection events in (B).

3.3: Model Description

To interpret the observed microdroplet reaction kinetics, we employ a combined modeling approach where molecular simulations are performed to constrain relevant parameters necessary to run a kinetic model executed using the stochastic-based simulation software, Kinetiscope©.[33] In addition to this system, Kinetiscope has been used to explore a number of other chemical and physical processes in microcompartments.[34,35] A comprehensive list of the kinetic steps implemented in Kinetiscope is provided in Appendix 3A and Table 3A.1.

3.3.A: Molecular Dynamics Simulations

Molecular dynamics simulations are used to study the behavior of O_3 and I^- at the air-water interface, providing information about surface concentrations and kinetic timescales for processes such as surface-desorption, diffusion, and bulk-solvation. The details of simulating O_3 at the air-water interface have been described in recent work,[21,36] and the present work uses the same approach. To investigate the interfacial chemical makeup of systems encountered in the experiments, simulations were performed with varying concentrations of NaI to observe how the effective surface concentration of I^- changes when transitioning from a dilute regime (mM concentrations) to a more concentrated one (M concentrations). A water slab with containing 768 water molecules in a box of $24.8\times 24.8 \times 111.8$ Å^3 was used to simulate an aqueous droplet where the larger dimension is perpendicular to the air-water interface. A classical polarizable force field, SWM4-NDP,[37] was employed for the molecular dynamics simulation. The nonbonded interactions were modelled with a Lennard-Jones potential.[21,36] We applied a rigid body dynamics for water and ozone molecules. A Drude oscillator model[38] was implemented to replicate polarization in the simulation. The simulated partitioning of I- between the bulk and interface was quantified using a simple Langmuir framework that was then directly used in the kinetic model as detailed below in Section 3.3.C.(ii). Additionally, mixtures of NaI and NaCl were simulated to explore the relative surface propensities of these ions in solution and any dependence on the relative quantities of different ions in solution. A more detailed review of the simulated mixture results and the potential influence on observed iodide-oxidation kinetics is provided in Appendix 3C.

3.3.B: Kinetic Model Framework

The kinetic model for multiphase oxidation draws on a number of recent publications detailing the mechanics of the model and discussing the origins of each kinetic step that is used.[21,26,39] In the following section, we summarize the main components of the kinetic model and introduce an approach to simulate sub-surface reaction dynamics. Our approach aims to identify spatial regions of the multiphase system with distinct governing kinetics, allowing for the relevant chemistry to be simulated in each region without explicitly resolving chemical gradients. A conceptual picture of these distinct kinetic regions and their related length scales is shown in Fig. 3.2. Up to this point, previous models using this approach have relied on discretizing the microdroplet into only two separate regions: the droplet surface, and the bulk interior.[26,35,39–41]

In Section 3.3.B, we briefly summarize the overall model geometry and the definition of the droplet surface region. In this section we describe the construction and implementation of a "reaction-diffusion" compartment, a sub-surface region that is distinct from the bulk interior and is directly related to the initial reaction diffusion length of O_3. In combination, the three kinetically distinct regions (surface, reaction-diffusion, and bulk-interior) govern the oxidation process in the entire droplet volume for different concentrations of NaI. In Section 3.3.C, we introduce and discuss the kinetic processes implemented in the model that are critical for distinguishing surface and bulk reactivity. In this final modeling section, we focus on the governing physical processes such as diffusion and adsorption of reagents to the droplet interface, emphasizing the model's relationship to earlier multiphase chemical descriptions and highlighting how molecular simulation results are integrated within the kinetic framework. Lastly, in Section 3.3.C we comment on the effective rate coefficient used for the $I^- + O_3$ reaction in the model at the droplet surface and in the bulk. While we have generally assumed the surface reaction to proceed at the same rate as the bulk, a comparison with experimental results below suggests the surface reaction is significantly slower than the bulk. The modeling mechanics for this are established in Section 3.3.C, and a larger discussion is included in Section 3.5.

(i) Overall Simulation Geometry & Surface Region Definition

The geometry of the simulated microdroplet follows the general approach used in previous studies.[35,42] The microdroplet is represented using a rectangular prism divided into sub-compartments with length scales weighted to give the correct scaling of a sphere. A surface compartment is defined with a 1x1 nm^2 area and a height of $\delta = 1$ nm, corresponding approximately to the length scale of water density attenuation across the interface (Fig. 3.2A). The remainder of the simulated prism (representing the remaining microdroplet volume) is then constrained to have area 1x1 nm^2 and a height of R/3, assuring that the simulation geometry conserves the surface area to volume ratio of a sphere. No sensitivity is observed to the absolute simulated area when the bulk to surface compartments are weighted in this way.

(ii) Sub-surface & Bulk Interior Region Definitions

To capture bulk chemistry occurring within the microdroplet, the inner $R/3$ droplet length is further divided into two distinct compartments: a sub-surface and bulk-interior region. The sub-surface region is conceptualized as the spherical shell beneath the outer surface where ozone diffusion is competitive with the reaction rate in the bulk. Naturally, the length scale of this region is defined using the "reaction-diffusion" length of O_3, $L_{\mathrm{rxn}} = \sqrt{\frac{D_{liq}}{k\cdot[\mathrm{I}^-]}}$, where D_{liq} is the diffusion coefficient of O_3 in solution and k_{rxn} the bimolecular reaction rate for $\mathrm{I}^- + O_3$. The reaction-diffusion length is commonly encountered in the study of chemical reactivity in liquids, and is especially relevant for chemical kinetics in microcompartments where physical dimensions are of the same order.[43] Fig. 3.2 provides a conceptual sketch of the sub-surface and bulk-interior regions in reference to a microdroplet and their respective projections into the simulation geometry.

Within Kinetiscope, this sub-surface region is implemented with a reaction-diffusion (RD) compartment situated between the surface and the bulk-interior compartments and is initialized with height L_{rxn} using the initial iodide concentration $[\mathrm{I}^-]_0$ for each experiment. This definition neglects the fact that L_{rxn} changes dynamically throughout the reaction as $[\mathrm{I}^-]$ is consumed. However, since L_{rxn} is inversely proportional to $\sqrt{[\mathrm{I}^-]}$, the change in L_{rxn} from its initial value as I^- is consumed is relatively small over the experimental timescale, and the initial L_{rxn} proves to be a reasonable approximation. Functionally, the RD compartment allows for droplet reactivity due to the ozone gradient extending into the droplet while avoiding the full gradient resolution as is commonly done to explore multiphase oxidation kinetics using multi-layer kinetic models.[44] An in-depth exploration of the utility of the RD compartment and its ability to capture the behavior of reaction-diffusion fronts in more general chemical kinetics will be provided in an upcoming publication, as a full discussion would be too exhaustive in the present work.

Since the entire simulated droplet height must equal $R/3$, the bulk-interior region is simulated with an inner-bulk compartment of height $L_{\mathrm{bulk}} = R/3 - L_{\mathrm{rxn}}$. This compartment represents the inner core of the droplet beyond the diffusive O_3 gradient where only a very small fraction of chemistry occurs. Functionally, this compartment is a source of I^- that diffuses into the RD and surface compartments. For the more general case where $L_{\mathrm{rxn}} > R/3$ (a case not encountered in the current work), L_{bulk} is defined to be 0 and the RD compartment height is defined to be $R/3$. Although we have only considered compartmentalization of the liquid phase, we include in Fig. 3.2 the same conceptual principle applied to the gas phase, with a gas-diffusive region and gas-adsorption region identified above the droplet surface. While we include this for conceptual completeness, these regions are not explicitly simulated in the current model and can be effectively included as single kinetic steps in the surface compartment (which, while applicable to this system, is not generally true for other multiphase processes). Details of the current gas-phase diffusion description and adsorption to the droplet surface are included below in Section 3.3.C.

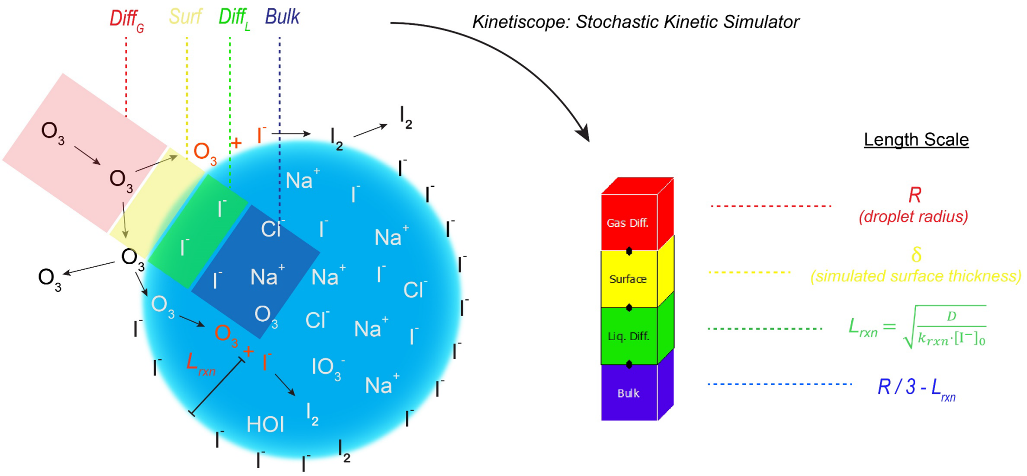

Fig. 3.2: Spatial model-representation overlay referenced to an aqueous microdroplet during reaction. Overlay shows conceptual kinetic regions of the kinetic model including an outer gas-diffusion layer, the droplet surface, the reaction-diffusion region, and the inner bulk region. Key physical length scales used to define the kinetic model compartments are included.

3.3.C: Physical and Chemical Mechanistic Steps

A number of mechanistic steps describing physical and chemical processes are defined in the model to simulate the overall reaction progress. The majority of these steps and overall reaction mechanism have been previously published[21,26,39] so an exhaustive discussion of these steps will not be provided. Instead, emphasis is given to the particular steps that distinguish this work from the previous, namely, the adsorption behavior of the iodide ion at the air-water interface, the diffusional transport of O_3 to the interface, and the surface vs. bulk rate coefficient used for the primary $I^- + O_3$ reaction. Since the chemical mechanism has been explored in detail in previous work,[21] this mechanism is largely reproduced for the current model. One additional chemical consideration is the reactivity of Cl^- with products of the $I^- + O_3$ reaction. Details on these additional mechanistic steps are included in Appendix 3A, with deviations from the previous model[21] being emphasized in bold.

(*i*) *Surface Concentrations and Langmuir-Adsorption of Aqueous Iodide*

Surface concentrations are of particular importance for distinguishing surface and bulk reactivity. In the kinetic model, surface concentrations of I^- and O_3 are described as simple Langmuir-adsorption. In previous work, particular attention was given to surface concentrations of O_3 and the adsorption/desorption kinetics at the interface. We refer the reader to previous work[21,36] for more discussion on O_3 density at the air water interface, and provide only a key result in Fig. 3.2A showing the enhanced O_3 concentration at the interface. Surface concentrations of iodide in the current model are related to the bulk using a kinetic step where bulk-aqueous phase iodide, having diffused into the surface compartment, can adsorb to an available site at the interface:

$$\mathrm{I}^-_{(blk)} + \text{site} \underset{k_{solv}}{\overset{k_{desolv}}{\rightleftarrows}} \mathrm{I}^-_{(ads)}. \qquad (A1)$$

The rate coefficients for desolvation and solvation, k_{desolv} and k_{solv}, are constrained using the Langmuir equilibrium coefficient $K_{eq}^{\mathrm{I}^-} = k_{desolv}/k_{solv}$ from an adsorption isotherm:

$$[\mathrm{I}^-_{(ads)}] = \frac{\Gamma_{\mathrm{I}^-}^{\infty}}{\delta} \cdot \frac{K_{eq}^{\mathrm{I}^-} \cdot [\mathrm{I}^-_{(b)}]}{1 + K_{eq}^{\mathrm{I}^-} \cdot [\mathrm{I}^-_{(b)}]}, \qquad \text{Eq. 3.1}$$

where $\Gamma_{\mathrm{I}^-}^{\infty}$ is the maximum surface coverage (molecule/cm^2) and δ the surface thickness of 1 nm, where the quantity $\frac{\Gamma_{\mathrm{I}^-}^{\infty}}{\delta}$ is the maximum site concentration for step (A1). As discussed previously,[21] values for $K_{eq}^{\mathrm{I}^-}$ and $\Gamma_{\mathrm{I}^-}^{\infty}$ (determined experimentally or theoretically) can deviate dramatically in the literature depending on methods used and frameworks employed for analysis. In the current approach, we conduct a series of simulations to obtain density profiles of I^- across a simulated water slab for different bulk iodide concentrations. Fig. 3.3B shows these density profiles for bulk concentrations ranging from 40 mM to 1 M, where the density scale is normalized to the bulk solution density. To obtain the Langmuir-type information necessary for the kinetic model, we use the results in Fig. 3.3B to extract an effective surface concentration under each condition by averaging the density across the top 1 nm of solution (from 14 Å to 24 Å) for each density profile. Surface concentrations defined in this way are then compared to their respective bulk concentration, averaged from 0 to 5 Å, as shown in Fig. 3.3C. We fit the results shown in Fig. 3.3C to the Langmuir equation (Eq. 3.1) and obtain $K_{eq}^{\mathrm{I}^-}$= 1 M^{-1} and $\Gamma_{\mathrm{I}^-}^{\infty}/\delta = 2$ M.

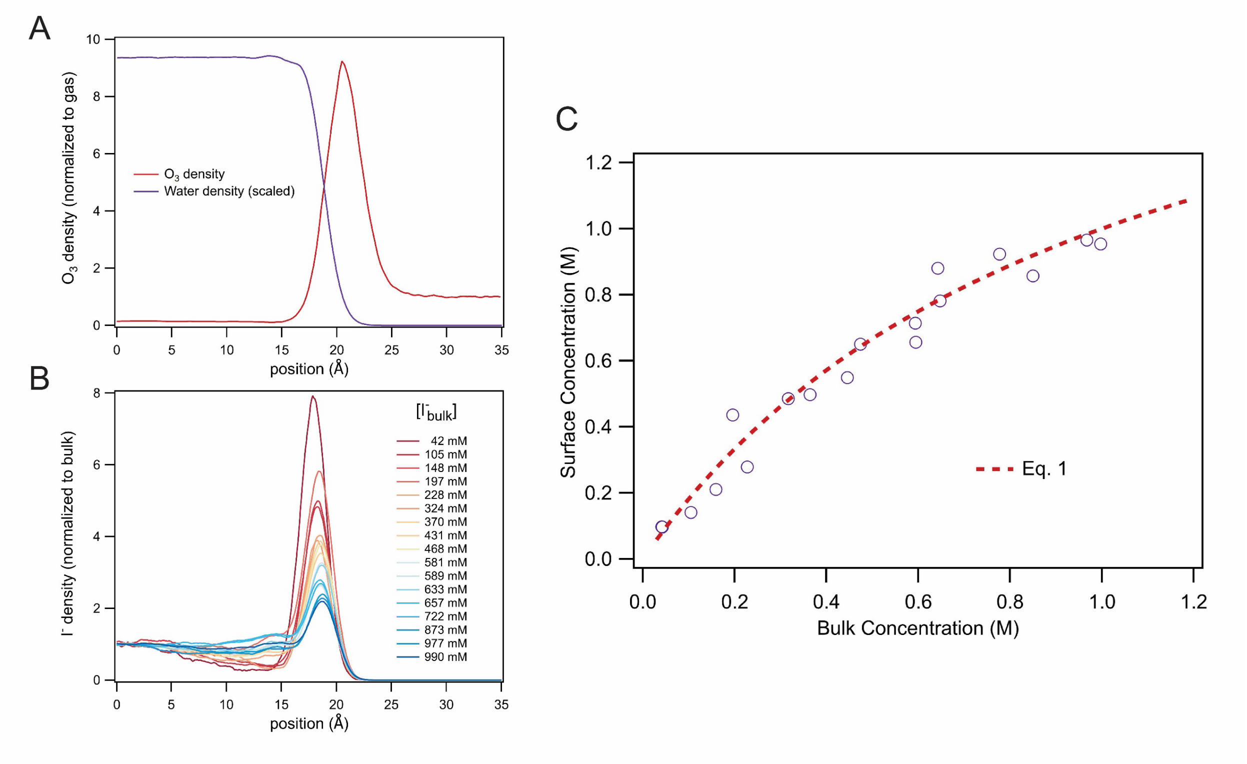

Fig. 3.3: (A) Ozone density profile at the air-water interface. (B) Iodide density profiles at the air-water interface. A series of density profiles are obtained by changing the overall ion number in the water slab to change the bulk concentration of iodide. (C) A surface vs. bulk concentration curve is constructed using results in (B) by defining the surface as the top 1 nm of solution. A fit to the Langmuir isotherm Eq. 3.1 is shown, yielding values for $K_{eq}^{\mathrm{I}^-}$ and $\Gamma_{\mathrm{I}^-}^{\infty}$.

We note the values obtained in this way deviate from our previously used values for Langmuir-adsorption of iodide, where we fixed the maximum site concentration to a literature value[15] and then determined $K_{eq}^{\mathrm{I}^-}$ from an I$^-$ density profile using a single concentration. These updated values provide a more realistic set of parameters to simulate the effective surface concentrations of sodium iodide within a Langmuir framework—although we acknowledge that the Langmuir framework may have limitations for describing ion adsorption to interfaces. For example, the subtle structural features in the density profiles in Fig. 3.3B are lost when using a simple Langmuir model. Nevertheless, this approach provides a surface vs. bulk description of the iodide ion, which generally agrees with the current literature, where the effective surface concentration of iodide is weakly enhanced and largely resembles the bulk, especially for more concentrated solutions. Lastly, we point out that while the Langmuir-fit approach above provides $K_{eq}^{\mathrm{I}^-} = k_{desolv}/k_{solv}$, this does not constrain the absolute values k_{desolv}, k_{solv}. A sensitivity test performed on the absolute rates shows that our kinetic results are independent of these values for $k_{solv} > 1000$ s^{-1}. While we are not sensitive to these rates above $k_{solv} = 1000$ s^{-1}, we note that one would generally expect the absolute solvation rates for small ions to be closer to a diffusional timescale across the interfacial thickness, resembling a rate constant $k_{solv} \sim 10^8 - 10^9$ s^{-1}.

(ii) Gas-Phase Diffusion and Adsorption of O_3

Adsorption and desorption of O_3 to the interface has been previously described,[21,36] where the timescale of desorption is calculated using the potential of mean force for O_3 at the air-water interface, computable from umbrella sampling.[21,36] This potential of mean force determines the density profile of O_3 at the interface (see Fig. 3.3A) and, along with a Langmuir-adsorption description, an adsorption rate to the interface. We find this adsorption rate (see step S2 in Table 3A.1) agrees well with a simple collision rate calculated from kinetic theory: $k_{col} = \frac{\bar{c}}{4 \cdot \delta} = 9\times10^{10}$ s^{-1}, where $\bar{c}$ is the mean molecular speed of O_3 in the gas phase at 293 K and δ the surface thickness $\delta = 1$ nm. We include an additional gas-phase transport step to simulate the diffusional timescale of O_3 across a spherical shell surrounding the droplet, illustrated in Fig. 3.2. The thickness of this shell is defined to be the droplet radius r, the length scale found in the steady-state solution of the diffusion equation with a spherical sink.[45] Gas diffusion across this shell functionally determines an upper-bound for the rate of O_3 transport to the droplet interface, limiting the overall reactivity if the loss rate of O_3 at the interface exceeds this diffusion rate. To identify this limiting rate for gas-diffusion, we consider the flux Q of O_3 through a surrounding gas shell for arbitrarily large thickness, which converges to a lower-bound for O_3 flux onto the droplet surface $Q = 4\pi r D_{gas}$ where D_{gas} is the diffusion coefficient of O_3 in air.[45,46] From an interfacial perspective, a first-order rate coefficient for the process describing diffusion from the gas to the near-surface region (prior to adsorption)

$$O_{3(gas)} \underset{k_{diff}}{\overset{k_{diff}}{\rightleftarrows}} O_{3(near-surface)} \qquad (A2)$$

can be simply expressed as $k_{diff} = \frac{D_{gas}}{r \cdot \delta}$, utilized to calculate the rate for step S1 in Table 3A.1. A detailed comparison of kinetic terms k_{col} and k_{diff} provides a novel route to describing the transition between molecular and continuum flow as discussed by Fuchs and Sutugin.[47] We leave an exposition of this description to future work.

(iii) Surface and Bulk Rate Coefficients for the I^- + O_3 Reaction

In general, it is difficult to anticipate if a surface rate coefficient should deviate from its bulk counterpart.[48–50] In the current approach we fix the bulk reaction rate to a reported aqueous value[51] of 1.2×10^9 M^{-1} s^{-1} (with literature values ranging from $1.0\text{-}3.4 \times10^9$ M^{-1} s^{-1} at 25°C)[52] and treat the surface reaction rate as an adjustable parameter. This in principle accounts for altered reaction rate barriers at the interface, as well as potential inaccuracies in $K_{eq}^{I^-}$ deduced from the simulations. We find an effective surface rate coefficient of 6×10^7 M^{-1} s^{-1} best explains the experimental results. The significance of this value, along with an assessment of uniqueness and uncertainty, is included below in Section 3.5.

3.4: Experimental Results

Kinetics of I^- oxidation by O_3 for initial iodide concentrations ranging from 8 mM to 3.8 M are presented in this section for microdroplets generated using acidic (pH 3) and basic (pH 12) solutions. Experimental results are shown in Figs. 3.4 and 3.5 alongside output from the kinetic simulations. We include two model scenarios with each experimental condition that are discussed in the analysis and discussion sections below. The primary model conforms to the full description above in Section 3.3 and contains all steps listed in Table 3A.1. A secondary model scenario, termed “bulk-only” simply shows a model simulation that omits the $I^- + O_3$ surface reaction.

Data in Fig. 3.4 shows results for droplet solution with pH 3 where individual points represent normalized peak areas for single OPSI-MS detection events at m/z = 126.9, as illustrated in Fig. 3.1. Each experimental condition includes data from 3 individual reaction trials using microdroplets with radius $r = 17 \pm 1$ µm. For all the acidic experiments, 300 mM of citric acid/citrate buffer was used to keep the pH close to the initial pH 3 during reaction. The shape of the kinetic profiles for the acidic experiments appears largely insensitive to initial concentration, where the profiles appear mostly linear, with a small but noticeable tail at longer reaction times. In the following analysis section, the degree of agreement between experiment and the kinetic model predictions is explored more closely, with special attention given to distinguishing surface vs. bulk reactivity.

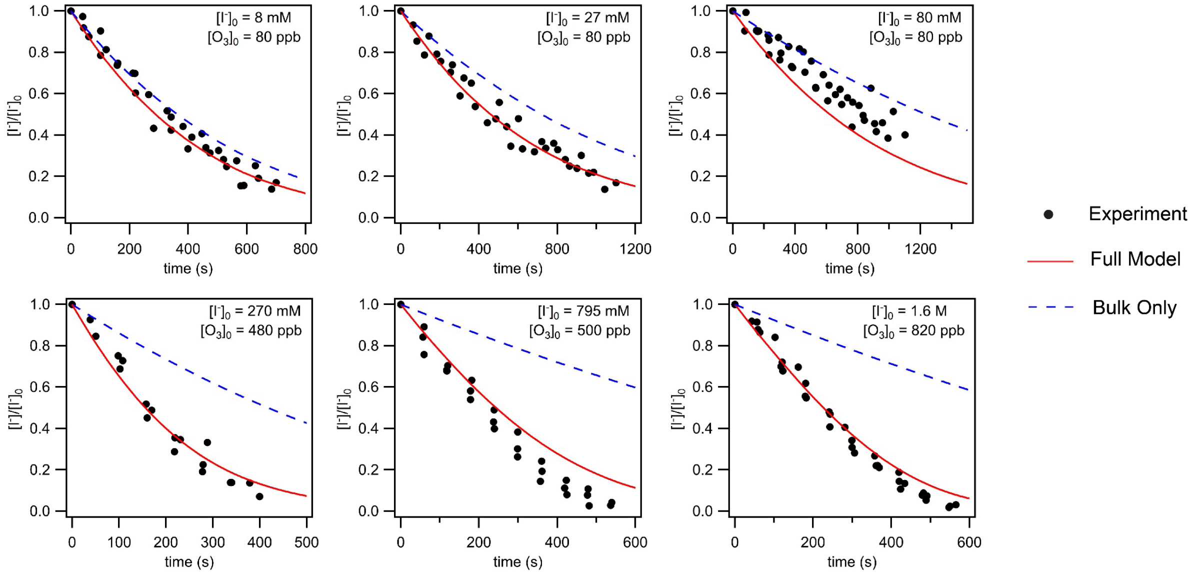

Fig. 3.4: Series of iodide-oxidation experiments showing decay of normalized iodide concentration $[I^-]/[I^-]_0$ for initial $[I^-]_0$ ranging from 8 mM to 1.6 M with solution pH 3. Datapoints represent individual microdroplet detection events quantified by peak area of iodide detection normalized to the initial unreacted peak area, as shown in Figs. 3.1B and 3.1C. Model results are included, showing two simulation cases. The full model case (black dashed lines) shows the entirety of the model detailed in Section 3.3. The bulk-only model (blue dotted lines) is simulated using the same model but neglecting the surface $I^- + O_3$ reaction. Concentration conditions for each experiment are provided in Appendix 3B, Table 3B.1.

Data in Fig. 3.5 shows the oxidation of aqueous iodide at pH 12, where each dataset originates from three individual trials conducted on microdroplets with an initial radius r = 17 µm. Experiments range from initial $[I^-]$ of 8 mM to 3.8 M, and in this case, the decay profiles exhibit a qualitative change with initial $[I^-]$. For concentrations ~100 mM and below, the decays resemble first-order kinetics, showing a linear profile, with a small but significant tail when the normalized iodide concentration $[I^-]/[I^-]_0$ ~25%. For concentrations >100 mM, a noticeable “plateau” is observed in the kinetics, where the rate of decay appears to suddenly slow when the remaining iodide is ~50% of its initial concentration.

As the plateau behavior is not recovered in the kinetic simulations, the origin of this effect remains unclear. However, IO^- likely becomes relatively concentrated in solution under these conditions, due to the higher initial $[I^-]$ and as suggested by the kinetic simulations. The self-disproportionation of IO^- to generate IO_3^- and I^- has long been observed experimentally,[53,54] and along with related transformations, has been subject to intense experimental and modeling investigation.[55–58] Furthermore, photochemistry of IO^- may become relevant due to ambient laboratory light or from the 532 nm laser used for droplet illumination. McKinon et al.[59] report both photodetachment and photodissociation of IO^- for exposure to a relatively broad wavelength range centered around 515 nm, albeit only evidenced in the gas phase. Regeneration of I^- from either the chemical or photo-chemical decomposition of IO^- would show a distinct slowing of I^- consumption kinetics, a trend consistent with the experimental kinetic profiles. To verify this mechanism, experiments targeting the full redox chemistry of IO^-, IO_2^-, and IO_3^- in aqueous iodide microdroplets should be investigated, along with a more complete chemical model to include this chemistry. While outside the scope of the current work, oxidation experiments under dark conditions are also needed to isolate any photochemistry of iodine-oxides from alternate chemical decomposition routes.

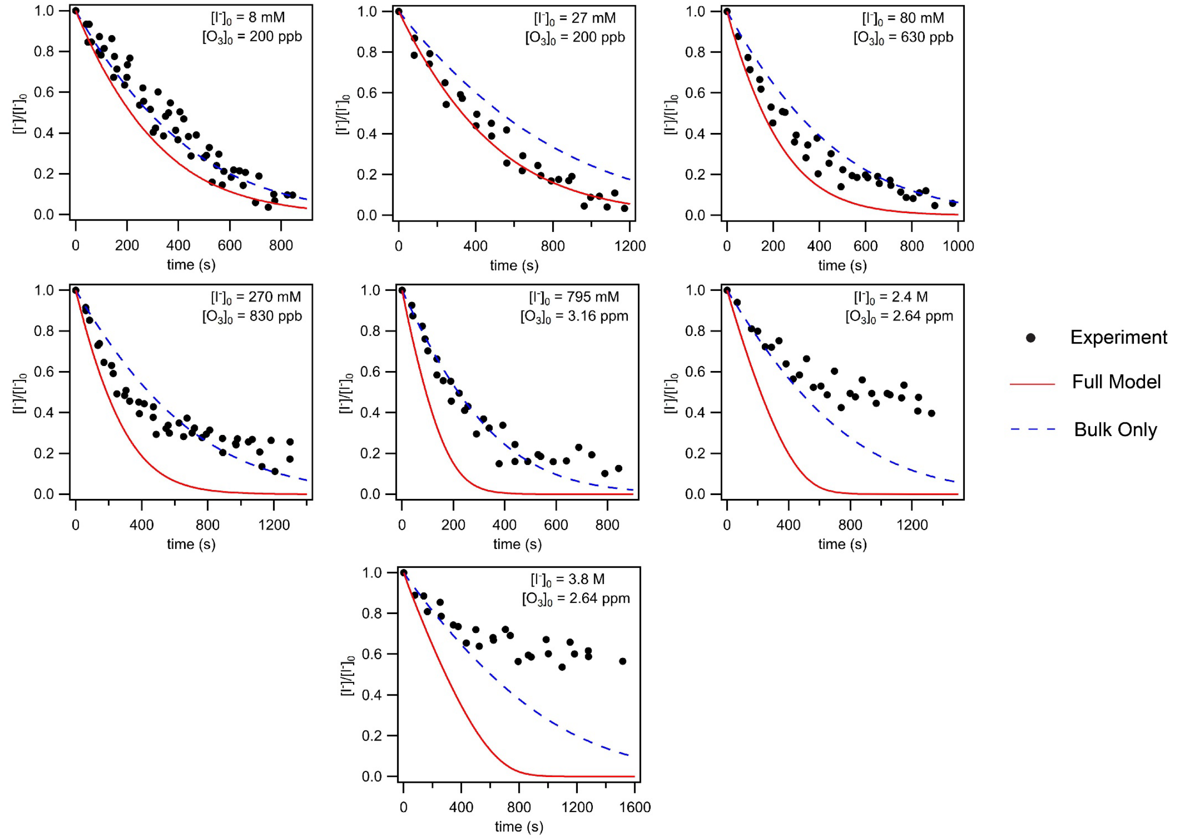

Fig. 3.5: Iodide-oxidation kinetics for initial $[I^-]_0$ ranging from 8 mM to 3.8 M with solution pH 12. Full model (black dashed lines) and bulk-only model (blue dotted lines) results are included for running the simulations at pH 12. Concentration conditions for each experiment are provided in Appendix 3B, Table 3B.2.

3.5: Analysis

In the following, model results included in Figs. 3.4 and 3.5 are analyzed and reactive uptake coefficients are calculated from the experiments and simulations. Specific attention is given to how uptake due to a surface vs. bulk reaction can be distinguished from the stochastic simulations using an analysis of event selection frequency of the respective kinetic steps. A comparison between the mechanism under acidic and basic conditions is made, as well as the transition point between bulk-dominated and surface-dominated reactive uptake. Finally, we compare the current model to the widely used resistor model formulation, commenting on the general agreement between the models for describing subsurface chemistry. While the majority of our analysis centers on iodide concentration and pH, the results may also be sensitive to the solution composition of each individual experimental condition since the [Cl^-] changes in experiments to compensate for changing [I^-]. A more detailed analysis of ion-ion interactions at the interface using molecular simulations is included in Appendix 3C.

Model results for the pH 3 solution are shown in Fig. 3.4, where the full model scenario is in reasonable agreement for the concentration range studied. Initial rates of decay are notably in agreement between model and experiment, with the model showing deviation from some experiments in the latter half of the decay profiles. This deviation is likely due to the static RD compartment length being fixed to the initial conditions rather than changing dynamically with [I^-], resulting in an underprediction of the overall I^- consumption with time. This constraint can likely be avoided by numerically evaluating the governing rate equations directly rather than using the stochastic simulation approach with a fixed geometry. In the pH 12 case shown in Fig. 3.5, general agreement is also observed, but exclusively for the bulk-only model where the surface reaction is neglected. The model does not reproduce the plateau-type decay behavior observed in the experiments with higher salt concentrations, suggesting the model neglects secondary processes that interfere with the primary consumption of I^- resulting from the $I^- + O_3$ reaction—likely involving the stability and reactivity of intermediates IO^- and IO_2^-, and potential routes to I^- regeneration. Nevertheless, initial reaction rates come into close agreement for all conditions studied.

Many of the insights mentioned above are also evident by comparing experimental and modeled uptake coefficients, shown in Fig. 3.6. Experimental uptake coefficients for each condition are calculated from the initial reaction rate k_{init} combined with a previous formulation for uptake[21,60]

$$\gamma_{exp} = \frac{4 \cdot r \cdot k_{init} \cdot \left[\mathrm{I}^-_{(b)}\right]_0}{3 \cdot [\mathrm{O}_{3(g)}] \cdot \bar{c}}. \qquad \text{Eq. 3.2}$$

Here, γ_{exp} is not corrected for the reaction stoichiometry, so γ_{exp} expresses an observed reactive uptake coefficient derived from the solute consumption rate. To calculate the true reactive uptake of O_3, γ_{exp} must be divided by a factor of two when I_2 is the product of the reaction. For simplicity, we consider only the observed uptake γ_{exp} in the following analysis.

Uptake coefficients from the model are calculated directly by analyzing the output of the stochastic simulations, which provides the number of selections for each kinetic step, or event, after a given simulation period. The reactive uptake coefficient in this case is simply the ratio of reaction events selected and ozone-surface collision events, N_{rxn} / N_{col}. To compare directly to the empirical approach used in Eq. 3.2, we use the expected collision selection number N_{col} which neglects the influence of gas-phase diffusion. Using this analysis, surface and bulk reactivity can be distinguished by using the N_{rxn} corresponding to the number of reaction events selected in the surface compartment or from the reactions selected in the bulk (comprising events selected in the RD compartment and inner bulk compartment but dominated by the RD compartment under our conditions). Uptake due to bulk and surface reactivity is shown in Fig. 3.6 following this approach, along with the sum total. Also included in Fig. 3.6A is a comparison to previous experimental measurements of ozone uptake in aqueous iodide droplets from droplet-train and flow tube experiments. In Fig. 3.6B we compare our results to model predictions of subsurface chemistry using the resistor-model formulation in the liquid-diffusion limited case.[61]

As shown in Fig. 3.6A, uptake for the pH 3 condition is mostly driven by bulk chemistry when iodide concentrations < 50 mM but dominated by surface chemistry when $[I^-] > 50$ mM. This result is expected, since the reaction-diffusion length decreases from ~14 nm to ~1 nm across this concentration range and the surface approaches its saturation concentration for I^-. With increasing $[I^-]$, the shape of the uptake curve suggests an approach to a limiting value of $\sim 10^{-2}$. This order of uptake has been similarly observed for O_3 uptake by concentrated aqueous iodide using a droplet-train apparatus[12] and a flow tube containing sub-micron iodide aerosol.[62,63] In the model, we find this upper-bound results from the reaction-rate limit at the surface, with only a small contribution from gas phase diffusive limitations. For the pH 12 shown in Fig. 3.6B, the uptake calculated from the bulk-only model is presented along with experiments (a comparison to the full model, including surface reaction, is provided in Appendix 3D). Below 500 mM, the uptake scales as $\sqrt{[\mathrm{I}^-]}$, as expected for liquid diffusion limited kinetics. For concentrated solutions, however, we observe a slight bend in the uptake dependence as the uptake begins to become limited by the solvation (or accommodation) mechanistic step, similarly observed in the resistor model when including accommodation and diffusive resistor terms. This observation demonstrates how chemistry in what might be considered strictly sub-surface or “bulk” regions are influenced by mass transport limitations occurring at the surface, whereas one may typically assume such phenomena to be decoupled.

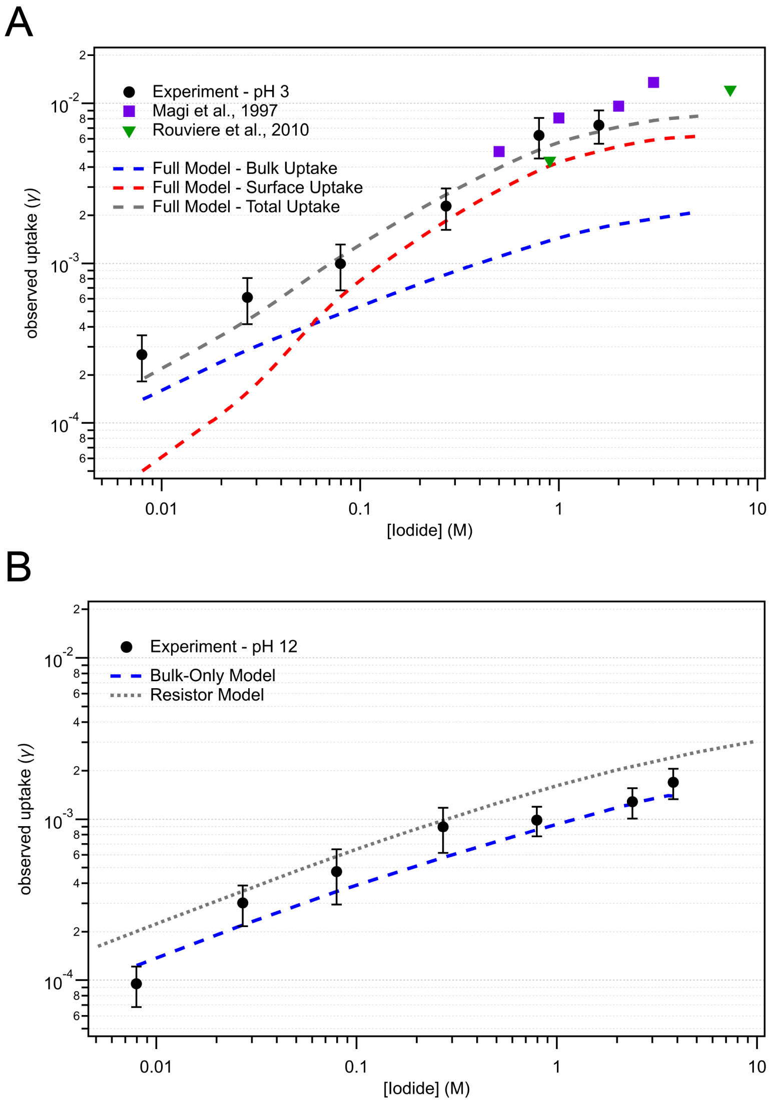

Fig. 3.6: (A) Uptake coefficients for droplet experiments and kinetic simulations at pH = 3. Error bars around individual data points represent the standard deviation above and below the mean calculated using three individual trials. The simulated uptake coefficient curves (dashed lines) show the bulk (blue) and surface (red) contributions to the total uptake (black). (B) Uptake coefficients from experiment and kinetic simulations at pH =12. Model results from the bulk-only model scenario are presented along with experiments and a comparison to the resistor model. A comparison to the full model scenario is provided in Appendix 3D.

3.6: Discussion

From the model comparison to the experimental results above, a number of features and implications warrant further discussion. The surface rate coefficient, found to agree with the experimental results at pH 3, is $k_{rxn} = 6\times10^{7}$ M^{-1} s^{-1} and approximately 20x smaller than the bulk reaction rate constant. The magnitude of this rate coefficient is coupled to the modelled surface concentration since the effective reactivity of the interface depends on both the iodide concentration and the rate coefficient. Therefore, a more accurate statement regarding surface and bulk reactivity at pH 3 is the surface reactive term $k_{rxn}^{srf} \cdot [\mathrm{I}^-_{(ads)}]$ is ~ 5% of the corresponding bulk reactive term $k_{rxn}^{bulk} \cdot [\mathrm{I}^-_{(bulk)}]$. The uncertainty in the true rate coefficient for the surface reaction is convoluted with any uncertainty in the modelled surface concentration.

Although a surface rate coefficient that is ~5% of the bulk value may seem unexpected, it is instructive to compare the liquid- and the gas-phase rate coefficients for additional context. One argument for the uniqueness of droplet chemistry is the potential for reaction coordinates at the gas-liquid interface to have energetic profiles that begin to resemble the profiles encountered in the gas phase.[64,65] Measurements of gas-phase $\mathrm{I}^- + \mathrm{O}_3$ kinetics within an ion trap[66] reported a forward rate coefficient of 6.6×10^{8} M^{-1} s^{-1}, a value that is slower than the corresponding aqueous value of 1×10^{9} M^{-1} s^{-1}.[51,52] Given the large difference in gas and liquid diffusivities, quantifying reactivity on a per-collision basis provides a cleaner comparison. In the gas phase, the reaction probability per encounter is reported to be $\varphi_g = 0.13\%$,[66] whereas for the corresponding liquid phase efficiency, we calculate $\varphi_l \sim 10\%$. The liquid phase estimate is computed by comparing the reported rate coefficient to an estimated diffusive encounter frequency in a bulk solution.[67] Given that the reactivity on a per-collision basis differs by almost two orders of magnitude in moving from the liquid to gas-phase, it is plausible that reactivity at the interface also decreases relative to the bulk, albeit not to the extent of the gas-phase. In addition to the $\mathrm{I}^- + \mathrm{O}_3$ reaction, measurements have been made on the O_3 oxidation of an iodide-water cluster $\mathrm{I(H_2O)}^-$, demonstrating significantly higher efficiency than the reaction with bare I^-.[68] While it is difficult to connect these observations directly to reactivity at air-water interface, these trends support our hypothesis that the reaction efficiency in solution likely tapers off across the air-water interface and approaches the gas-phase efficiency.

Uncertainty in $[\mathrm{I}^-_{(ads)}]$ in the kinetic model is complicated by the presence of chloride in the experiments, which has not been explicitly included at the interface. Furthermore, in order to maintain a constant droplet size under each experimental condition, the amount of Cl^- in each experiment varies with the overall iodide concentration, as shown in Tables 3B.1 and 3B.2. To investigate the ion-ion interactions between I^- and Cl^- at the interface, we perform molecular simulations of NaI/NaCl mixtures in water and analyze the density profiles and energetics at the air-water interface. Details of simulations and results from this analysis are included in Appendix 3C. Fig. 3C.2 provides density profiles for I^- and Cl^- in the simulated salt mixtures for a series of compositions where the I^-:Cl^- ion ratio is varied from 4:1 to 1:10. This ion ratio reports the total number of ions simulated within the water slab in entirety, not delineating between surface and bulk regions. The bulk concentrations of iodide in these simulations generally range between 50-70 mM, while the chloride concentrations are scaled between 1.2 M to 70 mM.

Chloride density profiles in Fig. 3C.2B show an unexpected enhancement of Cl^- near the air-water interface for concentrated conditions. With increasing surface $[\mathrm{Cl}^-]$, the surface density of I^- is suppressed as demonstrated in the density profile in Fig. 3C.2A and in the reduction of the solvation free energy profile in Fig. 3C.2C. However, even under the most concentrated chloride conditions, with ion ratio 1:10, the effective surface concentration of I^- is roughly half of what is predicted by the pure I^- case shown in Fig. 3.3B and Fig. 3.3C. As such, the Cl^- effect on the observed chemistry is likely to be relatively minor. Nevertheless, this effect could contribute to the shift between bulk and surface reaction mechanisms observed in Fig. 3.6A. These findings may be more relevant to natural systems where I^- is extremely dilute compared to Cl^-, as in the case of seawater. Since the I^-:Cl^- in seawater ~10^{-7}, we would expect iodide adsorption to the interface to be very energetically unfavorable. This concentration analysis, the discussion of gas and liquid rate coefficients above, along with a consideration of reaction-diffusion lengths, agrees well with the observation from Schneider et al.[69] that ozone-oxidation of simulated seawater proceeds through iodide oxidation in a subsurface layer on the order of ~10 μm.

Unlike the acidic case, the kinetic model suggests the surface reaction plays a very minor role (if any) in the oxidation kinetics at pH 12. This becomes evident when comparing model scenarios where the surface reaction is included vs. removed entirely. Similar to the discussion of the results at pH 3, we are limited in what specific surface information can be obtained from this observation. In this case, the surface reactivity term $k_{rxn}^{srf} \cdot [\mathrm{I}^-_{(ads)}]$ is completely masked by the corresponding reaction term in the bulk, so any degree of surface contribution cannot be identified. By inspecting the sensitivity of the surface rate coefficient in the model, we can only identify that the overall surface reactivity is equal or less than ~1% of the bulk term $k_{rxn}^{bulk} \cdot [\mathrm{I}^-_{(bulk)}]$.

As reported in recent work,[21] the apparent rate coefficient for the oxidation of iodide under basic conditions appears ~100x smaller than the measured reaction rate in acidic solution. We have hypothesized that this change in rate coefficient is related to the stability of the iodide-ozone adduct IOOO^- in solution and at the surface. However, given that the updated model can distinguish surface and sub-surface reactivity with higher fidelity, it is now apparent that the bulk rate likely remains constant from pH 3 to pH 12, with only the surface rate changing significantly. We propose two possible explanations for this observation. The first, that the IOOO^- intermediate is significantly stabilized at the interface under basic conditions, with the dissociation barrier to IO^- becoming larger in a partially solvated environment. Researchers observing the adduct BrOOO^- using XPS propose a similar hypothesis of surface-stabilization,[70] although under acidic conditions rather than basic. The second, and potentially more controversial, explanation is that the presence of ~ mM concentrations of OH^- in the alkaline solution greatly suppress $[\mathrm{I}^-]$ near the air water interface. While we believe this explanation is less likely than the first, given our assessment of ion-ion interactions at the interface at the pH 3, the presence of mM concentrations of OH^- could potentially alter the energetics of solvated I^- at the interface, an investigation of which is beyond the scope of the current work.

3.7: Conclusion

Surface reactivity is commonly invoked to explain unexpected kinetic observations in microdroplets due to the increasing surface-to-volume ratio of a spherical particle with decreasing radius. However, identifying the reactive contribution of the droplet surface compared to the bulk is notoriously challenging—not only due to the quantification of physical processes such as diffusion and adsorption at liquid interfaces, but also in the determination of reactant concentrations and reaction rates at the interface.[71] These quantities may be predicted to deviate dramatically from their bulk counterparts depending on the specifics of the system,[72,73] yet there are no generally recognized approaches for predicting how these quantities may change.

Here we have presented measurements of aqueous iodide oxidation by ozone in microdroplets while further developing a multiphase kinetic model for interpretation of the observed kinetics. This model accounts for the relative fraction of surface vs. bulk reactions occurring in the experiments presented using acidic and basic microdroplets for a range of iodide concentrations. Our comprehension of surface reactivity ultimately relies on a molecular picture of the air-water interface, constrained in the kinetic model by molecular simulations of $\mathrm{I}^-/\mathrm{Cl}^-$ and

O_3 at the interface and in solution. Both the static and dynamic physical properties of the simulated reactants are critical for designing an accurate representation of the interface, which in turn governs an effective representation of the bulk.

The conceptual framework for this multiphase mechanism has been refined to include both gas- and liquid-phase diffusive properties, a key description that allows us to identify unique surface processes. We find that the overall reactivity of $I^- + O_3$ at the interface is suppressed relative to the bulk and depends on the acidity of solution. Under acidic conditions, surface reaction is observed, but with an efficiency significantly lower than that of the bulk solution, and not dissimilar to the efficiency of the gas-phase reaction. Under basic conditions, no contribution of the surface is observed, which we ascribe to the unique stability of the adduct $IOOO^-$ at the interface. Experiment and theory, combined through application of the kinetic model, have suggested that the droplet surface is a unique chemical environment which requires future work to understand in full detail. Nevertheless, we have demonstrated that the current model framework and experimental approach provides a route to distinguishing reactive properties of the surface from the bulk, laying the groundwork for further investigations of more general chemical reactivity at gas-liquid interfaces.

3.8: Chapter 3 Appendix – Supplemental Information

Appendix 3A: Model reaction steps

Table 3A.1 shows a complete list of kinetic steps used to run the simulations in Kinetiscope.[33] Steps labeled as "S" are defined within the surface compartment only, whereas steps labeled "B" are defined in both the RD compartment and the inner-bulk compartment. Steps labeled as "D" provide the diffusion coefficient used to describe diffusion between adjacent compartments. These steps were developed in previous work,[21] and Table 3A.1 below largely reproduces the same model, with a few notable exceptions. Steps that deviate from the previous model are shown in bold in Table 3A.1. The main differences are the transport steps S1-S4 and reactive steps S11, S18-S21, B1 and B8-B11. The diffusive rate in S1 has been updated for the current droplet size and the approach described in the main text, Section 3.3.C.(ii). The adsorption rate in S2 and desolvation rate in S3 have changed to reflect an updated surface Henry's law of $H^{gs} = 4.97$. This updated Henry's law is slightly lower than the previously used H^{gs}, as we have averaged the O_3 density profile over the top 1 nm of solution instead of using the peak density value as done in Prophet et al.[21] Iodide solvation/desolvation coefficients also reflect the updated analysis using MD as presented in main text Section 3.3.C.(i).

The present reactive description uses a simplification of the previous reactive-intermediate description. Rather than simulate the adduct formation and decomposition steps explicitly, we use an effective rate for the process $I^- + O_3 \rightarrow IO^- + O_2$. The bulk rate coefficient for this reaction (step B1) is benchmarked to previous measurements,[51] $k_{rxn} = 1.2\times10^9$ M^{-1} s^{-1}. The surface rate coefficient for this reaction has been treated as an adjustable parameter in the model as discussed in the model framework section, Section 3.3.C.(iii), as well as in the discussion, Section 3.5. We find a single value that agrees with the experiment for the surface rate coefficient of $k_{rxn} = 6\times10^7$ M^{-1} s^{-1}, included as step S11. As explored in the main text, in addition to the model contained below, a "bulk-only" model has been run where we have simply removed step S11 from the simulation.

The updated chemical model also includes reactions between Cl^- and iodide-oxidation products HOI and I_2 which were not simulated with the previous model. These steps are highlighted in Table 3A.1. Steps included model the following reactions

$$\mathrm{HOI} + \mathrm{Cl}^- + \mathrm{H}^+ \underset{k_r}{\overset{k_f}{\rightleftarrows}} \mathrm{ICl} + \mathrm{H_2O},$$

$$\mathrm{ICl} + \mathrm{Cl}^- \underset{k_r}{\overset{k_f}{\rightleftarrows}} \mathrm{ICl_2^-},$$

$$\mathrm{I_2} + \mathrm{Cl}^- \underset{k_r}{\overset{k_f}{\rightleftarrows}} \mathrm{I_2Cl^-},$$

$$\mathrm{ICl} + \mathrm{I}^- \underset{k_r}{\overset{k_f}{\rightleftarrows}} \mathrm{I_2Cl^-}.$$

Forward and reverse rate coefficients for these reactions (steps S18-S21 and B8-B11 in Table 3A.1) are obtained from previous measurements.[74,75] This set of reactions and rate coefficients were recently employed in a study of the iodine flux off of simulated seawater during oxidation by ozone.[76] To avoid explicitly simulating Cl^- in the model, we assume $[Cl^-]$ is fixed for each experiment at the values found in Tables 3B.1 and 3B.2 and calculate a pseudo-first order rate coefficient from the bimolecular coefficients reported in Table 3A.1.

Lastly, values for evaporation coefficients also differ from the previous model. The same approach has been used where the Hertz-Knudsen flux is first calculated, then expressed as a first-order rate using a characteristic length scale for evaporation.[21,42,77] While previous descriptions have used the droplet radius (or more accurately, R/3) as this representative length scale, here we use an evaporative length scale of $\delta = 1$ nm, the thickness of the interface as defined in the model. The first-order evaporation rate coefficient for a species *X* evaporating from the surface with corresponding henry's law H_x (units of molecule m^{-3} Pa^{-1}) is therefore defined as:

$$k_{X\text{-evap}}\ (\mathrm{s}^{-1}) = \frac{1}{\delta} \cdot \frac{\alpha_e \cdot \left(\frac{1}{\mathrm{H}_x}\right)}{\sqrt{2\pi m_x k_B T}},$$

where α_e is the evaporation coefficient, here assume to be unity, and m_x the mass of species *X*. Lastly, as introduced in Section 3.3.C.(iv), we include the potential chemistry of Cl^- in our updated model, listed as steps S18-S21 and B8-B11, as well as the evaporation of ICl listed as S24.

Table 3A.1: Elementary kinetic steps used to simulate the model in Kinetiscope©. Steps defined in the surface compartment are labeled S, diffusion coefficients for transfer between adjacent compartments are labeled D, and steps defined in both the reaction-diffusion and inner-bulk compartments are labeled B.

#	**Step**	**Rate coefficient**	**Reference**

S1	$\mathbf{O_{3(g)}} \underset{k_{diff}}{\overset{k_{diff}}{\rightleftarrows}} \mathbf{O_{3(diff)}}$	$\boldsymbol{k_{diff} = 1.06 \times 10^{9}\ s^{-1}}$	see Section 3.3.C.(ii)
S2	$\mathbf{O_{3(diff)} + site_{O_3}} \underset{k_{des}}{\overset{k_{ads}}{\rightleftarrows}} \mathbf{O_{3(ads)}}$	$\boldsymbol{k_{ads} = 1.77 \times 10^{-11}\ cm^3\ molec.^{-1}\ s^{-1}}$ $\boldsymbol{k_{des} = 1.93 \times 10^{10}\ s^{-1}}$	21
S3	$\mathbf{O_{3(ads)}} \underset{k_{desolv}}{\overset{k_{solv}}{\rightleftarrows}} \mathbf{O_{3(b)} + site_{O_3}}$	$\boldsymbol{k_{solv} = 1.9 \times 10^{8}\ s^{-1}}$ $\boldsymbol{k_{desolv} = 1.2 \times 10^{-12}\ cm^3\ molec.^{-1}\ s^{-1}}$	21
S4	$\mathbf{I^-_{(ads)}} \underset{k_{desolv}}{\overset{k_{solv}}{\rightleftarrows}} \mathbf{I^-_{(b)} + site_I}$	$\boldsymbol{k_{solv} = 10^{3}\ s^{-1}}$ $\boldsymbol{k_{desolv} = 1.66 \times 10^{-18}\ cm^3\ molec.^{-1}\ s^{-1}}$	16,78
S5	$IO^-_{(ads)} \underset{k_{desolv}}{\overset{k_{solv}}{\rightleftarrows}} IO^-_{(b)} + site_I$	$k_{solv} = 1 \times 10^{3}\ s^{-1}$ $k_{desolv} = 1.66 \times 10^{-18}\ cm^3 \cdot molec.^{-1} \cdot s^{-1}$	16,78
S6	$IO^-_{2(ads)} \underset{k_{desolv}}{\overset{k_{solv}}{\rightleftarrows}} IO^-_{2(b)} + site_I$	$k_{solv} = 1 \times 10^{3}\ s^{-1}$ $k_{desolv} = 1.66 \times 10^{-18}\ cm^3 \cdot molec.^{-1} \cdot s^{-1}$	16,78
S8	$I_{2(ads)} \underset{k_{desolv}}{\overset{k_{solv}}{\rightleftarrows}} I_{2(b)} + site_I$	$k_{solv} = 1 \times 10^{3}\ s^{-1}$ $k_{desolv} = 1.66 \times 10^{-18}\ cm^3 \cdot molec.^{-1} \cdot s^{-1}$	16,78
S9	$HOI_{(ads)} \underset{k_{desolv}}{\overset{k_{solv}}{\rightleftarrows}} HOI_{(b)} + site_I$	$k_{solv} = 1 \times 10^{3}\ s^{-1}$ $k_{desolv} = 1.66 \times 10^{-18}\ cm^3 \cdot molec.^{-1} \cdot s^{-1}$	16,78
S10	$I^-_{3(ads)} \underset{k_{desolv}}{\overset{k_{solv}}{\rightleftarrows}} I^-_{3(b)} + site_I$	$k_{solv} = 1 \times 10^{3}\ s^{-1}$ $k_{desolv} = 1.66 \times 10^{-18}\ cm^3 \cdot molec.^{-1} \cdot s^{-1}$	16,78
S11	$\mathbf{I^-_{(ads)} + O_{3(ads)}} \xrightarrow{k_f} \mathbf{IO^-_{(ads)} + site_{O_3}}$	$\boldsymbol{k_f = 1 \times 10^{-13}\ cm^3 \cdot molec.^{-1} \cdot s^{-1}}$	see sections 3.3.C.(iii) and 3.5
S12	$IO^-_{(ads)} + O_{3(ads)} \xrightarrow{k_f} IO^-_{2(ads)} + site_{O_3}$	$k_f = 1.66 \times 10^{-11}\ cm^3 \cdot molec.^{-1} \cdot s^{-1}$	66
S13	$IO^-_{2(ads)} + O_{3(ads)} \xrightarrow{k_f} IO^-_{3(blk)} + site_I + site_{O_3}$	$k_f = 1.66 \times 10^{-11}\ cm^3 \cdot molec.^{-1} \cdot s^{-1}$	66
S14	$IO^-_{(ads)} + H^+ \underset{k_r}{\overset{k_f}{\rightleftarrows}} HOI_{(ads)}$	$k_f = 1.66 \times 10^{-10}\ cm^3 \cdot molec.^{-1} \cdot s^{-1}$ * $k_r = 1.58\ s^{-1}$	79,80
S15	$HOI_{(ads)} + I^-_{(ads)} \underset{k_r}{\overset{k_f}{\rightleftarrows}} I_2OH^-_{(ads)} + site_I$	$k_f = 6.64 \times 10^{-17}\ cm^3 \cdot molec.^{-1} \cdot s^{-1}$ $k_r = 1.34 \times 10^{2}\ s^{-1}$	81
S16	$I_2OH^-_{(ads)} + H^+ \underset{k_r}{\overset{k_f}{\rightleftarrows}} I_{2(ads)}$	$k_f = 3.32 \times 10^{-11}\ cm^3 \cdot molec.^{-1} \cdot s^{-1}$ * $k_r = 3.2\ s^{-1}$	81
S17	$HOI_{(ads)} + I^-_{(ads)} \underset{k_r}{\overset{k_f}{\rightleftarrows}} I_{2(ads)} + OH^- + site_I$	$k_f = 3.5 \times 10^{-18}\ cm^3 \cdot molec.^{-1} \cdot s^{-1}$ $k_r = 1.16 \times 10^{-16}\ cm^3 \cdot molec.^{-1} \cdot s^{-1}$ *	82
S18	$\mathbf{HOI_{(ads)} + Cl^- + H^+} \underset{k_r}{\overset{k_f}{\rightleftarrows}} \mathbf{ICl_{(ads)}}$	$\boldsymbol{k_f = 8 \times 10^{-32}\ cm^6\ molec.^{-2}\ s^{-1}}$ *‡ $\boldsymbol{k_r = 2.4 \times 10^{6}\ s^{-1}}$	74
S19	$\mathbf{ICl_{(ads)} + Cl^-} \underset{k_r}{\overset{k_f}{\rightleftarrows}} \mathbf{ICl^-_{2(ads)}}$	$\boldsymbol{k_f = 1.66 \times 10^{-13}\ cm^3\ molec.^{-1}\ s^{-1}}$ ‡ $\boldsymbol{k_r = 6 \times 10^{5}\ s^{-1}}$	75
S20	$\mathbf{I_{2(ads)} + Cl^-} \underset{k_r}{\overset{k_f}{\rightleftarrows}} \mathbf{I_2Cl^-_{(ads)}}$	$\boldsymbol{k_f = 1.38 \times 10^{-16}\ cm^3\ molec.^{-1}\ s^{-1}}$ ‡ $\boldsymbol{k_r = 5 \times 10^{4}\ s^{-1}}$	75
S21	$\mathbf{I^-_{(ads)} + ICl_{(ads)}} \underset{k_r}{\overset{k_f}{\rightleftarrows}} \mathbf{I_2Cl^-_{(ads)}}$	$\boldsymbol{k_f = 1.83 \times 10^{-12}\ cm^3\ molec.^{-1}\ s^{-1}}$ ‡ $\boldsymbol{k_r = 1.5\ s^{-1}}$	75
S22	$I_{2(ads)} + I^-_{(ads)} \leftrightarrow I^-_{3(ads)} + site_I$	$k_f = 1 \times 10^{-11}\ cm^3 \cdot molec.^{-1} \cdot s^{-1}$ ¶ $k_r = 8.64 \times 10^{6}\ s^{-1}$	83
S23	$I_{2(ads)} \xrightarrow{k_{evap}} I_{2(g)} + site_I$	$k_{evap} = 5.32 \times 10^{8}\ s^{-1}$ #	84
S24	$\mathbf{ICl_{(ads)}} \xrightarrow{k_{evap}} \mathbf{ICl_{(g)} + site_I}$	$\boldsymbol{k_{evap} = 1.81 \times 10^{7}\ s^{-1}}$ #	85
S25	$HOI_{(ads)} \xrightarrow{k_{evap}} HOI_{(g)} + site_I$	$k_{evap} = 5.16 \times 10^{6}\ s^{-1}$ #	86

D1	$I^-_{(b)}$	$D = 1.53 \times 10^{-5}\ cm^2 \cdot s^{-1}$ ¶	87
D2	$IO^-_{(b)}$	$D = 1.53 \times 10^{-5}\ cm^2 \cdot s^{-1}$ †¶	87
D3	$IO^-_{2(b)}$	$D = 1.53 \times 10^{-5} cm^2 \cdot s^{-1}$ †¶	87
D4	$IO^-_{3(b)}$	$D = 1.53 \times 10^{-5}\ cm^2 \cdot s^{-1}$ †	87
D5	$I_2OH^-_{(b)}$	$D = 1.53 \times 10^{-5}\ cm^2 \cdot s^{-1}$ †	87
D6	$I_2Cl^-_{(b)}$	$D = 1.53 \times 10^{-5}\ cm^2 \cdot s^{-1}$ †	87
D7	$Cl_2I^-_{(b)}$	$D = 1.53 \times 10^{-5}\ cm^2 \cdot s^{-1}$ †	87
D6	$I^-_{3(b)}$	$D = 1.07 \times 10^{-5}\ cm^2 \cdot s^{-1}$	88
D7	$I_{2(b)}$	$D = 1.15 \times 10^{-5}\ cm^2 \cdot s^{-1}$	89
D8	$HOI_{(b)}$	$D = 1.15 \times 10^{-5}\ cm^2 \cdot s^{-1}$ †	89
D9	$ICl_{(b)}$	$D = 1.15 \times 10^{-5}\ cm^2 \cdot s^{-1}$ †	89
D9	$O_{3(b)}$	$D = 1.76 \times 10^{-5}\ cm^2 \cdot s^{-1}$	90
B1	$\mathbf{I^-_{(ads)} + O_{3(ads)} \xrightarrow{k_f} IO^-_{(ads)} + site_{O_3}}$	$\boldsymbol{k_f = 2 \times 10^{-12}\ cm^3 \cdot molec.^{-1} \cdot s^{-1}}$	51
B2	$IO^-_{(b)} + O_{3(b)} \xrightarrow{k_f} IO^-_{2(b)}$	$k_f = 2.65 \times 10^{-15}\ cm^3 \cdot molec.^{-1} \cdot s^{-1}$	80
B3	$IO^-_{2(b)} + O_{3(b)} \xrightarrow{k_f} IO^-_{3(b)}$	$k_f = 2.65 \times 10^{-15}\ cm^3 \cdot molec.^{-1} \cdot s^{-1}$	80
B4	$IO^-_{(b)} + H^+ \xrightleftharpoons[k_r]{k_f} HOI_{(b)}$	$k_f = 1.66 \times 10^{-10}\ cm^3 \cdot molec.^{-1} \cdot s^{-1}$ * $k_r = 1.58\ s^{-1}$	79,80
B5	$HOI_{(b)} + I^-_{(b)} \xrightleftharpoons[k_r]{k_f} I_2OH^-_{(b)}$	$k_f = 6.64 \times 10^{-17}\ cm^3 \cdot molec.^{-1} \cdot s^{-1}$ $k_r = 1.34 \times 10^2\ s^{-1}$	81
B6	$I_2OH^-_{(b)} + H^+ \xrightleftharpoons[k_r]{k_f} I_{2(b)}$	$k_f = 3.32 \times 10^{-11}\ cm^3 \cdot molec.^{-1} \cdot s^{-1}$ * $k_r = 3.2\ s^{-1}$	81
B7	$HOI_{(b)} + I^-_{(b)} \xrightleftharpoons[k_r]{k_f} I_{2(b)} + OH^-$	$k_f = 3.5 \times 10^{-18}\ cm^3 \cdot molec.^{-1} \cdot s^{-1}$ $k_r = 1.16 \times 10^{-16}\ s^{-1}$ *	82
B8	$\mathbf{HOI_{(blk)} + Cl^- + H^+ \xrightleftharpoons[k_r]{k_f} ICl_{(blk)}}$	$\boldsymbol{k_f = 8 \times 10^{-32}\ cm^6\ molec.^{-2}\ s^{-1}}$ *‡ $\boldsymbol{k_r = 2.4 \times 10^6\ s^{-1}}$	74
B9	$\mathbf{ICl_{(blk)} + Cl^- \xrightleftharpoons[k_r]{k_f} ICl^-_{2(blk)}}$	$\boldsymbol{k_f = 1.66 \times 10^{-13}\ cm^3\ molec.^{-1}\ s^{-1}}$ ‡ $\boldsymbol{k_r = 6 \times 10^5\ s^{-1}}$	75
B10	$\mathbf{I_{2(blk)} + Cl^- \xrightleftharpoons[k_r]{k_f} I_2Cl^-_{(blk)}}$	$\boldsymbol{k_f = 1.38 \times 10^{-16}\ cm^3\ molec.^{-1}\ s^{-1}}$ ‡ $\boldsymbol{k_r = 5 \times 10^4\ s^{-1}}$	75
B11	$\mathbf{I^-_{(blk)} + ICl_{(blk)} \xrightleftharpoons[k_r]{k_f} I_2Cl^-_{(blk)}}$	$\boldsymbol{k_f = 1.83 \times 10^{-12}\ cm^3\ molec.^{-1}\ s^{-1}}$ ‡ $\boldsymbol{k_r = 1.5\ s^{-1}}$	75
B12	$I_{2(b)} + I^-_{(b)} \xrightleftharpoons[k_r]{k_f} I^-_{3(b)}$	$k_f = 1 \times 10^{-11}\ cm^3 \cdot molec.^{-1} \cdot s^{-1}$ ¶ $k_r = 8.64 \times 10^6\ s^{-1}$	83

* Simulated H^+ or OH^- are not explicitly included in the model, but rather, a pseudo-order rate condition is used by multiplying the reported rate coefficient with $[H^+]$ or $[OH^-]$ directly.

‡ Similar to the simulation of pH, Cl^- is not included explicitly, and initial $[Cl^-]$ for each experiment is used to calculate each rate depending on $[Cl^-]$.

¶ These steps—either chemical or diffusional—involve a rapid equilibrium which can inhibit the stochastic simulation when run in concert. For many simulations, the corresponding constants shown in the table are decreased by ~100-1000 in order to allow for reasonable simulation times. However, we have verified that the model results have no observable sensitivity to these coefficients in the range we can observe.

[†] Diffusion coefficients for these species are estimated using the *D* for I^- for ions, and the *D* for I_2 for neutrals.

[#] Evaporation steps have also been defined in surface compartment as first order in the "bulk" species rather than adsorbed. This effectively allows I_2, for example, to evaporate from either the adsorbed or solvated state. While the model should technically only allow for adsorbed volatiles to evaporate, we define evaporation from the entire surface compartment to avoid potential coupling of evaporation rates with the solvation/desolvation rates of these volatiles, which we have largely treated as unknowns.

Appendix 3B: Experimental

Additional information on the experimental results and conditions are provided in this section. In Fig. 3B.1, an example spectrum shows Mie scattering intensity vs. collection angle for an aqueous iodide droplet at pH 3. By calibrating the scattering response using polystyrene beads of radii 12.5 μm and 5 μm, microdroplet size in the experiments can be determined by analyzing the angular spacing between scattering peaks referenced to a library of simulated peak positions, as outlined in previous literature.[27] Droplet sizes are monitored throughout the experiments, where we observed droplet radii are r = 17 ± 1 μm under our conditions.

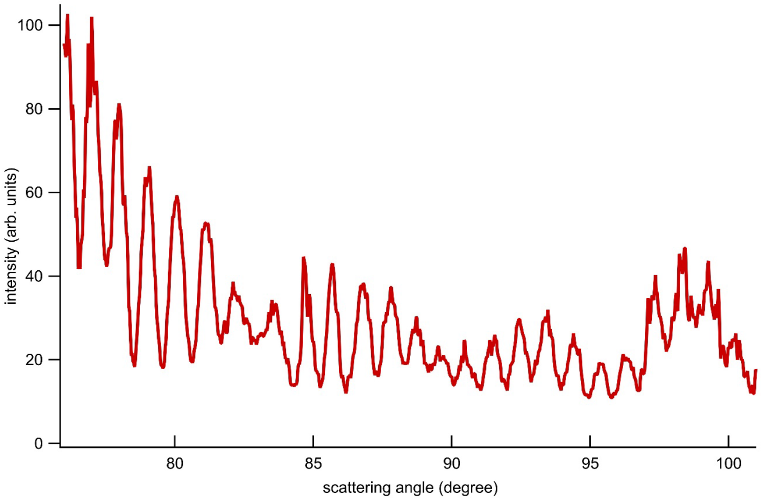

Fig. 3B.1: Scattering intensity vs. collection angle for Mie scattering from a 17 μm radius droplet composed of aqueous sodium iodide, sodium chloride, and citric acid. Peaks in the intensity response are located using a peak-finding algorithm, and the peak spacing referenced to a library of simulated peaks to find a best fit to droplet size.

Mass spectra showing droplet composition before and after reaction are shown in Fig. 3B.2. Spectra for microdroplets at pH 3 are in panel (A), where both an unreacted and a reacted droplet has been analyzed. An unreacted and reacted droplet at pH 12 is shown in panel (B). Common cluster peaks due to I^-, Cl^-, and Na^+ are labeled, as well as the citrate buffer signal for pH 3. Glycolic acid is also identified as a persistent background peak, likely present due to low levels of contamination in the methanol solvent and tubing used in the OPSI assembly. In the pH 3 case, iodide decay is observed comparing the reacted/unreacted spectra, with the relative citric acid (CA) signal slightly increasing with loss of iodide signal. In the pH 12 case, I^- decay is also observed, along with appearance of the soluble product IO_3^-. This product is only generated in any significant amount when pH > 10.8, the pKa of IO^-. At pH 3, all potential products (HOI, I_2, ICl) are volatile, so no soluble products are observed in the droplet analysis.

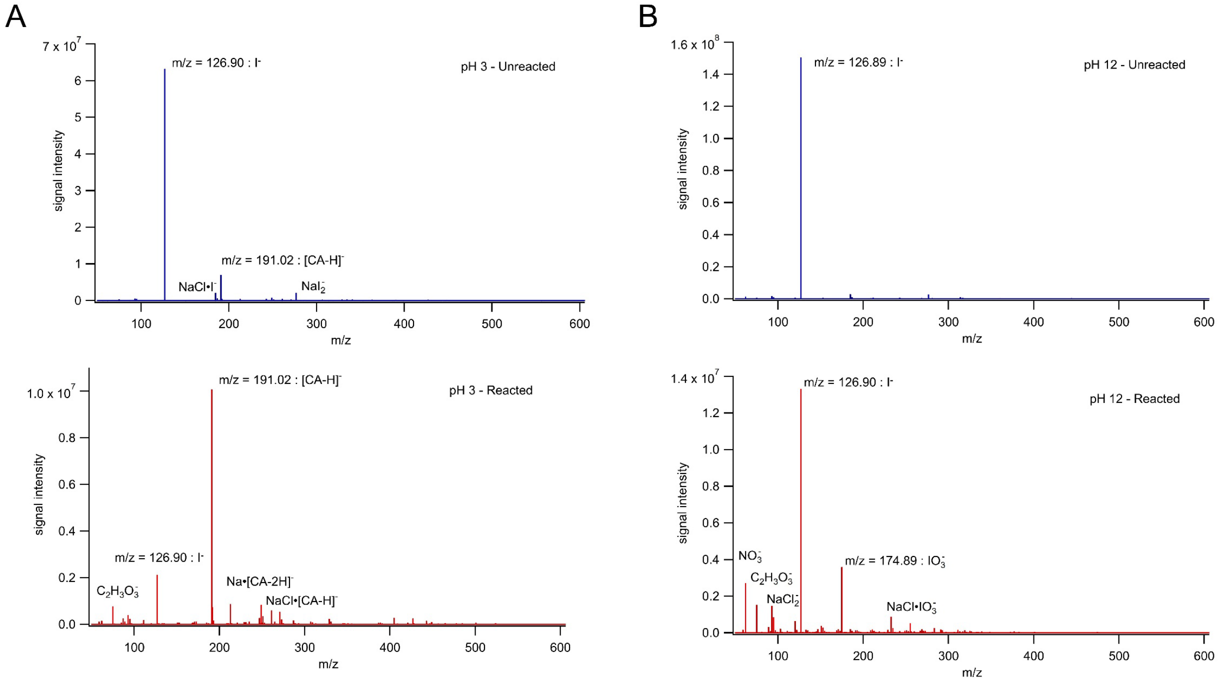

Fig. 3B.2: Mass spectra for unreacted and reacted microdroplets containing NaI at pH 3 in column (A) and pH 12 in column (B). Reacted spectra give the resulting spectrum when <5% of the original iodide signal is present after ozone oxidation. Major peaks are labeled including the citric acid buffer (CA) at pH 3, and the product iodate (IO_3^-) at pH 12. Common background peaks and clusters are indicated.

As referenced in the main text, the initial water activity in each solution is $a_w = 0.96 \pm 0.01$ in order to analyze the same droplet size while changing solution composition. To maintain this activity with decreasing [NaI], it is necessary to increase the [NaCl]. Tables 3B.1 and 3B.2 below provide the concentrations of sodium iodide and sodium chloride used for each experiment. For the pH 3 condition, 300 mM of citric acid was included to buffer the pH, leading to different [I] and [Cl] needed for the acidic and basic experiments.

Table 3B.1: Sodium iodide and sodium chloride droplet concentrations for experiments shown in Figs. 3.4 and 3.6A conducted at pH 3. For all experiments, 300 mM of citric acid was also used to buffer the pH during iodide oxidation. The [I^-] / [Cl^-] ratio is also provided to show how this quantity changes for different experimental conditions.

Salt Concentrations and I/Cl ratio of Initial Droplet Solution for pH 3 Experiments		
[NaI]	**[NaCl]**	**[I]/[Cl]**
8 mM	3.18 M	2.5×10^{-3}
27 mM	3.18 M	8.5×10^{-3}
80 mM	2.52 M	3.1×10^{-2}
270 mM	2.32 M	1.2×10^{-1}
800 mM	1.88 M	4.2×10^{-1}
1.6 M	817 mM	1.9

Table 3B.2: Sodium iodide and sodium chloride droplet concentrations for experiments shown in Figs. 3.5 and 3.6B conducted pH 12. The [I^-] / [Cl^-] ratio is also provided to show how this quantity changes for different experimental conditions.

Salt Concentrations and I/Cl ratio of Initial Droplet Solution for pH 12 Experiments		
[NaI]	**[NaCl]**	**[I]/[Cl]**
8 mM	4.25 M	1.9×10^{-3}
27 mM	4.23 M	6.4×10^{-3}
80 mM	4.17 M	1.9×10^{-2}
270 mM	3.95 M	6.8×10^{-2}
800 mM	3.04 M	2.6×10^{-1}
2.4 M	1.35 M	1.76
3.8 M	0 M	N.A.

Appendix 3C: Solution composition: simulated ion-ion effects at the air-water interface

In Section 3.4, Fig. 3.4B shows iodide density profiles obtained by molecular simulations at the air-water interface. The degree of effective surface enhancement decreases with increasing bulk concentration. This result can instead be observed by analyzing the relative free energy change for moving the I^- close to the interface. Fig. 3C.1 provides free energy profiles for the same density conditions provided in Fig. 3.4. In the free energy profiles, the general trend can be observed where the change in free energy at the interface decreases (less negative) with increasing overall concentration. This results from repulsion between I^- ions as the interface becomes more crowded. However, while movement to the interface becomes more favorable under dilute conditions, a significant barrier becomes apparent in the sub-surface region, indicating the role of Na^+ ordering below iodide in the simulations.

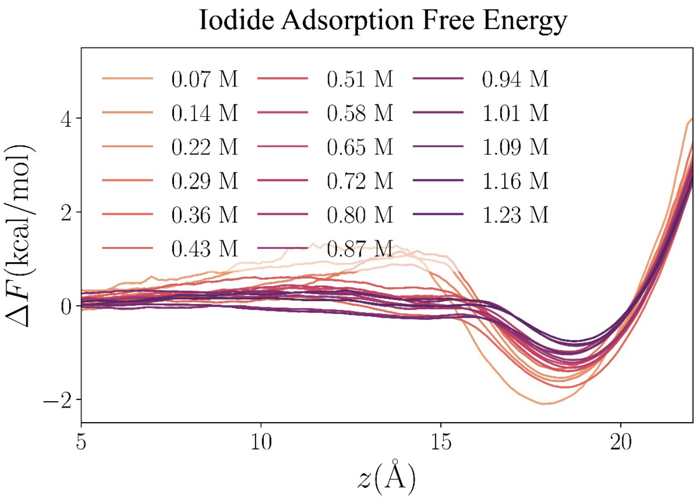

Fig. 3C.1: Free energy profiles for I^- obtained from molecular simulations, showing the change in free energy for the I^- ion across the simulated water slab referenced to the center.

In a similar manner, we have conducted simulations for mixtures of NaI and NaCl to explore potential effects of the changing I^-:Cl^- in the experiments. Shown in Tables 3B.1 and 3B.2, as $[I^-]_0$ decreases for the different initial conditions, $[Cl^-]_0$ ranges from ~500 mM to 1M. Therefore, experiments with $[I^-]_0$ concentrations in the mM range contain chloride that is ~100x more concentrated than iodide. To determine what, if any, effect the concentrated Cl^- ion has on the iodide oxidation kinetics, we simulated solution mixtures with different iodide-to-chloride ratios to investigate the interfacial structure of the ion density profiles. Panels (A) and (B) in Fig. 3C.2 show simulated iodide and chloride density profiles for iodide-to-chloride concentration ratios ranging from 4:1 to 1:10. Panel (C) in Fig. 3C.2 shows the corresponding change in free energy for I^- across the simulated water slab for the series of changing I^-:Cl^-. Panel (D) shows a similar result for Cl^-, but for changing $[Cl^-]$ with constant $[I^-]$ ~ 50 mM.

A stark difference in the density profiles is observed for the range of I^-:Cl^- ratios investigated. For the larger I^-:Cl^- cases shown in Fig. 3C.2A the I^- density profile generally agrees with the iodide-only case shown in Fig. 3.5, with a large density peak at the interface and a maximum value that is ~5-10x the bulk density value. As I^-:Cl^- decreases, the sharp enhancement of interfacial iodide soon vanishes and resembles the bulk density, even appearing to become partially depleted at the interface. Simultaneously, as shown in panel (B), Cl^- becomes more enhanced at the interface for lower I^-:Cl^-, effectively displacing iodide from the interface. While the structure of the density profiles clearly contain finer details, our analysis aims to describe the broader trends of surface and bulk concentrations.

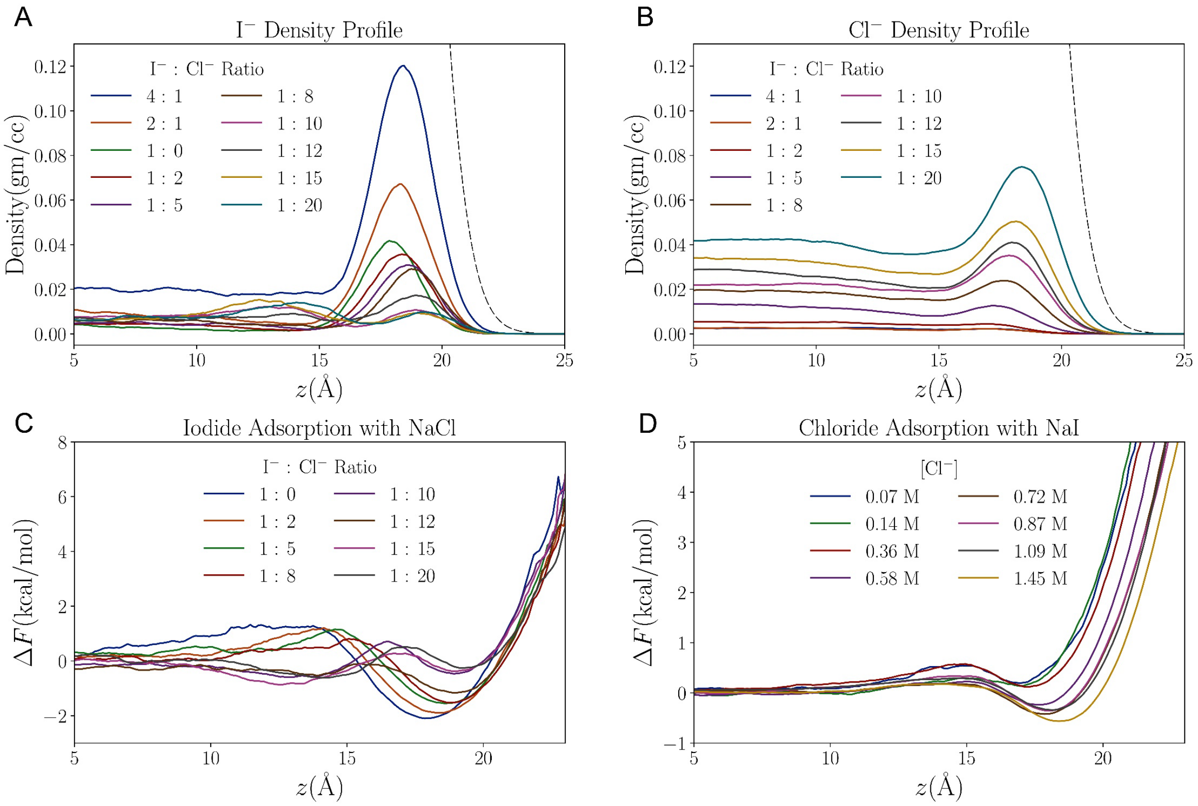

Fig. 3C.2: (A-B) Density profiles of I^- and Cl^- for varying mixture conditions. (C) Corresponding change in free energy profile of iodide at the air-water interface for changing I^-:Cl^-. (D) Free energy profile for Cl^- in solution, with profiles indicating increasing [Cl^-] with an approximately constant [I^-] ~ 50 mM.

Analyzing the trends in Fig. 3C.2C, the higher I^-:Cl^- simulations show a typical surficial iodide free energy minimum ~4 kJ/mol and agrees with the stabilization observed in the pure sodium iodide case. As the I^-:Cl^- gets small with increasing [Cl^-], however, the stabilization of I^- near the interface is suppressed, with this behavior trending towards destabilization of iodide at the interface with decreasing I^-:Cl^-. We propose that this interaction between ions at the interface, through the effective displacement of dilute I^- by concentrated Cl^-, may partially inhibit the surface reaction for conditions where [I^-]$_0$ < 100 mM. Overall, while these observations help us determine the degree to which like-charged ions interact near the interface, the effective concentrations of I^- at the interface for the most concentration Cl^- cases are still within ~ 2x of the pure iodide case, suggesting that the Cl^-/I^- interaction likely doesn't explain the transition from surface- to bulk-dominated reaction kinetics.

Appendix 3D: Model analysis and sensitivity

Although the model developed contains numerous parameters, the vast majority of these coefficients are referenced to literature values and previous measurements referred to in Table 3A.1. As discussed in length, the surface rate coefficient is treated instead as an adjustable parameter and found to agree with results at pH 3 using k_{rxn} = 6×10^{7} M^{-1} s^{-1}. Therefore, it is instructive to compare results from the full kinetic model with the "bulk-only" model found to agree with experiments at pH 12. In Fig. 3D.1, we include this comparison at pH 12 with uptake coefficients for (A) the full kinetic model (including surface and bulk contributions as defined in Section 3.5) and (B) for the bulk-only model, reproduced from Fig. 3.6B. As discussed in the main text, we observe the predicted kinetics from the full model scenario to systematically overestimate the observed kinetics, whereas the bulk-only model scenario comes into close agreement. This illustration is mainly to give a direct example of how the surface reaction changes the overall kinetics for a solution at a constant pH.

Other considerations of parameter sensitivity largely mirror our previous work[21] where we provide an example of the sensitivity of solvation/desolvation rates of ions in solution. This same general approach is used in the current model when absolute rates in an equilibrium expression cannot be obtained from the literature. We similarly observe no sensitivity in the solvation/desolvation rates for the condition $k_{solv} > 10^3$ s^{-1}. As noted in Table 3A.1, in some cases of fast equilibria or diffusion across short distances, smaller absolute rates for forward/reverse steps are decreased to avoid overwhelming the stochastic approach with multiple rapid equilibria. In such cases, we ensure that no model sensitivity exists in the absolute process rates, but only the equilibrium values established in the model.

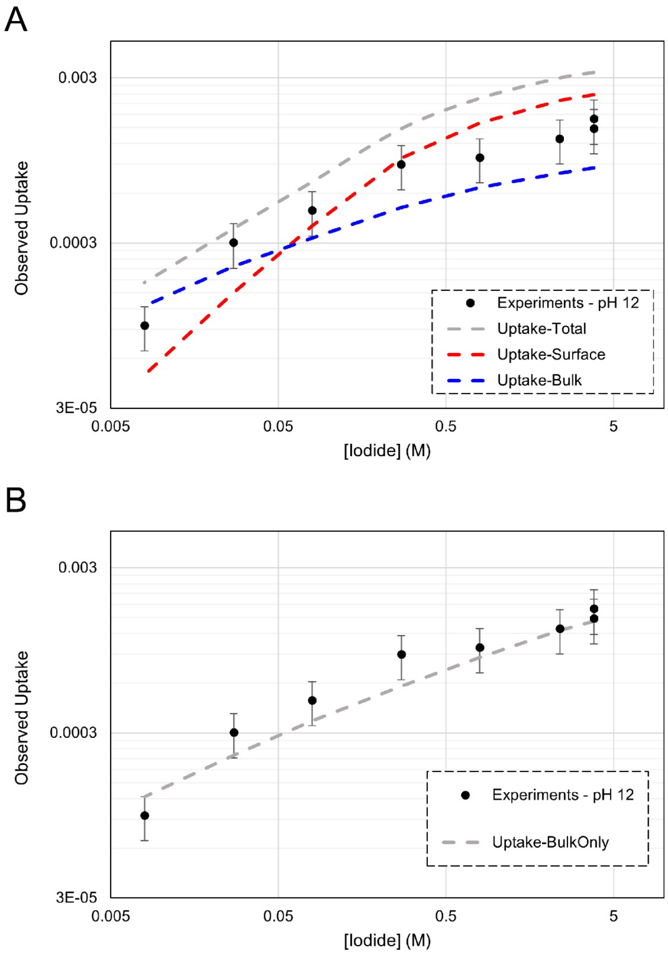

Fig. 3D.1: (A) Uptake coefficients from experiments at pH 12, along with full kinetic model predictions showing surface and bulk contributions. (B) Results reproduced from Fig. 3.6B showing a comparison to bulk-only model.

3.9: References

(1) Saiz-Lopez, A.; Fernandez, R. P.; Ordóñez, C.; Kinnison, D. E.; Gómez Martín, J. C.; Lamarque, J.-F.; Tilmes, S. Iodine Chemistry in the Troposphere and Its Effect on Ozone. *Atmospheric Chem. Phys.* **2014**, *14* (23), 13119–13143. https://doi.org/10.5194/acp-14-13119-2014.

(2) Stone, D.; Sherwen, T.; Evans, M. J.; Vaughan, S.; Ingham, T.; Whalley, L. K.; Edwards, P. M.; Read, K. A.; Lee, J. D.; Moller, S. J.; Carpenter, L. J.; Lewis, A. C.; Heard, D. E. Impacts of Bromine and Iodine Chemistry on Tropospheric OH and HO_2: Comparing Observations with Box and Global Model Perspectives. *Atmospheric Chem. Phys.* **2018**, *18* (5), 3541–3561. https://doi.org/10.5194/acp-18-3541-2018.

(3) Karagodin-Doyennel, A.; Rozanov, E.; Sukhodolov, T.; Egorova, T.; Saiz-Lopez, A.; Cuevas, C. A.; Fernandez, R. P.; Sherwen, T.; Volkamer, R.; Koenig, T. K.; Giroud, T.; Peter, T. Iodine Chemistry in the Chemistry–Climate Model SOCOL-AERv2-I. *Geosci. Model Dev.* **2021**, *14* (10), 6623–6645. https://doi.org/10.5194/gmd-14-6623-2021.

(4) Sherwen, T.; Evans, M. J.; Carpenter, L. J.; Andrews, S. J.; Lidster, R. T.; Dix, B.; Koenig, T. K.; Sinreich, R.; Ortega, I.; Volkamer, R.; Saiz-Lopez, A.; Prados-Roman, C.; Mahajan, A. S.; Ordóñez, C. Iodine's Impact on Tropospheric Oxidants: A Global Model Study in GEOS-Chem. *Atmospheric Chem. Phys.* **2016**, *16* (2), 1161–1186. https://doi.org/10.5194/acp-16-1161-2016.

(5) He, X.-C.; Simon, M.; Iyer, S.; Xie, H.-B.; Rörup, B.; Shen, J.; Finkenzeller, H.; Stolzenburg, D.; Zhang, R.; Baccarini, A.; Tham, Y. J.; Wang, M.; Amanatidis, S.; Piedehierro, A. A.; Amorim, A.; Baalbaki, R.; Brasseur, Z.; Caudillo, L.; Chu, B.; Dada, L.; Duplissy, J.; El Haddad, I.; Flagan, R. C.; Granzin, M.; Hansel, A.; Heinritzi, M.; Hofbauer, V.; Jokinen, T.; Kemppainen, D.; Kong, W.; Krechmer, J.; Kürten, A.; Lamkaddam, H.; Lopez, B.; Ma, F.; Mahfouz, N. G. A.; Makhmutov, V.; Manninen, H. E.; Marie, G.; Marten, R.; Massabò, D.; Mauldin, R. L.; Mentler, B.; Onnela, A.; Petäjä, T.; Pfeifer, J.; Philippov, M.; Ranjithkumar, A.; Rissanen, M. P.; Schobesberger, S.; Scholz, W.; Schulze, B.; Surdu, M.; Thakur, R. C.; Tomé, A.; Wagner, A. C.; Wang, D.; Wang, Y.; Weber, S. K.; Welti, A.; Winkler, P. M.; Zauner-Wieczorek, M.; Baltensperger, U.; Curtius, J.; Kurtén, T.; Worsnop, D. R.; Volkamer, R.; Lehtipalo, K.; Kirkby, J.; Donahue, N. M.; Sipilä, M.; Kulmala, M. Iodine Oxoacids Enhance Nucleation of Sulfuric Acid Particles in the Atmosphere. *Science* **2023**, *382* (6676), 1308–1314. https://doi.org/10.1126/science.adh2526.

(6) Sipilä, M.; Sarnela, N.; Jokinen, T.; Henschel, H.; Junninen, H.; Kontkanen, J.; Richters, S.; Kangasluoma, J.; Franchin, A.; Peräkylä, O.; Rissanen, M. P.; Ehn, M.; Vehkamäki, H.; Kurten, T.; Berndt, T.; Petäjä, T.; Worsnop, D.; Ceburnis, D.; Kerminen, V.-M.; Kulmala, M.; O'Dowd, C. Molecular-Scale Evidence of Aerosol Particle Formation via Sequential Addition of HIO3. *Nature* **2016**, *537* (7621), 532–534. https://doi.org/10.1038/nature19314.

(7) Baccarini, A.; Karlsson, L.; Dommen, J.; Duplessis, P.; Vüllers, J.; Brooks, I. M.; Saiz-Lopez, A.; Salter, M.; Tjernström, M.; Baltensperger, U.; Zieger, P.; Schmale, J. Frequent New Particle Formation over the High Arctic Pack Ice by Enhanced Iodine Emissions. *Nat. Commun.* **2020**, *11* (1), 4924. https://doi.org/10.1038/s41467-020-18551-0.

(8) Corella, J. P.; Maffezzoli, N.; Spolaor, A.; Vallelonga, P.; Cuevas, C. A.; Scoto, F.; Müller, J.; Vinther, B.; Kjær, H. A.; Cozzi, G.; Edwards, R.; Barbante, C.; Saiz-Lopez, A. Climate Changes Modulated the History of Arctic Iodine during the Last Glacial Cycle. *Nat. Commun.* **2022**, *13* (1), 88. https://doi.org/10.1038/s41467-021-27642-5.

(9) Tinel, L.; Adams, T. J.; Hollis, L. D. J.; Bridger, A. J. M.; Chance, R. J.; Ward, M. W.; Ball, S. M.; Carpenter, L. J. Influence of the Sea Surface Microlayer on Oceanic Iodine Emissions. *Environ. Sci. Technol.* **2020**, *54* (20), 13228–13237. https://doi.org/10.1021/acs.est.0c02736.

(10) Gilfedder, B. S.; Lai, S. C.; Petri, M.; Biester, H.; Hoffmann, T. Iodine Speciation in Rain, Snow and Aerosols. *Atmospheric Chem. Phys.* **2008**, *8* (20), 6069–6084. https://doi.org/10.5194/acp-8-6069-2008.

(11) Luther, G. W. Review on the Physical Chemistry of Iodine Transformations in the Oceans. *Front. Mar. Sci.* **2023**, *10*.

(12) Magi, L.; Schweitzer, F.; Pallares, C.; Cherif, S.; Mirabel, P.; George, C. Investigation of the Uptake Rate of Ozone and Methyl Hydroperoxide by Water Surfaces. *J. Phys. Chem. A* **1997**, *101* (27), 4943–4949. https://doi.org/10.1021/jp970646m.

(13) Utter, R. G.; Burkholder, J. B.; Howard, C. J.; Ravishankara, A. R. Measurement of the Mass Accommodation Coefficient of Ozone on Aqueous Surfaces. *J. Phys. Chem.* **1992**, *96* (12), 4973–4979. https://doi.org/10.1021/j100191a045.

(14) Stern, A. C.; Baer, M. D.; Mundy, C. J.; Tobias, D. J. Thermodynamics of Iodide Adsorption at the Instantaneous Air-Water Interface. *J. Chem. Phys.* **2013**, *138* (11), 114709–114709. https://doi.org/10.1063/1.4794688.

(15) Piatkowski, L.; Zhang, Z.; Backus, E. H. G.; Bakker, H. J.; Bonn, M. Extreme Surface Propensity of Halide Ions in Water. *Nat. Commun.* **2014**, *5* (1), 4083. https://doi.org/10.1038/ncomms5083.

(16) Woods, E.; Konys, C. A.; Rossi, S. R. Photoemission of Iodide from Aqueous Aerosol Particle Surfaces. *J. Phys. Chem. A* **2019**, *123* (13), 2901–2907. https://doi.org/10.1021/acs.jpca.8b12323.

(17) Otten, D. E.; Shaffer, P. R.; Geissler, P. L.; Saykally, R. J. Elucidating the Mechanism of Selective Ion Adsorption to the Liquid Water Surface. *Proc. Natl. Acad. Sci.* **2012**, *109* (3), 701–705. https://doi.org/10.1073/pnas.1116169109.

(18) Petersen, P. B.; Saykally, R. J. Probing the Interfacial Structure of Aqueous Electrolytes with Femtosecond Second Harmonic Generation Spectroscopy. *J. Phys. Chem. B* **2006**, *110* (29), 14060–14073. https://doi.org/10.1021/jp0601825.

(19) Credidio, B.; Pugini, M.; Malerz, S.; Trinter, F.; Hergenhahn, U.; Wilkinson, I.; Thürmer, S.; Winter, B. Quantitative Electronic Structure and Work-Function Changes of Liquid Water Induced by Solute. *Phys. Chem. Chem. Phys.* **2022**, *24* (3), 1310–1325. https://doi.org/10.1039/D1CP03165A.

(20) Seki, T.; Yu, C.-C.; Chiang, K.-Y.; Yu, X.; Sun, S.; Bonn, M.; Nagata, Y. Spontaneous Appearance of Triiodide Covering the Topmost Layer of the Iodide Solution Interface

Without Photo-Oxidation. *Environ. Sci. Technol.* **2024**, *58* (8), 3830–3837. https://doi.org/10.1021/acs.est.3c08243.

(21) Prophet, A. M.; Polley, K.; Van Berkel, G. J.; Limmer, D. T.; Wilson, K. R. Iodide Oxidation by Ozone at the Surface of Aqueous Microdroplets. *Chem. Sci.* **2024**, *15* (2), 736–756. https://doi.org/10.1039/D3SC04254E.

(22) Van Berkel, G. J.; Kertesz, V. An Open Port Sampling Interface for Liquid Introduction Atmospheric Pressure Ionization Mass Spectrometry. *Rapid Commun. Mass Spectrom.* **2015**, *29* (19), 1749–1756. https://doi.org/10.1002/rcm.7274.

(23) Kaur Kohli, R.; Van Berkel, G. J.; Davies, J. F. An Open Port Sampling Interface for the Chemical Characterization of Levitated Microparticles. *Anal. Chem.* **2022**, *94* (8), 3441–3445. https://doi.org/10.1021/acs.analchem.1c05550.

(24) Willis, M. D.; Rovelli, G.; Wilson, K. R. Combining Mass Spectrometry of Picoliter Samples with a Multicompartment Electrodynamic Trap for Probing the Chemistry of Droplet Arrays. *Anal. Chem.* **2020**, *92* (17), 11943–11952. https://doi.org/10.1021/acs.analchem.0c02343.

(25) Jacobs, M. I.; Davies, J. F.; Lee, L.; Davis, R. D.; Houle, F.; Wilson, K. R. Exploring Chemistry in Microcompartments Using Guided Droplet Collisions in a Branched Quadrupole Trap Coupled to a Single Droplet, Paper Spray Mass Spectrometer. *Anal. Chem.* **2017**, *89* (22), 12511–12519. https://doi.org/10.1021/acs.analchem.7b03704.

(26) Willis, M. D.; Wilson, K. R. Coupled Interfacial and Bulk Kinetics Govern the Timescales of Multiphase Ozonolysis Reactions. *J. Phys. Chem. A* **2022**, *126* (30), 4991–5010. https://doi.org/10.1021/acs.jpca.2c03059.

(27) Davies, J. F. Mass, Charge, and Radius of Droplets in a Linear Quadrupole Electrodynamic Balance. *Aerosol Sci. Technol.* **2019**, *53* (3), 309–320. https://doi.org/10.1080/02786826.2018.1559921.

(28) Hardy, D. A.; Robinson, J. F.; Hilditch, T. G.; Neal, E.; Lemaitre, P.; Walker, J. S.; Reid, J. P. Accurate Measurements and Simulations of the Evaporation and Trajectories of Individual Solution Droplets. *J. Phys. Chem. B* **2023**, *127* (15), 3416–3430. https://doi.org/10.1021/acs.jpcb.2c08909.

(29) Davies, J. F.; Haddrell, A. E.; Reid, J. P. Time-Resolved Measurements of the Evaporation of Volatile Components from Single Aerosol Droplets. *Aerosol Sci. Technol.* **2012**, *46* (6), 666–677. https://doi.org/10.1080/02786826.2011.652750.

(30) Berkel, V.; J, G. *Open Port Sampling Interface*; 11,313,841; Oak Ridge National Lab. (ORNL), Oak Ridge, TN (United States), 2022. https://www.osti.gov/doepatents/biblio/1892871.

(31) *AIOMFAC home*. http://www.aiomfac.caltech.edu/.

(32) Zuend, A.; Marcolli, C.; Booth, A. M.; Lienhard, D. M.; Soonsin, V.; Krieger, U. K.; Topping, D. O.; McFiggans, G.; Peter, T.; Seinfeld, J. H. New and Extended Parameterization of the Thermodynamic Model AIOMFAC: Calculation of Activity Coefficients for Organic-Inorganic Mixtures Containing Carboxyl, Hydroxyl, Carbonyl,

Ether, Ester, Alkenyl, Alkyl, and Aromatic Functional Groups. *Atmospheric Chem. Phys.* **2011**, *11* (17), 9155–9206. https://doi.org/10.5194/acp-11-9155-2011.

(33) Hinsberg, W. D.; Houle, F. A. *Kinetiscope*. https://hinsberg.net/kinetiscope/. https://hinsberg.net/kinetiscope/.

(34) Houle, F. A.; Wiegel, A. A.; Wilson, K. R. Predicting Aerosol Reactivity Across Scales: From the Laboratory to the Atmosphere. *Environ. Sci. Technol.* **2018**, *52* (23), 13774–13781. https://doi.org/10.1021/acs.est.8b04688.

(35) Wilson, K. R.; Prophet, A. M.; Rovelli, G.; Willis, M. D.; Rapf, R. J.; Jacobs, M. I. A Kinetic Description of How Interfaces Accelerate Reactions in Micro-Compartments. *Chem. Sci.* **2020**, *11* (32), 8533–8545. https://doi.org/10.1039/D0SC03189E.

(36) Polley, K.; Wilson, K. R.; Limmer, D. T. On the Statistical Mechanics of Mass Accommodation at Liquid–Vapor Interfaces. *J. Phys. Chem. B* **2024**, *128* (17), 4148–4157. https://doi.org/10.1021/acs.jpcb.4c00899.

(37) Lamoureux, G.; Harder, E.; Vorobyov, I. V.; Roux, B.; MacKerell Jr, A. D. A Polarizable Model of Water for Molecular Dynamics Simulations of Biomolecules. *Chem Phys Lett* **2006**, *418* (1–3), 245–249.

(38) Huang, J.; Lopes, P. E. M.; Roux, B.; MacKerell, A. D. Jr. Recent Advances in Polarizable Force Fields for Macromolecules: Microsecond Simulations of Proteins Using the Classical Drude Oscillator Model. *J. Phys. Chem. Lett.* **2014**, *5* (18), 3144–3150. https://doi.org/10.1021/jz501315h.

(39) Wilson, K. R.; Prophet, A. M.; Willis, M. D. A Kinetic Model for Predicting Trace Gas Uptake and Reaction. *J. Phys. Chem. A* **2022**, *126* (40), 7291–7308. https://doi.org/10.1021/acs.jpca.2c03559.

(40) Heine, N.; Houle, F. A.; Wilson, K. R. Connecting the Elementary Reaction Pathways of Criegee Intermediates to the Chemical Erosion of Squalene Interfaces during Ozonolysis. *Environ. Sci. Technol.* **2017**, *51* (23), 13740–13748. https://doi.org/10.1021/acs.est.7b04197.

(41) Brown, E. K.; Rovelli, G.; Wilson, K. R. pH Jump Kinetics in Colliding Microdroplets: Accelerated Synthesis of Azamonardine from Dopamine and Resorcinol. *Chem. Sci.* **2023**, *14* (23), 6430–6442. https://doi.org/10.1039/D3SC01576A.

(42) Wiegel, A. A.; Liu, M. J.; Hinsberg, W. D.; Wilson, K. R.; Houle, F. A. Diffusive Confinement of Free Radical Intermediates in the OH Radical Oxidation of Semisolid Aerosols. *Phys. Chem. Chem. Phys.* **2017**, *19* (9), 6814–6830. https://doi.org/10.1039/C7CP00696A.

(43) Wilson, K. R.; Prophet, A. M. Chemical Kinetics in Microdroplets. *Annu. Rev. Phys. Chem.* **2024**, *75*, 185–208. https://doi.org/10./1146/annurev-physchem-052623-120718.

(44) Shiraiwa, M.; Pfrang, C.; Pöschl, U. Kinetic Multi-Layer Model of Aerosol Surface and Bulk Chemistry (KM-SUB): The Influence of Interfacial Transport and Bulk Diffusion on the Oxidation of Oleic Acid by Ozone. *Atmospheric Chem. Phys.* **2010**, *10* (8), 3673–3691. https://doi.org/10.5194/acp-10-3673-2010.

(45) Crank, J. *The Mathematics of Diffusion*, 2nd ed.; Oxford University Press, 1975.

(46) Seinfeld, J. H.; Pandis, S. N. Mass Transfer Aspects of Atmospheric Chemistry. In *Atmospheric Chemistry and Physics: From Air Polution to Climate Change*; John Wiley & Sons, Inc., 1998.

(47) Fuchs, N. A.; Sutugin, A. G. High-Dispersed Aerosols. In *Topics in Current Aerosol Research*; Hidy, G. M., Brock, J. R., Eds.; International Reviews in Aerosol Physics and Chemistry; Pergamon, 1971; p 1. https://doi.org/10.1016/B978-0-08-016674-2.50006-6.

(48) Moon, S.; Limmer, D. T. Enhanced ClNO$_2$ Formation at the Interface of Sea-Salt Aerosol. arXiv March 13, 2024. https://doi.org/10.48550/arXiv.2403.09052.

(49) Galib, M.; Limmer, D. T. Reactive Uptake of N2O5 by Atmospheric Aerosol Is Dominated by Interfacial Processes. *Science* **2021**, *371* (6532), 921–925. https://doi.org/10.1126/science.abd7716.

(50) Singh, A. N.; Limmer, D. T. Peptide Isomerization Is Suppressed at the Air–Water Interface. *J. Phys. Chem. Lett.* **2022**, *13* (2), 574–579. https://doi.org/10.1021/acs.jpclett.1c03837.

(51) Liu, Q.; Schurter, L. M.; Muller, C. E.; Aloisio, S.; Francisco, J. S.; Margerum, D. W. Kinetics and Mechanisms of Aqueous Ozone Reactions with Bromide, Sulfite, Hydrogen Sulfite, Iodide, and Nitrite Ions. *Inorg. Chem.* **2001**, *40* (17), 4436–4442. https://doi.org/10.1021/ic000919j.

(52) Brown, L. V.; Pound, R. J.; Ives, L. S.; Jones, M. R.; Andrews, S. J.; Carpenter, L. J. Negligible Temperature Dependence of the Ozone–Iodide Reaction and Implications for Oceanic Emissions of Iodine. *Atmospheric Chem. Phys.* **2024**, *24* (7), 3905–3923. https://doi.org/10.5194/acp-24-3905-2024.

(53) Forster, E. L. C. Rate of Formation of Iodates in Alkaline Solutions of Iodine. *J. Phys. Chem.* **1903**, *7* (9), 640–651. https://doi.org/10.1021/j150054a002.

(54) Li, C. H.; White, C. F. Kinetics of Hypoiodite Decomposition. *J. Am. Chem. Soc.* **1943**, *65* (3), 335–339. https://doi.org/10.1021/ja01243a011.

(55) Truesdale, V. W. Kinetics of Disproportionation of Hypoiodous Acid at High pH,with an Extrapolation to Rainwater. *J. Chem. Soc. Faraday Trans.* **1997**, *93* (10), 1909–1914. https://doi.org/10.1039/A700226B.

(56) Haimovich, O.; Treinin, A. Disproportionation of Hypoiodite. *J. Phys. Chem.* **1967**, *71* (6), 1941–1943. https://doi.org/10.1021/j100865a068.

(57) Bichsel, Y.; von Gunten, U. Hypoiodous Acid: Kinetics of the Buffer-Catalyzed Disproportionation. *Water Res.* **2000**, *34* (12), 3197–3203. https://doi.org/10.1016/S0043-1354(00)00077-4.

(58) Wren, J. C.; Paquette, J.; Sunder, S.; Ford, B. L. Iodine Chemistry in the +1 Oxidation State. II. A Raman and Uv–Visible Spectroscopic Study of the Disproportionation of Hypoiodite in Basic Solutions. *Can. J. Chem.* **1986**, *64* (12), 2284–2296. https://doi.org/10.1139/v86-375.

(59) McKinnon, B. I.; Marlton, S. J. P.; Ucur, B.; Bieske, E. J.; Poad, B. L. J.; Blanksby, S. J.; Trevitt, A. J. Actinic Wavelength Action Spectroscopy of the IO– Reaction Intermediate. *J. Phys. Chem. Lett.* **2021**, *12* (49), 11939–11944. https://doi.org/10.1021/acs.jpclett.1c03456.

(60) Smith, J. D.; Kroll, J. H.; Cappa, C. D.; Che, D. L.; Liu, C. L.; Ahmed, M.; Leone, S. R.; Worsnop, D. R.; Wilson, K. R. The Heterogeneous Reaction of Hydroxyl Radicals with Sub-Micron Squalane Particles: A Model System for Understanding the Oxidative Aging of Ambient Aerosols. *Atmospheric Chem. Phys.* **2009**, *9* (9), 3209–3222. https://doi.org/10.5194/acp-9-3209-2009.

(61) Worsnop, D. R.; Morris, J. W.; Shi, Q.; Davidovits, P.; Kolb, C. E. A Chemical Kinetic Model for Reactive Transformations of Aerosol Particles. *Geophys. Res. Lett.* **2002**, *29* (20), 57-1-57–4. https://doi.org/10.1029/2002GL015542.

(62) Rouvière, A.; Sosedova, Y.; Ammann, M. Uptake of Ozone to Deliquesced KI and Mixed KI/NaCl Aerosol Particles. *J. Phys. Chem. A* **2010**, *114* (26), 7085–7093. https://doi.org/10.1021/JP103257D.

(63) Rouvière, A.; Ammann, M. The Effect of Fatty Acid Surfactants on the Uptake of Ozone to Aqueous Halogenide Particles. *Atmospheric Chem. Phys.* **2010**, *10* (23), 11489–11500. https://doi.org/10.5194/acp-10-11489-2010.

(64) Martins-Costa, M. T. C.; Ruiz-López, M. F. Electrostatics and Chemical Reactivity at the Air–Water Interface. *J. Am. Chem. Soc.* **2023**, *145* (2), 1400–1406. https://doi.org/10.1021/jacs.2c12089.

(65) Rovelli, G.; Jacobs, M. I.; Willis, M. D.; Rapf, R. J.; Prophet, A. M.; Wilson, K. R. A Critical Analysis of Electrospray Techniques for the Determination of Accelerated Rates and Mechanisms of Chemical Reactions in Droplets. *Chem. Sci.* **2020**, *11* (48), 13026–13043. https://doi.org/10.1039/D0SC04611F.

(66) Bhujel, M.; L. Marshall, D.; T. Maccarone, A.; I. McKinnon, B.; J. Trevitt, A.; Silva, G. da; J. Blanksby, S.; J. Poad, B. L. Gas Phase Reactions of Iodide and Bromide Anions with Ozone: Evidence for Stepwise and Reversible Reactions. *Phys. Chem. Chem. Phys.* **2020**, *22* (18), 9982–9989. https://doi.org/10.1039/D0CP01498B.

(67) Smoluchowski, M. V. Versuch Einer Mathematischen Theorie Der Koagulationskinetik Kolloider Lösungen. *Z. Für Phys. Chem.* **1917**, No. 92, 129–168.

(68) Teiwes, R.; Elm, J.; Bilde, M.; Pedersen, H. B. The Reaction of Hydrated Iodide I(H2O)− with Ozone: A New Route to IO2− Products. *Phys. Chem. Chem. Phys.* **2019**, *21* (32), 17546–17554. https://doi.org/10.1039/C9CP01734H.

(69) Schneider, S. R.; Lakey, P. S. J.; Shiraiwa, M.; Abbatt, J. P. D. Reactive Uptake of Ozone to Simulated Seawater: Evidence for Iodide Depletion. *J. Phys. Chem. A* **2020**, *124* (47), 9844–9853. https://doi.org/10.1021/ACS.JPCA.0C08917.

(70) Artiglia, L.; Edebeli, J.; Orlando, F.; Chen, S.; Lee, M.-T.; Corral Arroyo, P.; Gilgen, A.; Bartels-Rausch, T.; Kleibert, A.; Vazdar, M.; Andres Carignano, M.; Francisco, J. S.; Shepson, P. B.; Gladich, I.; Ammann, M. A Surface-Stabilized Ozonide Triggers Bromide

Oxidation at the Aqueous Solution-Vapour Interface. *Nat. Commun.* **2017**, *8* (1), 700. https://doi.org/10.1038/s41467-017-00823-x.

(71) Limmer, D. T.; Götz, A. W.; Bertram, T. H.; Nathanson, G. M. Molecular Insights into Chemical Reactions at Aqueous Aerosol Interfaces. *Annu. Rev. Phys. Chem.* **2024**, *75* (Volume 75, 2024), 111–135. https://doi.org/10.1146/annurev-physchem-083122-121620.

(72) Seki, T.; Yu, C.-C.; Chiang, K.-Y.; Greco, A.; Yu, X.; Matsumura, F.; Bonn, M.; Nagata, Y. Ions Speciation at the Water–Air Interface. *J. Am. Chem. Soc.* **2023**, *145* (19), 10622–10630. https://doi.org/10.1021/jacs.3c00517.

(73) AbouHaidar, R.; Duflot, D.; Toubin, C. Theoretical Characterization of the Kinetics of the Multiphase Ozonolysis of an Aqueous Maleic Acid Droplet. *Aerosol Sci. Technol.* **2024**, *58* (4), 337–355. https://doi.org/10.1080/02786826.2023.2286341.

(74) Wang, Y. L.; Nagy, J. C.; Margerum, D. W. Kinetics of Hydrolysis of Iodine Monochloride Measured by the Pulsed-Accelerated-Flow Method. *J. Am. Chem. Soc.* **1989**, *111* (20), 7838–7844. https://doi.org/10.1021/ja00202a026.

(75) Margerum, D. W.; Dickson, P. N.; Nagy, J. C.; Kumar, K.; Bowers, C. P.; Fogelman, K. D. Kinetics of the Iodine Monochloride Reaction with Iodide Measured by the Pulsed-Accelerated-Flow Method. *Inorg. Chem.* **1986**, *25* (27), 4900–4904. https://doi.org/10.1021/ic00247a025.

(76) Schneider, S. R.; Lakey, P. S. J.; Shiraiwa, M.; Abbatt, J. P. D. Iodine Emission from the Reactive Uptake of Ozone to Simulated Seawater. *Environ. Sci. Process. Impacts* **2023**, *25* (2), 254–263. https://doi.org/10.1039/D2EM00111J.

(77) Heine, N.; Arata, C.; Goldstein, A. H.; Houle, F. A.; Wilson, K. R. Multiphase Mechanism for the Production of Sulfuric Acid from SO2by Criegee Intermediates Formed during the Heterogeneous Reaction of Ozone with Squalene. *J. Phys. Chem. Lett.* **2018**, *9* (12), 3504–3510. https://doi.org/10.1021/acs.jpclett.8b01171.

(78) Jungwirth, P.; Tobias, D. J. Ions at the Air/Water Interface. *J. Phys. Chem. B* **2002**, *106* (25), 6361–6373. https://doi.org/10.1021/jp020242g.

(79) Paquette, J.; Wren, J. C.; Sunder, S.; Ford, B. L. *The Disproportionation of Iodine (I)*; 0-7058-1073–9; United Kingdom, 1986; pp 29–45.

(80) Bichsel, Y.; von Gunten, U. Oxidation of Iodide and Hypoiodous Acid in the Disinfection of Natural Waters. *Environ. Sci. Technol.* **1999**, *33* (22), 4040–4045. https://doi.org/10.1021/es990336c.

(81) Lengyel, I.; Epstein, I. R.; Kustin, K. Kinetics of Iodine Hydrolysis. *Inorg. Chem.* **1993**, *32* (25), 5880–5882. https://doi.org/10.1021/ic00077a036.

(82) Sebők-Nagy, K.; Körtvélyesi, T. Kinetics and Mechanism of the Hydrolytic Disproportionation of Iodine. *Int. J. Chem. Kinet.* **2004**, *36* (11), 596–602. https://doi.org/10.1002/kin.20033.

(83) Palmer, D. A.; Ramette, R. W.; Mesmer, R. E. Triiodide Ion Formation Equilibrium and Activity Coefficients in Aqueous Solution. *J. Solut. Chem.* **1984**, *13* (9), 673–683. https://doi.org/10.1007/BF00650374.

(84) Sanemasa, I.; Kobayashi, T.; Piao, C. Y.; Deguchi, T. Equilibrium Solubilities of Iodine Vapor in Water. *Bull. Chem. Soc. Jpn.* **1984**, *57* (5), 1352–1357. https://doi.org/10.1246/bcsj.57.1352.

(85) Sander, R. Compilation of Henry's Law Constants (Version 5.0.0) for Water as Solvent. *Atmospheric Chem. Phys.* **2023**, *23* (19), 10901–12440. https://doi.org/10.5194/acp-23-10901-2023.

(86) Lin, C.-C. Volatility of Iodine in Dilute Aqueous Solutions. *J. Inorg. Nucl. Chem.* **1981**, *43* (12), 3229–3238. https://doi.org/10.1016/0022-1902(81)80094-2.

(87) Dunlop, P. J.; Stokes, R. H. The Diffusion Coefficients of Sodium and Potassium Iodides in Aqueous Solution at 25°1. *J. Am. Chem. Soc.* **1951**, *73* (11), 5456–5457. https://doi.org/10.1021/ja01155a520.

(88) Darrall, K. G.; Oldham, G. The Diffusion Coefficients of the Tri-Iodide Ion in Aqueous Solutions. *J. Chem. Soc. Inorg. Phys. Theor.* **1968**, 2584. https://doi.org/10.1039/j19680002584.

(89) Gregory, D. P.; Riddiford, A. C. 731. Transport to the Surface of a Rotating Disc. *J. Chem. Soc. Resumed* **1956**, 3756. https://doi.org/10.1039/jr9560003756.

(90) Gottschalk, C.; Libra, J. A.; Saupe, A. *Ozonation of Water and Waste Water: A Practical Guide to Understanding Ozone and Its Applications*, 2nd Edition.; Wiley-VCH Verlag GmbH & Co., 2010.

Chapter 4: Surfactant Adsorption Inhibits Surface Reactions in Aqueous Microdroplets

4.1: Introduction

Gas-liquid interfaces are unique chemical environments recently characterized by unexpected reaction kinetics.[1–3] These kinetics are generally difficult to interpret from experiments in the literature as reactive contributions from the gas-phase, bulk-phase, and interface are typically not distinguished, which has been shown to lead to erroneous conclusions on microdroplet reactivity.[4,5] Key kinetic parameters such as reagent concentrations, droplet radii, and the rates of gas-liquid partitioning and evaporation are often difficult to constrain in microdroplet-based analyses—leading similarly to exaggerated claims of interfacial reactivity.[6,7] Furthermore, debate around the evidence and mechanism of "spontaneous" chemistry initiated by purported strong electric fields at the interface is ongoing.[8–13]

While there is no general consensus on any particular features of interfacial reactivity in this regard, reaction rates at the gas-liquid interface do likely deviate from their bulk analogs for a number of reasons. Reactant concentrations at the interface are known to differ dramatically from their corresponding bulk concentrations for many chemical species due to unique thermodynamic stability at the interface[14–18] or the kinetics of competing diffusion and adsorption timescales in nonequilibrium systems.[19–21] Additionally, the energetics of the reaction coordinate itself can be strongly influenced by the partial-solvation environment of the interface,[22,23] although empirical investigations of this are limited. Given the high degree of uncertainty for processes governing surface reactivity, there remains a need for novel kinetic approaches and detailed models of chemistry at interfaces.[24]

Due to interest in the molecular makeup and properties of interfaces in aerosol and microdroplets specifically, a natural avenue of inquiry is the behavior of surfactants in these systems. An increasing amount of literature aims to describe the role of surfactant adsorption and surface tension in the activation of cloud condensation nuclei.[25–31] Additionally, the direct effects of surfactant-adsorption on chemical reactivity at interfaces has long been pursued to clarify the chemical nature of the gas-liquid interface.[32–34] Work investigating the static properties of surfactant-containing systems has shown unique equilibrium properties of surface tension in microdroplets deriving from finite-volume effects of pico-liter samples.[35–37] Beyond statics, recent work interrogating the dynamics of surfactant adsorption in microdroplets has shown that timescales for interfacial equilibration span up to milliseconds for freshy generated microdroplets with radius r ~ 25 μm.[38] In addition to the growing number of mechanistic approaches to study interfacial effects in relatively simple systems, the analysis of surfactant behavior and interactions of complex mixtures in simulated[39,40] and real-world systems[41] is ongoing.

Here, we report and analyze experiments that integrate the concepts outlined above in which levitated aqueous microdroplets are used to study the kinetics of the $I^- + O_3$ reaction with varying concentrations of the nonionic surfactant Triton X-100 (TX). The oxidation reaction of iodide by ozone in aqueous solution is a relatively well characterized system that exhibits chemical reactivity at the interface under acidic conditions. Similarly, Triton X-100 adsorption to the interface in bulk aqueous systems and in microdroplets has been well characterized.[35,42–44] We observe a characteristic inhibition of the surface reaction with increasing [TX], indicative of both the "bulk depletion" effect of surfactants in microdroplets[35,36] and the competitive adsorption of TX and I^- at the gas-liquid interface.

To quantitatively understand this effect, a multiphase chemical kinetics model is applied first to simulate the droplet chemistry using numerical simulations and then to derive an analytical expression for reactive uptake that includes the non-reactive influence of interfacial TX. Molecular transport at the interface in the kinetic model is parameterized by density profiles and timescales obtained by MD simulations and by referencing macroscopic-scale surface tension measurements of Triton X-100. Consequently, the reaction locus can be identified to a high degree, as summarized in Fig. 4.1, where the overall uptake of O_3 is limited by the surface reaction for low [TX] and by liquid diffusion of O_3 through the sub-surface region (extending < 2 nm beneath the surface) for high [TX], demonstrating that the interfacial I^- available to react with O_3 is characteristically excluded from the top 1 nm of the droplet with increasing surface coverage of TX.

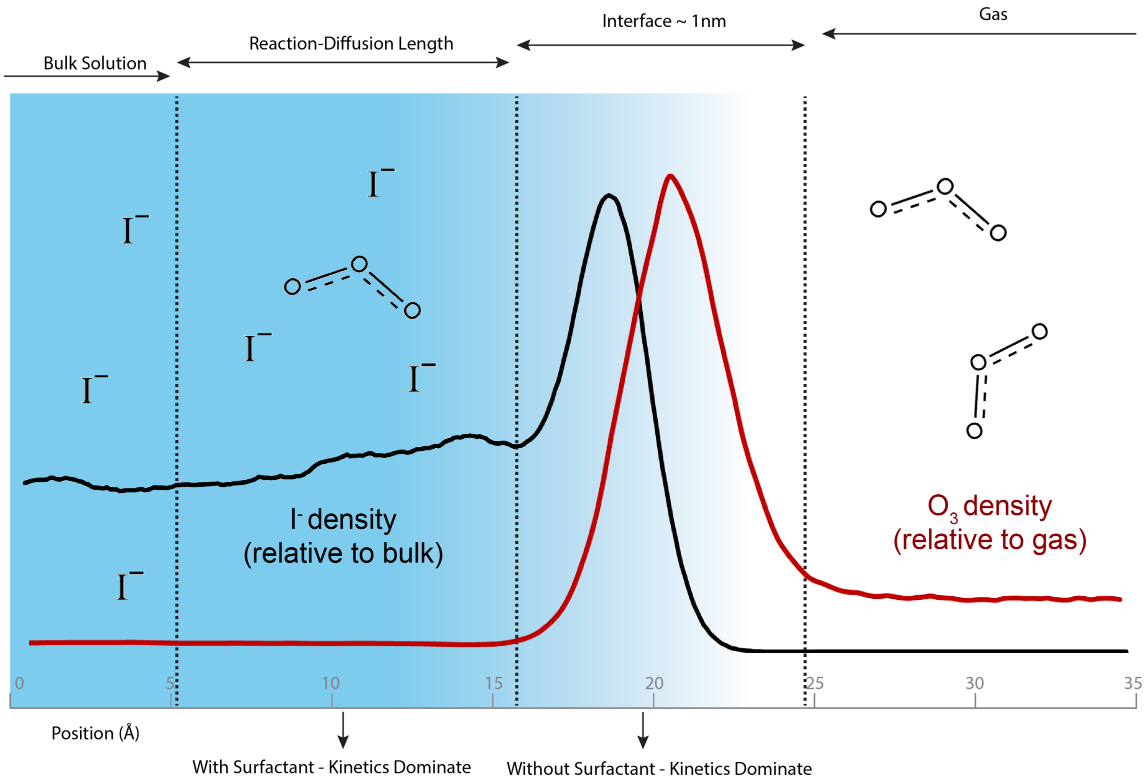

Fig. 4.1: Conceptual scheme of the modeled droplet interface showing I^- density extending into the bulk solution, and O_3 density in the gas phase. Density profiles for these reagents are normalized with respect to their bulk density, and both show some degree of density enhancement at the interface. Notably, the density profiles overlap across the ~ 1 nm range where the overall density attenuates, which we identify herein as the surface. The subsurface region we denote as the "reaction-diffusion" region as this extends the length of the reaction-diffusion length as defined for O_3 under the experimental salt concentration, of L_{rxn} = 1.36 nm. As indicated on the bottom axis, increasing concentrations of the strongly surface-active Triton X-100 displaces the I^- density at the interface and shuts off the surface reaction that dominates in its absence.

4.2: Experimental

Microdroplet oxidation kinetics were measured as previously reported using a quadrupole electrodynamic trap (QET)[45] combined with an open-port sampling interface (OPSI) for mass spectrometry (MS).[46] This particular assembly has been recently described in multiple works, along with comparable configurations.[46–48] In the experimental assembly, the QET charges and traps individual microdroplets generated from a piezo-electric droplet dispenser (Microfab). Arrays of ~100 microdroplets are trapped while oxidant is introduced to the enclosed assembly, initiating reaction. Single microdroplets are then sized using a collected Mie scattering pattern[49,50] before being ejected from the QET and into the OPSI-MS analyzer. Droplet signals obtained from OPSI-MS allow for the quantitative determination of solute remaining in each droplet. Additional information and a schematic of the experimental apparatus is provided in Appendix 4A.

The ion signal from iodide in aqueous microdroplets and detected by OPSI-MS is presented in Fig. 4.2A, showing a time series of microdroplet detection events resulting in signal at m/z = 126.89. Example mass spectra are provided in Appendix 4A. Peak areas integrated from the time-series are used to observe the remaining [I^-] in individual droplets during exposure to O_3, as shown in Fig. 4.2B. Solutions prepared to generate the microdroplets contain NaI and citric acid to buffer the pH at pH 3, along with NaCl to maintain high enough water activity to keep the droplet trapped over the course of reaction. For experiments reported herein, the humidity of the trap was maintained at 88%. As such, the final water activity in the microdroplets is $a_w = 0.88$. Using this final water activity and the radius of the droplet, initial droplet concentrations are $[NaI]_0 = 795$ mM, 1 M NaCl, and 1M citric acid/sodium citrate. Triton X-100 is included in the initial droplet solution and ranges from 6 uM to 1.6 mM in concentration. Solutions containing surfactant were first prepared via serial dilution, before adding to the salt solution to obtain the final concentration.

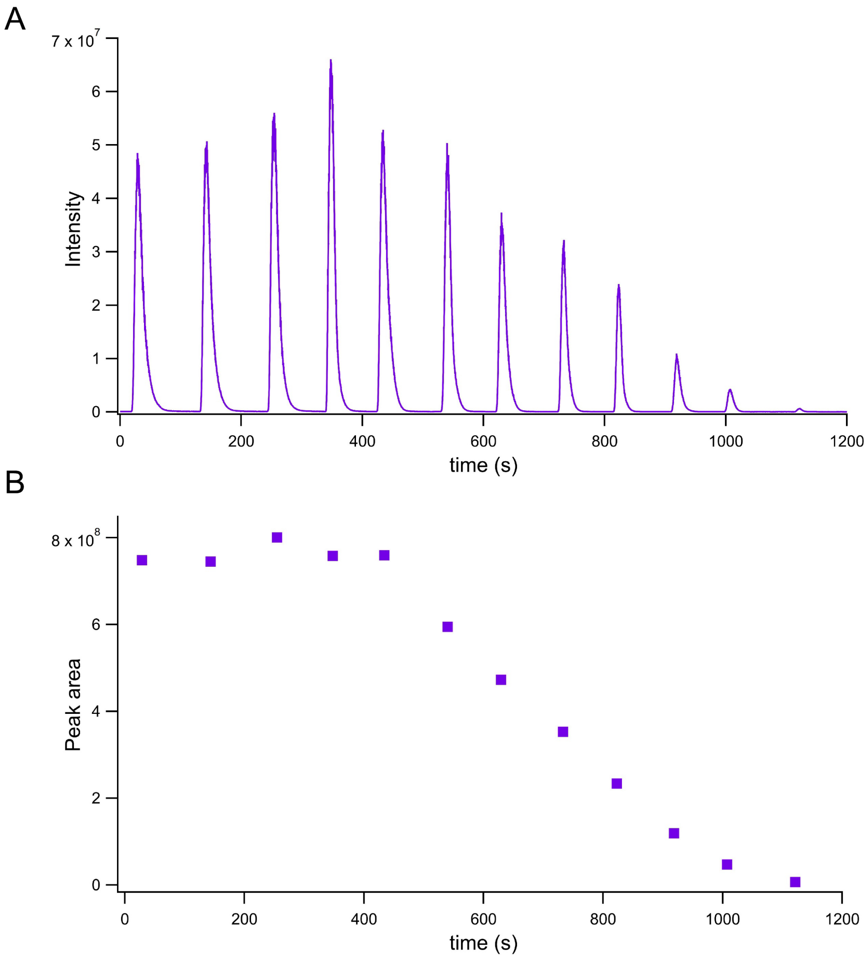

Fig. 4.2: Microdroplet detection events using OPSI-MS. Panel A shows a droplet detection time-series where initial, unreacted droplets are first detected, followed by iodide decay resulting from O_3 exposure. Panel B shows peak areas from overall intensity trace in A.

4.3: Results

Iodide reaction-decay profiles for experiments with varying droplet concentrations of Triton X-100 are shown in Fig. 4.3. In Panel A, results from the [TX] = 32 μM and [TX] = 1.6 mM conditions are provided on the same time-domain to show the reaction suppression with increasing [TX]. The experimental dataset across the entire [TX] range analyzed is provided in panel B, where [TX] ranges from 6 μM to 3.2 mM. The O_3 concentration for all experiments was measured to be 500 ± 10 ppb and initial droplet radius r = 17 ± 1 μm. As shown in Fig. 4.3, the overall rate of I^- decay decreases with increasing [TX]. Explicit kinetic simulations are included for each condition in Fig. 4.3, applying a previously developed kinetic model for iodide oxidation in microdroplets, augmented with an additional step to include Triton X-100 adsorption to the air-water interface. Details of the kinetic model and an overview of the Triton X-100 adsorption description are included in the following analysis section.

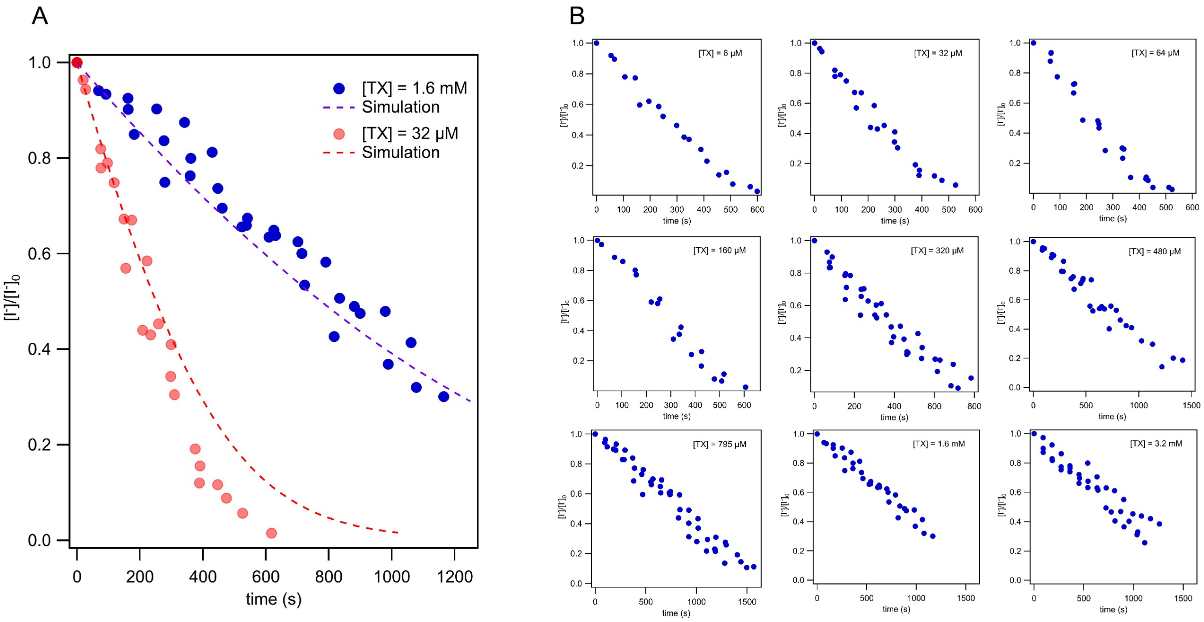

Fig. 4.3: Experimental decay profiles of $[I^-]$ in microdroplets during O_3 oxidation. Data series show oxidation of 17 µm radius aqueous droplets containing 795 mM [NaI] and variable Triton-X concentrations. Droplets are exposed to 500 ppb $[O_3]$. Decay profiles show the rate of reaction slowing with additional Triton-X.

Although the $I^- + O_3$ reaction rate appears to decrease upon the addition of surfactant, the dependence on [TX] is not straightforward. This observation is summarized in Fig. 4.4 where reactive uptake coefficients are calculated for each condition, providing a useful indication of the degree of overall reactivity observed in each experiment. Initial rates of decay k_{init} for each experiment are used to compute reactive uptake coefficients γ_{exp} for O_3 uptake using a previously introduced formulation:[51]

$$\gamma_{exp} = \frac{4 \cdot r \cdot k_{init} \cdot \left[\mathrm{I}^-_{(b)}\right]_0}{3 \cdot \left[\mathrm{O}_{3(gas)}\right] \cdot \bar{c}}, \qquad \text{Eq. 4.1}$$

where r is the droplet radius and $\bar{c}$ the mean speed of O_3 in the gas-phase. Uptake coefficients calculated in this way are shown in Fig. 4.4. When viewing the reaction kinetics in this manner, a distinct shape of the Triton X-100 concentration dependence is observed. For [TX] < 100 µM, the reaction kinetics are largely unaffected by the addition of TX with the observed uptake equal to $\gamma_{exp} \sim 5.5\times10^{-3}$. This uptake coefficient is consistent with reactive uptake on the same sized microdroplets in the absence of [TX] at pH 3 (see Chapter 3). For 100 µM < [TX] < 500 µM, a relatively sharp transition in kinetics occurs and the observed uptake drops to $\sim1.5\times10^{-3}$. Interestingly, increasing the [TX] > 500 µM has no effect on the measured kinetics. Qualitatively, this behavior agrees with a simple mechanistic description in which addition of TX increasingly suppresses the surface reaction of $I^- + O_3$, effectively shutting off any surface reaction for [TX] ≥ 500 µM. The plateau observed for higher [TX] indicates that once the surface is saturated with TX, only reactivity within the sub-surface of the microdroplet can be observed, yielding an overall smaller uptake coefficient. Although one may predict this saturation point to agree with the CMC of Triton X-100 in solution (~200 µM), this inflation of the observed saturation bulk concentration to ~500 µM is a property of surfactant adsorption in microdroplets, as explored in the following section.

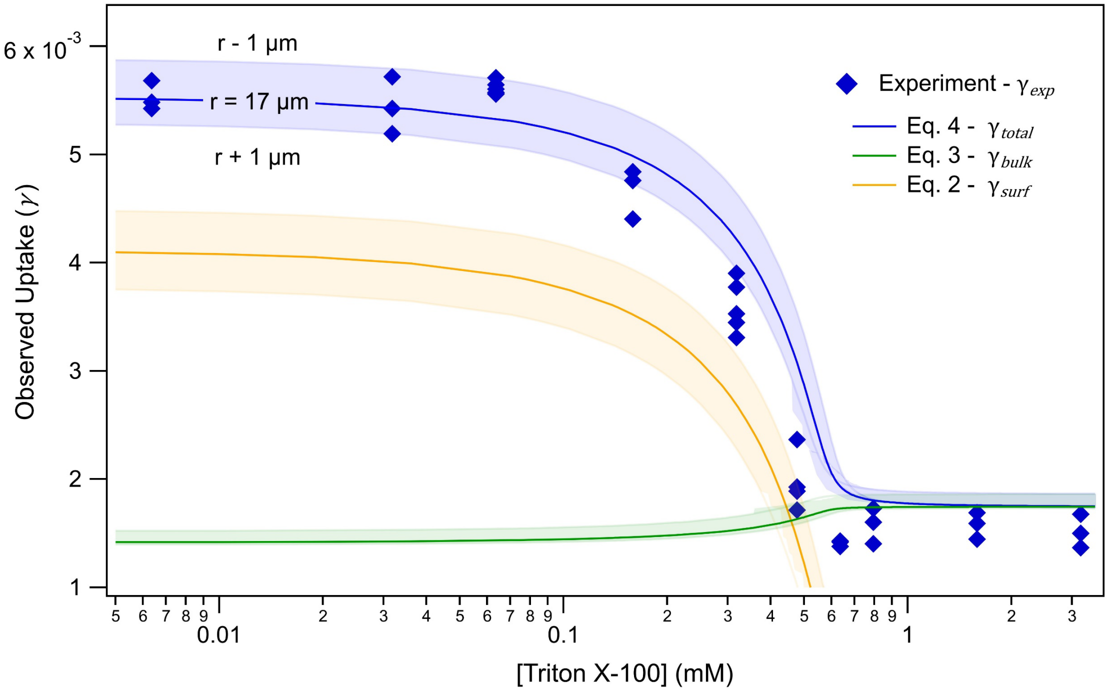

Fig. 4.4: Experimental kinetics summarized using reactive uptake coefficients of O_3 for the range of droplet [Triton X-100] studied. Analytical expressions Eqs. 4.2-4.4 are compared to experimental values. Error bars indicated around model results represent the predicted values for ± 1 µm in radius.

4.4: Analysis

Experimental results in Fig. 4.3 and summarized in Fig. 4.4 qualitatively suggest the addition of TX inhibits the $I^- + O_3$ reaction at the air-water interface. To understand this effect quantitatively, a competitive adsorption model of I^- and TX is developed. The development of this model derives from the same multiphase kinetic framework used to execute the kinetic simulations in Fig. 4.3A. The kinetic simulations are performed using the stochastic-simulator kinetic software Kinetiscope, as discussed at length in previous work[46,47] and in Chapters 2-3. Chemistry in this model is treated as in Chapter 3, delineating between surface and sub-surface chemistry in the microdroplet, where the sub-surface is identified as the reaction-diffusion (RD) region. The RD region is aptly defined using the reaction-diffusion length of O_3 in solution. The reaction-diffusion length, as discussed elsewhere,[52–54] is the average distance an O_3 molecule will diffusive in solution before undergoing reaction. In the current work, a single kinetic step is added to model Triton X-100 adsorption to the interface. Since the kinetic model and simulation methods have been thoroughly described in recent works, we will instead emphasize the introduction of analytical expressions for uptake coefficients at the surface and within the reaction-diffusion region below. These uptake expressions are similarly built off of previous work and are augmented with the addition of TX adsorption.[55]

Reactive uptake coefficients γ_s and γ_{rd} resulting from O_3 loss on the droplet surface (S) and within the reaction-diffusion length (RD), respectively, can be expressed using an approach adapted from Wilson et al.[55]

$$\gamma_s = \frac{4 \cdot r \cdot k_{rxn}^{srf} \cdot [\mathrm{O}_{3(ads)}][\mathrm{I}^-_{(ads)}]}{3 \cdot \bar{c} \cdot [\mathrm{O}_{3(g)}]} \cdot \frac{r^3 - (r-\delta)^3}{r^3}, \qquad \text{Eq. 4.2}$$

$$\gamma_{rd} = \frac{4 \cdot r \cdot k_{rxn}^{blk} \cdot [\mathrm{O}_{3(rd)}][\mathrm{I}^-_{(rd)}]}{3 \cdot \bar{c} \cdot [\mathrm{O}_{3(g)}]} \cdot \frac{(r-\delta)^3 - (r-\delta-L_{rd})^3}{r^3}, \qquad \text{Eq. 4. 3}$$

$$\gamma_{total} = \gamma_s + \gamma_{rd}, \qquad \text{Eq. 4. 4}$$

where δ is the surface thickness defined as $\delta = 1$ nm and L_{rd} the reaction-diffusion length of O_3 in solution under the given conditions, $L_{rd} = \sqrt{\frac{D}{k_{rxn}^{blk} \cdot [\mathrm{I}^-]_0}} = 1.36$ nm. Equations 4.2 and 4.3 possess the same general form in which a reaction term is defined using local concentrations (indicated with subscripts *s* or *rd* to denote relevant region), normalized by the O_3 collisional flux on the droplet surface. Each equation also contains a volumetric weighting term to account for the relative fraction of the entire droplet volume that constitutes the specific reactive region (surface or reaction-diffusion region). We note that there is an additional contribution γ_b to the overall uptake arising from the inner bulk or "core" of the droplet, beyond the depth of the reaction diffusion length L_{rd} (the core, in fact, comprises by far most of the droplet volume). However, since $L_{rd} \sim$ nm for the current experiments, virtually all reactivity occurs on the surface or within the reactive diffusive region. Therefore, we can neglect the uptake contribution of γ_b in the following analysis.

Given that equations Eq. 4.2 & 4.3 contain the correct spherical geometric weighting, the governing concentrations in each region much be defined: $[\mathrm{I}^-_{(ads)}]$ and $[\mathrm{O}_{3(ads)}]$ in the surface region, and $[\mathrm{I}^-_{(rd)}]$ and $[\mathrm{O}_{3(rd)}]$ in the RD region. To accomplish this, an analytical approach is constructed by applying a steady-state assumption to the kinetic framework used in the stochastic simulations. More details on this approach are included in Appendix 4C. In this approach, we assume that shortly after the reaction has begun, local concentrations of reactants defined in each geometric region rapidly achieve a steady-state condition which is governed by mass transport kinetics and chemical reactivity. The governing transport kinetics rely heavily on both gas- and liquid-phase diffusion for O_3, as well as desorption and solvation kinetics across the energetic barrier at the interface. For liquid solutes, I^- and TX in this case, diffusional transport is simpler and can be neglected. This is generally a reasonable approximation for the "trace gas" condition where the aqueous reactant concentration is many orders of magnitude in excess of the co-reactant. In this case, the steady-state subsurface concentration in the RD region, $[\mathrm{I}^-_{(rd)}]$ is simply the initial bulk concentration $[\mathrm{I}^-_{b}]_0$.

Assuming the interfacial concentration of I^- is not perturbed by the reaction (also generally true for the "trace gas" condition with concentrated solute), the steady-state surface-adsorbed concentration of iodide $[\mathrm{I}^-_{(ads)}]$ can be modeled with a competitive-adsorption Langmuir isotherm including Triton-X 100:

$$[\mathrm{I}^-_{(ads)}] = \frac{\Gamma_\infty^{\mathrm{I}^-}}{\delta} \cdot \frac{s_{\mathrm{I}^-} \cdot K_{eq}^{\mathrm{I}^-} \cdot [\mathrm{I}^-_{(bulk)}]}{1 + s_{\mathrm{I}^-} \cdot K_{eq}^{\mathrm{I}^-} \cdot [\mathrm{I}^-_{(bulk)}] + s_{TX} \cdot K_{eq}^{TX} \cdot [\mathrm{TX}_{(bulk)}]}, \qquad \text{Eq. 4.5}$$

where $\Gamma_{\infty}^{\mathrm{I}^-}$ represents the maximum coverage term (in molecules/cm^2) of iodide at the interface, expressed as a volumetric concentration by dividing by the surface thickness δ, and $K_{eq}^{\mathrm{I}^-}$ is the Langmuir adsorption equilibrium constant, which relates the bulk concentration of I^- to the surface adsorbed concentration. Constants $s_{\mathrm{I}^-} = 5$ and $s_{TX} = 3$ are weighting factors necessary in the competitive isotherm to account for the different effective areas of I^- and TX. The parameters $K_{eq}^{\mathrm{I}^-}$ and $\Gamma_{\infty}^{\mathrm{I}^-}$ are taken from Chapter 3 where MD simulations were used to investigate I^- densities at the aqueous interface for varying concentrations to express the surface-to-bulk relation of I^- as a simple Langmuir expression.

To constrain the adsorption behavior of TX in the model, a corresponding set of adsorption parameters (Γ_{∞}^{TX}, K_{eq}^{TX}) are needed for the surfactant. To obtain these, surface tension measurements of aqueous TX solutions by Bzdek et al.[35] are fit using the Szyszkowski equation-of-state (EOS):[56]

$$\gamma - \gamma_{0.5\mathrm{M\ NaCl}} = -\Gamma_{\infty}^{TX} \cdot R \cdot T \cdot \ln(1-\theta)\,, \qquad \text{Eq. 4.6}$$

where R is the gas constant, T the temperature, and $\gamma_{0.5\mathrm{M\ NaCl}}$ the surface tension of 0.5 M NaCl solution. This EOS depends on a fractional surface coverage term θ relating the bulk to the surface concentration. Here, we model θ with a standard Langmuir adsorption isotherm:

$$\theta = \frac{K_{eq}^{TX} \cdot \left[TX_{(bulk)}\right]}{1 + K_{eq}^{TX} \cdot \left[TX_{(bulk)}\right]}. \qquad \text{Eq. 4.7}$$

Fig. 4.5 shows surface tension measurements for a 0.5 M NaCl solution containing various concentrations of Triton X-100 measured by Bzdek et al.[35] and includes a fit to Eq. 4.6—providing unique values for $\Gamma_{\infty}^{TX} = 2\times10^{14}$ molecules/cm^2 and $K_{eq}^{TX} = 1.1\times10^{-15}$ cm^3 molecule^{-1} s^{-1}. The kinetic model is adapted to include this information by defining an adsorption step for Triton X-100:

$$\mathrm{TX}_{(bulk)} + \mathrm{site} \underset{k_{solv}}{\overset{k_{desolv}}{\rightleftarrows}} \mathrm{TX}_{(ads)}. \qquad \text{S1}$$

The site species in step S1 is defined as previously discussed for O_3 and I^-,[46,47,55] where the maximum surface coverage Γ_{∞}^{TX} constrains the site area and related volumetric concentration within the model geometry. Kinetic coefficients k_{desolv} and k_{solv} are directly related to the Langmuir adsorption equilibrium coefficient $K_{eq}^{TX} = k_{desolv}/k_{solv}$. While the equilibrium coefficient only constrains the ratio of coefficients, we choose a value of $k_{solv} = 1$ s^{-1} to constrain k_{desolv}. This choice of k_{solv} falls within the range of timescales from previous measurements,[38,57] although we note there exists substantial deviation in these timescales for different surfactants, and a unique measurement for Triton X-100 has not been made to the best of our knowledge. Nevertheless, the model results are in fact not sensitive to the absolute values of k_{solv} and k_{desolv} since the experimental time-scale is much longer than the equilibration time of the surfactant at the interface which is expected to be ~ ms.[38]

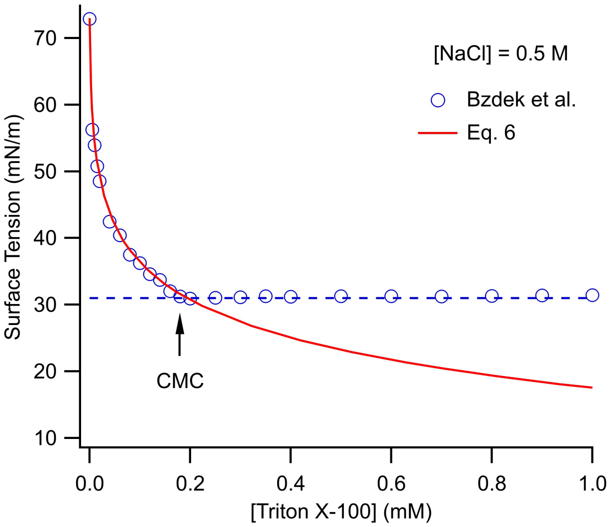

Fig. 4.5: Surface tension measurements by Bzdek et al.[35] of Triton X-100 solution in 0.5 M NaCl above and below the CMC ~ 0.2 mM. A fit to Eq. 4.6 is obtained to provide the maximum surface coverage Γ_{∞}^{TX} and Langmuir adsorption equilibrium coefficient K_{eq}^{TX} that are used directly in the kinetic model.

Benchmarked to macroscopic measurements, the partitioning of TX to the interface can be modeled in microdroplets using the same general mechanism. An important consequence of applying this description to micron-scale volumes is that the surface coverage fraction diverges from that expected in the macro-scale limit.[54] As demonstrated in Fig. 4.6A, divergence from the macroscopic behavior increases with smaller radii. This finite-volume effect arises from the depletion of surfactant concentration in the bulk interior when the surfactant partitions to the droplet interface.[58] Considering surface-to-volume constraints for a single droplet radius and the partitioning kinetics parametrized above for TX, a simple expression for adsorbed concentration and the corresponding depleted bulk concentration is obtained (see Appendix 4C for derivation):

$$\left[TX_{(ads)}\right] = \frac{1}{2 \cdot N_1} \cdot \left(N_2 - \sqrt{N_2^2 - 4 \cdot N_1 \cdot N_3}\right), \qquad \text{Eq. 4.8}$$

$$\left[TX_{(bulk)}\right] = [\mathrm{TX}]_0 - \left(\frac{3\,\delta}{r}\right) \cdot \frac{1}{2 \cdot N_1} \cdot \left(N_2 - \sqrt{N_2^2 - 4 \cdot N_1 \cdot N_3}\right), \qquad \text{Eq. 4.9}$$

where

$$N_1 = 3 \cdot k_{desolv} \cdot \delta^2, \qquad \text{Eq. 4.10a}$$

$$N_2 = 3 \cdot k_{desolv} \cdot \Gamma_{\infty}^{TX} \cdot \delta + k_{desolv} \cdot [\mathrm{TX}]_0 \cdot \delta \cdot r + k_{solv} \cdot \delta \cdot r, \qquad \text{Eq. 4.10b}$$

$$N_3 = k_{desolv} \cdot \Gamma_{\infty}^{TX} \cdot [\mathrm{TX}]_0 \cdot r. \qquad \text{Eq. 4.10c}$$

In Eqs. 4.8-4.10c, $[\mathrm{TX}]_0$ represents the nominal concentration of Triton X-100, equivalent to the bulk concentration in the total absence of finite-volume effects, *i.e.* the equivalent surfactant concentration in macro-scale volumes. This nominal concentration $[\mathrm{TX}]_0$ is taken as the independent quantity for most considerations and is used as the domain axis in Figs. 4.6A and 4.6B. While Eq. 4.8 provides the equilibrium surfactant concentration at the interface, Eq. 4.9

provides an expression for the corresponding equilibrium bulk concentration. This demonstrates how the true bulk concentration $[TX_{(bulk)}]$ in the microdroplet deviates from the nominal bulk concentration $[TX]_0$ as the droplet radius decreases, shown for an array of sizes and concentrations in Fig. 4.6B. Importantly, this equilibrated concentration $[TX_{(bulk)}]$ as defined by Eq. 4.9 is the relevant bulk concentration to describe competitive adsorption between I^- and TX. As such, the expression for $[TX_{(bulk)}]$ defined by Eq. 4.9 is used in Eq. 4.5 to accurately model the adsorbed concentration of I^- as a function of both $[I^-_{(bulk)}]$ and $[TX_{(bulk)}]$.

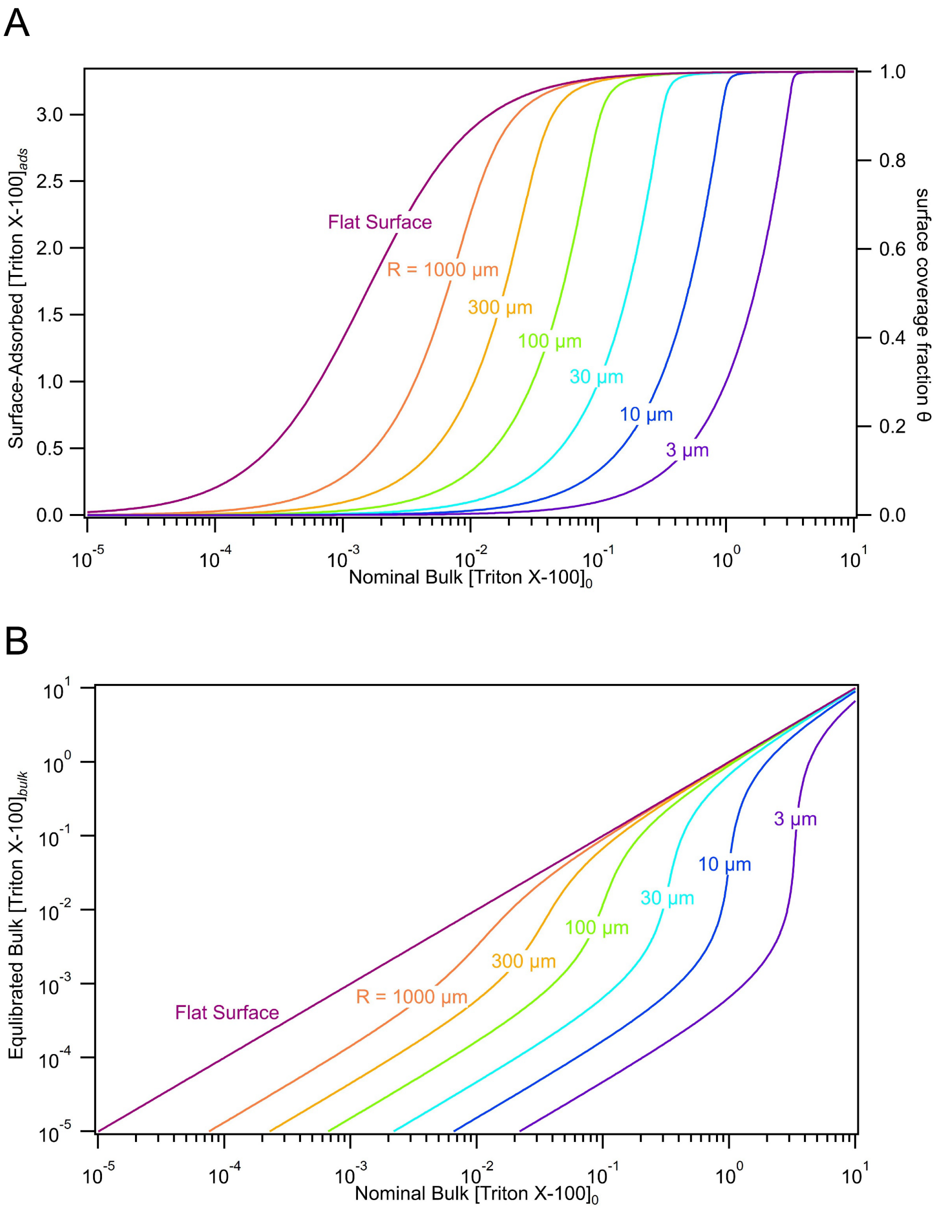

Fig. 4.6: Panel (A) shows the surface-adsorbed concentration (or fractional surface coverage) for [Triton X-100] ranging from 10^{-5}-10 mM in droplets with various radii. The suppression of coverage fraction for smaller microdroplets is a finite-volume effect, where adsorption to the interface is coupled to depletion of the bulk concentration. This is also demonstrated in panel (B), where the equilibrium [TX] is shown vs the nominal bulk concentration.

Using the definitions of $[\mathrm{I}^-_{(ads)}]$ (Eq. 4.5) and $[\mathrm{I}^-_{(rd)}]$ (simply the bulk iodide concentration $[\mathrm{I}^-_{(bulk)}]_0$), steady-state concentrations of O_3 in the respective regions can be defined. This is accomplished by applying a quasi-steady-state condition to the entire kinetic framework, with details provided in Appendix 4C. Resulting concentrations are defined in terms of the rate coefficients for the surface- and bulk-reaction ($k_{rxn}^{surf}, k_{rxn}^{bulk}$) and coefficients pertaining to mass transport including gas-diffusion (k_{diff}^{gas}), liquid-diffusion ($k_{diff1}^{liq}, k_{diff2}^{liq}$), adsorption and desorption from the gas to the interface (k_{ads}, k_{des}), and desolvation/solvation from the liquid to the interface (k_{desolv}, k_{solv}):

$[\mathrm{O}_{3(ads)}] =$

$$\left(\frac{k_{diff}^{gas}\, k_{ads}}{k_{diff}^{gas} + k_{ads}}\right) \cdot [\mathrm{O}_{3(gas)}] \Bigg/ \left(\begin{array}{c} k_{des} + k_{solv} + [\mathrm{I}^-_{(ads)}] k_{rxn}^{surf} - \left(\frac{k_{des}\, k_{ads}}{k_{diff}^{gas} + k_{ads}}\right) - \left(\frac{k_{desolv}\, k_{solv}}{k_{diff1}^{liq} + k_{desolv}}\right) - \\ \left(\frac{k_{diff1}^{liq}\, k_{diff2}^{liq}\, k_{desolv}\, k_{solv}}{\left(k_{diff2}^{liq} + k_{desolv}\right) \times \left(k_{desolv}\, [\mathrm{I}^-_{(rd)}]\, k_{rxn}^{bulk} + k_{diff1}^{liq} [\mathrm{I}^-_{(rd)}] k_{rxn}^{bulk} + k_{diff2}^{liq}\, k_{desolv}\right)}\right) \end{array} \right),$$

Eq. 4.11

$$[\mathrm{O}_{3(rd)}] = \frac{k_{diff2}^{liq}\, k_{solv}\, [\mathrm{O}_{3(ads)}]}{k_{desolv}\, [\mathrm{I}^-_{(rd)}]\, k_{rxn}^{bulk} + k_{desolv}\, k_{diff2}^{liq} + k_{diff1}^{liq} [\mathrm{I}^-_{(rd)}]\, k_{rxn}^{bulk}}. \qquad \text{Eq. 4.12}$$

Note that Eq. 4.12 is defined implicitly in terms of the adsorbed ozone concentration in Eq. 4.11 for the sake of brevity.

The origin of the many kinetic coefficients found in Eq. 4.11 and Eq. 4.12 are explained in more detail in Chapter 3 and in Appendix 4C. Briefly, the reaction rate $k_{rxn}^{bulk} = 1.2\times10^9$ M^{-1} s^{-1} is from previous literature measurements[59,60] and $k_{rxn}^{surf} = 6\times10^7$ M^{-1} s^{-1} is identified in Chapter 3 proposing a diminished overall surface reactivity for this specific reaction system. The pairs of kinetic constants k_{solv}/k_{desolv} and k_{des}/k_{ads} are obtained through an analysis of the timescales associated with molecular motions as observed in MD simulations of O_3 at the air-water interface.[46,61] Diffusional constants k_{diff}^{gas}, k_{diff1}^{liq}, and k_{diff2}^{liq} originate from geometric constraints—applying flux-matching condition at spherical boundaries[62] (see Chapter 5 Appendix 5C) along with the use of Fick's first law.[63] These terms come out to be simple expressions of diffusion over a combined relevant length scale:

$$k_{diff}^{gas} = \frac{D_{gas}}{r\,\delta},$$

$$k_{diff1}^{liq} = \frac{2\,D_{liq}}{(L_{RD} + \delta)\delta},$$

$$k_{diff2}^{liq} = \frac{2\,D_{liq}}{(L_{RD} + \delta)L_{RD}}.$$

Expressions for the uptake coefficients given in Eqs. 4.2 and 4.3 are now fully defined by Eqs. 4.11 and 4.12. We highlight that the competitive adsorption isotherm defining $[\mathrm{I}^-_{(ads)}]$ in Eq. 4.5 is necessary to calculate $[\mathrm{O}_{3(ads)}]$ in Eq. 4.11 and $[\mathrm{O}_{3(rd)}]$ in Eq. 4.12. Note that the competitive adsorption description in Eq. 4.5 itself relies on the depletion equation for $[TX_{(bulk)}]$ in Eq. 4.9.

4.5: Discussion

By implementing the approach outlined above, a quantitative assessment of the observed kinetics is achieved. As shown in Fig. 4.4, the total uptake calculated by Eq. 4.4 agrees with the measured uptake coefficients as [TX] increases from 6 μM to 3.2 mM. Individual uptake contributions from the surface region (Eq. 4.2) and RD region (Eq. 4.3) demonstrate that the overall reactivity is dominated by the surface reaction when [TX] < 150 μM, which becomes increasingly inhibited when [TX] > 150 μM, accompanied by a slight rise in the overall reactivity of the RD region. Importantly, the degree of reaction suppression plateaus when [TX] > 500 μM, indicating the microdroplet surface is virtually saturated by Triton X-100 and devoid of I^-. In this scenario, reactivity becomes almost purely due to sub-surface reactivity in the RD region since I^- is completely displaced from the surface by TX. The surface-to-subsurface transition point in the $[TX]_0$ domain and the shape of the uptake dependence observed in experiment is reproduced by the analytical expression Eq. 4.4.

The unique chemical kinetics observed in the experiments and the analytical expression arise from multiple factors that are highly specific to the conditions of the experiment. The first, and most clear, is the increasing displacement of I^- at the air-water interface with increasing [TX]. The potential for I^- displacement by TX has been modeled using a competitive Langmuir adsorption isotherm parametrized from surface-tension measurements of aqueous TX and from molecular dynamics simulations for I^-. Although a competitive-adsorption framework is utilized, we note that due to the much greater preference for TX to the interface than I^-, the actual adsorption competition is very weak. The second key observation reflected in the uptake coefficients is the range over which TX inhibits the surface reaction and the shape of the affected uptake. This concentration range and shape are unique to the depletion of TX within the bulk interior of the microdroplet which is highly dependent on droplet radius, as previously noted, and mirrors the surface fractional coverage for microdroplets shown in Fig. 4.6A.

A similar degree of $I^- + O_3$ reaction suppression was previously reported by Rouvière et al. in the study of O_3 uptake onto deliquesced submicron KI aerosol with varying dry-mass fraction of added fatty acid.[64] The series of fatty acids investigated are varied in carbon-chain length, with larger molecular footprints generally resulting in larger degrees of reaction suppression, up to over an order of magnitude decrease in overall uptake with increasing surfactant concentration. However, these submicron experiments are not directly comparable to the current work as the fatty acids are included at much higher mass fractions than the current work and far above the solubility limit. As such, Rouvière et al.[64] observe reaction suppression largely due to surface-film formation rather than monolayer coverage as investigated in the present work. Chemical effects of films and monolayers also become relevant for understanding the reactivity of iodide in the sea-surface microlayer, which contains a complex mixture of inorganic and surface-active organic molecules. Work from Tinel et al.[65] has analyzed the volatile product distributions from O_3 oxidation of simulated seawater and real SSM samples, demonstrating that microlayer composition has a marked effect on I_2 formation rates. Similarly, Schneider et al.[66] measured the production of I_2 from the ozone uptake onto aqueous iodide solutions under varying conditions with proxies to seawater and microlayer conditions. While the impact of surfactant adsorption to iodide-chemistry in the SSM is likely significant, we note that the behavior analyzed here applies more directly to concentrated solutions where surface reactions dominate—whereas the dilute [I^-] found in seawater indicate a regime already dominated by liquid-diffusion limitations in the reaction-diffusion region.[67]

We emphasize that the inclusion of Triton X-100 into the previously developed chemical kinetic framework[46] involves no adjustable parameters, and the mechanistic addition of TX relies only on previous surface-tension measurements[35] and assuming Langmurian adsorption behavior. While the Langmuir-adsorption description is generally accepted to be an oversimplification (especially for describing gas-liquid dynamics), the additive behavior of a Langmuir-adsorption description in the current work shows remarkable agreement with experiment. We believe this is the case because TX adsorption to the interface is much more favorable than I^-, while we expect this simplistic model to potentially break down for two (or more) strongly adsorbing reagents, especially in a highly concentrated regime.

4.6: Conclusion

Chemical reactivity at interfaces is increasingly explored and invoked to explain broad changes in observed chemical kinetics in environments where surfaces become relevant. Aerosol and microdroplet chemistry, unsurprisingly, is at the forefront of such exploration since these systems often show distinct signatures that indicate the presence of surface reactions and provide a convenient reaction platform for investigating interfacial effects. Here, we present a prototypical example of coupled interfacial phenomena directly inhibiting the $I^- + O_3$ surface reaction in levitated microdroplets. The surfactant Triton X-100 is observed to suppress the surface reaction when the surface coverage fraction is high enough to displace I^- from the air water interface, agreeing with a Langmuir-type adsorption description. The TX concentration dependence of O_3 reactive uptake reflects the coverage function of TX—demonstrating a microdroplet-specific signature due to the bulk-depletion effect of TX adsorption to the air-water interface. An analytical expression for reactive uptake on the aqueous surface and within the sub-surface region was derived based on a previously developed framework and in light of additional surface tension measurements of aqueous TX. This work demonstrates how insights into molecular timescales of mass transfer across interfaces, combined with macroscopic surface tension measurements, inform on chemical reactivity in micron-scale compartments containing a mixture of organic and inorganic components.

4.7: Chapter 4 Appendix – Supplemental Information

Appendix 4A: Experimental

Here we provide supplementary information about the experimental conditions used. The experimental scheme is identical to the QET-OPSI assembly described in Chapters 2 & 3 (See Fig. 2.1 and Fig. 3.1). An example mass spectrum is provided in Fig. 4A.1 showing the strong signal intensity at m/z = 126.9 resulting from the iodide ion. The citric acid buffer can also be observed both before and after the reaction. An example scattering phase function used to quantify the droplet radii for each experiment is provided in Fig. 4A.2. The angular spacing between peaks in the interference pattern is used to identify the radius of a given microdroplet by referencing a library of simulated peak positions and spacings. The details of this approach and the algorithm employed can be found in previous work[45] and by Davies and co-workers.[50,68]

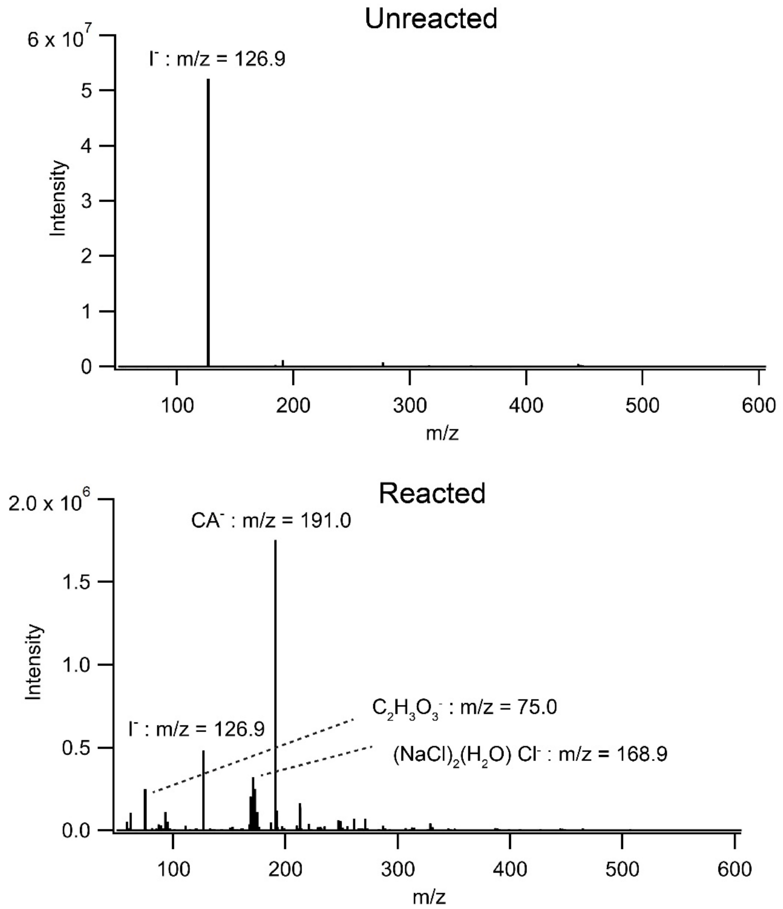

Fig. 4A.1: Mass spectra for unreacted and reacted microdroplets containing NaI, NaCl, citric acid buffer at pH 3 with 32 μM of Triton X-100. The only noticeable change in the spectra is loss of I^- due to oxidation by O_3 and a more visible background.

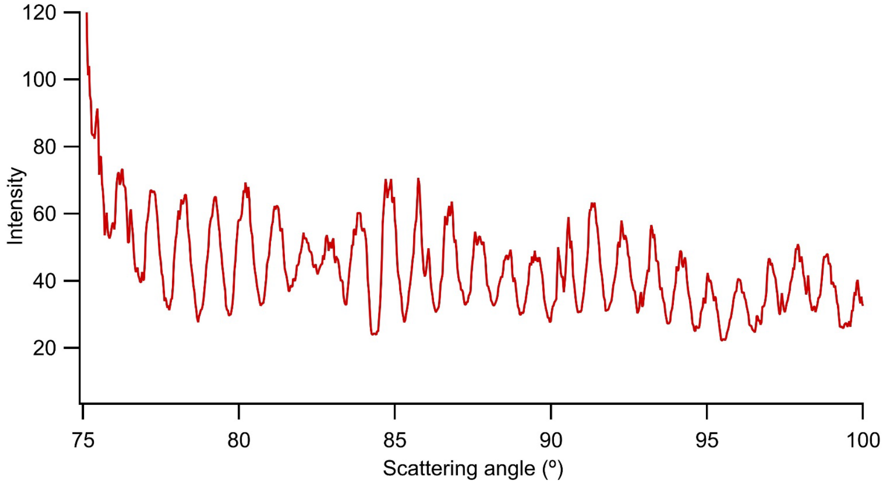

Fig. 4A.2: Scattering intensity vs. collection angle for Mie scattering from a 17 μm radius droplet.

Appendix 4B: Model Framework & Kinetic Simulations

The kinetic model used for the present analysis has been discussed extensively in recent works.[46,47,55] For details on the conceptual model framework, we reference the reader to Chapter 3—which provides an overview of the updated framework to include sub-surface reactivity. Each step used to generate the simulated kinetic profiles is also provided therein. The underlying chemical mechanism for this reaction system, including pH dependence, was explored in more detail in previous work.[46] The current model framework follows exactly that described by Chapter 3 Appendix 3A, with the addition of a Triton X-100 adsorption step, as explained in the main text, Section 4.4. The adsorption step was included in the surface-compartment of the kinetic description to run all simulations.

Appendix 4C: Steady-state analysis methods

Here we provide further detail on the steady-state approach used to derive the analytical expressions. The core assumption used in this approach is that once the droplet is dispensed and reaction has begun, a quasi-steady-state condition is quickly attained which can be approximated by defining instantaneous concentrations of each species defined in the kinetic model framework. We briefly outline the derivation of the surfactant adsorption equations governing the "bulk-depletion" effect to demonstrate the utility of this approach and the origin of Eqs 4.8-4.10a in Section 4.4. Subsequently, we demonstrate how the same approach is used to quantify steady-state concentration of reactants [O_3] in the two relevant kinetic domains (i.e., the surface and the subsurface or "reaction-diffusion" region).

(i) Surfactant Adsorption

As illustrated in the main text, surfactant adsorption is treated with the kinetic step

$$\mathrm{TX}_{(bulk)} + \mathrm{site} \underset{k_{solv}}{\overset{k_{desolv}}{\rightleftarrows}} \mathrm{TX}_{(ads)}, \qquad (S1)$$

where the kinetics are described by a standard Langmuir-adsorption isotherm:

$$\left[TX_{(ads)}\right] = \frac{\Gamma_\infty^{TX}}{\delta}\frac{K_{eq}^{TX}\cdot\left[TX_{(bulk)}\right]}{1+K_{eq}^{TX}\cdot\left[TX_{(bulk)}\right]}. \qquad \text{Eq. 4C. 1}$$

Recall that $K_{eq}^{TX} = \frac{k_{desolv}}{k_{solv}}$ and that $\frac{\Gamma_\infty^{TX}}{\delta}$ represents the maximum concentration of available surface sites for Triton X-100. Noting the process expressed by Step S1, the dynamics of surfactant adsorption in the microdroplet can be expressed with the differential:

$$\frac{d\left[TX_{(ads)}\right]}{dt} = k_{desolv}\,[\mathrm{site}]\left[TX_{(bulk)}\right] - k_{solv}\left[TX_{(ads)}\right]. \qquad \text{Eq. 4C. 2}$$

We now use the steady-state assumption, $\frac{d\left[TX_{(ads)}\right]}{dt} = 0$, to relate the concentrations of $\left[TX_{(ads)}\right]$ and $\left[TX_{(bulk)}\right]$:

$$k_{solv}\left[TX_{(ads)}\right] = k_{desolv}\,[\mathrm{site}]\left[TX_{(bulk)}\right], \qquad \text{Eq. 4C. 3}$$

where the available site concentration is

$$[\text{site}] = \frac{\Gamma_{\infty}^{TX}}{\delta} - \left[TX_{(ads)}\right]. \qquad \text{Eq. 4C. 4}$$

Furthermore, $\left[TX_{(ads)}\right]$ and $\left[TX_{(bulk)}\right]$ must be related by conserving the total number of TX molecules present in the microdroplet, providing a further constraint

$$\left[TX_{(bulk)}\right]_0 = \left[TX_{(bulk)}\right] + \frac{3\,\delta}{r}\left[TX_{(ads)}\right], \qquad \text{Eq. 4C. 5}$$

where δ is the thickness of the droplet interface (1 nm) and *r* is the droplet radius. In Eq. 4C.5, $\left[TX_{(bulk)}\right]_0$ is the bulk concentration at t = 0, where we assume $\left[TX_{(ads)}\right] = 0$. Solving Eqs. 4C.3-4C.5 provides expressions for $\left[TX_{(ads)}\right]$ and $\left[TX_{(bulk)}\right]$, presented as Eqs. 4.8 and 4.9. Lastly, we note that the approach outlined here assumes a static droplet radius *r*. Allowing *r* to change (due to evaporation or condensation of water, for example), provides similar equations, but with more geometric detail.

(ii) Surface-Adsorbed and Solvated Ozone concentrations

An analogous approach is used to obtain expressions for ozone concentrations at the interface and within the sub-surface layer. While we do not provide an extensive discussion of how steady-state concentrations are derived, we provide a brief conceptual overview of the approach—while reserving a larger discussion to future work. The steady-state concentrations of O_3 at the interface and within the sub-surface are conceptually grounded in the kinetic model built in Kinetiscope. In the mechanics of this model, the surface adsorbed $O_{3(ads)}$ and the subsurface (or reaction-diffusion compartment) species $O_{3(rd)}$ are related through a solvation/desolvation process occurring in the top nm of solution, and a liquid diffusion description extending the length of the reaction-diffusion length. This is conceptually outlined in Fig. 4C.1. As shown, this description invokes an intermediate "surface-to-bulk" species, termed $O_{3(sb)}$ that represents the O_3 which has undergone solvation across the interface but has yet to diffuse into the reaction-diffusion compartment. As such, no reaction for $O_{3(sb)}$ is defined as the species acts mostly as a bookkeeping concentration to define solvation and diffusion from the interface. In parallel, on the other side of the interface, a very similar approach is used to define another transient "gas-to-surface" species $O_{3(gs)}$, indicating ozone which has diffused from the gas-phase to the droplet interface but has yet to undergo actual adsorption and thermal accommodation to the interface (or equivalently, O_3 which has desorbed from the interface, but has yet to diffuse away from the droplet surface). These transient species $O_{3(sb)}$ and $O_{3(gs)}$ are necessary to fully implement the steady state approach but are effectively eliminated when solving for the species of interest $O_{3(ads)}$ and $O_{3(rd)}$. As noted in Section 4.4, we choose to ignore the ozone reactivity in the inner bulk compartment, $[O_{3(bulk)}]$ since the vast majority of reactivity occurs at the surface or in the reaction-diffusion region.

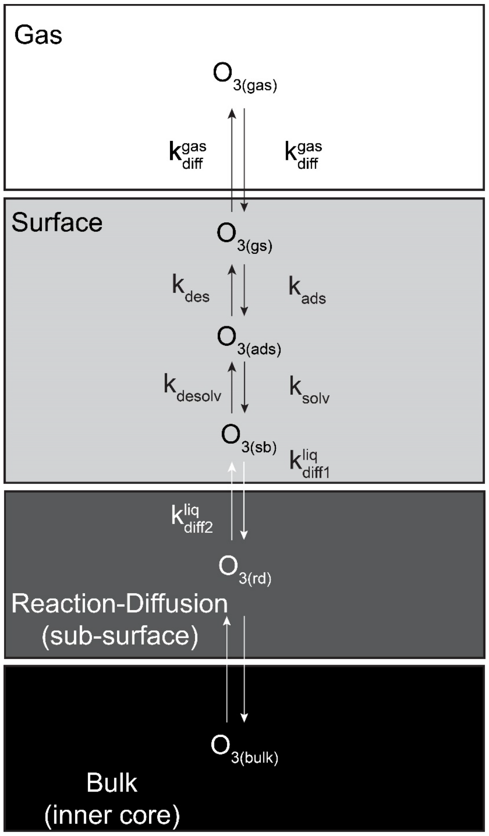

Fig. 4C.1: Kinetic scheme showing mass transport pathways in model framework. The five related species can be used to create steady-state concentrations of $O_{3(ads)}$ and $O_{3(rd)}$ in the current work. As noted in the text, $O_{3(bulk)}$ is found to be negligible and so omitted in the analysis.

To solve for the concentrations $[O_{3(ads)}]$ and $[O_{3(rd)}]$, rate equations are first defined for the four species identified, where $[O_{3(gas)}]$ represents the static gas phase concentration arbitrarily far from the droplet surface:

$$\frac{d[O_{3(gs)}]}{dt} = k^{gas}_{diff}[O_{3(gas)}] + k_{des}[O_{3(ads)}] - k^{gas}_{diff}[O_{3(gs)}] - k_{ads}\frac{\Gamma_{\infty(O_3)}}{\delta}[O_{3(gs)}], \qquad \text{Eq. 4C. 6}$$

$$\frac{d[O_{3(ads)}]}{dt} = k_{ads}\frac{\Gamma_{\infty(O_3)}}{\delta}[O_{3(gs)}] + k_{desolv}\frac{\Gamma_{\infty(O_3)}}{\delta}[O_{3(sb)}] - k_{des}[O_{3(ads)}] - k_{solv}[O_{3(ads)}] - k^{srf}_{rxn}[I^-_{(ads)}][O_{3(ads)}], \qquad \text{Eq. 4C. 7}$$

$$\frac{d[O_{3(sb)}]}{dt} = k_{solv}[O_{3(ads)}] + k^{liq}_{diff1}[O_{3(rd)}] - k_{desolv}\frac{\Gamma_{\infty(O_3)}}{\delta}[O_{3(ads)}] - k^{liq}_{diff1}[O_{3(sb)}], \qquad \text{Eq. 4C. 8}$$

$$\frac{d[O_{3(rd)}]}{dt} = k^{liq}_{diff2}[O_{3(sb)}] - k^{liq}_{diff2}[O_{3(rd)}] - k^{blk}_{rxn}[I^-_{(rd)}][O_{3(rd)}], \qquad \text{Eq. 4C. 9}$$

Kinetic coefficients found in Eq. 4C.6-4C.9 can be found in the associated kinetic simulation description. The liquid diffusion rate coefficients k_{diff}^{liq1} and k_{diff}^{liq2} are explored more rigorously in the following Chapter 5, Appendix 5B, but are simply defined to reproduce the flux between adjacent regions through the application of Fick's first law, with

$$k_{diff1}^{liq} = \frac{2D}{(L_{RD} + \delta)\delta},$$

$$k_{diff2}^{liq} = \frac{2D}{(L_{RD} + \delta)L_{RD}},$$

where L_{rxn} is the reaction diffusion length of O_3 in solution given the initial [I^-], (which also defines the length of the RD compartment).

Applying a steady-state assumption, all differentials Eq. 4C.6-4C.9 are assumed to be zero, enabling one to solve for each of the four concentrations in terms of the overall gas concentration [$O_{3(gas)}$] and the iodide concentration, (where [$I^-_{(rd)}$] and [$I^-_{(ads)}$]) are related through a Langmuir isotherm as outlined in the main text. Solving in this manner produces expressions for [$O_{3(ads)}$] and [$O_{3(rd)}$] as given in Eq. 4.11 and Eq. 4.12 in Section 4.4.

4.8: References

(1) Wei, Z.; Li, Y.; Cooks, R. G.; Yan, X. Accelerated Reaction Kinetics in Microdroplets: Overview and Recent Developments. *Annual Review of Physical Chemistry* **2020**, *71* (Volume 71, 2020), 31–51. https://doi.org/10.1146/annurev-physchem-121319-110654.

(2) Brown, E. K.; Rovelli, G.; Wilson, K. R. pH Jump Kinetics in Colliding Microdroplets: Accelerated Synthesis of Azamonardine from Dopamine and Resorcinol. *Chemical Science* **2023**, *14* (23), 6430–6442. https://doi.org/10.1039/D3SC01576A.

(3) Wilson, K. R.; Prophet, A. M.; Rovelli, G.; Willis, M. D.; Rapf, R. J.; Jacobs, M. I. A Kinetic Description of How Interfaces Accelerate Reactions in Micro-Compartments. *Chemical Science* **2020**, *11* (32), 8533–8545. https://doi.org/10.1039/D0SC03189E.

(4) Nam, I.; Lee, J. K.; Nam, H. G.; Zare, R. N. Abiotic Production of Sugar Phosphates and Uridine Ribonucleoside in Aqueous Microdroplets. *Proceedings of the National Academy of Sciences* **2017**, *114* (47), 12396–12400. https://doi.org/10.1073/pnas.1714896114.

(5) Jacobs, M. I.; Davis, R. D.; Rapf, R. J.; Wilson, K. R. Studying Chemistry in Micro-Compartments by Separating Droplet Generation from Ionization. *Journal of the American Society for Mass Spectrometry* **2019**, *30* (2), 339–343. https://doi.org/10.1007/s13361-018-2091-y.

(6) Rovelli, G.; Jacobs, M. I.; Willis, M. D.; Rapf, R. J.; Prophet, A. M.; Wilson, K. R. A Critical Analysis of Electrospray Techniques for the Determination of Accelerated Rates and Mechanisms of Chemical Reactions in Droplets. *Chemical Science* **2020**, *11* (48), 13026–13043. https://doi.org/10.1039/D0SC04611F.

(7) J. Chen, C.; R. Williams, E. The Role of Analyte Concentration in Accelerated Reaction Rates in Evaporating Droplets. *Chemical Science* **2023**, *14* (18), 4704–4713. https://doi.org/10.1039/D3SC00259D.

(8) Lee, J. K.; Walker, K. L.; Han, H. S.; Kang, J.; Prinz, F. B.; Waymouth, R. M.; Nam, H. G.; Zare, R. N. Spontaneous Generation of Hydrogen Peroxide from Aqueous Microdroplets. *Proceedings of the National Academy of Sciences* **2019**, *116* (39), 19294–19298. https://doi.org/10.1073/pnas.1911883116.

(9) Gallo, A.; Farinha, A. S. F.; Dinis, M.; Emwas, A.-H.; Santana, A.; Nielsen, R. J.; Goddard, W. A.; Mishra, H. The Chemical Reactions in Electrosprays of Water Do Not Always Correspond to Those at the Pristine Air–Water Interface. *Chemical Science* **2019**, *10* (9), 2566–2577. https://doi.org/10.1039/C8SC05538F.

(10) Xiong, H.; Lee, J. K.; Zare, R. N.; Min, W. Strong Electric Field Observed at the Interface of Aqueous Microdroplets. *J. Phys. Chem. Lett.* **2020**, *11* (17), 7423–7428. https://doi.org/10.1021/acs.jpclett.0c02061.

(11) Martins-Costa, M. T. C.; Ruiz-López, M. F. Probing Solvation Electrostatics at the Air–Water Interface. *Theor Chem Acc* **2023**, *142* (3), 29. https://doi.org/10.1007/s00214-023-02969-y.

(12) Ahmad Eatoo, M.; Mishra, H. Busting the Myth of Spontaneous Formation of H 2 O 2 at the Air–Water Interface: Contributions of the Liquid–Solid Interface and Dissolved Oxygen Exposed. *Chemical Science* **2024**, *15* (9), 3093–3103. https://doi.org/10.1039/D3SC06534K.

(13) Heindel, J. P.; LaCour, R. A.; Head-Gordon, T. The Role of Charge in Microdroplet Redox Chemistry. *Nat Commun* **2024**, *15* (1), 3670. https://doi.org/10.1038/s41467-024-47879-0.

(14) Valsaraj, K. T. Hydrophobic Compounds in the Environment: Adsorption Equilibrium at the Air-Water Interface. *Water Research* **1994**, *28* (4), 819–830. https://doi.org/10.1016/0043-1354(94)90088-4.

(15) Vaikuntanathan, S.; Shaffer, P. R.; Geissler, P. L. Adsorption of Solutes at Liquid–Vapor Interfaces: Insights from Lattice Gas Models. *Faraday Discuss.* **2013**, *160* (0), 63–74. https://doi.org/10.1039/C2FD20106B.

(16) Otten, D. E.; Shaffer, P. R.; Geissler, P. L.; Saykally, R. J. Elucidating the Mechanism of Selective Ion Adsorption to the Liquid Water Surface. *Proceedings of the National Academy of Sciences* **2012**, *109* (3), 701–705. https://doi.org/10.1073/pnas.1116169109.

(17) Goss, K.-U. Predicting Adsorption of Organic Chemicals at the Air−Water Interface. *J. Phys. Chem. A* **2009**, *113* (44), 12256–12259. https://doi.org/10.1021/jp907347p.

(18) Devlin, S. W.; Benjamin, I.; Saykally, R. J. On the Mechanisms of Ion Adsorption to Aqueous Interfaces: Air-Water vs. Oil-Water. *Proceedings of the National Academy of Sciences* **2022**, *119* (42), e2210857119. https://doi.org/10.1073/pnas.2210857119.

(19) Zou, Y.-S.; Fukuta, N. The Effect of Diffusion Kinetics on the Supersaturation in Clouds. *Atmospheric Research* **1999**, *52* (1), 115–141. https://doi.org/10.1016/S0169-8095(99)00025-3.

(20) Bell, A. K.; Kind, J.; Hartmann, M.; Kresse, B.; Höfler, M. V.; Straub, B. B.; Auernhammer, G. K.; Vogel, M.; Thiele, C. M.; Stark, R. W. Concentration Gradients in Evaporating Binary Droplets Probed by Spatially Resolved Raman and NMR Spectroscopy. *Proceedings*

of the National Academy of Sciences **2022**, *119* (15), e2111989119. https://doi.org/10.1073/pnas.2111989119.

(21) Karmakar, T.; Finney, A. R.; Salvalaglio, M.; Yazaydin, A. O.; Perego, C. Non-Equilibrium Modeling of Concentration-Driven Processes with Constant Chemical Potential Molecular Dynamics Simulations. *Acc. Chem. Res.* **2023**, *56* (10), 1156–1167. https://doi.org/10.1021/acs.accounts.2c00811.

(22) Qiu, L.; Wei, Z.; Nie, H.; Cooks, R. G. Reaction Acceleration Promoted by Partial Solvation at the Gas/Solution Interface. *ChemPlusChem* **2021**, *86* (10), 1362–1365. https://doi.org/10.1002/cplu.202100373.

(23) Martins-Costa, M. T. C.; Ruiz-López, M. F. Electrostatics and Chemical Reactivity at the Air–Water Interface. *J. Am. Chem. Soc.* **2023**, *145* (2), 1400–1406. https://doi.org/10.1021/jacs.2c12089.

(24) Limmer, D. T.; Götz, A. W.; Bertram, T. H.; Nathanson, G. M. Molecular Insights into Chemical Reactions at Aqueous Aerosol Interfaces. *Annual Review of Physical Chemistry* **2024**, *75* (Volume 75, 2024), 111–135. https://doi.org/10.1146/annurev-physchem-083122-121620.

(25) Prisle, N. L.; Raatikainen, T.; Laaksonen, A.; Bilde, M. Surfactants in Cloud Droplet Activation: Mixed Organic-Inorganic Particles. *Atmospheric Chemistry and Physics* **2010**, *10* (12), 5663–5683. https://doi.org/10.5194/acp-10-5663-2010.

(26) Ruehl, C. R.; Davies, J. F.; Wilson, K. R. An Interfacial Mechanism for Cloud Droplet Formation on Organic Aerosols. *Science* **2016**, *351* (6280), 1447–1450. https://doi.org/10.1126/science.aad4889.

(27) Ovadnevaite, J.; Zuend, A.; Laaksonen, A.; Sanchez, K. J.; Roberts, G.; Ceburnis, D.; Decesari, S.; Rinaldi, M.; Hodas, N.; Facchini, M. C.; Seinfeld, J. H.; O' Dowd, C. Surface Tension Prevails over Solute Effect in Organic-Influenced Cloud Droplet Activation. *Nature* **2017**, *546* (7660), 637–641. https://doi.org/10.1038/nature22806.

(28) Davies, J. F.; Zuend, A.; Wilson, K. R. Technical Note: The Role of Evolving Surface Tension in the Formation of Cloud Droplets. *Atmospheric Chemistry and Physics* **2019**, *19* (5), 2933–2946. https://doi.org/10.5194/acp-19-2933-2019.

(29) Lin, J. J.; Kristensen, T. B.; Calderón, S. M.; Malila, J.; Prisle, N. L. Effects of Surface Tension Time-Evolution for CCN Activation of a Complex Organic Surfactant. *Environ. Sci.: Processes Impacts* **2020**, *22* (2), 271–284. https://doi.org/10.1039/C9EM00426B.

(30) McGraw, R.; Wang, J. Surfactants and Cloud Droplet Activation: A Systematic Extension of Köhler Theory Based on Analysis of Droplet Stability. *The Journal of Chemical Physics* **2021**, *154* (2), 024707. https://doi.org/10.1063/5.0031436.

(31) Prisle, N. L. Surfaces of Atmospheric Droplet Models Probed with Synchrotron XPS on a Liquid Microjet. *Acc. Chem. Res.* **2024**, *57* (2), 177–187. https://doi.org/10.1021/acs.accounts.3c00201.

(32) Bunton, C. A. Reaction Kinetics in Aqueous Surfactant Solutions. *Catalysis Reviews* **1979**, *20* (1), 1–56. https://doi.org/10.1080/03602457908065104.

(33) Park, S.-C.; Burden, D. K.; Nathanson, G. M. Surfactant Control of Gas Transport and Reactions at the Surface of Sulfuric Acid. *Acc. Chem. Res.* **2009**, *42* (2), 379–387. https://doi.org/10.1021/ar800172m.

(34) Samiey, B.; Cheng, C.-H.; Wu, J. Effects of Surfactants on the Rate of Chemical Reactions. *Journal of Chemistry* **2014**, *2014* (1), 908476. https://doi.org/10.1155/2014/908476.

(35) Bzdek, B. R.; Reid, J. P.; Malila, J.; Prisle, N. L. The Surface Tension of Surfactant-Containing, Finite Volume Droplets. *Proceedings of the National Academy of Sciences* **2020**, *117* (15), 8335–8343. https://doi.org/10.1073/pnas.1915660117.

(36) Bain, A.; Ghosh, K.; Prisle, N. L.; Bzdek, B. R. Surface-Area-to-Volume Ratio Determines Surface Tensions in Microscopic, Surfactant-Containing Droplets. *ACS Cent. Sci.* **2023**, *9* (11), 2076–2083. https://doi.org/10.1021/acscentsci.3c00998.

(37) Singh, M.; Jones, S. H.; Kiselev, A.; Duft, D.; Leisner, T. The Viscosity and Surface Tension of Supercooled Levitated Droplets Determined by Excitation of Shape Oscillations. *Atmospheric Measurement Techniques* **2023**, *16* (21), 5205–5215. https://doi.org/10.5194/amt-16-5205-2023.

(38) Bain, A.; Lalemi, L.; Croll Dawes, N.; Miles, R. E. H.; Prophet, A. M.; Wilson, K. R.; Bzdek, B. R. Surfactant Partitioning Dynamics in Freshly Generated Aerosol Droplets. *J. Am. Chem. Soc.* **2024**. https://doi.org/10.1021/jacs.4c03041.

(39) Swanson, B. E.; Frossard, A. A. Influence of Selected Cationic, Anionic, and Nonionic Surfactants on Hygroscopic Growth of Individual Aqueous Coarse Mode Aerosol Particles. *Aerosol Science and Technology* **2022**, *57* (1), 63–76. https://doi.org/10.1080/02786826.2022.2144114.

(40) Frossard, A. A.; Gérard, V.; Duplessis, P.; Kinsey, J. D.; Lu, X.; Zhu, Y.; Bisgrove, J.; Maben, J. R.; Long, M. S.; Chang, R. Y.-W.; Beaupré, S. R.; Kieber, D. J.; Keene, W. C.; Nozière, B.; Cohen, R. C. Properties of Seawater Surfactants Associated with Primary Marine Aerosol Particles Produced by Bursting Bubbles at a Model Air–Sea Interface. *Environ. Sci. Technol.* **2019**, *53* (16), 9407–9417. https://doi.org/10.1021/acs.est.9b02637.

(41) Dommer, A. C.; Wauer, N. A.; Angle, K. J.; Davasam, A.; Rubio, P.; Luo, M.; Morris, C. K.; Prather, K. A.; Grassian, V. H.; Amaro, R. E. Revealing the Impacts of Chemical Complexity on Submicrometer Sea Spray Aerosol Morphology. *ACS Cent. Sci.* **2023**, *9* (6), 1088–1103. https://doi.org/10.1021/acscentsci.3c00184.

(42) Makievski, A. V.; Fainerman, V. B.; Joos, P. Dynamic Surface Tension of Micellar Triton X-100 Solutions by the Maximum-Bubble-Pressure Method. *Journal of Colloid and Interface Science* **1994**, *166* (1), 6–13. https://doi.org/10.1006/jcis.1994.1264.

(43) Fainerman, V. B.; Lylyk, S. V.; Aksenenko, E. V.; Makievski, A. V.; Petkov, J. T.; Yorke, J.; Miller, R. Adsorption Layer Characteristics of Triton Surfactants: 1. Surface Tension and Adsorption Isotherms. *Colloids and Surfaces A: Physicochemical and Engineering Aspects* **2009**, *334* (1), 1–7. https://doi.org/10.1016/j.colsurfa.2008.09.015.

(44) Robinson, J. E.; Sutton, C. M.; Reid, G. F. Dilute Triton X-100 in Water as a Reference Liquid for Hydrometer Calibration Using Cuckow's Method. *Measurement* **2014**, *57*, 132–137. https://doi.org/10.1016/j.measurement.2014.08.001.

(45) Willis, M. D.; Rovelli, G.; Wilson, K. R. Combining Mass Spectrometry of Picoliter Samples with a Multicompartment Electrodynamic Trap for Probing the Chemistry of Droplet Arrays. *Anal. Chem.* **2020**, *92* (17), 11943–11952. https://doi.org/10.1021/acs.analchem.0c02343.

(46) Prophet, A. M.; Polley, K.; Van Berkel, G. J.; Limmer, D. T.; Wilson, K. R. Iodide Oxidation by Ozone at the Surface of Aqueous Microdroplets. *Chemical Science* **2024**, *15* (2), 736–756. https://doi.org/10.1039/D3SC04254E.

(47) Willis, M. D.; Wilson, K. R. Coupled Interfacial and Bulk Kinetics Govern the Timescales of Multiphase Ozonolysis Reactions. *J. Phys. Chem. A* **2022**, *126* (30), 4991–5010. https://doi.org/10.1021/acs.jpca.2c03059.

(48) Kaur Kohli, R.; Van Berkel, G. J.; Davies, J. F. An Open Port Sampling Interface for the Chemical Characterization of Levitated Microparticles. *Anal. Chem.* **2022**, *94* (8), 3441–3445. https://doi.org/10.1021/acs.analchem.1c05550.

(49) Jacobs, M. I.; Davies, J. F.; Lee, L.; Davis, R. D.; Houle, F.; Wilson, K. R. Exploring Chemistry in Microcompartments Using Guided Droplet Collisions in a Branched Quadrupole Trap Coupled to a Single Droplet, Paper Spray Mass Spectrometer. *Analytical Chemistry* **2017**, *89* (22), 12511–12519. https://doi.org/10.1021/acs.analchem.7b03704.

(50) Davies, J. F. Mass, Charge, and Radius of Droplets in a Linear Quadrupole Electrodynamic Balance. *Aerosol Science and Technology* **2019**, *53* (3), 309–320. https://doi.org/10.1080/02786826.2018.1559921.

(51) Smith, J. D.; Kroll, J. H.; Cappa, C. D.; Che, D. L.; Liu, C. L.; Ahmed, M.; Leone, S. R.; Worsnop, D. R.; Wilson, K. R. The Heterogeneous Reaction of Hydroxyl Radicals with Sub-Micron Squalane Particles: A Model System for Understanding the Oxidative Aging of Ambient Aerosols. *Atmospheric Chemistry and Physics* **2009**, *9* (9), 3209–3222. https://doi.org/10.5194/acp-9-3209-2009.

(52) Kuramoto, Y. Effects of Diffusion on the Fluctuations in Open Chemical Systems. *Progress of Theoretical Physics* **1974**, *52* (2), 711–713. https://doi.org/10.1143/PTP.52.711.

(53) Houle, F. A.; Wiegel, A. A.; Wilson, K. R. Predicting Aerosol Reactivity Across Scales: From the Laboratory to the Atmosphere. *Environ. Sci. Technol.* **2018**, *52* (23), 13774–13781. https://doi.org/10.1021/acs.est.8b04688.

(54) Wilson, K. R.; Prophet, A. M. Chemical Kinetics in Microdroplets. *Annual Review of Physical Chemistry* **2024**, *75*, 185–208. https://doi.org/10./1146/annurev-physchem-052623-120718.

(55) Wilson, K. R.; Prophet, A. M.; Willis, M. D. A Kinetic Model for Predicting Trace Gas Uptake and Reaction. *J. Phys. Chem. A* **2022**, *126* (40), 7291–7308. https://doi.org/10.1021/acs.jpca.2c03559.

(56) Szyszkowski, B. von. Experimentelle Studien über kapillare Eigenschaften der wässerigen Lösungen von Fettsäuren. *Zeitschrift für Physikalische Chemie* **1908**, *64U* (1), 385–414. https://doi.org/10.1515/zpch-1908-6425.

(57) He, Y.; Yazhgur, P.; Salonen, A.; Langevin, D. Adsorption–Desorption Kinetics of Surfactants at Liquid Surfaces. *Advances in Colloid and Interface Science* **2015**, *222*, 377–384. https://doi.org/10.1016/j.cis.2014.09.002.

(58) Alvarez, N. J.; Walker, L. M.; Anna, S. L. Diffusion-Limited Adsorption to a Spherical Geometry: The Impact of Curvature and Competitive Time Scales. *Phys. Rev. E* **2010**, *82* (1), 011604. https://doi.org/10.1103/PhysRevE.82.011604.

(59) Liu, Q.; Schurter, L. M.; Muller, C. E.; Aloisio, S.; Francisco, J. S.; Margerum, D. W. Kinetics and Mechanisms of Aqueous Ozone Reactions with Bromide, Sulfite, Hydrogen Sulfite, Iodide, and Nitrite Ions. *Inorg. Chem.* **2001**, *40* (17), 4436–4442. https://doi.org/10.1021/ic000919j.

(60) Brown, L. V.; Pound, R. J.; Ives, L. S.; Jones, M. R.; Andrews, S. J.; Carpenter, L. J. Negligible Temperature Dependence of the Ozone–Iodide Reaction and Implications for Oceanic Emissions of Iodine. *Atmospheric Chemistry and Physics* **2024**, *24* (7), 3905–3923. https://doi.org/10.5194/acp-24-3905-2024.

(61) Polley, K.; Wilson, K. R.; Limmer, D. T. On the Statistical Mechanics of Mass Accommodation at Liquid–Vapor Interfaces. *J. Phys. Chem. B* **2024**, *128* (17), 4148–4157. https://doi.org/10.1021/acs.jpcb.4c00899.

(62) Fuchs, N. A.; Sutugin, A. G. High-Dispersed Aerosols. In *Topics in Current Aerosol Research*; Hidy, G. M., Brock, J. R., Eds.; International Reviews in Aerosol Physics and Chemistry; Pergamon, 1971; p 1. https://doi.org/10.1016/B978-0-08-016674-2.50006-6.

(63) Fick, A. V. On Liquid Diffusion. *The London, Edinburgh, and Dublin Philosophical Magazine and Journal of Science* **1855**, *10* (63), 30–39. https://doi.org/10.1080/14786445508641925.

(64) Rouvière, A.; Ammann, M. The Effect of Fatty Acid Surfactants on the Uptake of Ozone to Aqueous Halogenide Particles. *Atmospheric Chemistry and Physics* **2010**, *10* (23), 11489–11500. https://doi.org/10.5194/acp-10-11489-2010.

(65) Tinel, L.; Adams, T. J.; Hollis, L. D. J.; Bridger, A. J. M.; Chance, R. J.; Ward, M. W.; Ball, S. M.; Carpenter, L. J. Influence of the Sea Surface Microlayer on Oceanic Iodine Emissions. *Environ. Sci. Technol.* **2020**, *54* (20), 13228–13237. https://doi.org/10.1021/acs.est.0c02736.

(66) Schneider, S. R.; Lakey, P. S. J.; Shiraiwa, M.; Abbatt, J. P. D. Iodine Emission from the Reactive Uptake of Ozone to Simulated Seawater. *Environ. Sci.: Processes Impacts* **2023**, *25* (2), 254–263. https://doi.org/10.1039/D2EM00111J.

(67) Schneider, S. R.; Lakey, P. S. J.; Shiraiwa, M.; Abbatt, J. P. D. Reactive Uptake of Ozone to Simulated Seawater: Evidence for Iodide Depletion. *The Journal of Physical Chemistry A* **2020**, *124* (47), 9844–9853. https://doi.org/10.1021/ACS.JPCA.0C08917.

(68) Kaur Kohli, R.; Davis, R. D.; Davies, J. F. Tutorial: Electrodynamic Balance Methods for Single Particle Levitation and the Physicochemical Analysis of Aerosol. *Journal of Aerosol Science* **2023**, *174*, 106255. https://doi.org/10.1016/j.jaerosci.2023.106255.

Chapter 5: A General Kinetic Description of Multiphase Chemistry in Microdroplets

5.1: Introduction

The preceding chapters have considered the specifics of iodide chemistry in aqueous microdroplets. In addition to informing on the behavior of this set of reactions, the study of this chemistry has provided insight into constructing a more general description of multiphase kinetics and identifying the mechanistic steps involved. In the present chapter, we outline a general approach for quantifying multiphase kinetics using a discretized representation of the relevant phases and kinetic regions of the system—as introduced more broadly in Chapter 1. This work was largely developed from the use of simulations run in Kinetiscope©. Here, with some comment on the use of stochastic simulations, focus is given to analytical forms expressing uptake coefficients using a steady-state approach, along with the derivation of a set of analytical expressions for time-dependent kinetics—accompanied by numerical evaluations of the governing differential equations using numerical solving methods. After a brief introduction of the general approach, we outline six relevant kinetic cases and compare model predictions with data from the literature and previous model approaches.

As introduced in Chapter 1, the model construction operates on the principle of identifying individual kinetic regions where reagent concentrations are governed by reaction and diffusion. These regions generally derive from spatial regions where density profiles are changing significantly due to a process like reaction or solvation/evaporation. Fig. 5.1 provides a conceptual overview with an example microdroplet suspended in air—not unlike Fig. 3.2 in Chapter 3 for the iodide oxidation reaction. In this more general diagram, however, we consider an aqueous droplet containing species (Y) suspended in a gas containing species (X). For simplicity we assume Y is non-volatile and X is a trace-gas with a droplet solubility given by a gas-to-bulk (gb) Henry's law coefficient where, at equilibrium, $[\mathrm{X}_{(aq)}] = H_{gb} \cdot [\mathrm{X}_{(gas)}]$ (for a discussion of the Henry's law coefficients defined herein, see Chapter 1 Section 1.3). Fig 5.1 has labeled the primary kinetic regions and length scales that are relevant for the cases explored in this chapter. The very outer region is isolated from the droplet itself, where the gas X is simply maintained at a constant concentration denoted $[\mathrm{X}_{gas}^{\infty}]$. Closer to the droplet, extending one radial length from the droplet surface is a gas-diffusion region. What distinguishes this gas-diffusion region from the outer-gas region is the ability for the droplet surface to perturb local concentrations inside the gas-diffusion region. As will be examined below, for chemical reactions X + Y faster than a characteristic diffusion rate into this gas region, the concentration in the diffusion region $[\mathrm{X}_{gas}^{diff}]$ cannot maintain the outer concentration $[\mathrm{X}_{gas}^{\infty}]$ and becomes depleted $\left[\mathrm{X}_{gas}^{diff}\right] < [\mathrm{X}_{gas}^{\infty}]$, limiting the overall rate of reaction.

The droplet surface region is defined as the top 1 nm of the aqueous droplet. While the definition of a liquid surface is not as straightforward as a solid surface, we define the surface as the length over which the overall density moves from that of the liquid to the gas. As shown in Fig. 4.1 and Fig. 3.3, molecular simulations suggest this length scale is ~ 1 nm, which we use to define the surface thickness δ. It should be noted that this definition of surface is not universal—with many researchers defining the surface in various ways, e.g. the topmost layer of water molecules, with a thickness of only a few Å. Reasonably, these different definitions of the "surface" or "interface" have led to different classifications about relative "surface" activities of different solutes. Nevertheless, our working definition of the surface appears useful insofar as this length scale corresponds to the particular region where chemical densities deviate the most from their bulk-phase values (see Fig. 6.1 showing density profiles of O_3 and I^-, for instance.)

A subsurface region is defined beneath the outer surface, extending some distance beneath the surface region and extending radially towards the droplet center. In the present work, we identify this region as a "reaction-diffusion" (*rd*) region, through which the impinging gas X will diffuse before reacting with solute Y. The length scale of this region is the reaction-diffusion length, defined by $L_{rd} = \sqrt{D^{\mathrm{X}}_{(aq)}/k^{bulk}_{rxn} \cdot [\mathrm{Y}_{bulk}]}$ where $D^{\mathrm{X}}_{(aq)}$ is the aqueous diffusion coefficient of X and k^{bulk}_{rxn} the rate coefficient for reaction X + Y in the bulk aqueous phase (as opposed to the reaction rate k^{surf}_{rxn} which may be particular to the surface reaction.) Using this definition for the subsurface region, the chemical gradient of O_3 extending radially into the droplet is represented using the average concentration in this region. This concept will be explored with comparisons to continuous forms in the following chapter. In addition, the inclusion of two *rd* regions, one for each chemical gradient of X and Y, is also possible as will be explored in Section 5.4. Beyond the distance L_{rd} from the outer surface is the inner core of the droplet, generally referred to as the bulk region or inner bulk of the droplet. The length scale of this region L_{bulk} likewise depends on L_{rd}, since the total droplet radius must equal the sum of compartment lengths $r = L_{bulk} + L_{rxn} + \delta$. Typically, no reactivity occurs within this bulk region since the *rd* region is defined to include the vast majority of chemical loss for X. Nevertheless, this region often contains the bulk of species Y and acts as the reservoir that facilitates diffusional transport of Y into the *rd* region. This role is especially important for cases where Y becomes depleted at the surface and even the *rd* region. For cases where $L_{rxn} \geq r,\ L_{bulk}$ effectively goes to zero using the formalism that will be discussed below.

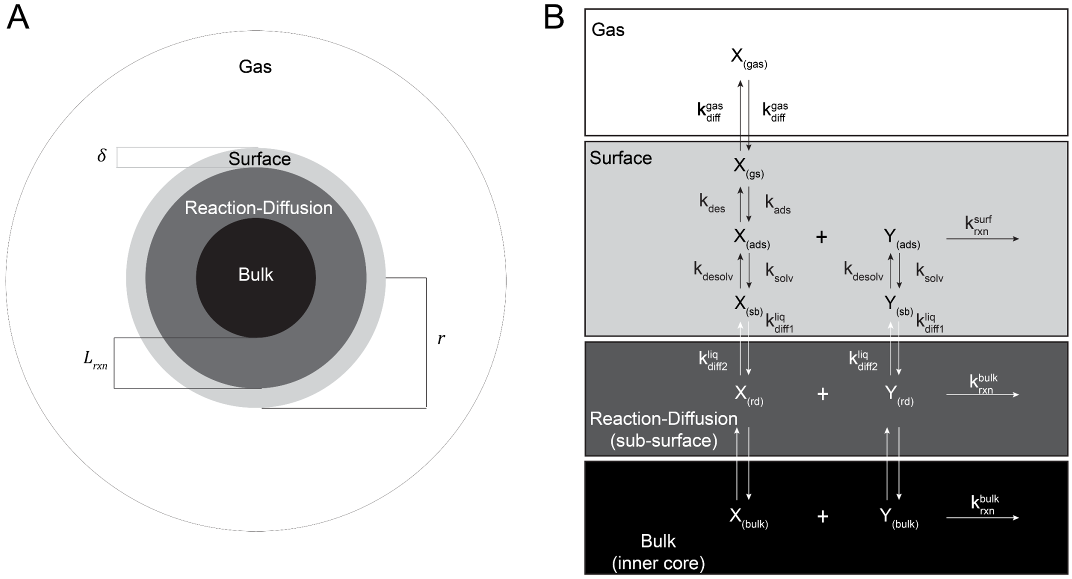

Fig. 5.1: (A) Conceptual layout for gas-liquid droplet system. (B) Overview of general kinetic scheme for reactivity between gaseous species X and solute Y, with kinetic regions labeled.

Using the conceptual spatial framework outlined above, six cases for chemical reactivity can occur depending on the droplet radius, concentrations of reagents, and the rate coefficients involved for the particular reactions. In the following section, we review the general form of the uptake coefficients expressions encountered in the previous chapters, with a brief recapitulation of the steady-state approach used to define local concentrations. In Section 3, we comment on the approaches used to obtain the time-dependent kinetics—focusing on the analytical approach that yields closed-form solutions for some cases, and the numerical approach that can be used to explore time-dependent concentrations for all cases. The following Section 4 walks through the kinetic cases commonly encountered in microdroplet chemistry, with a discussion of each case and comparisons made between model approaches and experiments. Section 5 provides an overview of the mass transport terms that arise in the model description, with details provided on the kinetic approach used to describe diffusion, and comment on the origin of the adsorption/desorption terms used to describe mass transport across the interface. The final part of this chapter, Section 6, consists of an analysis of the steady-state assumption used in the model and a comparison between the discretization approach used here and previous models where analytical forms are obtained describing the chemical gradients encountered in droplet chemistry.

5.2: Reactive Uptake Coefficients and Steady-State Concentrations

The reactive uptake coefficient for the trace gas X due to reaction with the solute Y in a microdroplet of radius r can be written as the sum of the uptake originating from the chemical reactions on the surface, within reaction-diffusion region, and inside the inner core of the droplet:

$$\gamma_{total} = \gamma_{surf} + \gamma_{rd} + \gamma_{bulk}, \qquad \text{Eq. 5.1}$$

$$\gamma_{surf} = \frac{4 \cdot r \cdot k_{rxn}^{srf} \cdot [\mathrm{X}_{(ads)}][\mathrm{Y}_{(ads)}]}{3 \cdot \bar{c} \cdot [\mathrm{X}_{gas}^{\infty}]} \cdot \frac{r^3 - (r-\delta)^3}{r^3}, \qquad \text{Eq. 5.2}$$

$$\gamma_{rd} = \frac{4 \cdot r \cdot k_{rxn}^{blk} \cdot [\mathrm{X}_{(rd)}][\mathrm{Y}_{(rd)}]}{3 \cdot \bar{c} \cdot [\mathrm{X}_{gas}^{\infty}]} \cdot \frac{(r-\delta)^3 - \left(r - \delta - \frac{L_{rd}}{1 + r^{-1} \cdot L_{rd}}\right)^3}{r^3}, \qquad \text{Eq. 5.3}$$

$$\gamma_{bulk} = \frac{4 \cdot r \cdot k_{rxn}^{blk} \cdot [\mathrm{X}_{(bulk)}][\mathrm{Y}_{(bulk)}]}{3 \cdot \bar{c} \cdot [\mathrm{X}_{gas}^{\infty}]} \cdot \frac{\left(r - \delta - \frac{L_{rd}}{1 + r^{-1} \cdot L_{rd}}\right)^3}{r^3}. \qquad \text{Eq. 5.4}$$

The uptake components γ_{surf}, γ_{rd}, and γ_{bulk} above possess the same general form, containing a recognizable rate term $k_{rxn} \cdot [\mathrm{X}][\mathrm{Y}]$ for each particular region, a surface-collisional term $\bar{c} \cdot [\mathrm{X}_{(gas)}]$, and a volumetric term that is the ratio of the specific region-volume to the entire droplet volume (e.g., the surface volume $\frac{4}{3}\pi r^3 - \frac{4}{3}\pi (r-\delta)^3$ divided by the entire droplet volume $\frac{4}{3}\pi r^3$ yields ratio $r^3 - (r-\delta)^3/r^3$ for γ_{surf}). In the work that follows, the shorthand *Vx* is used to indicate the relevant factor in region *x* defined as

$$V_{surf} = \frac{4}{3}\pi r^3 - \frac{4}{3}\pi (r-\delta)^3,$$

$$V_{rd} = \frac{4}{3}\pi (r-\delta)^3 - \frac{4}{3}\pi \left(r - \delta - \frac{L_{rxn}}{1 + r^{-1} \cdot L_{rxn}}\right)^3,$$

$$V_{bulk} = \frac{4}{3}\pi\left(r - \delta - \frac{L_{rxn}}{1 + r^{-1} \cdot L_{rxn}}\right)^3,$$

$$V_{total} = \frac{4}{3}\pi r^3.$$

The length of the reaction-diffusion region is defined using a "transition function" which closely approximates the reaction-diffusion length L_{rxn} when $L_{rxn} < r$ and approximates r when $L_{rxn} > r$, as shown in Fig. 5.2. This definition of length scale allows γ_{rd} to account for the reactive uptake in the reaction diffusion region (see the liquid-diffusion Case 2 outlined in Fig. 5.3 and Section 4.B), while simultaneously allowing γ_{rd} to account for reactivity in the entire particle when the reaction diffusion length is greater than the radius (see the phase-mixed Case 1 in Fig 5.3 and Section 4.A). Note that when using this description, the volumetric term in the definition for γ_{rd} approaches 1 when $L_{rxn} >> r$, while the analogous term for γ_{bulk} approaches 0. Furthermore, since γ_{rd} is defined to encompass the region defined by depth L_{rxn}, very little reactivity occurs beyond this length inside of the inner core region. Therefore, γ_{bulk} is generally negligible compared to γ_{surf} and γ_{rd}, and we will largely ignore its reactive contribution. The validity of ignoring γ_{bulk} is revisited in Section 5.

The concentrations for X and Y found in Eqs. 5.2-5.4 are defined for each individual case encountered in Section 4. For each case, two distinct approaches are used to define [X] and [Y] in each spatial region. One approach (we term the static-approach) simply assumes the species' concentration is equal to the concentration determined by the initial conditions, e.g., in reference to the liquid-diffusion case (see Fig. 5.3), a droplet containing initial concentration $[\mathrm{Y}]_0$ = 10 mM the $[\mathrm{Y}_{(rd)}]$ in the reaction-diffusion region is simply $[\mathrm{Y}_{(rd)}] = [\mathrm{Y}]_0$. This static-approach is also regularly applied to the surface, where $[\mathrm{Y}_{(ads)}]$ is assumed to be equal to the value defined by a Langmuir equilibrium isotherm. The alternate approach that is used to define reagent concentrations in each region is the steady-state approach. This approach uses the assumption that a concentration in a given region may deviate from the concentration initially specified, but quickly equilibrates to a new "steady-state" which is governed by mass transport and the presence of reaction. For example, in the liquid-diffusion case, the $[\mathrm{X}_{(rd)}]$ in the reaction-diffusion region is initially equal to zero, but increases at a rate governed by the derivative:

$$\frac{d[\mathrm{X}_{(rd)}]}{dt} = k^{liq}_{diff2}[\mathrm{X}_{(sb)}] - k^{liq}_{diff2}[\mathrm{X}_{(rd)}] - k^{blk}_{rxn}[\mathrm{Y}_{(rd)}][\mathrm{X}_{(rd)}]. \quad \text{Eq. 5.5}$$

Using the steady-state assumption, Eq. 5.5 is equal to zero, and the concentration $[\mathrm{X}_{(rd)}]$ is

$$[\mathrm{X}_{(rd)}] = \frac{k^{liq}_{diff2}[\mathrm{X}_{(sb)}]}{k^{liq}_{diff2} + k^{blk}_{rxn}[\mathrm{Y}_{(rd)}]}, \quad \text{Eq. 5.6}$$

where k^{liq}_{diff2} and species $[\mathrm{X}_{(sb)}]$ describes the rate of diffusion between surface and *rd* region, as shown in Fig. 5.1B (see Appendix 5.A for definitions of liquid diffusional terms k^{liq}_{diff1}, k^{liq}_{diff2}, and k^{liq}_{diff3}). In this case, the steady-state concentration $[\mathrm{X}_{(rd)}]$ depends on the concentration $[\mathrm{X}_{(sb)}]$ which is defined using an analogous rate equation and steady-state assumption. The particular definitions used for each chemical case will be specified in Section 4.

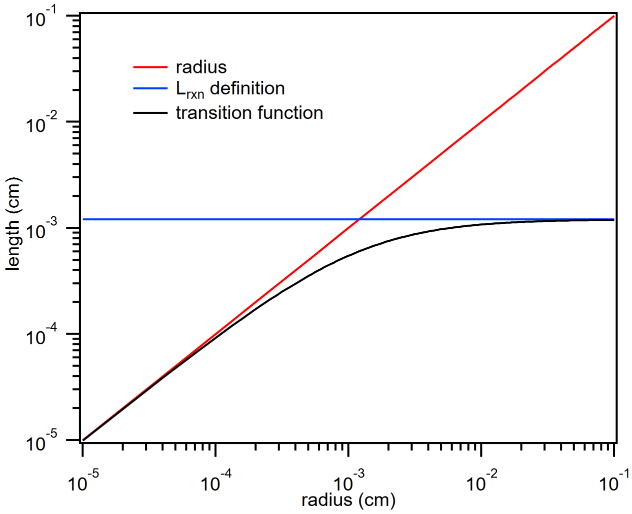

Fig. 5.2: Length scale defined for the “reaction diffusion” region indicated by the “transition function.” This length approaches the true reaction diffusion length L_{rxn} when droplet radius r is $r > L_{rxn}$ and approaches r when $r < L_{rxn}$. L_{rxn} computed in this example uses $[Y_0]$ = 100 nM and $k_{rxn} = 1.2\times10^8$ M^{-1} s^{-1}.

5.3: Time-Dependent Methods

Once reactive uptake coefficients and local concentrations have been defined, a number of methods can be used to obtain time-dependent trajectories of concentrations [X] and [Y]. One method to obtain this time-dependence is using stochastic simulations executed in Kinetiscope as we’ve extensively explored in Chapters 2-4 for iodide oxidation. Example simulations are included in some of the cases analyzed in the following section when comparison between methods is valuable. As noted above, however, we emphasize the ability to model the time-dependence using analytical expressions derived for some chemical cases, which we also compare to numerical solutions to the governing rate equations when possible.

The general approach to calculating time-dependent kinetics of the decay of solute Y starts with the rate equation

$$\frac{d[\mathrm{Y}_{(total)}]}{dt} = -k_{rxn}[\mathrm{Y}_{(total)}][\mathrm{X}_{(aq)}] \qquad \text{Eq. 5.7}$$

for some concentration of gaseous species X solvated in the particle and the X + Y rate coefficient k_{rxn}. Eq. 5.7 can also be expressed in terms of the reactive uptake coefficient of X due to reaction with Y:

$$\frac{d[\mathrm{Y}_{(total)}]}{dt} = -S_{rxn}\frac{3\cdot\bar{c}\cdot[\mathrm{X}_{gas}^{\infty}]\cdot\gamma_{total}}{4\cdot r}, \qquad \text{Eq. 5.8}$$

where γ_{total} is the sum defined in Eq. 5.1 and S_{rxn} is an added stoichiometry factor that is necessary to approximate reactivity where the stoichiometry of the overall chemistry isn’t 1:1 for Y:X (for example, S_{rxn} for the I^- + O_3 reaction under acidic conditions is 2 since I_2 is the major product, so the observed stoichiometry is 2:1 for I^- : O_3). Eq. 5.8 in tandem with Eqs. 5.1-5.4 can be used to obtain numerical solutions to the time dependence of the overall concentration $[\mathrm{Y}_{(total)}]_t$ which accounts for different local concentrations and reactivity in the regions outlined in Section 1. For select chemical cases, Eq. 5.8 can be integrated directly (or approximated) to obtain closed-form solutions for $\left[\mathrm{Y}_{(total)}\right]_t$. In Section 4 we point out where analytical methods are not possible and include numerical solutions to Eq. 5.8 obtained either through stochastic simulations or a numeric differential solver such as those found in Wolfram Mathematica, MATLAB, or Python.

Analytical Approach

Here we outline the basic approach used to obtain analytic expressions for the time dependence of [Y] and [X] for a given chemical case. Analytic expressions are not always possible to obtain depending on the given assumptions for each case. In the following section, analytic forms are derived where possible. When not possible, numerical solutions to Eq. 5.8 are provided along with some comments on how one may approximate the solution analytically. Starting by expanding Eq. 5.8, we see

$$\begin{aligned}\frac{d\left[\mathrm{Y}_{(total)}\right]}{dt} &= -S_{rxn}\frac{3\cdot\bar{c}\cdot[\mathrm{X}_{gas}^{\infty}]\cdot\gamma_{surf}}{4\cdot r} - S_{rxn}\frac{3\cdot\bar{c}\cdot[\mathrm{X}_{gas}^{\infty}]\cdot\gamma_{rd}}{4\cdot r}\\ &= -S_{rxn}\left(k_{rxn}^{srf}\cdot\left[\mathrm{X}_{(ads)}\right]\left[\mathrm{Y}_{(ads)}\right]\cdot\frac{V_{surf}}{V_{total}} + k_{rxn}^{bulk}\cdot\left[\mathrm{X}_{(rd)}\right]\left[\mathrm{Y}_{(rd)}\right]\cdot\frac{V_{rd}}{V_{total}}\right), \qquad \text{Eq. 5.9}\end{aligned}$$

where we have neglected the reactive contribution of γ_{bulk}. The method generally employed in the following is to first determine the time dependence of $\left[\mathrm{Y}_{(total)}\right]$ given the reactive contribution of only γ_{rd} or γ_{surf} before then finding the behavior due to both γ_{rd} and γ_{surf}. Therefore, we first solve for $\left[\mathrm{Y}_{(total)}\right]$ given reactivity only in the reactive-diffusion region:

$$\frac{d\left[\mathrm{Y}_{(total)}\right]}{dt} = -S_{rxn}\cdot k_{rxn}^{bulk}\cdot\left[\mathrm{X}_{(rd)}\right]\left[\mathrm{Y}_{(rd)}\right]\cdot\frac{V_{rd}}{V_{total}}. \qquad \text{Eq. 5.10}$$

Solutions to Eq. 5.10 depend on the assumptions made for each case. As shown in Section 2, $\left[\mathrm{X}_{(rd)}\right]$ and $\left[\mathrm{Y}_{(rd)}\right]$ may both be functions of $\left[\mathrm{Y}_{(total)}\right]$ (in fact, besides in Cases 5 and 6, we assume $\left[\mathrm{Y}_{(rd)}\right] = \left[\mathrm{Y}_{(total)}\right]$), allowing us to integrate after separating variables:

$$\int_{\left[\mathrm{Y}_{(total)}\right]_0}^{\left[\mathrm{Y}_{(total)}\right]_t} \frac{1}{\left[\mathrm{X}_{(rd)}\right]\left[\mathrm{Y}_{(rd)}\right]}\, d\left[\mathrm{Y}_{(total)}\right] = \int_0^t -S_{rxn}\cdot k_{rxn}^{bulk}\cdot\frac{V_{rd}}{V_{total}}\,dt. \qquad \text{Eq. 5.11}$$

In the first four cases outlined in Section 5, the concentration of Y is assumed to be well-mixed throughout the droplet. Therefore, the concentration in the *rd* region in these cases is equal to the total concentration in the droplet, and the integral in Eq. 5.11 is evaluated to

$$\begin{aligned}&\left[\mathrm{Y}_{(total)}\right]_t + \ln\left[\mathrm{Y}_{(total)}\right]_t\\ &\qquad = \left[\mathrm{Y}_{(total)}\right]_0 + \ln\left[\mathrm{Y}_{(total)}\right]_0 - S_{rxn}\cdot k_{rxn}^{bulk}\cdot H_{gb}\left[\mathrm{X}_{gas}^{\infty}\right]\cdot\frac{V_{rd}}{V_{total}}t. \qquad \text{Eq. 5.12}\end{aligned}$$

Solving Eq. 5.12 for $\left[\mathrm{Y}_{(total)}\right]_t$ is accomplished using the Lambert *W* function:

$$\left[\mathrm{Y}_{(total)}\right]_t = \boldsymbol{W}\left\{\left[\mathrm{Y}_{(rd)}\right]_0 \cdot e^{\left[\mathrm{Y}_{(rd)}\right]_0 - S_{rxn}\cdot k_{rxn}^{bulk}\cdot H_{gb}\left[\mathrm{X}_{gas}^{\infty}\right]\cdot\frac{V_{rd}}{V_{total}}t}\right\}. \qquad \text{Eq. 5.13}$$

While this exercise has obtained $\left[\mathrm{Y}_{(total)}\right]_t$ due to reaction only in the reaction-diffusion region, the solution for $\left[\mathrm{Y}_{(total)}\right]_t$ due to the surface reaction alone is of the same general form, with specifics provided in the following section. The resulting time dependence equations for surface-only and reaction-diffusion-only can then be convoluted to provide a single time dependent $\left[\mathrm{Y}_{(total)}\right]_t$ that includes contributions from the entire droplet. This will be shown explicitly in the following section.

5.4: Chemical Cases for Multiphase Reactivity in Microdroplets

Six chemical cases are now identified for multiphase chemical reactivity in microdroplets using the approaches outlined above. These cases are summarized in Fig. 5.3, with case names provided and an illustration of reagent distribution for each scenario. These cases have been organized into three different classifications: (1) phase-mixed, (2) trace-gas, and (3) trace-solute. Our introduction of these cases is ordered somewhat in terms of complexity, with the phase-mixed scenario being relatively straightforward, and with trace-solute and multi-solute cases being more involved.

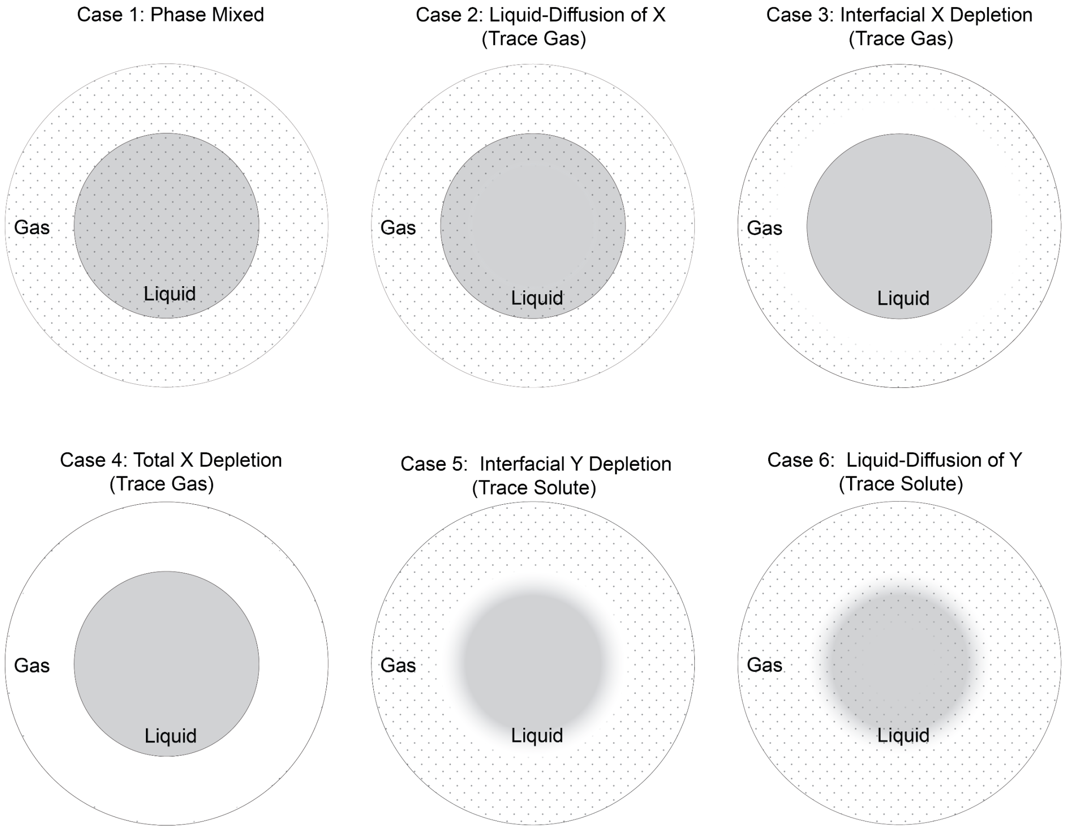

Fig. 5.3: Graphical summary of chemical cases explored in Section 5. Dotted area represents gas X and solid gray represents solute Y. Gradients represent where X or Y become depleted for each case.

5.4.A: Case 1: Phase-Mixed

This simplest case corresponds to the scenario where gas X has equilibrated with the entire droplet volume, and the aqueous concentration of X throughout the droplet is simply $\left[\mathrm{X}_{(aq)}\right] = H_{\mathrm{X}}^{gb} \cdot [\mathrm{X}_{gas}^{\infty}]$. This is referred to as the "dilute-limit" by Worsnop et al.[1] and the phase-mixed case originally by Schwartz.[2] This case is commonly encountered when the rate of reaction k_{rxn} between X and Y is slow. More specifically, the aqueous concentration $\left[\mathrm{X}_{(aq)}\right]$ can attain the Henry's law condition when the rate of X diffusion through the particle, $k_{diff}\ (s^{-1}) \sim \frac{2\,D_{\mathrm{X}}}{r^2}$ is faster than the rate at which X is lost to reaction, $k'_{rxn}(s^{-1}) = k_{rxn}[\mathrm{Y}]$. This condition holds approximately when $L_{rd} > r$. Uptake coefficients due to surface reactivity γ_{surf} and bulk reactivity γ_{rd} in this case are:

$$\gamma_{surf} = \frac{4\,r\,k_{rxn}^{srf} \cdot H_{\mathrm{X}}^{gs}\left[\mathrm{X}_{gas}^{\infty}\right] \cdot \frac{\Gamma_{\infty}^{\mathrm{Y}}}{\delta} \frac{K_{eq}^{\mathrm{Y}}\left[\mathrm{Y}_{(total)}\right]}{1 + K_{eq}^{\mathrm{Y}}\left[\mathrm{Y}_{(total)}\right]}}{3\,\bar{c}\,[\mathrm{X}_{gas}^{\infty}]} \cdot \frac{V_{surf}}{V_{total}}, \qquad \text{Eq. 5.14}$$

$$\gamma_{rd} = \frac{4\,r\,k_{rxn}^{blk} \cdot H_{\mathrm{X}}^{gb}\left[\mathrm{X}_{gas}^{\infty}\right] \cdot \left[\mathrm{Y}_{(total)}\right]}{3\,\bar{c}\,[\mathrm{X}_{gas}^{\infty}]}, \qquad \text{Eq. 5.15}$$

where the volumetric term in Eq. 5.15 is equal to unity since we assume X is well mixed throughout the entire droplet volume. Fig. 5.4 shows results from Eq. 5.14 and Eq. 5.15 as well as the total uptake for varying droplet radius *r*, solute concentration $\left[\mathrm{Y}_{(total)}\right]$, and rate coefficients k_{rxn}^{blk} and k_{rxn}^{srf}. Note that uptake coefficients in this case have no gas-concentration dependence due to the cancelation of $\left[\mathrm{X}_{gas}^{\infty}\right]$.

(i) Reaction-Diffusion Region Kinetics

To obtain time-dependent expressions for $\left[\mathrm{Y}_{(total)}\right]$ due to reaction, we follow the integration approach introduced in Section 3. We first solve for the time dependent loss of $\left[\mathrm{Y}_{(total)}\right]$ due to reaction only in the reaction-diffusion region. Assuming $S_{rxn} = 1$, Eq. 5.10, or the reaction-diffusion component of Eq. 5.9 becomes:

$$\frac{d\left[\mathrm{Y}_{(total)}\right]}{dt} = -k_{rxn}^{blk} \cdot H_{\mathrm{X}}^{gb}\left[\mathrm{X}_{gas}^{\infty}\right] \cdot \left[\mathrm{Y}_{(total)}\right]. \qquad \text{Eq. 5.16}$$

Integrating after separating variables yields a simple exponential:

$$\left[\mathrm{Y}_{(total)}\right]_t = \left[\mathrm{Y}_{(total)}\right]_0 \cdot e^{-k_{rxn}^{blk} \cdot H_{\mathrm{X}}^{gs}[\mathrm{X}_{gas}^{\infty}] \cdot t}\,. \qquad \text{Eq. 5.17}$$

(ii) Surface Reaction Kinetics

The analogous solution for the surface reaction contribution to the overall time-dependence of $\left[\mathrm{Y}_{(total)}\right]_t$ is obtained by taking the surface-reaction component of Eq. 5.9:

$$\frac{d\left[\mathrm{Y}_{(total)}\right]}{dt} = -k_{rxn}^{srf} \cdot H_{\mathrm{X}}^{gs}\left[\mathrm{X}_{gas}^{\infty}\right] \cdot \frac{\Gamma_{\infty}^{\mathrm{Y}}}{\delta} \frac{K_{eq}^{\mathrm{Y}}\left[\mathrm{Y}_{(total)}\right]}{1 + K_{eq}^{\mathrm{Y}}\left[\mathrm{Y}_{(total)}\right]} \cdot \frac{V_{surf}}{V_{total}}. \qquad \text{Eq. 5.18}$$

Again, separating variables and integrating yields

$$\int_{[\mathrm{Y}_{(total)}]_0}^{[\mathrm{Y}_{(total)}]_t} \frac{1 + K_{eq}^{\mathrm{Y}}[\mathrm{Y}_{(total)}]}{[\mathrm{Y}_{(total)}]} d[\mathrm{Y}_{(total)}] = \int_0^t -k_{rxn}^{srf} \cdot \frac{\Gamma_\infty^{\mathrm{Y}}}{\delta} K_{eq}^{\mathrm{Y}} \cdot H_{\mathrm{X}}^{gs}[\mathrm{X}_{gas}^{\infty}] \cdot \frac{V_{rd}}{V_{total}} dt \quad \text{Eq. 5.19}$$

which evaluates to

$$K_{eq}^{\mathrm{Y}}[\mathrm{Y}_{(total)}]_t + \ln[\mathrm{Y}_{(total)}]_t = K_{eq}^{\mathrm{Y}}[\mathrm{Y}_{(rd)}]_0 + \ln[\mathrm{Y}_{(rd)}]_0 - k_{rxn}^{srf} \cdot \frac{\Gamma_\infty^{\mathrm{Y}}}{\delta} K_{eq}^{\mathrm{Y}} \cdot H_{\mathrm{X}}^{gs}[\mathrm{X}_{gas}^{\infty}] \cdot \frac{V_{surf}}{V_{total}} \cdot t. \quad \text{Eq. 5.20}$$

As shown in Section 3, the Lambert W function is used to solve for $[\mathrm{Y}_{(total)}]_t$

$$[\mathrm{Y}_{(total)}]_t = \frac{1}{K_{eq}^{\mathrm{Y}}} \cdot \boldsymbol{W}\left\{K_{eq}^{\mathrm{Y}}[\mathrm{Y}_{(total)}]_0 \cdot e^{K_{eq}^{\mathrm{Y}}[\mathrm{Y}_{(total)}]_0 - k_{rxn}^{srf} \cdot \frac{\Gamma_\infty^{\mathrm{Y}}}{\delta} K_{eq}^{\mathrm{Y}} \cdot H_{\mathrm{X}}^{gs}[\mathrm{X}_{gas}^{\infty}] \cdot \frac{V_{surf}}{V_{total}} \cdot t}\right\}. \quad \text{Eq. 5.21}$$

Eq. 5.21 provides the time dependence of $[\mathrm{Y}_{(total)}]$ due to reactivity only at the droplet surface in this case. A comparison between the time-dependence predicted for reaction only at the surface or only in the reaction-diffusion region is made in Fig. 5.4, using a set of example parameters where reactivity is expected both at the surface and within the reaction-diffusion length. This comparison shows Eq. 5.17 for the reaction-diffusion contribution alone, and Eq. 5.21 for only the surface reaction contribution.

(iii) Combined Expression for Phase-Mixed Case

The full time-dependence of $[\mathrm{Y}_{(total)}]$ resulting from both reaction at the surface and within the bulk is obtained by combining Eq. 5.21 and 5.17. To accomplish this, we substitute $[\mathrm{Y}_{(total)}]_0$ in the Eq. 5.21 with the definition of $[\mathrm{Y}_{(total)}]_t$ in Eq. 5.17:

$$\begin{aligned}[\mathrm{Y}_{(total)}]_t = \frac{1}{K_{eq}^{\mathrm{Y}}} \\ &\cdot \boldsymbol{W}\Bigg\{K_{eq}^{\mathrm{Y}}[\mathrm{Y}_{(total)}]_0 \cdot e^{-k_{rxn}^{blk} \cdot H_{\mathrm{X}}^{gs}[\mathrm{X}_{gas}^{\infty}] \cdot t} \\ &\cdot e^{K_{eq}^{\mathrm{Y}}[\mathrm{Y}_{(total)}]_0 \cdot e^{-k_{rxn}^{blk} \cdot H_{\mathrm{X}}^{gs}[\mathrm{X}_{gas}^{\infty}] \cdot t} - k_{rxn}^{srf} \cdot \frac{\Gamma_\infty^{\mathrm{Y}}}{\delta} K_{eq}^{\mathrm{Y}} \cdot H_{\mathrm{X}}^{gs}[\mathrm{X}_{gas}^{\infty}] \cdot \frac{V_{surf}}{V_{total}} \cdot t}\Bigg\}.\end{aligned}$$

$$\text{Eq. 5.22}$$

Results from Eq. 5.22, Eq. 5.21, and Eq. 17 are all compared in Fig. 5.4, where we show the relative surface-bulk contributions, for an example range of droplet radius.

Uptake coefficients shown in panels A-C in Fig. 5.4 provide a broad overview of trends for the dependence of γ defined in Case 1 on the kinetic parameters r, $[\mathrm{Y}_{(total)}]$, and k_{rxn}. In the small radial limit, reactivity is typically governed by the surface reaction—this is a consequence of the increasing surface-to-volume ration with smaller droplet sizes. With a higher surface reaction rate (not picture in Fig. 5.4) this becomes more dramatic, with the surface dominating at larger sizes. Scaling of γ with solute concentration and k_{rxn} (here assuming that the surface and bulk rate coefficients are equal) both appear approximately linear. This case will increasingly overestimate uptake coefficients for larger [$Y_{(total)}$] and k_{rxn} since an increasing loss rate of X leads to bulk depletion as explored in the following case. Therefore, the case here applies only when $L_{rxn} > r$. As classified by Worsnop et al.,[1] this can be thought of as the "dilute limit" because increasing dilution of Y implies larger L_{rxn} for X. Panels D-F in Fig. 5.4 provide time dependent kinetics of Case 1 for particles with radii 100 nm, 1 µm, and 10 µm, respectively. Profiles are provided for results of reaction-diffusion kinetics only (also referred to as the bulk reaction), surface reaction only, and the convolution of both surface and bulk reactions. This again shows that the surface reaction becomes increasingly relevant for smaller radii.

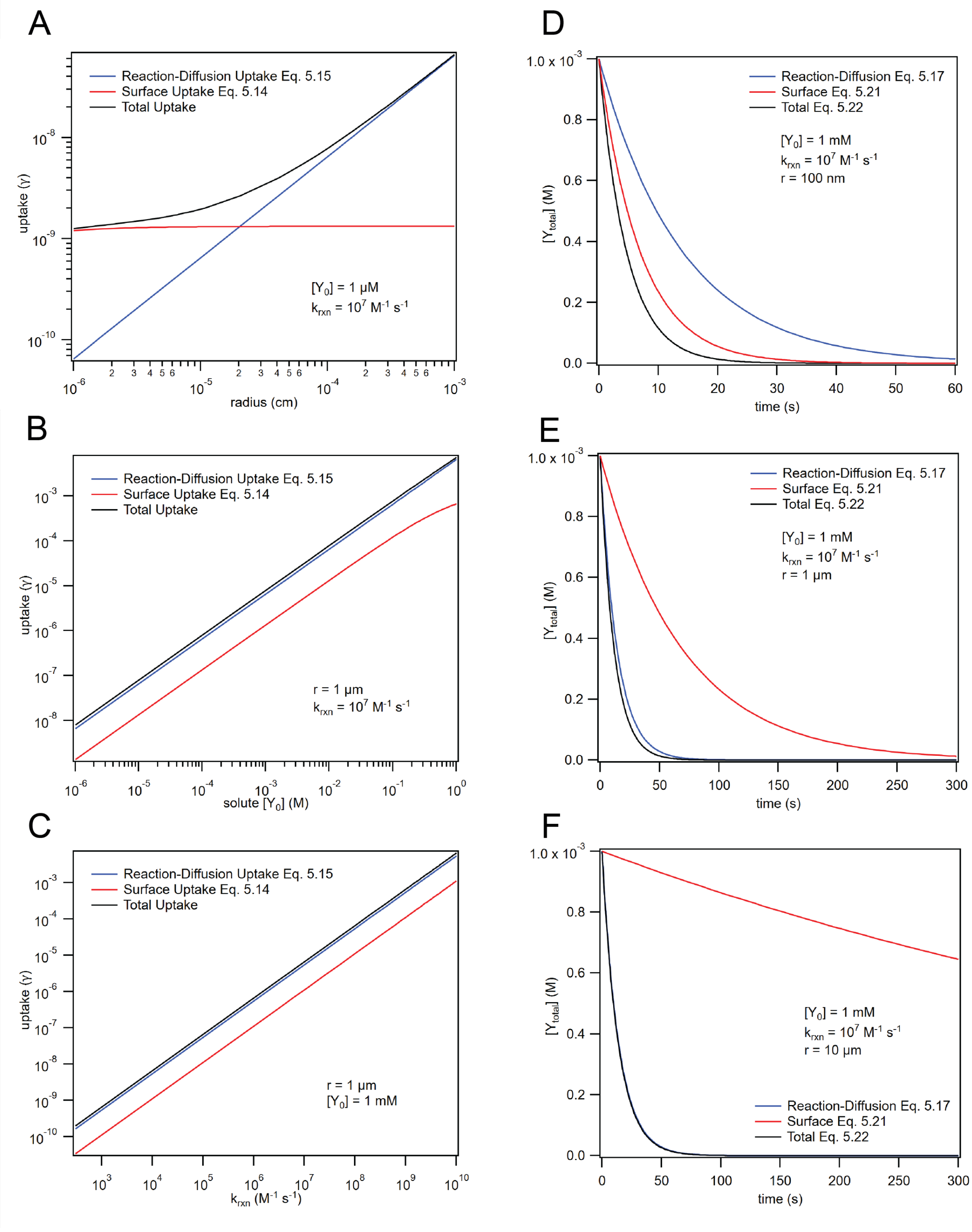

Fig. 5.4: Panels A-C shows uptake coefficients calculated for Case 1 using Eqs. 5.14-5.15 along with the summation, showing uptake dependence on r, $[Y_{(total)}]$, and k_{rxn}, respectively. Panels D-F show time dependence from Eqs. 5.17, 5.21, and 5.22 for particles with radius 100 nm, 1 µm, and 10 µm, respectively. Reaction conditions for each scenario are provided in the individual panels.

5.4.B: Case 2: Liquid-Diffusion Controlled

The reactive uptake of X by Y is controlled by the liquid diffusion of X when $L_{rd} < r$ and when the interfacial concentration of X is equal to the Henry's Law concentration. This case is very common for microdroplet reactivity as a broad range of reactive conditions lead to the $L_{rd} < r$ condition. In this case, we assume that X is equilibrated at the interface, i.e. $[\mathrm{X}_{(ads)}] = H_{\mathrm{X}}^{gs} \cdot [\mathrm{X}_{gas}^{\infty}]$, and that reactions occur at the surface and within the *rd* region. To acquire a time-dependent expression for this case, we follow the method of Section 3 and follow the example of Case 1 where we assume reactivity at the surface and in the reaction-diffusion region are independent, and first solve for reactivity occurring only due to γ_{rd} and then γ_{surf}.

The uptake coefficients defined for γ_{surf} and γ_{rd} in this case are:

$$\gamma_{surf} = \frac{4\, r\, k_{rxn}^{srf} \cdot H_{\mathrm{X}}^{gs}\left[\mathrm{X}_{gas}^{\infty}\right] \cdot \frac{\Gamma_{\infty}^{\mathrm{Y}}}{\delta} \frac{K_{eq}^{\mathrm{Y}}\left[\mathrm{Y}_{(total)}\right]}{1 + K_{eq}^{\mathrm{Y}}\left[\mathrm{Y}_{(total)}\right]}}{3 \cdot \bar{c} \cdot \left[\mathrm{X}_{gas}^{\infty}\right]} \cdot \frac{V_{surf}}{V_{total}} \qquad \text{Eq. 5.23}$$

$$\gamma_{rd} = \frac{4\, r\, k_{rxn}^{blk} \dfrac{k_{diff2}^{liq}\, k_{solv}\, H_{\mathrm{X}}^{gs}\, \left[\mathrm{X}_{gas}^{\infty}\right]\left[\mathrm{Y}_{(total)}\right]}{k_{desolv}\, k_{diff2}^{liq} + k_{desolv}\, k_{rxn}^{bulk}\left[\mathrm{Y}_{(total)}\right] + k_{diff1}^{liq} k_{rxn}^{bulk}\left[\mathrm{Y}_{(total)}\right]}}{3\, \bar{c}\left[\mathrm{X}_{gas}^{\infty}\right]} \cdot \frac{V_{rd}}{V_{total}}.$$

$$\text{Eq. 5.24}$$

Eqs. 5.23 and 5.24 are evaluated in Fig. 5.5 while varying *r*, $[\mathrm{Y}_{(total)}]$, and k_{rxn}.

(i) Reaction-Diffusion Region Kinetics

In the case of reaction controlled by liquid-diffusion of X, we have assumed that the interface is at all times equilibrated with both X and Y and that [Y] is uniform throughout the droplet. Computing the steady-state concentration of $\left[\mathrm{X}_{(rd)}\right]$ following the approach used in Appendices 4C and 5B, Eq. 5.10 can be written

$$\frac{d\left[\mathrm{Y}_{(total)}\right]}{dt} =$$

$$-k_{rxn}^{blk} \cdot \frac{k_{diff2}^{liq}\, k_{solv}\, H_{\mathrm{X}}^{gs} \cdot \left[\mathrm{X}_{gas}^{\infty}\right]}{k_{desolv}\, k_{diff2}^{liq} + k_{desolv}\, k_{rxn}^{bulk}\left[\mathrm{Y}_{(total)}\right] + k_{diff1}^{liq} k_{rxn}^{bulk}\left[\mathrm{Y}_{(total)}\right]} \cdot \left[\mathrm{Y}_{(total)}\right] \cdot \frac{V_{rd}}{V_{total}}.$$

$$\text{Eq. 5.25}$$

Separating variables, in this case, we obtain

$$\frac{\left(k_{desolv}\, k_{diff2}^{liq} + k_{desolv}\, k_{rxn}^{bulk}\left[\mathrm{Y}_{(total)}\right] + k_{diff1}^{liq} k_{rxn}^{bulk}\left[\mathrm{Y}_{(total)}\right]\right)}{k_{diff2}^{liq}\, k_{solv}\left[\mathrm{Y}_{(total)}\right]}\, d\left[\mathrm{Y}_{(total)}\right]$$
$$= \left(-k_{rxn}^{blk} \cdot H_{\mathrm{X}}^{gs}\left[\mathrm{X}_{gas}^{\infty}\right] \cdot \frac{V_{rd}}{V_{total}}\right) dt.$$

Eq. 5.26

We note that the definition of V_{rd} relies on L_{rxn}, which depends on the solute concentration [Y]. However, for simplicity we assume L_{rxn} is constant and defined by the initial concentration $\left[\mathrm{Y}_{(total)}\right]_0$. Eq. 5.26 is now integrated as

$$\int_{\left[\mathrm{Y}_{(rd)}\right]_0}^{\left[\mathrm{Y}_{(rd)}\right]_t} \frac{\left(k_{desolv}\, k_{diff2}^{liq} + \left(k_{desolv} + k_{diff1}^{liq}\right) k_{rxn}^{bulk} \left[\mathrm{Y}_{(total)}\right]\right)}{k_{diff2}^{liq}\, k_{solv} \left[\mathrm{Y}_{(total)}\right]}\, d\left[\mathrm{Y}_{(total)}\right] = \int_0^t \left(-k_{rxn}^{blk}\, H_{\mathrm{X}}^{gs} \cdot \left[\mathrm{X}_{gas}^{\infty}\right] \cdot \frac{V_{rd}}{V_{total}}\right) dt,$$

Eq. 5.27

to yield

$$\frac{\left(k_{desolv} + k_{diff1}^{liq}\right) k_{rxn}^{bulk}}{k_{desolv}\, k_{diff2}^{liq}} \left[\mathrm{Y}_{(total)}\right]_t + \ln\left[\mathrm{Y}_{(total)}\right]_t = \frac{\left(k_{desolv} + k_{diff1}^{liq}\right) k_{rxn}^{bulk}}{k_{desolv}\, k_{diff2}^{liq}} \left[\mathrm{Y}_{(total)}\right]_0 + \ln\left[\mathrm{Y}_{(total)}\right]_0 - k_{rxn}^{blk} \frac{k_{solv}}{k_{desolv}} H_{\mathrm{X}}^{gs} \left[\mathrm{X}_{gas}^{\infty}\right] \cdot \frac{V_{rd}}{V_{total}} t,$$

Eq. 5.28

which can be solved for $\left[\mathrm{Y}_{(total)}\right]_t$ using a Lambert W function:

$$\left[\mathrm{Y}_{(rd)}\right]_t = \frac{k_{desolv}\, k_{diff2}^{liq}}{\left(k_{desolv} + k_{diff1}^{liq}\right) k_{rxn}^{bulk}} \cdot \boldsymbol{W}\left\{\frac{\left(k_{desolv} + k_{diff1}^{liq}\right) k_{rxn}^{bulk} \left[\mathrm{Y}_{(total)}\right]_0}{k_{desolv}\, k_{diff2}^{liq}} \cdot e^{\frac{\left(k_{desolv}+k_{diff1}^{liq}\right) k_{rxn}^{bulk} \left[\mathrm{Y}_{(total)}\right]_0}{k_{desolv}\, k_{diff2}^{liq}} - k_{rxn}^{blk} \frac{k_{solv}}{k_{desolv}} H_{\mathrm{X}}^{gs} \left[\mathrm{X}_{gas}^{\infty}\right] \cdot \frac{V_{rd}}{V_{total}} t}\right\}.$$

Eq. 5.29

(ii) Surface Reaction Kinetics

The time dependence of $\left[\mathrm{Y}_{(total)}\right]$ due to the surface reaction alone in this case is equivalent to the result from Case 1 provided in Eq. 5.21. This results because both Cases 1 and 2 assume surface-adsorbed X is maintained at the surface-Henry's law concentration.

(iii) Combined Expression for Liquid-Diffusion Controlled Case

Just as Eq. 5.21 and Eq. 5.17 were used to create a combined expression for the time dependence of $\left[\mathrm{Y}_{(total)}\right]_t$ due to surface and bulk reaction, we now use the surface reaction equation Eq. 5.21 again where we substitute $\left[\mathrm{Y}_{(total)}\right]_0$ with the term $\left[\mathrm{Y}_{(rd)}\right]_t$ which we define as the bulk-reaction contribution given by Eq. 5.29:

$$\left[\mathrm{Y}_{(total)}\right]_t = \frac{1}{K_{eq}^{\mathrm{Y}}} \cdot \boldsymbol{W}\left\{K_{eq}^{\mathrm{Y}}\left[\mathrm{Y}_{(rd)}\right]_t \cdot e^{K_{eq}^{\mathrm{Y}}\left[\mathrm{Y}_{(rd)}\right]_t - k_{rxn}^{srf} \cdot \frac{\Gamma_{\infty}^{\mathrm{Y}}}{\delta} K_{eq}^{\mathrm{Y}} \cdot H_{\mathrm{X}}^{gs}\left[\mathrm{X}_{gas}^{\infty}\right] \cdot \frac{V_{surf}}{V_{total}} \cdot t}\right\}. \text{ Eq. 5.30}$$

Eq. 5.30, with $\left[\mathrm{Y}_{(rd)}\right]_t$ provides the full analytical solution to the Liquid-Diffusion Controlled case. This time-dependence includes reactive contributions from both the surface and the reaction-diffusion region. As in Case 1, we again compare output from Eq. 5.30, Eq. 5.29, and Eq. 5.21 in Fig. 5.5 for a set of example parameters.

Uptake coefficients and kinetics are reviewed for this case in Fig. 5.5 Panels A-C show the trends of γ in Case 2 with the kinetic parameters r, $[\mathrm{Y}_{(total)}]$, and k_{rxn}. This case agrees with Case 1 for small radius but becomes limited to a maximum γ for increasing radius. This shows the effect on depletion kinetics in the bulk—which ultimately limits γ. This depletion effect also manifests explicitly in the solute and k_{rxn} dependence, where the bulk becomes unfavorable compared to surface reactivity with shorter L_{rxn}. Panels D-F show time-dependent kinetics for Case 2 which similarly shows the increasing importance of the bulk reaction for larger radii. Unlike Case 1, the contribution of bulk reactivity cannot increase without bound and the relative surface-to-bulk reactivity approaches a constant.

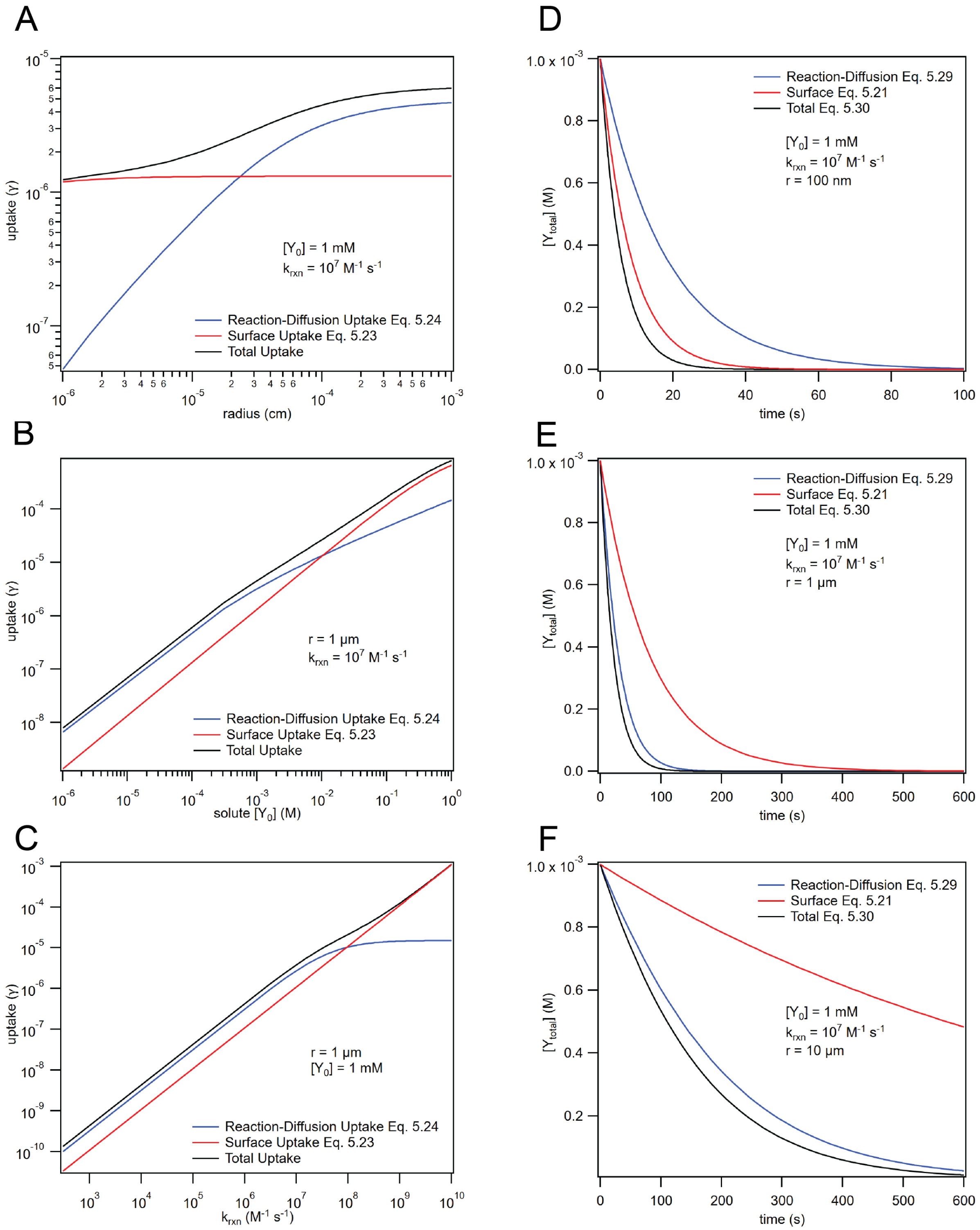

Fig. 5.5: Panels A-C shows uptake coefficients calculated for Case 2 using Eqs. 5.23-5.24 along with the summation, showing uptake dependence on *r*, [$Y_{(total)}$], and k_{rxn}, respectively. Panels D-F show time dependent kinetics from Eqs. 5.21, 5.29, and 5.30 for particles with radius 100 nm, 1 μm, and 10 μm, respectively. Reaction conditions for each scenario are provided in the individual panels.

5.4.C: Case 3: Interfacial-Depletion of X (Transition Kinetics)

In relaxing the Henry's law assumption for X at the interface, Case 3 is obtained where the concentration of X at the surface can be perturbed by reactivity with Y. The uptake coefficient expressions that define this case are:

$$\gamma_{surf} = \frac{4\,r\,k_{rxn}^{srf} \cdot \left(\frac{k_{diff}^{gas}\,k_{ads}}{k_{diff}^{gas} + k_{ads}}\right)\frac{\left[\mathrm{X}_{gas}^{\infty}\right]}{\phi} \cdot \frac{\Gamma_{\infty}^{\mathrm{Y}}}{\delta}\,\frac{K_{eq}^{\mathrm{Y}}\left[\mathrm{Y}_{(total)}\right]}{1 + K_{eq}^{\mathrm{Y}}\left[\mathrm{Y}_{(total)}\right]}}{3 \cdot \bar{c} \cdot \left[\mathrm{X}_{gas}^{\infty}\right]} \cdot \frac{V_{surf}}{V_{total}}, \qquad \text{Eq. 5.31}$$

$$\gamma_{rd} = \frac{4\,r\,k_{rxn}^{blk}\,\frac{k_{diff2}^{liq}\,k_{solv}\left(\frac{k_{diff}^{gas}\,k_{ads}}{k_{diff}^{gas} + k_{ads}}\right)\frac{\left[\mathrm{X}_{gas}^{\infty}\right]}{\phi}}{k_{desolv}\,k_{diff2}^{liq} + k_{desolv}\,k_{rxn}^{bulk}\left[\mathrm{Y}_{(rd)}\right] + k_{diff1}^{liq}k_{rxn}^{bulk}\left[\mathrm{Y}_{(rd)}\right]}\left[\mathrm{Y}_{(total)}\right]}{3\,\bar{c}\left[\mathrm{X}_{gas}^{\infty}\right]} \cdot \frac{V_{rd}}{V_{total}},$$

$$\text{Eq. 5.32}$$

where

$$\phi = k_{des} + k_{solv} + \left[\mathrm{Y}_{(ads)}\right]k_{rxn}^{surf} - \left(\frac{k_{des}\,k_{ads}}{k_{diff}^{gas} + k_{ads}}\right) - \left(\frac{k_{desolv}\,k_{solv}}{k_{diff1}^{liq} + k_{desolv}}\right)$$
$$- \left(\frac{k_{diff1}^{liq}\,k_{diff2}^{liq}\,k_{desolv}\,k_{solv}}{\left(k_{diff2}^{liq} + k_{desolv}\right) \times \left(k_{desolv}\left[\mathrm{Y}_{(rd)}\right]k_{rxn}^{bulk} + k_{diff1}^{liq}\left[\mathrm{Y}_{(rd)}\right]k_{rxn}^{bulk} + k_{diff2}^{liq}\,k_{desolv}\right)}\right).$$

Equations 5.31 and 5.32 provide uptake coefficients that include the full description of *X* depletion. These uptake coefficients are shown in Fig. 5.6 for a range of kinetic parameters, as previously seen for Cases 1 and 2. Furthermore, these uptake coefficients can be used to compute the full time-dependent numerical solution to Eq. 5.9. While the equations are somewhat cumbersome, they provide the entire kinetic information shown for the X species in Fig. 5.3 under the "trace-gas" condition, i.e., when assuming Y is equilibrated throughout the droplet. In keeping with the other cases, uptake coefficients are shown across a range of the droplet parameters *r*, $[\mathrm{Y}_{(total)}]$, and k_{rxn}.

To acquire an approximation for the analytical form for the $\left[\mathrm{Y}_{(total)}\right]_t$ time-dependence in this case we assume the γ_{rd} contribution to overall reactivity is small enough to assume that the time-dependence due to γ_{rd} is approximated by Eq. 5.29 from the previous Case 2. We then augment γ_{surf} by assuming the 4th order term in ϕ is negligible and subtracting $k_{rxn}^{srf}\left[\mathrm{Y}_{(ads)}\right]$ to define

$$\theta = k_{des} + k_{solv} - \left(\frac{k_{des}\,k_{ads}}{k_{diff}^{gas} + k_{ads}}\right) - \left(\frac{k_{desolv}\,k_{solv}}{k_{diff1}^{liq} + k_{desolv}}\right)$$

and solve for the time dependence $\left[\mathrm{Y}_{(total)}\right]_t$ due to surface reaction including depletion of X:

$$\frac{d\left[\mathrm{Y}_{(total)}\right]}{dt} = -k_{rxn}^{srf} \cdot \frac{\left(\frac{k_{diff}^{gas}\, k_{ads}}{k_{diff}^{gas} + k_{ads}}\right)\left[\mathrm{X}_{gas}^{\infty}\right]}{\theta + k_{rxn}^{srf} \frac{\Gamma_{\infty}^{\mathrm{Y}}}{\delta} \frac{K_{eq}^{\mathrm{Y}}\left[\mathrm{Y}_{(total)}\right]}{1 + K_{eq}^{\mathrm{Y}}\left[\mathrm{Y}_{(total)}\right]}} \cdot \frac{\Gamma_{\infty}^{\mathrm{Y}}}{\delta} \frac{K_{eq}^{\mathrm{Y}}\left[\mathrm{Y}_{(total)}\right]}{1 + K_{eq}^{\mathrm{Y}}\left[\mathrm{Y}_{(total)}\right]} \cdot \frac{V_{surf}}{V_{total}}.$$

Eq. 5.33

Integrating Eq. 5.33 as before and using the Lambert function provides the time dependence for loss of $\left[\mathrm{Y}_{(total)}\right]$ due to the surface reaction:

$$\left[\mathrm{Y}_{(total)}\right]_t = \frac{\theta}{\frac{\Gamma_{\infty}^{\mathrm{Y}}}{\delta} K_{eq}^{\mathrm{Y}} k_{rxn}^{srf} + K_{eq}^{\mathrm{Y}}\theta} \cdot \boldsymbol{W}\left\{\frac{\frac{\Gamma_{\infty}^{\mathrm{Y}}}{\delta} K_{eq}^{\mathrm{Y}} k_{rxn}^{srf} + K_{eq}^{\mathrm{Y}}\theta}{\theta}\left[\mathrm{Y}_{(rd)}\right]_0 \cdot e^{\frac{\frac{\Gamma_{\infty}^{\mathrm{Y}}}{\delta} K_{eq}^{\mathrm{Y}} k_{rxn}^{srf} + K_{eq}^{\mathrm{Y}}\theta}{\theta}\left[\mathrm{Y}_{(rd)}\right]_0 - \frac{\left(\frac{k_{diff}^{gas}\, k_{ads}}{k_{diff}^{gas} + k_{ads}}\right)\frac{\Gamma_{\infty}^{\mathrm{Y}}}{\delta} K_{eq}^{\mathrm{Y}} k_{rxn}^{srf}\left[\mathrm{X}_{gas}^{\infty}\right]}{\theta} \cdot \frac{V_{surf}}{V_{total}} \cdot t}\right\}.$$

Eq. 5.34

As previously, we obtain the complete time-dependent expression

$$\left[\mathrm{Y}_{(total)}\right]_t = \frac{\theta}{\frac{\Gamma_{\infty}^{\mathrm{Y}}}{\delta} K_{eq}^{\mathrm{Y}} k_{rxn}^{srf} + K_{eq}^{\mathrm{Y}}\theta} \cdot \boldsymbol{W}\left\{\frac{\frac{\Gamma_{\infty}^{\mathrm{Y}}}{\delta} K_{eq}^{\mathrm{Y}} k_{rxn}^{srf} + K_{eq}^{\mathrm{Y}}\theta}{\theta}\left[\mathrm{Y}_{(rd)}\right]_t \cdot e^{\frac{\frac{\Gamma_{\infty}^{\mathrm{Y}}}{\delta} K_{eq}^{\mathrm{Y}} k_{rxn}^{srf} + K_{eq}^{\mathrm{Y}}\theta}{\theta}\left[\mathrm{Y}_{(rd)}\right]_t - \frac{\left(\frac{k_{diff}^{gas}\, k_{ads}}{k_{diff}^{gas} + k_{ads}}\right)\frac{\Gamma_{\infty}^{\mathrm{Y}}}{\delta} K_{eq}^{\mathrm{Y}} k_{rxn}^{srf}\left[\mathrm{X}_{gas}^{\infty}\right]}{\theta} \cdot \frac{V_{surf}}{V_{total}} \cdot t}\right\},$$

Eq. 5.35

by substituting $\left[\mathrm{Y}_{(rd)}\right]_0$ in Eq. 5.34 with the expression for the reaction-diffusion contribution $\left[\mathrm{Y}_{(rd)}\right]_t$, as defined by Eq. 5.29 (assuming that the reaction-diffusion contribution in this case approximates that of Case 2). The validity of this assumption is checked in Fig. 5.7 by comparing Eq. 5.35 with the numerical solution to Eq. 5.9 using uptake definitions in Eq. 5.31 and Eq. 5.32.

Results for uptake coefficients and the time-dependence kinetics for this case are provided in Fig. 5.6. These results are similar to Case 2, with the notable exception that the overall bulk reactivity can now be influenced by the gas-phase diffusion of X. On example of this effect in Fig. 5.6 is the decreasing contribution of the bulk reaction with larger k_{rxn}, where the surface reaction can now limit the number of X molecules that can solvate into the *rd* region. Fig. 5.7 compares the closed-form expressions in this case with the numerical solutions to Eq. 5.9, demonstrating that the analytical expressions virtually reproduce the full time-dependence.

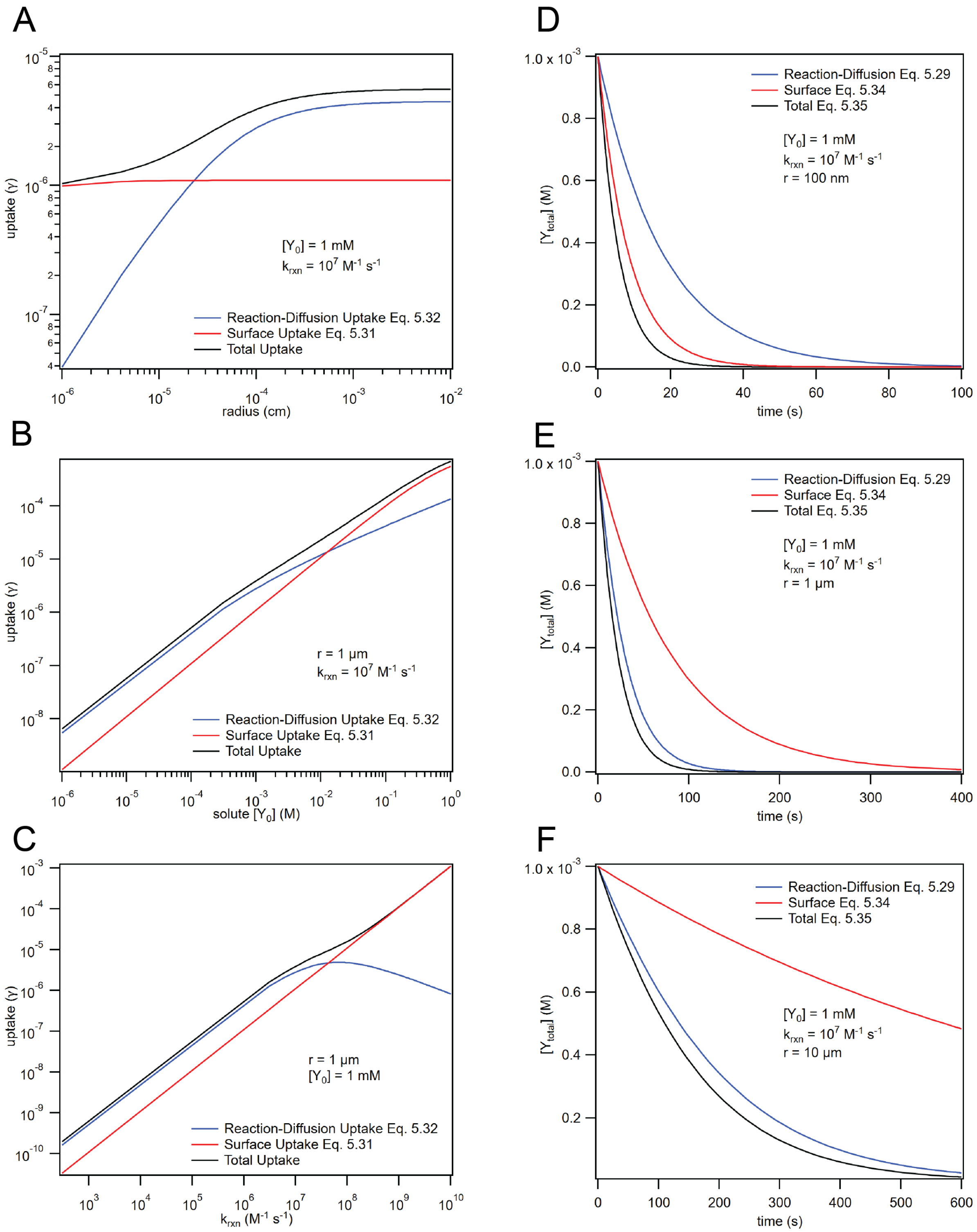

Fig. 5.6: Panels A-C shows uptake coefficients calculated for Case 3 using Eqs. 5.31-5.32 along with the summation, showing uptake dependence on r, $[Y_{(total)}]$, and k_{rxn}, respectively. Panels D-F show time dependent kinetics from Eqs. 5.29, 5.34, and 5.35 for particles with radius 100 nm, 1 µm, and 10 µm, respectively. Reaction conditions for each scenario are provided in the individual panels.

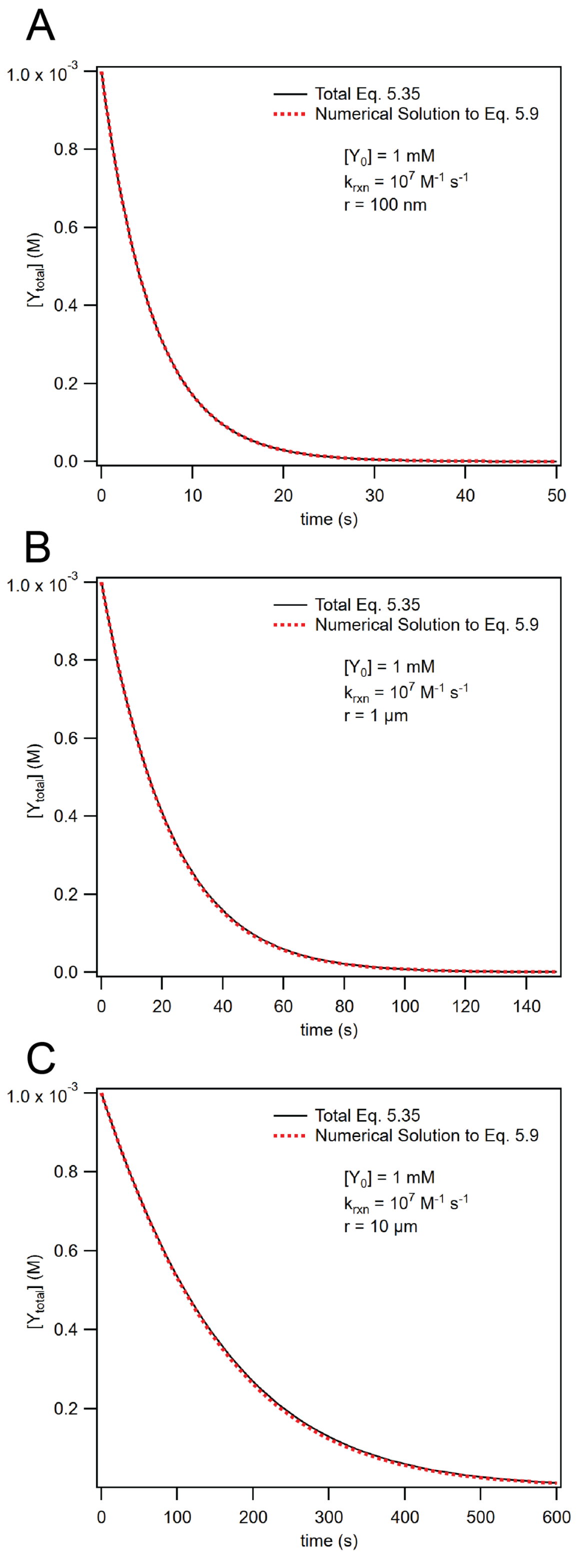

Fig. 5.7: Kinetic profiles for results from Case 3 using Eq. 5.35 compared to numerical evaluations of Eq. 5.9 using uptake coefficients defined in Eq. 5.31 and Eq. 5.32. Evaluations are presented for droplet radii 100 nm to 10 µm.

5.4.D: Case 4: Total Depletion of X (Gas-Diffusion Limit)

This case expresses the upper bound for γ_{total} determined by gas-transport using the same expressions in Case 3. For increasing radius *r*, gas diffusion to the surface becomes slower relative to the expected collision rate. Therefore, γ_{total} does not approach the surface-reaction probability with increasing $[\mathrm{Y}_{total}]$, as may be expected, but instead approaches a value governed by the surface-reaction probability modulated by a gas-phase diffusion description. This concept was explored by Fuchs & Sutugin[3] using a continuum description of diffusion to a droplet surface, and flux-matching condition at a spherical boundary surrounding the droplet. These dynamics are similarly captured in the current kinetic model, with a diffusional description agreeing with the results of Fuchs & Sutugin. This behavior is discussed in detail in Appendix 5.C.

Uptake coefficients in this limiting case are obtained by considering the behavior of Eq. 5.31 and Eq. 5.32 when the diffusion rate k_{diff}^{gas} becomes significantly smaller than k_{ads}. In this case,

$$\gamma_{surf} = \frac{4\,r\,k_{rxn}^{srf} \cdot k_{diff}^{gas} \frac{\left[\mathrm{X}_{gas}^{\infty}\right]}{\phi} \cdot \frac{\Gamma_{\infty}^{\mathrm{Y}}}{\delta} \frac{K_{eq}^{\mathrm{Y}}\left[\mathrm{Y}_{(total)}\right]}{1 + K_{eq}^{\mathrm{Y}}\left[\mathrm{Y}_{(total)}\right]}}{3 \cdot \bar{c} \cdot \left[\mathrm{X}_{gas}^{\infty}\right]} \cdot \frac{V_{surf}}{V_{total}}, \qquad \text{Eq. 5.36}$$

$$\gamma_{rd} = \frac{4\,r\,k_{rxn}^{blk} \frac{k_{diff2}^{liq}\,k_{solv} \cdot\, k_{diff}^{gas} \frac{\left[\mathrm{X}_{gas}^{\infty}\right]}{\phi}}{k_{desolv}\,k_{diff2}^{liq} + k_{desolv}\,k_{rxn}^{bulk}\left[\mathrm{Y}_{(rd)}\right] + k_{diff1}^{liq} k_{rxn}^{bulk}\left[\mathrm{Y}_{(rd)}\right]} \left[\mathrm{Y}_{(total)}\right]}{3\,\bar{c}\left[\mathrm{X}_{gas}^{\infty}\right]} \cdot \frac{V_{rd}}{V_{total}},$$

$$\text{Eq. 5.37}$$

where

$$\phi = k_{solv} + \left[\mathrm{Y}_{(ads)}\right] k_{rxn}^{surf} - \left(\frac{k_{desolv}\,k_{solv}}{k_{diff1}^{liq} + k_{desolv}}\right) - \left(\frac{k_{diff1}^{liq}\,k_{diff2}^{liq}\,k_{desolv}\,k_{solv}}{\left(k_{diff2}^{liq} + k_{desolv}\right) \times \left(k_{desolv}\left[\mathrm{Y}_{(rd)}\right] k_{rxn}^{bulk} + k_{diff1}^{liq}\left[\mathrm{Y}_{(rd)}\right] k_{rxn}^{bulk} + k_{diff2}^{liq}\,k_{desolv}\right)}\right).$$

Using the same approximations as in Case 3, we define

$$\theta' = k_{solv} - \left(\frac{k_{desolv}\,k_{solv}}{k_{diff1}^{liq} + k_{desolv}}\right)$$

and obtain the time-dependent analytical form for this case:

$$\left[\mathrm{Y}_{(total)}\right]_t =$$

$$\frac{\theta'}{\frac{\Gamma_{\infty}^{\mathrm{Y}}}{\delta} K_{eq}^{\mathrm{Y}} \cdot k_{rxn}^{srf} + K_{eq}^{\mathrm{Y}}\theta'} \cdot \boldsymbol{W}\left\{\frac{\frac{\Gamma_{\infty}^{\mathrm{Y}}}{\delta} K_{eq}^{\mathrm{Y}} \cdot k_{rxn}^{srf} + K_{eq}^{\mathrm{Y}}\theta'}{\theta'}\left[\mathrm{Y}_{(rd)}\right]_t \cdot e^{\frac{\frac{\Gamma_{\infty}^{\mathrm{Y}}}{\delta} K_{eq}^{\mathrm{Y}} \cdot k_{rxn}^{srf} + K_{eq}^{\mathrm{Y}}\theta'}{\theta'}\left[\mathrm{Y}_{(rd)}\right]_t - \frac{k_{diff}^{gas} \cdot \frac{\Gamma_{\infty}^{\mathrm{Y}}}{\delta} K_{eq}^{\mathrm{Y}} \cdot k_{rxn}^{srf}\left[\mathrm{X}_{gas}^{\infty}\right]}{\theta'} \cdot \frac{V_{surf}}{V_{total}} \cdot t}\right\},$$

Eq. 5.38

where once again $\left[\mathrm{Y}_{(rd)}\right]_t$ is defined by Eq. 5.29. We provide a brief comparison between results from Case 4 and Case 3 in Fig. 5.8 to demonstrate the limiting behavior observed by Case 3 and defined by Case 4.

In the comparison of Fig. 5.8, it's observed that γ in Case 4 is always greater than γ in Case 3. Since Case 4 is derived by assuming the gas-diffusion step limits all transport phenomena, this by definition defines an upper bound for γ. Panels D-F in Fig. 5.8 show the time-dependent kinetics for these two cases. Unlike the previous comparisons, the kinetics here appear to be approximately linear in time. This is expected since the gas-diffusion limit of X implies first-order kinetics in [Y], as noted in Chapter 2. The time-dependent kinetics for Case 4 are also shown to converge to Case 3 with increasing radius, demonstrating the effect of increasing size on the effective gas-transport rate which is fixed to an upper-limit in Case 4, but dynamically varies in Case 3.

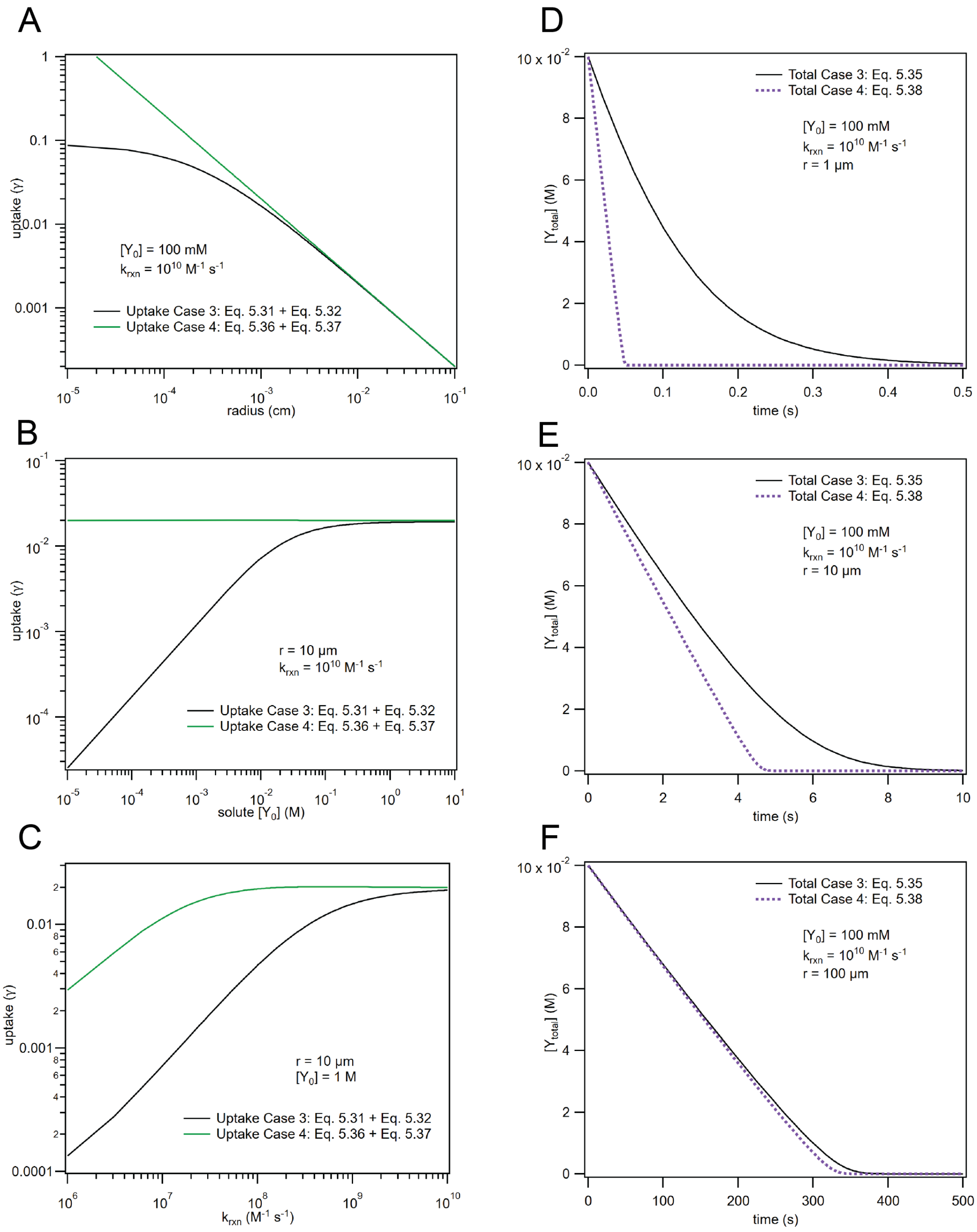

Fig. 5.8: Panels A-C shows uptake coefficients calculated from Case 4 compared to Case 3 showing uptake dependence on *r*, [$Y_{(total)}$], and k_{rxn}, respectively. Panels D-F show time dependent kinetics from Eq. 5.35 for Case 3 and Eq. 5.38 for Case 4 for particles with radius1 μm, 10 μm, and 100 μm. Reaction conditions for each scenario are provided in the individual panels.

5.4.E: Case 1-4 Summary

We interlude between case descriptions to provide a summary of Cases 1-4, which all assume that the solute [Y] is well mixed throughout the particle. In short, Case 1 describes the limiting case in which both X and Y are well mixed in the particle. Case 2 accounts for kinetics due to the bulk depletion of X, but still assumes X is well mixed at the interface. Case 3 relaxes this assumption and allows X to become depleted at the interface and in the gaseous region surrounding the particle. Case 4 describes the limiting case in which the rate of transport of X to the droplet is bounded by the rate of gas-diffusion to the droplet surface. In panels A-C in Fig. 5.9, Cases 1-3 are compared while varying the parameters r, $[\mathrm{Y}_{(total)}]$, and k_{rxn}. For a comparison with Case 4, we refer the reader to the previous Section 5.4.D. Panels D-F in Fig. 5.9 explore the effect of different values for the surface and bulk reaction rate. In this comparison, the bulk reaction rate k_{rxn}^{bulk} is fixed while k_{rxn}^{srf} is varied across orders of magnitude. As shown, the value of k_{rxn}^{bulk} effectively defines a lower bound for the potential value of γ, while an increasing k_{rxn}^{srf} generally increases γ. Case 3 demonstrates the upper bound for γ with increasing k_{rxn}^{srf}—realized for short enough L_{rxn} where gas-phase limitations begin to dominate.

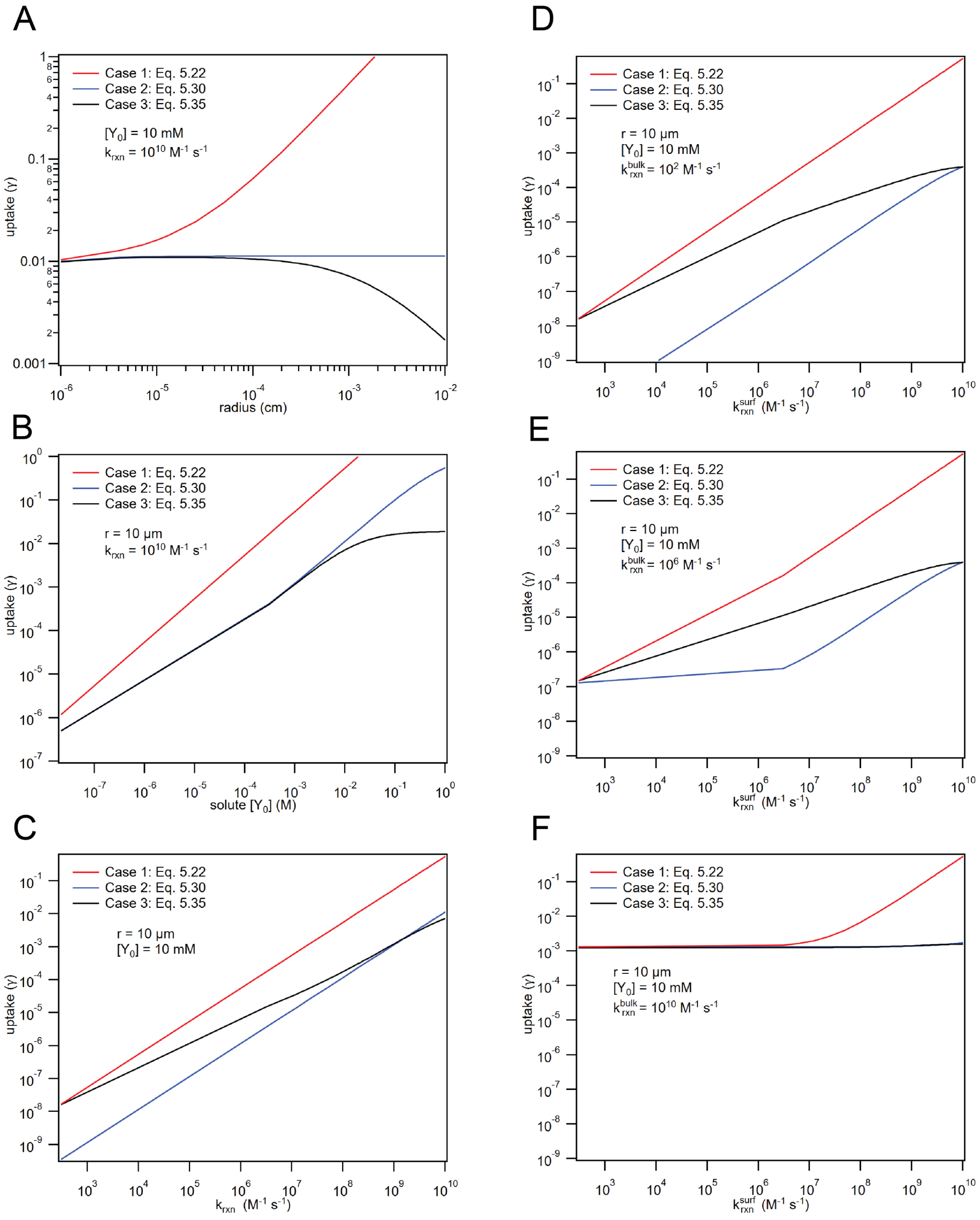

Fig. 5.9: Panels A-C compare uptake coefficients calculated from Cases 1-3 by varying radius, solute concentration, and rate coefficient, respectively. Panels D-F evaluate the uptake dependence on the surface reaction rate coefficient k_{srxn} for three fixed values of k_{brxn}.

5.4.F: Case 5: Interfacial-Depletion of Y

The "trace solute" Cases 5 and 6 round out the conceptual series resulting from reaction between X and Y. In the cases above, we have assumed that [Y] >> [X] in the droplet for all times, such that reaction X + Y may deplete [X] at the surface or bulk, but [Y] does not become depleted. Cases 5 and 6 consider the kinetic trends possible when [Y] is depleted by the reaction both at the surface (Case 5) and in the bulk (Case 6). The present case considers the scenario where X and Y react at the droplet interface, but [Y] is dilute enough to become depleted by reaction with X. For simplicity, we assume that [X] is at all times equilibrated at the surface, i.e., $[\mathrm{X}_{(ads)}] = H_{gs}[\mathrm{X}_{gas}^{\infty}]$ and that reactivity only occurs at the droplet surface. While this may not seem like a particularly relevant case for aqueous aerosol chemistry, this case may be particularly relevant for more viscous aerosol or even emulsion-type systems where an aqueous microdroplet suspending in an oil phase undergoes reaction only at the phase boundaries. In such a system, the solute Y in the aqueous phase and the solute X in the oil phase may only be sparingly soluble in the reverse phase but may undergo reactivity at the interface.

Assuming that [X] has a fixed concentration at the droplet surface allows us to explore the case where interfacial reactivity is limited by the mass transport of solute Y to the droplet interface. This limitation may be due to the diffusion of Y through the droplet, or due to an energetic barrier for solute adsorption to the interface. To treat this case in a general manner, a new kinetic region must be identified that relates to the potential chemical gradient of Y generated through loss of Y at the interface. The length scale that defines this gradient in the current model is the adsorption length L_{ads} of Y which, in this case, can substitute the reaction-diffusion length in the framework discussed so far, as illustrated in Fig. 5.10. Diffusion from the bulk interior of the droplet into the adsorption region then determines the kinetics of overall reaction at the interface when Y is depleted. This model representation has recently been demonstrated to replicate experimental dynamics of surfactant partitioning to aqueous droplet interfaces.[4] In that scenario, the large preference of the surfactant for the interface results in surfactant depletion near the interface and establishes a transient chemical gradient while the system approaches equilibrium.

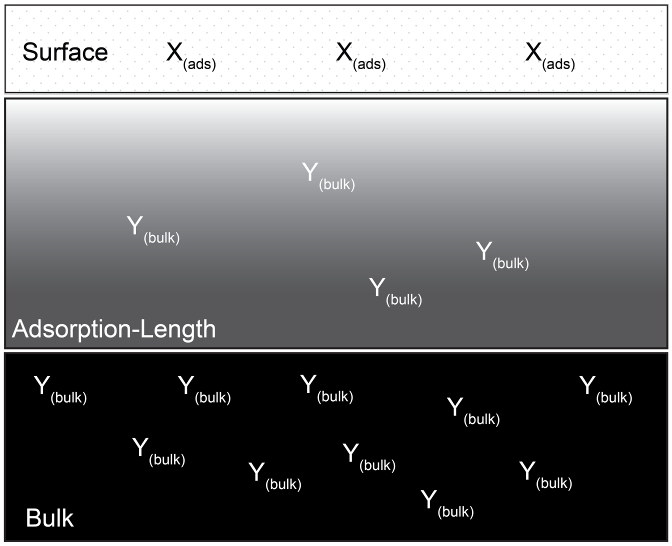

Fig. 5.10: Illustration of regions identified in Case 5. In this case, the surface is assumed to be equilibrated with X and only the surface reaction is considered. For a high enough loss rate of Y, the reaction will become limited by the mass transport of Y. This can be modeled by introducing a diffusion region for Y defined by the length scale L_{ads}.

The chemical case encountered here is similar in that the rapid loss of Y at the interface causes the overall rate of reaction to become limited by Y diffusion across the adsorption length L_{ads}. The adsorption length for Y is defined as the length scale obtained by the ratio of surface concentration $[\mathrm{Y}_{(ads)}]$ (in surficial units molecule/cm^2) to the bulk concentration $[\mathrm{Y}_{(total)}]$ in the equilibrated system. Defining $[\mathrm{Y}_{(ads)}]$ with our standard Langmuir Adsorption description, L_{ads} can be defined with the equilibrium adsorption constant K_{eq}, the maximum interfacial coverage Γ^{∞}, and the bulk concentration $[\mathrm{Y}_{(total)}]$:

$$L_{ads} = \frac{\Gamma^{\infty} K_{eq}}{1 + K_{eq}[\mathrm{Y}_{(total)}]}. \qquad \text{Eq. 5.39}$$

Following the same methods to describe depletion of species X at the interface, we find the steady state surface concentration of solute $[\mathrm{Y}_{(ads)}]$ to be

$$\left[\mathrm{Y}_{(ads)}\right] = \frac{k^{Y}_{desolv}\, k^{Yliq}_{Ads1}\, k^{Yliq}_{Ads3} \cdot [\mathrm{Y}_{(total)}]}{\left(k^{Y}_{solv} + k^{srf}_{rxn}\, H_{gs}\left[\mathrm{X}^{\infty}_{gas}\right]\right)\Omega - k^{Y}_{desolv}\, k^{Y}_{solv}\left(k^{Yliq}_{Ads2} + k^{Yliq}_{Ads3}\right)}, \qquad \text{Eq. 5.40}$$

where

$$\Omega = \left(k^{Y}_{desolv} + k^{Yliq}_{Ads1}\right)\left(k^{Yliq}_{Ads2} + k^{Yliq}_{Ads3}\right) - k^{Yliq}_{Ads1}\, k^{Yliq}_{Ads2}.$$

We note that to derive this expression for $\left[\mathrm{Y}_{(ads)}\right]$, we have assumed that $\left[\mathrm{Y}_{(total)}\right]$ dilute enough to ignore saturation effects at the interface, or in other words $\left[\mathrm{Y}_{(ads)}\right] \sim K_{eq}[\mathrm{Y}_{(total)}]$. Care should be taken when using this case to assure that the scaling of $\left[\mathrm{Y}_{(ads)}\right]$ with $\left[\mathrm{Y}_{(tota)}\right]$ is in the “linear” portion of the Langmuir isotherm.

The kinetic coefficients $k_{Ads\#}^{Yliq}$ in Eq. 5.40 refer to the diffusional transport coefficients that describe diffusion between the bulk compartment and the adsorption-length compartment outlined in Fig. 5.10. These are defined using the same method outlined for coefficients $k_{diff\#}^{liq}$ describing diffusion of X in the reaction diffusion region (see Appendix 5.A). The value for k_{Ads1}^{Yliq}, for example, is defined

$$k_{Ads1}^{Yliq} = \frac{2\, D_{\mathrm{Y}}}{\left(\frac{L_{ads}}{1 + \frac{1}{r} L_{ads}} + \delta\right)\delta}, \qquad \text{Eq. 5.41}$$

where D_Y is the diffusion coefficient of Y in the aqueous phase. Coefficients k_{desolv}^{Y} and k_{solv}^{Y} are related to the equilibrium adsorption coefficient for Y, $K_{eq} = k_{desolv}^{Y} / k_{solv}^{Y}$.

The uptake coefficient for this case is

$$\gamma_{total} = \gamma_{surf} =$$

$$\frac{4\, r\, k_{rxn}^{srf} \cdot H_{gs}[\mathrm{X}_{gas}^{\infty}] \cdot \dfrac{k_{desolv}^{Y}\, k_{Ads1}^{Yliq}\, k_{Ads3}^{Yliq} \cdot [\mathrm{Y}_{(total)}]}{(k_{solv}^{Y} + k_{rxn}^{srf}\, H_{gs}\, [\mathrm{X}_{gas}^{\infty}])\Omega - k_{desolv}^{Y}\, k_{solv}^{Y}(k_{Ads2}^{Yliq} + k_{Ads3}^{Yliq})}}{3 \cdot \bar{c} \cdot [\mathrm{X}_{gas}^{\infty}]} \cdot \frac{V_{surf}}{V_{total}}, \qquad \text{Eq. 5.42}$$

which defines the total uptake in this case since we have assumed X is completely depleted in the bulk. Fig. 5.11 demonstrates how the uptake coefficient now exhibits a dependence on $[\mathrm{X}_{gas}^{\infty}]$ since this concentration now determines the degree of $[\mathrm{Y}_{(ads)}]$ depletion at the interface.

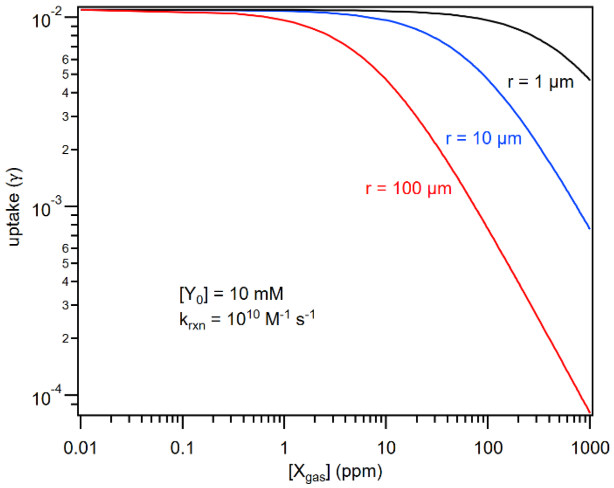

Fig. 5.11: Uptake coefficients vs concentration of gaseous species X in Case 5 evaluated with Eq. 5.42. The three different curves show uptake for a droplet of radius 1 µm, 10 µm, and 100 µm.

The time-dependent expression for $[\mathrm{Y}_{(total)}]$ in this case is simply an exponential as was found for Case 1:

$$\left[\mathrm{Y}_{(total)}\right]_t = \left[\mathrm{Y}_{(total)}\right]_0 e^{-\frac{k_{desolv}^{Y}\, k_{Ads1}^{Yliq}\, k_{Ads3}^{Yliq}}{\left(k_{solv}^{Y} + k_{rxn}^{srf}\, H_{gs}\, [\mathrm{X}_{gas}^{\infty}]\right)\Omega - k_{desolv}^{Y}\, k_{solv}^{Y}\left(k_{Ads2}^{Yliq} + k_{Ads3}^{Yliq}\right)} - k_{rxn}^{srf} \cdot H_{gs} [\mathrm{X}_{gas}^{\infty}] \cdot \frac{V_{surf}}{V_{total}}\, t}.$$

Eq. 5.43

Because the steady-state concentration of [Y*(ads)*] depends on the diffusion coefficient D_Y and the absolute values of the desolvation coefficients k_{desolv}^{Y} and k_{solv}^{Y}, so do equations Eq. 5.42 and Eq. 5.41. To demonstrate the effect, Fig. 5.11 compares droplet $\left[\mathrm{Y}_{(total)}\right]_t$ kinetics using Eq. 5.42 and the surface-only reaction expression encountered in Case 3, which ignores any surface depletion of [Y]. In Fig. 5.12A, using a set of example kinetic parameters, the diffusion coefficient D_Y varies over orders of magnitude to show the effect of the Y diffusion on the decay kinetics compared to Case 3 when ignoring transport limitations of Y. Similarly, Fig. 5.12B demonstrates the analogous effect of modulating the desolvation rate k_{desolv}^{Y}.

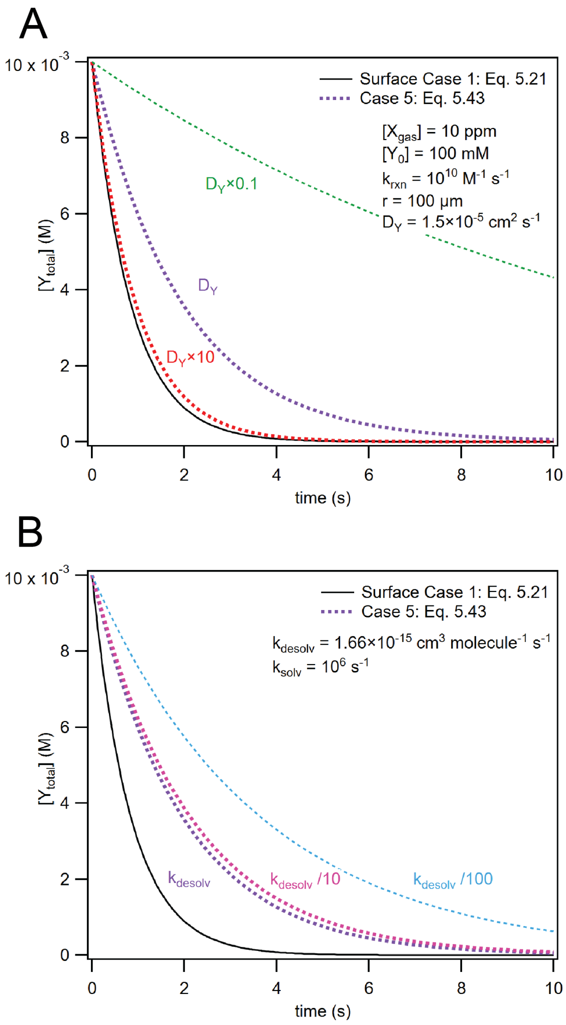

Fig. 5.12: Time dependent kinetics for Case 5 compared to Case 1. Panel (A) shows the effect of varying the diffusion coefficient D_Y in Case 5, whereas Panel (B) shows the effect of varying the kinetic coefficient k_{desolv}.

5.4.G: Case 6: Bulk-Depletion of Y (Multi Gradient Methods)

While Case 5 investigated the limits of chemical kinetics at interfaces where aqueous solute [Y] is depleted, this case investigates the further notion where [Y] depletion extends beyond the interface and into the bulk aqueous phase. This is achieved by relaxing the assumption that the reaction occurs only at the interface—and allowing X to diffuse through the aqueous phase and react with Y. Fig. 5.13 shows the conceptual picture that pertains to this case, one that epitomizes a "reaction-diffusion" system for a two-component chemical reaction.

Within the current kinetic framework, uptake coefficients can be derived for this type of system by including one additional conceptual region or compartment. As noted in the introduction and in Chapter I, the modeling philosophy employed is built to discretize gradients wherever they may occur, and therefore, we can approach this problem with one chemical gradient region for X and one chemical gradient region for Y. As we will show, this approach is remarkably successful when comparing models that approximate a continuum—effectively trying to resolve the entire gradient of X and Y and the chemistry that results from the overlap. Using only two adjacent "regions" this resulting overlap chemistry can be reproduced with the current approach.

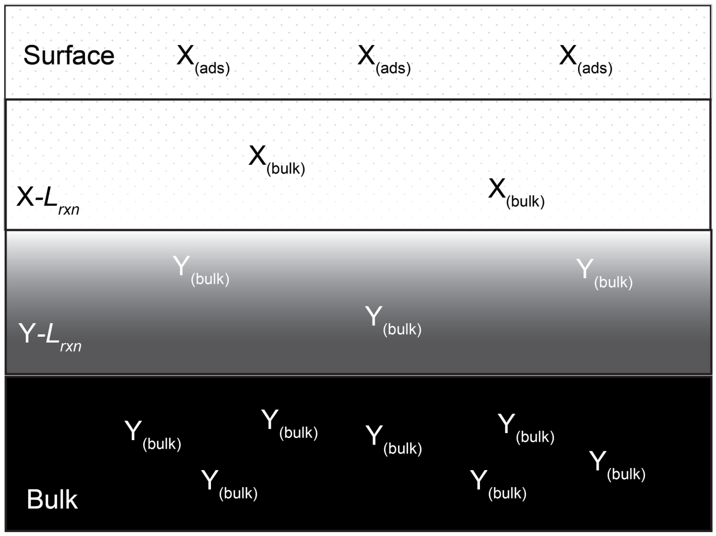

Fig. 5.13: Illustration of regions identified in Case 6. In this case, the surface is still assumed to be equilibrated with X but includes X diffusion into the bulk. Depletion of both X and Y in the near-surface region can be modeled using two adjacent L_{rxn} compartments, one for X and one for Y defined by initial conditions in this case.

To construct this, we first assume (in opposition to Case 5) that reactivity only occurs in the bulk phase, with no surface reaction occurring. Using this assumption, the adsorption length description found in the previous case can be discarded. We now assume again that X is equilibrated at the interface and can diffuse into its reaction-diffusion region defined as in Case 2. An additional reaction-diffusion region is now defined for the solute Y. Following the same logic as the reaction-diffusion region for X, the reaction-diffusion length for Y is

$$L_{rxn}^{Y} = \sqrt{\frac{D_{(aq)}^{Y}}{k_{rxn}^{bulk} \cdot H_{gb}\left[\mathrm{X}_{gas}^{\infty}\right]}}.$$

The uptake of X in this system then depends on reactive loss in the L_{rxn}^{X} and L_{rxn}^{Y} regions as shown conceptually in Fig. 5.13. The reactivity is ultimately determined by the steady-state concentrations of [X] and [Y] in both regions, which depends on diffusion of X and Y from their respective bulk regions into L_{rxn}^{Y} and L_{rxn}^{X}. Uptake coefficients due to reaction in the *X*-diffusion region and the *Y*-diffusion region are therefore:

$$\gamma_{total} = \gamma_{Xdiff} + \gamma_{Ydiff}, \qquad \text{Eq. 5.44}$$

$$\gamma_{Xdiff} = \frac{4\,k_{rxn}^{bulk} \cdot \left[\mathrm{X}_{Xdiff}\right] \cdot \left[\mathrm{Y}_{Xdiff}\right]}{\bar{c} \cdot \left[\mathrm{X}_{gas}^{\infty}\right]} \cdot \frac{SA\,L_{rxn}^{X}}{SA}, \qquad \text{Eq. 5.45}$$

$$\gamma_{Xdiff} = \frac{4\,k_{rxn}^{bulk} \cdot \left[\mathrm{X}_{Ydiff}\right] \cdot \left[\mathrm{Y}_{Ydiff}\right]}{\bar{c} \cdot \left[\mathrm{X}_{gas}^{\infty}\right]} \cdot \frac{SA\,L_{rxn}^{Y}}{SA}, \qquad \text{Eq. 5.46}$$

where we have introduced a slightly more general definition of γ using the surface area (*SA*) of the multiphase system rather than restrict to a spherical system. The steady-state concentrations for [X] and [Y] then depend on the diffusion and reaction terms relevant for each region:

$$\left[\mathrm{X}_{Xdiff}\right] = \frac{k_{Xdiff}^{liq1} \cdot H_{gb}\left[\mathrm{X}_{gas}^{\infty}\right] + k_{Xdiff}^{liq2}\left[\mathrm{X}_{Ydiff}\right]}{k_{Xdiff}^{liq1} + k_{Xdiff}^{liq2} + k_{rxn}^{bulk}\left[\mathrm{Y}_{Xdiff}\right]}, \qquad \text{Eq. 5.47}$$

$$\left[\mathrm{X}_{Ydiff}\right] = \frac{k_{Xdiff}^{liq3}\left[\mathrm{X}_{Xdiff}\right]}{k_{Xdiff}^{liq3} + k_{rxn}^{bulk}\left[\mathrm{Y}_{Ydiff}\right]}, \qquad \text{Eq. 5.48}$$

$$\left[\mathrm{Y}_{Xdiff}\right] = \frac{k_{Ydiff}^{liq1} \cdot \left[\mathrm{Y}_{Ydiff}\right]}{k_{Ydiff}^{liq1} + k_{rxn}^{bulk}\left[\mathrm{X}_{Xdiff}\right]}, \qquad \text{Eq. 5.49}$$

$$\left[\mathrm{Y}_{Ydiff}\right] = \frac{k_{Ydiff}^{liq2} \cdot \left[\mathrm{Y}_{Xdiff}\right] + k_{Ydiff}^{liq3} \cdot \left[\mathrm{Y}_{(total)}\right]}{k_{Ydiff}^{liq2} + k_{Ydiff}^{liq3} + k_{rxn}^{bulk}\left[\mathrm{X}_{Ydiff}\right]}. \qquad \text{Eq. 5.50}$$

Retrieval of γ_{total} is possible by solving equations Eq. 5.43-5.49 simultaneously. While it is technically possible to evaluate γ_{total} analytically, we solve these equations numerically as the analytical solutions become too cumbersome. Fig. 5.14 provides γ_{total} for an example set of droplet parameters. Like Case 5, uptake in this case exhibits a dependence on $\left[\mathrm{X}_{gas}^{\infty}\right]$ since the reaction diffusion length of Y and the steady state concentrations depend explicitly on $\left[\mathrm{X}_{gas}^{\infty}\right]$.

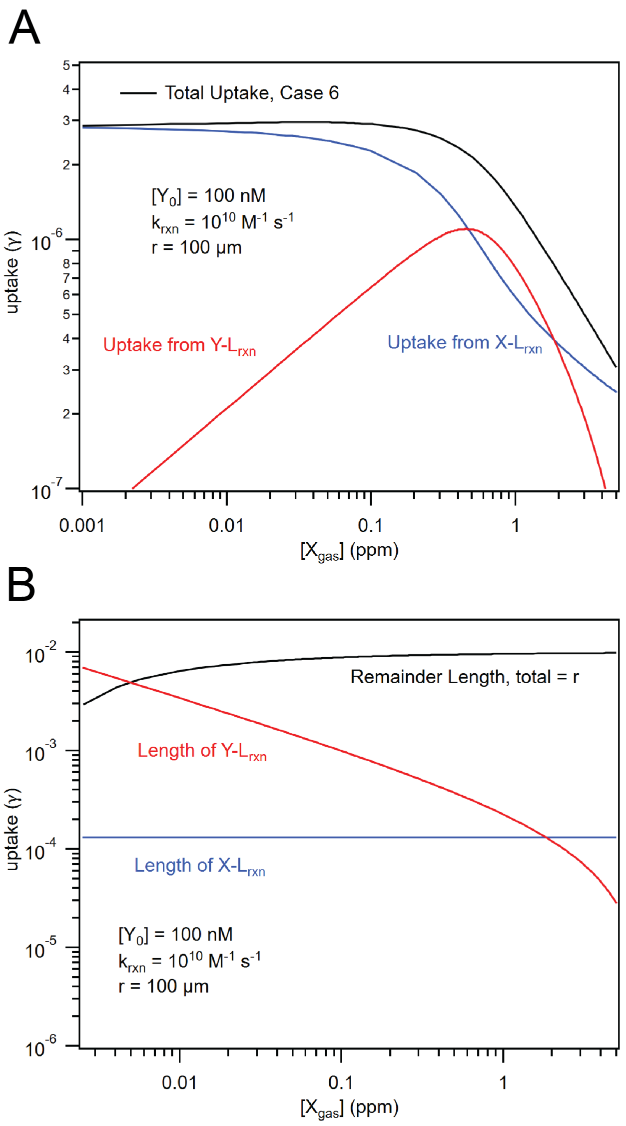

Fig. 5.14: (A) Uptake coefficients vs concentration of species X for Case 6 evaluated using Eqs. 5.44-5.46. (B) Length scales defined with changing [X_{gas}], which alters the reaction diffusion length of Y and therefore the remaining length of the droplet.

Lastly, we compare predictions from Case 6 with experimental uptake coefficients measured for ozone deposition onto a macroscopic surface of artificial seawater. Work by Schneider et al.[5] studied the uptake of O_3 onto simulated seawater by detecting O_3 depletion in a flow tube where a flow of O_3 was passed over a quartz half-tube containing [I^-] = 390 nM. The trend was observed where increasing [O_3] decreased the overall uptake onto the liquid surface. Analysis using a multilayer-kinetic model suggested this was due to depletion of iodide in the top ~ mm or so of the liquid solution. This is consistent with current results from Case 6, wherein we use the physical parameters outlined by Schneider et al. for the total surface area *SA*, the average depth *d* of the macroscopic solution, and the Henry's law coefficient for O_3 in the salt solution.

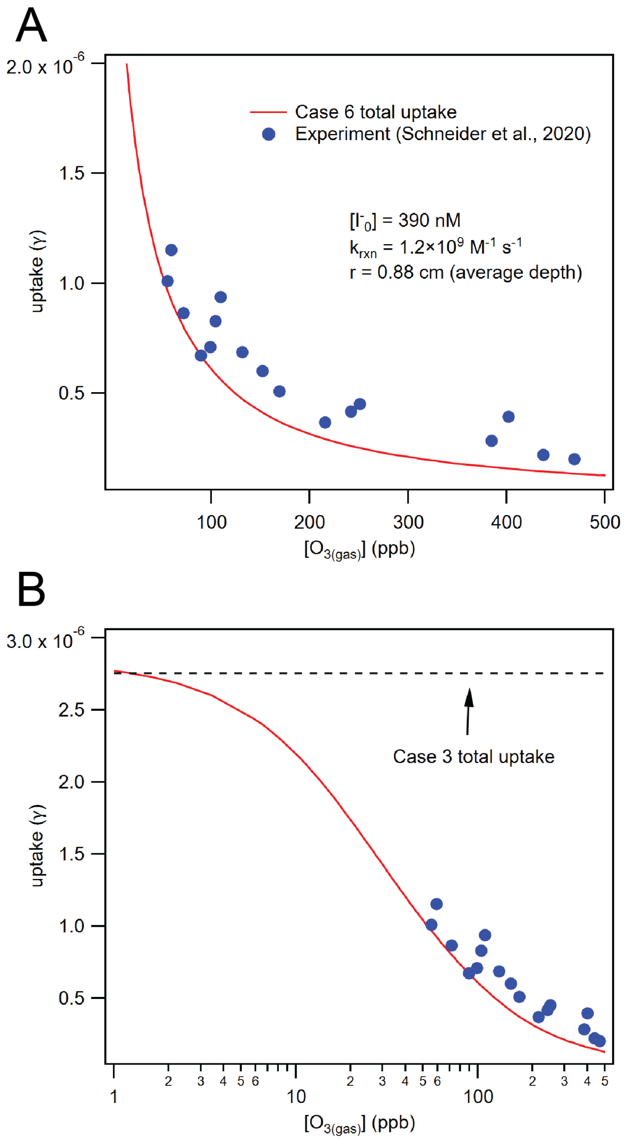

Fig. 5.15: Uptake coefficients vs. concentration [O$_3$] from Case 6 compared with data from Schneider et al.[5] Panel (A) shows the steep decrease in uptake with increasing [O$_3$] due to [I$^-$] depletion near the interface. Panel (B) shows how Case 6 predicts the uptake converges to Case 3 for diminishing [O$_3$] where iodide depletion is negligible.

5.5: Analysis of Steady-State Methods and Droplet Core Contributions

5.5.A: Steady-State Approach, Discrete and Continuum Models

In this section we take a closer look at the mechanics of the model employed, and how this model relates to earlier descriptions of multiphase chemistry. As noted in Chapter 1, the basis of this work builds off the early work of Danckwerts,[6,7] Schwartz and Freiberg,[2,8] and Davidovits and coworkers[1,9–11] who used a variety of analytical methods to build model descriptions of mass transport across interfaces and reagent diffusion coupled to chemical reaction in variety of gas-liquid systems. For our current treatment of the gas-phase diffusion process and adsorption to the interface, we direct the reader to Appendices 5B and 5C for an in-depth description and discussion, with comparisons to previous methods.

An illustrative comparison between methods can be made in the liquid-diffusion case where the solvation and reaction of the gaseous species X establishes a gradient within the condensed phase. As noted in Chapter 1 and exemplified in cases above, the present model approach approximates spatial gradients as discretized spatial regions that contain average properties that allow for the replication of dynamics observed in models that include much greater resolution of chemical gradients. Here we demonstrate using a continuous reaction-diffusion description that the number of X molecules within the gradient region is successfully approximated by the number of X molecules in the reaction-diffusion region as defined in Section 1. In the continuous spatial description, as described by Danckwerts[6] and Schwartz,[2] the concentration of X at the droplet surface is first assumed to be equal to the bulk Henry's law value $[\mathrm{X}_{\mathrm{surface}}] = \mathrm{H}_{\mathrm{gb}}$ $[\mathrm{X}_{\mathrm{gas}}]$. X can then be described to diffuse radially into the particle while simultaneously undergoing reaction with solute Y, assumed to be a constant $[\mathrm{Y}_{\mathrm{bulk}}]$. After an initial equilibration time, a steady-state concentration profile of $[\mathrm{X}_{\mathrm{bulk}}]$ will be realized. For a droplet of radius r = R, the steady-state concentration profile of X in the bulk-phase as a function of radial distance, $[\mathrm{X}_{\mathrm{bulk}}](r)$ is expressed:

$$[\mathrm{X}_{bulk}](r) = \left[\mathrm{X}_{surface}\right]\frac{R}{r}\frac{\sinh\left(r\sqrt{\frac{k_{rxn}[\mathrm{Y}_{bulk}]}{D_{\mathrm{X}}}}\right)}{\sinh\left(R\sqrt{\frac{k_{rxn}[\mathrm{Y}_{bulk}]}{D_{\mathrm{X}}}}\right)} = \left[\mathrm{X}_{surface}\right]\frac{R}{r}\frac{\sinh\left(\frac{rq}{R}\right)}{\sinh(q)}, \qquad \mathrm{Eq.\,5.51}$$

where the q parameter as used by Schwartz is equal to $q = R\sqrt{\frac{k_{rxn}[\mathrm{Y}_{bulk}]}{D_{\mathrm{X}}}}$. Here, D_X denotes the liquid-phase diffusion coefficient of X.

Integrating Eq. 5.51 from the droplet surface to a radial depth L provides an average concentration of X within the spherical shell volume defined by the shell region $L \leq r \leq R$. The average concentration of X throughout the droplet if we consider only the X molecules residing in the reactive region defined by $L = L_{rxn}$ can be defined as $[\mathrm{X}]_{avg}^{c}$ below, where we indicate the "continuous" approach with the superscript *c*:

$$[\mathrm{X}]_{avg}^{c} = \frac{3\,R^3\,\mathrm{csch}(q)}{q^2\left(R^3 - {L_{rxn}}^3\right)}H^{gb}\left(\,q\,r\,\cosh q - r\sinh(q) - q\,L\cosh\left(\frac{q\,L_{rxn}}{R}\right) + r\sinh\left(\frac{q\,L_{rxn}}{R}\right)\right). \qquad \mathrm{Eq.\,5.52}$$

The equivalent averaged concentration obtained from our discretized framework $[\mathrm{X}]_{avg}^{d}$ (where the "discrete" approach is indicated with superscript *d*) is simply the steady-state concentration of X inside the reaction-diffusion region, weighted by the relevant volumetric correction:

$$[\mathrm{X}]_{avg}^{d} = [\mathrm{X}_{rd}]\cdot V_{rd} = \frac{\left(\frac{k_{diff}^{gas}\,k_{ads}}{k_{diff}^{gas} + k_{ads}}\right)\left[\mathrm{X}_{gas}\right]}{k_{des} + k_{solv} + \left[\mathrm{Y}_{(ads)}\right]k_{rxn}^{surf} - \psi}\cdot\frac{V_{rd}}{V_{total}}, \qquad \mathrm{Eq.\,5.53}$$

where

$$\psi = \left(\frac{k_{des}\,k_{ads}}{k_{diff}^{gas} + k_{ads}}\right) + \left(\frac{k_{desolv}\,k_{solv}}{k_{diff1}^{liq} + k_{desolv}}\right) + \left(\frac{k_{diff1}^{liq}\,k_{diff2}^{liq}\,k_{desolv}\,k_{solv}}{\left(k_{diff2}^{liq} + k_{desolv}\right) \times \left(k_{desolv}\,[\mathrm{Y}_{(rd)}]\,k_{rxn}^{bulk} + k_{diff1}^{liq}[\mathrm{Y}_{(rd)}]k_{rxn}^{bulk} + k_{diff2}^{liq}\,k_{desolv}\right)}\right).$$

The averaged-continuous concentration $[\mathrm{X}]_{avg}^{c}$ and discretized concentration $[\mathrm{X}]_{avg}^{d}$ resulting from the coupled-equilibria approach are compared in Fig. 5.16. Recall that these concentrations indicate average concentrations of X throughout the whole droplet, but only account for the X molecules within the outer shell defined by L. We include Eq. 5.52 evaluated with $L = L_{rxn}$ and $L = 0$ for comparison, where $L = 0$ indicates the result averaged throughout the entire droplet volume.

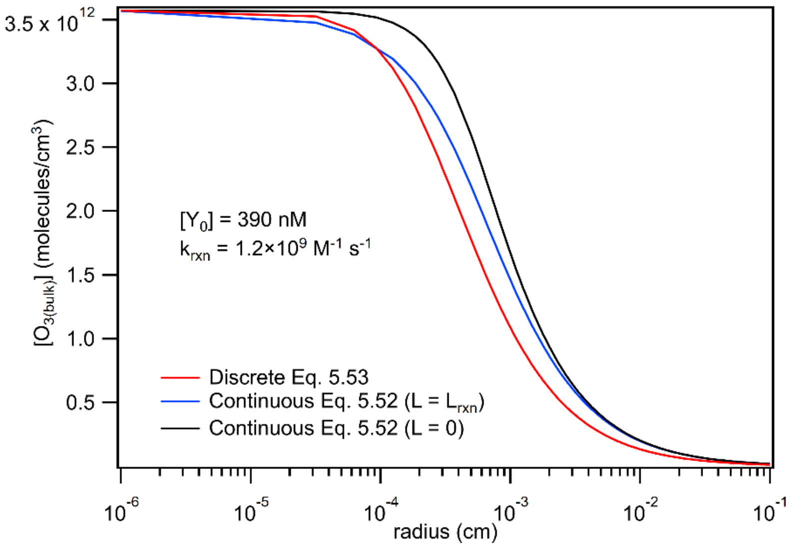

Fig. 5.16: Comparison of steady-state approaches, with the continuous description integrated from the droplet surface to depth L aside the steady-state concentration of the reaction diffusion compartment modified by the entire droplet volume.

In Fig. 5.16, the discrete approach obtained using the coupled-equilibria framework is shown to closely approximate the equivalent evaluation using continuous methods, where Eq. 5.52 is evaluated to the depth of the reaction diffusion length L_{rxn}. Results in Fig. 5.16 demonstrate the radial-dependence of the bulk-depletion effect in droplets, where the bulk concentration of X approaches the Henry's law condition for smaller radii (when $L_{rxn} > r$) but becomes significantly depleted—approaching zero—when $L_{rxn} < r$. As shown in Fig. 5.16, the discretized concentration is generally found to be numerically smaller than the continuous evaluation. This is due to the fact that $[\mathrm{X}]_{avg}^{d}$ is not only influenced by reaction and liquid diffusion, but by gas diffusion as well, which is not accounted for in the continuous approach producing $[\mathrm{X}]_{avg}^{c}$. Therefore, we expect the full coupled-equilibria approach including both diffusional contributions to provide a more accurate approximation to the steady-state droplet concentration compared to the continuous approach.

5.5.B: Bulk Core Uptake Contribution

Although the coupled-equilibria approach using a reaction-diffusion compartment closely approximates the integrated concentration gradient, the approach has explicitly neglected the inner "core" of the droplet beyond depth L_{rxn}. However, the framework applied so far allows us to define uptake contributions from the inner region of the droplet by using the same steady-state methods. Given a steady-state concentration of $[\mathrm{X}_{rd}]$ in the reaction-diffusion length, the steady-state concentration in the inner bulk region is simply:

$$[\mathrm{X}_{bulk}] = \frac{k_{diff3}^{liq}[\mathrm{X}_{rd}]}{k_{diff3}^{liq} + k_{rxn}^{bulk}\left[\mathrm{Y}_{(bulk)}\right]}, \qquad \text{Eq. 5.54}$$

where the diffusion rate coefficient is defined for transport between the reaction-diffusion region and the bulk, as defined in Appendix 5.A, with $k_{diff3}^{liq} = 2\, D_{\mathrm{X}}/r^2$. Uptake due to reaction in the inner core is found to be almost negligible under all conditions, as the vast majority of reactivity is defined to occur with the "reaction-diffusion" region. Uptake due to the inner bulk region has been observed to contribute only up to ~1% of reactivity compared to the reaction-diffusion region. The inner bulk contributions to overall γ can be calculated using Eq. 5.54 combined with Eq. 5.4, analogous to that of the reaction-diffusion region Eq. 5.3 and surface region Eq. 5.2.

5.6: Conclusions & Future Work

The methods and results throughout this chapter have outlined the general application of the "coupled-equilibria" kinetic model as introduced in Chapter 1 and utilized throughout Chapters 2-4, where average concentrations in discrete spatial regions can be combined to predict observable uptake coefficients in gas-liquid systems. We have identified six chemical kinetics scenarios for a spherical geometry that depend on a set of assumptions for concentrations and mixing times for generic reactants X and Y. The cases defined can be simply summarized with the particular assumptions employed. In cases 1-4, Y is uniformly distributed throughout the liquid phase and the distribution of X is assumed to vary in each case as follows: (1) X is distributed throughout the entire gas-liquid system according to Henry's law, (2) X is uniformly distributed in the gas-phase but is depleted in the liquid phase, (3) X is depleted in the liquid phase and at the interface, with partial depletion in the gas-phase, and (4) X is completely depleted throughout the gas-liquid system. Cases 5 and 6 relax the uniformity of Y and assume that (5) reactivity occurs only at the interface where X is fixed, and (6) X and Y are both partially depleted in the liquid phase and establish overlapping chemical gradients during reaction. This general approach has established a framework for representing chemical gradients with average quantities that can then be treated with simple rate law expressions to predict more complex chemical kinetics. In future work, we will demonstrate how the contents of this chapter agree with a number of experimental observations from aerosol- and heterogeneous-chemistry literature, suggesting a broad applicability of the modeling approach. Furthermore, future development of this approach will demonstrate that the application is not unique to descriptions of chemical kinetics but can also express the dynamics of condensation and evaporation processes, along with heat-transfer and the formation of temperature gradients in gas-liquid systems.

5.7: Chapter 5 Appendix: Mass-Transport Descriptions

Of particular importance for describing multiphase chemical kinetics is the diffusional description that governs larger-scale transport between the two phases, and the adsorption/desorption terms that govern molecular-scale transport across an interface. We first review the methods used to calculate liquid-phase diffusion kinetic constants that govern diffusional transport between adjacent liquid regions in Appendix 5A, followed by a derivation and discussion of the gas-phase diffusion kinetic constant in Appendix 5B.

Appendix 5A: Liquid-Diffusion Description

Starting with Fick's First Law, we obtain

$$J\left(\frac{molec.}{cm^2\ \cdot s}\right) = -D\,\nabla[\mathrm{X}] = -D\,\frac{([\mathrm{X}_1]-[\mathrm{X}_2])}{\frac{1}{2}\cdot(L_1+L_2)}, \qquad \text{Eq. 5A. 1}$$

where $[X_1]$ and $[X_2]$ are the concentrations of species X in hypothetical compartments 1 & 2, respectively. L_1 and L_2 refer to the lengths of the respective compartments and D is a generic diffusion coefficient of X. Multiplying Eq. 5A.1 by a cross-sectional area gives molecules transferred per second:

$$Molecular\ rate\left(\frac{molec.}{s}\right) = -2\cdot D\cdot\frac{([\mathrm{X}_1]-[\mathrm{X}_2])}{\frac{1}{2}\cdot(L_1+L_2)}\cdot A, \qquad \text{Eq. 5A. 2}$$

where A is the area connecting the adjacent compartments.

Dividing Eq. 5A. 2 by some volume provides a rate equation

$$Rate\left(\frac{molec.}{s\ cm^3}\right) = -2\cdot D\cdot\frac{([\mathrm{X}_1]-[\mathrm{X}_2])}{\frac{1}{2}\cdot(L_1+L_2)}\cdot\frac{A}{\boldsymbol{V}}, \qquad \text{Eq. 5A. 3}$$

where volume $\boldsymbol{V}$ can be either $\boldsymbol{V_1} = A\ L_1$ or $\boldsymbol{V_2} = A\ L_2$, depending on the specific kinetic process. As demonstrated below, this choice of $\boldsymbol{V}$ is simply governed by which differential the rate in Eq. 5A.3 is meant to describe.

(i) Kinetic Description

To describe diffusion between two adjacent compartments analytically, four kinetic steps need to be considered. These four steps can be visualized using two idealized processes:

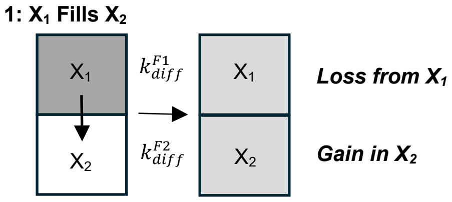

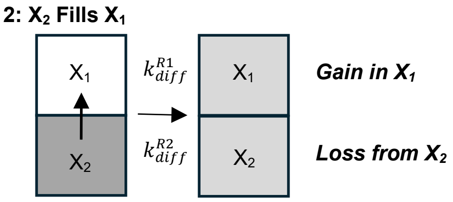

In reality, these two processes occur simultaneously as the system equilibrates. Regardless of the initial conditions, rate equations for concentrations $[X_1]$ and $[X_2]$ are

$$\frac{d[\mathrm{X}_1]}{dt} = -k_{diff}^{F1}[\mathrm{X}_1] + k_{diff}^{R1}[\mathrm{X}_2], \qquad \text{Eq. 5A. 4}$$

$$\frac{d[\mathrm{X}_2]}{dt} = -k_{diff}^{R2}[\mathrm{X}_2] + k_{diff}^{F2}[\mathrm{X}_1], \qquad \text{Eq. 5A. 5}$$

Here the convention is used that all rate coefficients are positive, and the sign of each term on the RHS denotes loss or gain of the concentration described in the differential. To calculate a specific term (e.g. k_{diff}^{F1}) we use Eq. 5A.3. Assuming $[\mathrm{X}_2] = 0$, this evaluates to

$$k_{diff}^{F1}\,[\mathrm{X}_1] = |Rate| = \left|2 \cdot D \cdot \frac{([\mathrm{X}_1] - 0)}{(L_1 + L_2)} \cdot \frac{A}{\boldsymbol{V_1}}\right|,$$

$$k_{diff}^{F1} = \frac{2 \cdot D}{(L_1 + L_2) \cdot L_1}. \qquad \text{Eq. 5A. 6}$$

Importantly, $\boldsymbol{V_1}$ is selected as the relevant volume in Eq. 5A.6 because k_{diff}^{F1} is defined by Eq. 5A.4, which describes concentration changes occurring within $\boldsymbol{V_1}$.

Following the same derivation of k_{diff}^{R1} gives the same result:

$$k_{diff}^{R1}\,[\mathrm{X}_2] = |Rate| = \left|2 \cdot D \cdot \frac{(0 - [\mathrm{X}_2])}{(L_1 + L_2)} \cdot \frac{A}{\boldsymbol{V_1}}\right|,$$

$$k_{diff}^{R1} = \frac{2 \cdot D}{(L_1 + L_2) \cdot L_1} = k_{diff}^{F1}. \qquad \text{Eq. 5A. 7}$$

This shows that within a given differential, e.g. Eq. 5A.4, the forward and reverse diffusion rate constants are equivalent (recall the sign has been defined in Eq. 5A.4—and we have taken the absolute value for the coefficients in Eq. 5A.6 and 5A.7). Similarly, the forward and reverse rate constants in the other differential, Eq. 5A.5 are:

$$k_{diff}^{R2} = \frac{2 \cdot D}{(L_1 + L_2) \cdot L_2} = k_{diff}^{F2},$$

which we obtain from the same procedure but using $\boldsymbol{V_2}$ instead.

Example: O_3 transport from surface (sb) compartment into reaction-diffusion (rd) compartment

Skipping the details, the steady-state concentration of O_3 in the *rd* compartment $[O_{3(rd)}]$ depends on the steady-state concentration $[O_{3(sb)}]$ the surface compartment, which in turn depends on the steady-state concentration of adsorbed ozone $[O_{3(ads)}]$. Ignoring the definition of $[O_{3(ads)}]$ for now, we define $[O_{3(sb)}]$:

$$[O_{3(sb)}] = \frac{k_{solv}\,[O_{3(ads)}] + k_{diff}^{R1}[O_{3(rd)}]}{k_{desolv} + k_{diff}^{F1}}.$$

As noted above, while k_{diff}^{R1} and k_{diff}^{F1} do refer to different directions, their magnitude is the same so a single kinetic coefficient (k_{diff}^{1}) can be defined:

$$k^{1}_{diff} = \frac{2D}{(\delta + L) \cdot \delta} = k^{F1}_{diff} = k^{R1}_{diff},$$

where L is the length of *rd*. Writing out $[\mathrm{O}_{3(rd)}]$, we get

$$[\mathrm{O}_{3(rd)}] = \frac{k^{F2}_{diff}[\mathrm{O}_{3(sb)}]}{k_{rxn} + k^{R2}_{diff}}.$$

The diffusion rate k^{2}_{diff} can be defined similarly to k^{1}_{diff} as

$$k^{2}_{diff} = \frac{2D}{(\delta + L) \cdot L} = k^{F2}_{diff} = k^{R2}_{diff}.$$

Substituting $[\mathrm{O}_{3(sb)}]$ and solving for $[\mathrm{O}_{3(rd)}]$ then gives

$$[\mathrm{O}_{3(rd)}] = \frac{k^{2}_{diff}\ k_{solv}\ [\mathrm{O}_{3(ads)}]}{k_{desolv}\ k^{RD}_{rxn} + k_{desolv}\ k^{2}_{diff} + k^{1}_{diff}\ k_{rxn}}.$$

For the definition of $[\mathrm{O}_{3(ads)}]$, see Eq. 4.11 in Chapter 4.

Appendix 5B: Gas Adsorption & Collision Kinetics

Of particular importance for describing multiphase chemical kinetics is the diffusional description that governs larger-scale transport between the two phases, and the adsorption/desorption terms that govern molecular-scale transport across an interface. This Appendix addresses how the kinetic adsorption coefficient is related to the collision frequency of a gas X on the droplet interface. The following Appendix 5C unites this collisional picture with a diffusional picture and ties this relationship back to macroscopic gas-transport descriptions.

For convenience, we use the gas X = O_3 here to make the derivation more concrete and applicable to Chapters 2-5. To understand the O_3 adsorption rate and address its relationship to collisional flux and the maintenance of Henry's law surface concentrations, we start with the primary expression for collisional flux Eq. 5B.1, and the Henry's law definition Eq. 5B.2:

$$J\left(\frac{molec}{cm^{2}\ s}\right) = \frac{c}{4} \cdot [\mathrm{O}_{3(gas)}], \qquad \text{Eq. 5B.1}$$

$$H^{gs} = \frac{[\mathrm{O}_3^{ads}]}{[\mathrm{O}_3^{gas}]} = \frac{k^{1}_{ads}}{k_{des}} = \frac{k^{2}_{ads}}{k_{des}} \cdot \frac{\Gamma^{\infty}}{\delta}. \qquad \text{Eq. 5B.2}$$

In Eq. 5B.2, the first-order adsorption rate is the product of the second-order rate multiplied by site concentration in simulated surface compartment $k^{1}_{ads} = k^{2}_{ads} \cdot \frac{\Gamma^{\infty}}{\delta}$.

Using the standard $\frac{\Gamma^{\infty}}{\delta^{sim}} = 5.42 \times 10^{21}\ \text{site/cm}^3$ for O_3 and model values $H^{gs} = 4.97$ and $k_{des} = 1.93 \times 10^{10}\ s^{-1}$, the rates in Eq. 5B.2 evaluate to

$$k^{1}_{ads} = k_{des} \cdot H^{gs} = 9.59 \times 10^{10}\ \mathrm{s}^{-1}, \qquad \text{Eq. 5B.3}$$

$$k^{2}_{ads} = k_{des} \cdot H^{gs} \cdot \frac{\delta}{\Gamma^{\infty}} = 1.77 \times 10^{-11}\ \mathrm{cm^3/molecule\ s^{-1}}. \qquad \text{Eq. 5B.4}$$

Using Eq. 5B.1, we can write the rate equation for O_3 colliding with simulation area A^{sim} and entering simulation volume $V^{sim} = A^{sim} \cdot \delta^{sim}$

$$\text{Rate}\left(\frac{molec}{cm^3\ s}\right) = J \cdot \frac{A^{sim}}{V^{sim}} = \frac{c}{4 \cdot \delta^{sim}} \cdot \left[\mathrm{O}_{3(gas)}\right], \qquad \text{Eq. 5B. 5}$$

which defines the first and second-order collision rates:

$$k_{col}^{1} = k_{col}^{2} \cdot \frac{\Gamma^{\infty}}{\delta^{sim}} = \frac{c}{4 \cdot \delta^{sim}} \qquad \text{Eq. 5B. 6}$$

Using the values $\Gamma^{\infty} = 5.42 \times 10^{14}$ site/cm^2 and $\delta^{sim} = 1$ nm, the coefficients in Eq. 5B.6 evaluate to

$$k_{col}^{1} = 9 \times 10^{10}\ \mathrm{s}^{-1}, \qquad \text{Eq. 5B. 7}$$

$$k_{col}^{2} = \frac{c}{4 \cdot \Gamma^{\infty}} = 1.66 \times 10^{-11}\ \mathrm{cm}^3/\mathrm{molecule}\ \mathrm{s}^{-1}. \qquad \text{Eq. 5B. 8}$$

Sets of Equations (5B.3, 5B4) and (5B.7, 5B.8) demonstrate that the adsorption kinetic coefficients (derived ultimately from the molecular simulations of Chapter 2 and Polley et al.[12]) and collisional coefficients differ by only ~ 5%. This difference is likely due to assumptions made about the constants $\Gamma^{\infty}$and δ^{sim}.

Appendix 5C: Gas Diffusion: Kinetic Approach to Discrete and Continuum Models

Having reconciled the adsorption and collision rate for a gas X on the droplet surface, we now turn to the diffusional description of X in the surrounding gas phase. This description builds off the concepts introduced in Appendix B, where the collisional flux onto a surface was discussed and the kinetic coefficient k_{ads} defined. Here we assume that $k_{ads} = k_{col}$ as found to be the case in the preceding example. Contrary to a strictly collisional description, an alternative flux equation relying on diffusional transport of X that describes the molecular flow at the boundary of a sphere of radius *r* can be written[13]

$$J_c\left(\frac{molec}{s}\right) = 4\,\pi\ \cdot D_{gas}^{X}\, r \cdot \left[\mathrm{X}_{gas}^{\infty}\right], \qquad \text{Eq. 5C. 1}$$

where J_c indicates the flux in the “continuum” regime, as referenced later.

An equivalent molecular flux description in a collisional (or kinetic) framework is written

$$J_k\left(\frac{molec}{s}\right) = 4\,\pi\, r \frac{\bar{c}}{4} \cdot \left[\mathrm{X}_{gas}^{\infty}\right], \qquad \text{Eq. 5C. 2}$$

where J_k similarly indicates flux in the “kinetic” or molecular regime. In the most basic treatment of diffusion used in this (and preceding) chapters, transport of X is described by diffusion of $\left[\mathrm{X}_{gas}^{\infty}\right]$ into the droplet surface region (with thickness δ) using Eq. 5C.1. X that enters the surface region contributes to the near-surface concentration $\left[\mathrm{X}_{gs}\right]$, which then adsorbs to the interface following the kinetics of Eq. 5C.2, equivalent to the definition of k_{ads}. Written out in kinetic steps, we describe the process with two reversible steps

$$[\mathrm{X}_{gas}^{\infty}] \underset{k_{diff}^{gas}}{\overset{k_{diff}^{gas}}{\rightleftarrows}} [\mathrm{X}_{gs}], \tag{S1}$$

$$[\mathrm{X}_{gs}] + [site_X] \underset{k_{des}}{\overset{k_{ads}}{\rightleftarrows}} [\mathrm{X}_{(ads)}], \tag{S2}$$

where *site*$_X$ denotes a surface site for X, with maximum coverage given by Γ_X^{∞}/δ as previously discussed. As noted in Appendix B, the collision rate is equal to the pseudo-first order adsorption rate, with $k_{col} = k_{ads}\frac{\Gamma_X^{\infty}}{\delta}$. The rate coefficient k_{diff}^{gas} is derived from Eq. 5C.1, but with the use of a more general form from Crank[14] for diffusion of species X through the spherical wall with outer boundary *b* and inner boundary *a:*

$$J\left(\frac{molec}{s}\right) = 4\,\pi \cdot D_{gas}^{X}\,\frac{b\cdot a}{b-a}([X_b]-[X_a]), \qquad \text{Eq. 5C.3}$$

where we consider the inner boundary *a* = *r*, $[X_b] = [\mathrm{X}_{gas}^{\infty}]$ and $[X_a] = 0$. This final condition indicates the upper limit of diffusion transport where the surface concentration at *r* is completely depleted. For the outer boundary *b*, we consider the limit *b* → ∞ in order to identify the lower bound of *J* where the rate of diffusional transport to the spherical interface will realize a minimum. In the limit *b* → ∞, Eq. 5C.3 becomes

$$J\left(\frac{molec}{s}\right) = 4\,\pi \cdot D_{gas}^{X}\,r \cdot [\mathrm{X}_{gas}^{\infty}], \qquad \text{Eq. 5C.4}$$

which is equivalent to Eq. 5C.1. To recognize the rate coefficient of interest, we divide Eq. 5C.4 by the spherical shell volume of the surface to define the rate equation

$$J\left(\frac{molec}{cm^3\,s}\right) = \frac{4\pi\,D_{gas}^{X}\,r}{\frac{4}{3}\pi\,(r^3-(r-\delta)^3)}\cdot[\mathrm{X}_{gas}^{\infty}] \approx \frac{4\pi\,D_{gas}^{X}\,r}{4\pi\,r^2\,\delta}\cdot[\mathrm{X}_{gas}^{\infty}], \qquad \text{Eq. 5C.5}$$

where the surface volume can be reasonable approximated by the product of the spherical surface area and the surface thickness when *r* >> δ. From Eq. 5C.5, the rate of diffusion to the interface can be written as

$$J\left(\frac{molec}{cm^3\,s}\right) = k_{diff}^{gas}\cdot[\mathrm{X}_{gas}^{\infty}] \qquad \text{Eq. 5C.6}$$

with the gas-diffusion rate coefficient defined as

$$k_{diff}^{gas} = \frac{D_{gas}^{X}}{r\,\delta}. \qquad \text{Eq. 5C.7}$$

Note that this rate coefficient controls both the rate of X into the surface compartment generating $[\mathrm{X}_{gs}]$, but also the rate at which $[\mathrm{X}_{gs}]$ diffuses away from the surface, re-generating $[\mathrm{X}_{gas}^{\infty}]$, as indicated by kinetic step S1.

During the net-adsorption process the diffusional process described above and the interfacial adsorption process occur simultaneously, and therefore, the near-surface species $[\mathrm{X}_{gs}]$ has both diffusional and adsorption contributions to it's steady-state value. In the limit of complete surface loss after surface adsorption, the steady-state concentration of $[\mathrm{X}_{gs}]$ is

$$[\mathrm{X}_{gs}] = \frac{k_{diff}^{gas}}{k_{ads}\frac{\Gamma_X^{\infty}}{\delta} + k_{diff}^{gas}}[\mathrm{X}_{gas}^{\infty}] = \frac{\frac{D_{gas}^{X}}{r\,\delta}}{\frac{\bar{c}}{4\,\delta} + \frac{D_{gas}^{X}}{r\,\delta}}[\mathrm{X}_{gas}^{\infty}] = \frac{J}{J_k}[\mathrm{X}_{gas}^{\infty}]. \qquad \text{Eq. 5C.8}$$

Eq. 5C.8 denotes the "effective" concentration of X from the perspective of the interface. During adsorption and loss of X, the near-surface concentration $[\mathrm{X}_{gs}]$ resembles $[\mathrm{X}_{gas}^{\infty}]$ when the radius r is small but becomes significantly depleted when r is large—since the adsorption loss to the interface becomes faster than the diffusional transport, which slows with increasing r as in Eq. 5C.7. From an alternative point of view, Eq. 5C.8 expresses that the near-surface gas concentration is related to the true gas concentration by a transport probability term that expresses how much the near-surface gas behavior resembles the "molecular" behavior expected by the purely collisional description used for adsorption. As included in Eq. 5C.8, this can be expressed by a simple ratio of flux terms, where the true gas flux divided by a reference flux (the molecular flux J_K in this case) provides the same fractional term.

This first observation is equivalent to that of Fuchs & Sutugin[3] using the method of flux-matching to a boundary sphere of radius $r + \Delta$ for the elementary case where $\Delta = 0$, expressed in terms of the Knudsen number $\mathrm{Kn} = \frac{3\,D_{gas}^{X}}{\bar{c}\,r}$:

$$F_{\Delta=0}^{k} = \frac{J}{J_k} = \frac{1}{1 + \frac{3}{4}\mathrm{Kn}^{-1}}. \qquad \text{Eq. 5C.9}$$

Note that Eq. 5C.9 can instead be represented as the fraction of the diffusional flux rather than kinetic flux, which applies under the continuum regime where:

$$F_{\Delta=0}^{c} = \frac{J}{J_c} = \frac{1}{1 + \frac{4}{3}\mathrm{Kn}}, \qquad \text{Eq. 5C.10}$$

given the relation

$$\frac{J_c}{J_k} = \frac{4}{3}\mathrm{Kn}. \qquad \text{Eq. 5C.11}$$

Although the gas-transport term in Eq. 5C.8 and Fuchs' expression for $\Delta = 0$ agree exactly, the transport Eq. 5C.8 can be slightly modified to agree with Fuchs' general expression for a general boundary sphere of $r + \Delta$. To accomplish this, we set up a simple expression that is in fact equivalent to Fuchs' continuous description of boundary-sphere flux matching. We define the flux-matching boundary condition by asserting that the number of molecules that diffuse from the gas phase into the near-surface region must equal the sum of the number of molecules colliding with the droplet surface and diffusing back out into the outer gas phase:

$$4\pi\, D_{gas}^{X}\,(r+\,\Delta)\big[\mathrm{X}_{gas}^{\infty}\big] = 4\pi\, D_{gas}^{X}\,(r+\,\Delta)\big[\mathrm{X}_{gs}\big] + 4\pi\, r^{2}\frac{\bar{c}}{4}\big[\mathrm{X}_{gs}\big], \qquad \text{Eq. 5C. 12}$$

which can be rearranged to express the steady state concentration of near-surface gas concentration, analogous to Eq. 5C.8:

$$\big[\mathrm{X}_{gs}\big] = \frac{4\pi\, D_{gas}^{X}\,(r+\,\Delta)}{4\pi\, r^{2}\frac{\bar{c}}{4} + 4\pi\, D_{gas}^{X}\,(r+\,\Delta)}\big[\mathrm{X}_{gas}^{\infty}\big]. \qquad \text{Eq. 5C. 13}$$

The gas-transport term in Eq. 5C.13 can be rearranged using the definition of Kn to yield

$$\frac{4\pi\, D_{gas}^{X}\,(r+\,\Delta)}{4\pi\, r^{2}\frac{\bar{c}}{4} + 4\pi\, D_{gas}^{X}\,(r+\,\Delta)} = \frac{J}{J_k} = \frac{1+\mathrm{Kn}\,{}^{\Delta}\!/_{\lambda}}{1+0.75\,\mathrm{Kn}^{-1}+\mathrm{Kn}\,{}^{\Delta}\!/_{\lambda}}, \qquad \text{Eq. 5C. 14}$$

where λ is the mean free path defined here as $\lambda = \frac{3\,D_{gas}^{X}}{\bar{c}\,r}$. This shows that the discrete or coupled-equilibria approach to describing near-gas concentrations within a shell of length Δ results in exactly the results of Fuchs & Sutugin[3] when integrating the steady-state condition for the concentration profile at position $r + \Delta$ with boundary conditions set by an equivalent flux matching condition.

Given that Eq. 5C.13 maps onto the description of Fuchs & Sutugin,[3] this description equivalently maps onto the "Fuchs correction" used to account for diffusional "resistance" in the widely-applied resistor formulation of multiphase kinetics.[1,9,15] We note, however, that the Fuchs correction follows the expanded method outline by Fuchs & Sutugin[3] in which Eq. 5C.14 is slightly adapted to agree with numerical solutions to the Boltzmann equation across the Kn range. For completeness, we include this adapted transport term:

$$\frac{J}{J_k} = \frac{1+\mathrm{Kn}\,{}^{\Delta}\!/_{\lambda}}{1+0.283+0.75\,\mathrm{Kn}^{-1}+\mathrm{Kn}\,{}^{\Delta}\!/_{\lambda}} = \gamma_{fuchs}, \qquad \text{Eq. 5C. 15}$$

which includes a small augmentation of the denominator with additional constant 0.283. We note that typically, the boundary sphere distance Δ is typically chosen to equal approximately the mean free path λ which further simplifies Eq. 5C.13. As shown in Fig. 5.17, the transport terms found in Eq. 5C.8, Eq. 5C.13, and Eq. 5C.15 are all numerically close to each other, differing only modestly in the transition regime.

To summarize, our standard method for treating diffusion yields kinetic coefficients

$$k_{diff}^{gas} = \frac{D_{gas}^{X}}{r\,\delta},$$

$$k_{col} = k_{ads}\frac{\Gamma_X^{\infty}}{\delta} = \frac{\bar{c}}{4\,\delta},$$

which, when analyzed in light of mechanistic steps S1 and S2, yields an identical gas-to-surface transport efficiency as described by the simplest case from Fuchs & Sutugin[3] with the boundary sphere distance $\Delta = 0$. To account for a nonzero boundary-sphere thickness Δ, the rate coefficient for the diffusional process above can be modified to include the flux at distance $r + \Delta$, respective to the surface region by dividing by the surface volume:

$$k_{diff}^{gas} = \frac{4\pi\, D_{gas}^{X}(r+\Delta)}{4\pi\, r^2\, \delta} = \frac{D_{gas}^{X}(r+\Delta)}{r^2\, \delta}$$

$$k_{col} = \frac{4\pi\, r^2\, {}^{\bar{c}}/_{4}}{4\pi\, r^2\, \delta} = \frac{\bar{c}}{4\,\delta}.$$

Fig. 5.17 (A) summarizes these observations, providing results from Eqs. 5C.8 and 5C.13 compared to the Fuchs Correction Eq. 5C.15. For reference, panel (B) in Fig. 5.17 evaluates the radial dependence of k_{col} and k_{diff}^{gas} with $\bar{c}$ = 360 m/s, D_{gas}^{X} = 0.18 cm^2/s, and δ = 1 nm.

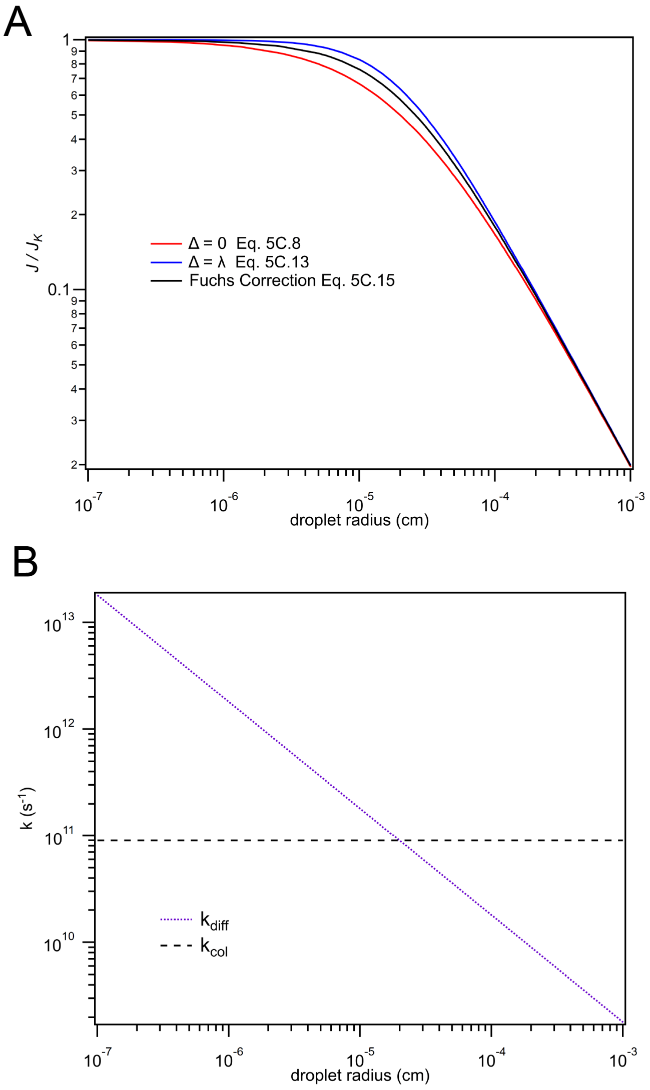

Fig. 5.17: (A) Comparison of diffusional descriptions, showing the fraction of collisional-type flux vs. droplet radius for the three descriptions encountered in Eqs. 5C.8, 5C.13, and 5C.15. (B) Radial dependence of the kinetic coefficients k_{diff} and k_{col}.

5.8: References

(1) Worsnop, D. R.; Morris, J. W.; Shi, Q.; Davidovits, P.; Kolb, C. E. A Chemical Kinetic Model for Reactive Transformations of Aerosol Particles. *Geophys. Res. Lett.* **2002**, *29* (20), 57-1-57–4. https://doi.org/10.1029/2002GL015542.

(2) Schwartz, S. E. Mass-Transport Considerations Pertinent to Aqueous Phase Reactions of Gases in Liquid-Water Clouds; Springer Berlin Heidelberg: Berlin, Heidelberg, 1986; pp 415–471.

(3) Fuchs, N. A.; Sutugin, A. G. High-Dispersed Aerosols. In *Topics in Current Aerosol Research*; Hidy, G. M., Brock, J. R., Eds.; International Reviews in Aerosol Physics and Chemistry; Pergamon, 1971; p 1. https://doi.org/10.1016/B978-0-08-016674-2.50006-6.

(4) Bain, A.; Lalemi, L.; Croll Dawes, N.; Miles, R. E. H.; Prophet, A. M.; Wilson, K. R.; Bzdek, B. R. Surfactant Partitioning Dynamics in Freshly Generated Aerosol Droplets. *J. Am. Chem. Soc.* **2024**. https://doi.org/10.1021/jacs.4c03041.

(5) Schneider, S. R.; Lakey, P. S. J.; Shiraiwa, M.; Abbatt, J. P. D. Reactive Uptake of Ozone to Simulated Seawater: Evidence for Iodide Depletion. *J. Phys. Chem. A* **2020**, *124* (47), 9844–9853. https://doi.org/10.1021/ACS.JPCA.0C08917.

(6) Danckwerts, P. V. Absorption by Simultaneous Diffusion and Chemical Reaction. *Trans. Faraday Soc.* **1950**, *46* (0), 300–304. https://doi.org/10.1039/TF9504600300.

(7) Danckwerts, P. V. Absorption by Simultaneous Diffusion and Chemical Reaction into Particles of Various Shapes and into Falling Drops. *Trans. Faraday Soc.* **1951**, *47* (0), 1014–1023. https://doi.org/10.1039/TF9514701014.

(8) Schwartz, S. E.; Freiberg, J. E. Mass-Transport Limitation to the Rate of Reaction of Gases in Liquid Droplets: Application to Oxidation of SO2 in Aqueous Solutions. *Atmospheric Environ. 1967* **1981**, *15* (7), 1129–1144. https://doi.org/10.1016/0004-6981(81)90303-6.

(9) Kolb, C. E.; Davidovits, P.; Jayne, J. T.; Shi, Q.; Worsnop, D. R. Kinetics of Trace Gas Uptake by Liquid Surfaces. *Prog. React. Kinet. Mech.* **2002**, *27* (1), 1–46. https://doi.org/10.3184/007967402103165324.

(10) Jayne, J. T.; Worsnop, D. R.; Kolb, C. E.; Swartz, E.; Davidovits, P. Uptake of Gas-Phase Formaldehyde by Aqueous Acid Surfaces. *J. Phys. Chem.* **1996**, *100* (19), 8015–8022. https://doi.org/10.1021/jp953196b.

(11) Davidovits, P.; Jayne, J. T.; Duan, S. X.; Worsnop, D. R.; Zahniser, M. S.; Kolb, C. E. Uptake of Gas Molecules by Liquids: A Model. *J. Phys. Chem.* **1991**. https://doi.org/10.1021/j100169a048.

(12) Polley, K.; Wilson, K. R.; Limmer, D. T. On the Statistical Mechanics of Mass Accommodation at Liquid–Vapor Interfaces. *J. Phys. Chem. B* **2024**, *128* (17), 4148–4157. https://doi.org/10.1021/acs.jpcb.4c00899.

(13) Seinfeld, J. H.; Pandis, S. N. Mass Transfer Aspects of Atmospheric Chemistry. In *Atmospheric Chemistry and Physics: From Air Polution to Climate Change*; John Wiley & Sons, Inc., 1998.

(14) Crank, J. *The Mathematics of Diffusion*, 2nd ed.; Oxford University Press, 1975.

(15) Hanson, D. R.; Ravishankara, A. R.; Lovejoy, E. R. Reaction of BrONO2 with H2O on Submicron Sulfuric Acid Aerosol and the Implications for the Lower Stratosphere. *J. Geophys. Res. Atmospheres* **1996**, *101* (D4), 9063–9069. https://doi.org/10.1029/96JD00347.